Die approbierte Originalversion dieser Dissertation ist in der Hauptbibliothek der Technischen Universität Wien aufgestellt und zugänglich.
http://www.ub.tuwien.ac.at

The approved original version of this thesis is available at the main library of the Vienna University of Technology.
http://www.ub.tuwien.ac.at/eng

DISSERTATION

Mechanical and Electrical Properties of Amorphous Silicon Nitride Thin Films for MEMS

zur Erlangung des akademischen Grades

Doktor der technischen Wissenschaften (Dr. techn.)

Institut für Sensor- und Aktuatorsysteme

Technische Universität Wien

Dipl.-Ing. Dávid Dergez

Matrikelnummer: 0828458

Wien, 2017

Verteidigung:	Wien, 18.12.2017
Betreuer und Prüfer:	Univ.-Prof. Dr. rer. nat. Ulrich Schmid
	Technische Universität Wien, Österreich
Erstgutachter und Prüfer:	Univ.-Prof. Dipl.-Ing. Dr. mont. Paul Heinz Mayrhofer
	Technische Universität Wien, Österreich
Zweitgutachter:	Univ.-Prof. Dr. sc. Silvan Schmid
	Technische Universität Wien, Österreich
Vorsitzender:	Univ.-Prof. Dr. Gottfried Strasser
	Technische Universität Wien, Österreich

Acknowledgements

Although only one name stands as author at the front of a doctoral dissertation, this work had never been completed without the help of great many people.

First and foremost, my utmost gratitude goes to Univ.-Prof. Dr. rer. nat. Ulrich Schmid, who invited me to join his group as a PhD candidate after being the supervisor of my Master's thesis. His expert guidance, attitude in aiming for excellence, and staunch support at all times were invaluable assets. Furthermore, our postdoctoral researchers: Dr. Achim Bittner and Dr. Michael Schneider, deserve the highest appreciation for their helpfulness and valuable inputs.

The experience and expertise of Dr. Johannes Schalko and Dr. Artur Jachimowicz have been most helpful in technological matters. In addition, I would like to thank our technologists: Sophia Ewert, Edeltraud Svasek, Peter Svasek, Patrick Meyer, and Michael Buchholz for their assistance. Further thanks go to Martina Nuhsbaumer, Andreas Astleitner and Franz Prewein for providing me administrative, moral and technical support, thus enabling me to concentrate on the scientific questions. During my work, I had opportunity to supervise the Master's thesis of Natalia Pawlak, many thanks goes to her for her collaboration.

The thesis supported within the European Union 7th Framework Programme project ALBICAN, for which I am eternally grateful. The collaboration with external project partners has been a very uplifting experience. My thanks go to Dr. Ernest J. Fantner of SCL Sensor Tech. Fabrication GmbH, Vladimir Stavrov of AMG Technology Ltd., and all the involved colleagues.

For a cheerful and supportive workplace atmosphere, I would like to thank all my fellow PhD students of the institute, especially Dr. Andreas Backes, Dr. Frank Steinhäußer and Dr. Martin Kucera, whom I had the pleasure of sharing an office and many memories.

Finally, I would like to express my deepest gratitude to my friends and family, my parents, István Dergez and Rózsa Élő for their continuous support throughout the many years of my studies, and to my partner Ági for her patience and for being at my side.

Abstract

Besides well-established markets such as automotive, microelectromechanical systems (MEMS) devices are readily integrated in a growing number of consumer, industrial, and medical applications. The diversity of these application scenarios often demands the fulfilment of very specific requirements with respect to the materials being implemented. The engineering of thin film material systems enables to deliver tailored solutions that are both optimal for the application, and for a later commercialization in the ideal case compatible with existing CMOS technologies.

Silicon nitride (SiN_x) thin films have found their use in microelectronic and MEMS devices as standard materials in various functionalities, including electrical isolation, capping passivation, optical waveguides and structural-mechanical layers. Despite their widespread usage and associated experience, SiN_x thin films still offer a large untouched potential by exploiting the full flexibility of certain deposition processes.

In this work, amorphous silicon nitride films were synthesized using two different plasma processes: inductively coupled plasma chemical vapour deposition (ICP-CVD) and reactive magnetron sputter deposition. The deposited samples were characterized using a wide range of analytical equipment with regards to their mechanical, optical and electrical properties, as well as their chemical composition.

The properties of ICP-CVD deposited SiN_x films were found to be strongly dependent on the ratio of the precursor gases $R_{N2/SiH4}$. A too low value leads to extremely silicon rich films, with a high amount of biaxial stress and poor insulating performance, while a too high ratio results in a material with significant concentrations of even unbound H_2, and is permeable to water vapour. This leads to post-deposition oxidation and an overall unstable behaviour. Setting $r_{N2/SiH4}$ to about 0.75, however, results in low-stress ($\sigma < 100$ MPa), stable films with high electrical performance ($\rho > 10^{15}$ Ω·cm) whose characteristics are tuneable by exploiting other deposition parameters, including the usage of additional capacitively coupled plasma.

Sputter deposited (both RF and DC) SiN_x thin films were found to be less sensitive to their deposition conditions than their ICP-CVD counterparts, with the most influential parameter being the average kinetic energy of the sputtered particles, which can essentially be influenced through the back pressure and plasma power given a nominally unheated substrate. While the biaxial stress was tuneable in the range of -1.3 GPa to basically stress-free when sputtered in DC mode, RF sputtered SiN_x samples exhibited high compressive stress ($\sigma < -2$ GPa) independent of the sputter deposition parameters. The dominating mechanisms of electrical conduction through sputtered SiN_x films were identified by temperature-dependent leakage current measurements. These were found to have either Ohmic conduction at low electric fields ($E < 0.1$ MV/cm) or by Poole-Frenkel emission ($E > 0.3$ MV/cm). Film resistivity values at room temperature were in the range of 10^{13} to 10^{14} Ω·cm.

Kurzfassung

Mikroelektromechanische Systeme (MEMS) sind bereits in einer Vielzahl von automobilen, industriellen, medizinischen und auch Consumer-Anwendungen integriert. Die Vielfalt dieser Anwendungsszenarien erfordert maßgeschneiderten Eigenschaften der verwendeten Werkstoffe wie Substraten oder Dünnschichtsystemen, um die sehr spezifischen Anforderungen in mikro- oder nanotechnisch hergestellten Bauelementen zu erfüllen. Um die Integration in bestehende Bauelementkonzepte zu erleichtern, ist die Verwendung von CMOS kompatiblen Technologien und Materialien von Vorteil.

Siliziumnitrid (SiN_x) Dünnfilme werden in mikroelektronischen und MEMS-Bauteilen als Standardmaterial in verschiedenen Funktionalitäten verwendet, wie z.B. bei der elektrischen Isolierung, der robusten Passivierung von Oberflächen, als Lichtwellenleiter, und als struktureller Werkstoff für die Realisierung von mechanisch belastetsten Komponenten, wie Cantilevern und Membranen. Trotz ihrer jahrzehntelangen Verwendung und der damit einhergehenden Kenntnis ihrer grundsätzlichen Schichteigenschaften besitzen SiN_x Dünnfilme immer noch ein hohes, ungenutztes Potenzial, wenn Abscheidungsprozesse in Kenntnis ihrer vollen Bandbreite und Flexibilität genutzt werden würden.

Im Rahmen dieser Arbeit wurden amorphe Siliziumnitrid-Dünnfilme mittels zweier unterschiedlicher Plasmaprozesse synthetisiert: induktiv gekoppelte, plasmaunterstütze Gasphasenabscheidung (ICP-CVD) und reaktive Magnetron-Kathodenzerstäubung (Sputtertechnik). Die mit beiden Verfahren abgeschiedenen Proben werden anschließend mit einer Vielzahl von analytischen Verfahren charakterisiert, um ihrer mechanischen, optischen und elektrischen Eigenschaften zu bewerten, sowie ihre chemische Zusammensetzung zu erfassen.

Die Eigenschaften von ICP-CVD SiN_x Dünnfilme hängen nachhaltig von dem Verhältnis der beiden Precursorgasflüsse, $R_{N2/SiH4}$ ab. Ein zu niedriges Wert führt zu siliziumreichen Schichten, die eine hohe Druckverspannung und ein schlechtes, elektrisches Isolierverhalten aufweisen, während ein zu hohes Verhältnis bei der Schichtabscheidung zu einer hohen Konzentration von ungebundenem Wasserstoff resultiert. Ferner kann Luftsauerstoff bzw. Feuchtigkeit selbst bei Raumtemperatur in die zuletzt genannten Schichten eindringen, was sich in einer nachträglichen Oxidation und in weiterer Folge in einer steigen Zunahme der kompressiven Schichtspannungskomponente zeigt. Wird aber das Verhältnis $r_{N2/SiH4}$ auf einen Wert von 0,75 fixiert, können stabile, stressarme (σ < 100 MPa) Schichten abgeschieden werden, die einen hohen elektrischen Schichtwiderstand von $\rho > 10^{15}\ \Omega \cdot cm$ aufweisen. Um diesen Arbeitspunkt können Schichteigenschaften mittels der anderen Abscheideparameter

insbesondere durch die Verwendung von einem zusätzlichen kapazitiv gekoppelten Plasma verändert werden.

Im Bereich der mit Sputtertechnik (RF und DC) abgeschiedenen SiN_x Dünnfilme kann festgehalten werden, dass diese weniger sensitiv auf ihre Abscheidebedingungen sind als die ICP-CVD-Proben. Der Parameter mit dem höchsten Einfluss stellt bei den gesputterten Schichten die mittlere kinetische Energie der gesputterten Teilchen dar, die im Wesentlichen durch den Kammerdruck und die gewählte Plasmaleistung bei nominell ungeheiztem Substrat beeinflusst werden kann. Während die Schichtspannung von DC-gesputterte Proben in einem breiten Bereich von -1,3 GPa bis zum annähernd stressfreien Zustand angepasst werden kann, weisen RF-gesputterte Schichten starke Druckspannungen bis zu -2 GPa auf. Die dominierenden elektrischen Leitungsmechanismen wurden mittels temperaturabhängigen Leckstrom-Messungen bis 300°C an Luft identifiziert. Bei niedrigen elektrischen Feldstärken ($E < 0.1$ MV/cm) liegt ein ohmscher Leitungsmechanismus vor, während bei $E > 0.3$ MV/cm Poole-Frenkel Emission dominiert. Bei Raumtemperatur liegen spezifische Widerstandswerte bei 10^{13} bis 10^{14} Ω·cm.

Contents

Acknowledgements ... v
Abstract ... vii
Kurzfassung ... ix
Chapter 1: Introduction and Motivation ... 1
1.1. Motivation — MEMS and silicon nitride ... 1
1.2. Goals and structure of this thesis ... 2
Chapter 2: Deposition and patterning of thin films ... 4
2.1. Physical vapour deposition ... 4
2.1.1. Vacuum evaporation ... 5
2.1.2. Sputtering ... 7
2.2. Chemical vapour deposition ... 13
2.2.1. LPCVD ... 15
2.2.2. PECVD ... 17
2.2.3 ICP-CVD ... 22
2.3. Patterning ... 24
2.3.1. Photolithography ... 24
2.3.2. Etching ... 26
2.4. Summary ... 31
Chapter 3: Methods for analysis and characterization of thin films ... 32
3.1. Electron microscopy ... 32
3.1.1. Transmission electron microscopy ... 32
3.1.2. Scanning electron microscopy ... 35
3.2. X-Ray photoelectron spectroscopy ... 37
3.3. Fourier-transform infrared spectroscopy ... 38
3.4. Mechanical surface profilometry ... 39
3.5. Nanoindentation ... 40
3.6. Spectral reflectometry ... 41
3.7. Wafer geometry gauge ... 41
3.8. Thermal effusion measurement ... 42
3.9. Summary ... 42
Chapter 4: Physical and microstructural properties of silicon nitride thin films deposited by ICP-CVD 43
4.1. Experimental details of a-SiN_x:H thin film deposition ... 43
4.2. Screening experiments and the influence of ICP power, deposition pressure, and substrate temperature on film properties ... 46

4.3. Influence of the precursor gas flow rate ratio ... 56
4.4. Influence of CCP power ... 63
4.5. Summary ... 76
Chapter 5: Mechanical and morphological properties of silicon nitride thin films deposited by magnetron sputtering ... 77
5.1. Experimental details of the SiN_x thin film sputter deposition ... 77
5.2 RF sputter deposited silicon nitride ... 81
5.3 DC sputter deposited SiN_x thin films ... 93
5.4. Summary ... 99
Chapter 6: Electrical characterization of silicon nitride thin films ... 100
6.1. Sample preparation and measurement methods ... 100
6.1.1. Sample preparation ... 100
6.1.2. Measurement setup and methods ... 102
6.1.3. On the electrical conduction and dielectric breakdown in insulators ... 105
6.2. ICP-CVD deposited a-SiN_x:H thin films ... 108
6.2.1. Type I films ... 108
6.2.2 Type II films ... 124
6.2.3. Intermediate Type films ... 126
6.2.4. Type RF films ... 129
6.3. RF sputtered a-SiN_x thin films ... 132
6.4. DC sputtered a-SiN_x thin films ... 139
6.5 Summary ... 145
Chapter 7: Summary and Outlook ... 146
7.1. Summary ... 146
7.2. Application Scenario and Outlook ... 149
Bibliography ... 153
List of Figures ... 161
List of Tables ... 168
List of Symbols and Abbreviations ... 169
About the Author ... 173
List of Publications ... 174
Appendix ... 175
A: Biaxial stress stability of sputter deposited SiN_x thin films ... 175
B: Parameter-dependence of bias voltage for DC magnetron sputtering of SiN_x ... 176
60 sccm Ar ... 176
40 sccm Ar, 20 sccm N_2 ... 177
20 sccm Ar, 40 sccm N_2 ... 178

60 sccm N_2 179
C: Temperature correction curve for the wafer probe station 180
D: Supplementary leakage current measurements of Type I a-SiN_x:H films 180
E: Breakdown characteristics of 50/300m thick Type I a-SiN_x:H films 181
BD statistics 181
BD characteristics 182
F: Additional leakage current characteristics of sputter deposited SiN_x thin films 185
RF sputtered SiN_x 185
DC sputtered SiN_x 187
G: Additional breakdown measurements of RF sputtered SiN_x thin films 189
100 nm thin RF sputtered films 189
40 nm thin RF sputtered films 190
300 nm thin RF sputtered films 191
H: Additional breakdown measurements of DC sputtered SiN_x thin films 192
100 nm thin DC sputtered films 192
40 nm thin DC sputtered films 193
300 nm thin DC sputtered Films 194

Chapter 1: Introduction and Motivation

1.1. Motivation — MEMS and silicon nitride

MEMS (microelectromechanical systems) devices are found in steadily growing numbers not only in consumer electronics such as microphones, but also in automotive (especially inertial, pressure, and gas sensors), industrial, as well as medical and scientific applications. Despite the growth potential in the MEMS market (from $11.9 billion in 2015 to a projected $20 billion in 2021 [1]), the average selling price per unit is continuously decreasing. Whereas some branches continue to grow (e.g. RF MEMS, acoustics MEMS, gas sensors), others segments seem to have settled (e.g. inertial sensors) [2]. The lack of demand in certain applications, accompanied by the reduction of price-per-unit due to technological development both limit the revenue growth.

Potential strategies besides cost-reduction to pursue in the future are expansion to new markets such as e-cigarettes [3], industrial drones [4], internet of things [5], home monitoring [6], as well is the improvement of existing designs with the incorporation of new materials, exploitation of novel technologies, and further miniaturization. Moreover, significant value can be created by implementing additional features [7], like the integration of multiple sensor elements into a single product such as inertial measurement units [8].

The ongoing miniaturization of new generations of MEMS devices [9, 10], as well as tailored devices for specific applications, often call for numerous requirements towards the functional materials being used in the device. This necessitates the utilization of robust engineered materials [11, 12], which allow to implement the desired physical, chemical, electrical, and mechanical properties, specifically tailored for the given application scenario.

Silicon nitride thin films are well established as standard material in both MEMS and microelectronic devices due to a number of outstanding properties: high electrical resistivity and dielectric strength, hardness, and chemical robustness. These features enabled silicon nitride to be utilized most successfully as electrical insulators [13], surface passivation for silicon and thin-film solar cells [14], and as structural layers for the realization of mechanically loaded components [15].

Silicon nitride thin films are employed in cantilever-based devices, such as capacitive shunt RF MEMS switches [16], micro-hotplate gas sensors [17], and atomic force microscope probes and tips [18]. Silicon nitride membranes have been adopted in numerous applications including seawater desalination[19], micro-resonators [20], and condenser microphones [21].

Frequent requirements regarding the adoption of material properties of silicon nitride thin films in these applications include, but are not limited to their biaxial stress [22], Young's modulus [15], chemical composition [23], and dielectric breakdown strength [24]. Basically, the flexibility in silicon nitride deposition processes [25] can be seen as a major asset in meeting these demands.

1.2. Goals and structure of this thesis

Despite the fact that silicon nitride amorphous thin films have found extensive usage in the past for over five decades in a large variety of applications, and are regarded as standard material, there still remains much to be explored and understood in depth about the resulting material properties independent whether innovative or even well-established deposition processes are applied. A more solid knowledge about the impact of individual deposition parameters and how they influence the resulting chemical, mechanical, and electrical properties of silicon nitride thin films would allow to further exploit the full potential this material system.

The main goal of this thesis is to focus on two, less established techniques for the synthesis of amorphous silicon nitride thin films: inductively coupled plasma enhanced chemical vapour deposition (ICP-CVD) and reactive magnetron sputtering. More specifically, the thesis addresses the following two topics: the first being more basic research oriented, with the goal of understanding the underlying physical, and chemical processes that dominate the resulting properties of the silicon nitride thin films, as a function of the process parameters. The second, equally important goal is to evaluate the thin film properties with respect to their applicability in different mainly MEMS-related application scenarios. The performance metrics for evaluation are based on common requirements. A very important point is how to tune the material properties in order to fulfil application-specific requirements. In order to provide a solid basis for the evaluation of different silicon nitride samples, some theoretical and instrumental considerations have to be addressed in the first chapters. Chapter 2 gives an overview of common manufacturing technologies, including additive deposition and patterning (i.e. etching) processes used later in this work. Special emphasis is put on a few specific techniques such as plasma-enhanced chemical vapour deposition and magnetron sputtering, and their relevance in the processing of silicon nitride and related materials. Detailed descriptions of the processing instrumentation used for the preparation of samples are also provided. In Chapter 3, some key techniques for the evaluation of dielectric thin film properties are discussed. Optical, electron-optical and mechanical measurement methods, as well as specific instruments such as spectral reflectometry, Fourier-transform infrared spectroscopy and scanning electron microscopy used for the analyses are considered.

Chapter 4 deals with amorphous hydrogenated silicon nitride films deposited using the ICP-CVD (inductively coupled plasma chemical vapour deposition) technique. The wide range of material properties including chemical composition and mechanical quantities achievable by an appropriate selection of the deposition parameters is demonstrated. At the same time, the physical reasons and processes the specific parameters' influence on the material properties are discussed in detail. Additionally, some techniques, such as tight control of specific deposition parameters to synthesize materials with tuneable characteristics (specifically biaxial film stress), optimized to their application scenario, are considered.

Another popular method for the synthesis of amorphous silicon nitride thin films is magnetron sputter deposition. Physical properties and chemical composition of silicon nitride materials deposited using (DC and RF) variations of this technique are covered in Chapter 5. The influence of the individual process parameters on the resulting characteristics and properties of the deposited material are discussed in detail. This includes also fabrication-relevant aspects, such as the resistance against some standard etchants typically used in MEMS processing.

One of the main function of silicon nitride thin films in MEMS devices is electrical insulation. In Chapter 6, the ability of different amorphous silicon nitride thin films to serve as high performance material is evaluated, using two criteria. The first one is *how well* do they insulate under typical loads, and is assessed by performing leakage current measurements at temperatures up to 300°C in air. The second one is what *maximal electrical load* can they withstand, and is determined by their temperature-dependent time-zero dielectric breakdown performance. Both aspects of insulator performance are tested over the range of silicon nitride materials investigated in the former chapters. With the help of temperature-dependent characteristics, the physical processes dominating electrical conduction through the samples can be identified. Using these results, strong links can be established between the electrical performance, morphology, and deposition conditions of the different silicon nitride materials. Based on these findings, some consequences are drawn regarding the adaptability silicon nitride layers for specific application scenarios.

Chapter 2: Deposition and patterning of thin films

This chapter deals with the relevant technological processes and techniques used in this work to deposit and pattern silicon nitride as well as metallic thin films necessary for characterization.

2.1. Physical vapour deposition

Physical vapour deposition (PVD) is a term which is used to cover a broad range of thin film deposition techniques. There are a few general features though that encompass and differentiate PVD from other deposition techniques, such as chemical vapour deposition (see Chapter 2.2.), namely that films are deposited from the gaseous phase using the flux of *neutral* or *ionic* particles [26]. Physical vapour deposition techniques include, but are not limited to evaporative techniques (subsection 2.1.1.), such as electron-beam, thermal and reactive evaporation, molecular beam epitaxy (MBE), ion plating, sputter processes (DC and RF, magnetron and reactive sputtering, see subsection 2.1.2.) and deposition from arc sources (not covered here).

There are several advantageous properties that PVD processes feature in contrast to some of the alternatives (e. g. chemical vapour deposition, plasma spraying etc.). These include but are not limited to [27]:

- A broad range of material compositions can be deposited (metals, alloys, compounds).
- Adhesion to the substrate and surface finish (topology) can be both excellent.
- The deposited materials typically exhibit a very high purity.
- The substrate temperature can be varied over a wide range.
- Deposition of thin films with different crystallographic modifications (including amorphous materials) is feasible.

However, PVD processes also have some limitations:

- Generally, polymeric organic materials cannot be deposited (there are a few exceptions though).
- They generally need more sophisticated, and hence, more expensive equipment than some of their alternatives.

In the following, the two PVD techniques relevant to this work – evaporation and sputter deposition – will be presented.

2.1.1. Vacuum evaporation

Vacuum evaporation is based on the transition of the solid or liquid source material into the gaseous phase by means of either resistive, inductive or electron-beam heating [27]. The particles boil off or sublimate from the source (i.e. the container with the evaporant material) and travel through a low-pressure region before precipitating on cold surfaces, including the substrate. The flux F is the number of molecules leaving the unit area of the evaporant per second and is given by the following equation [28]:

$$F = N_0 exp - \left(\frac{\Phi_e}{k_B T}\right) \tag{2.1}$$

where N_0 is a slowly varying function of the absolute temperature T, Φ_e is the activation energy, and k_B the Boltzmann constant. Having a good vacuum during evaporation is important for two reasons. Firstly, the formation of contaminating monolayers on the substrate surface should be inhibited, since it would contaminate the targeted chemical composition of the deposited film. This can be done by simply reducing the base pressure of the deposition chamber. Secondly, the mean free path λ is a measure for the average distance a particle can travel between two collisions. For the evaporated particles to be able to deposit onto the substrate without suffering collisions, λ has to be significantly larger than the distance d between the source and the substrate. The arrival rate at the substrate for this case follows the cosine law:

$$A \propto \frac{cos\beta cos\theta}{d^2} \tag{2.2}$$

with β being the angle between the substrate normal and radial vector connecting the source to the point being considered on the surface, and θ between the normal of the source and the aforementioned radial vector. In cases where $\theta = 0$, the deposition thickness at different locations on the substrate is proportional to the local β value (see Figure 1).

A typical vacuum evaporation system is schematically depicted in Figure 2, consisting of a vacuum chamber, a vacuum pumping system, vacuum gauges, evaporation sources, substrate holders, shutter, and rate monitor. The vacuum chamber can be a bell jar or a rectangular box shaped enclosure, or even a more sophisticated hardware including load-lock systems. Because a low base pressure in the range of 10^{-5} – 10^{-6} mbar is required, commonly two-stage pumping systems are employed, with the pre-pump being a rotary vane pump and the second stage a diffusion, cryogenic

or turbomolecular type. Since during operation the deposition chamber is routinely flooded with atmospheric pressure and evacuated, there is a need to measure the pressure over several orders of magnitude. For that reason, vacuum evaporation systems are outfitted with a number of pressure gauges, both for total and partial pressure measurement covering a wide pressure range.

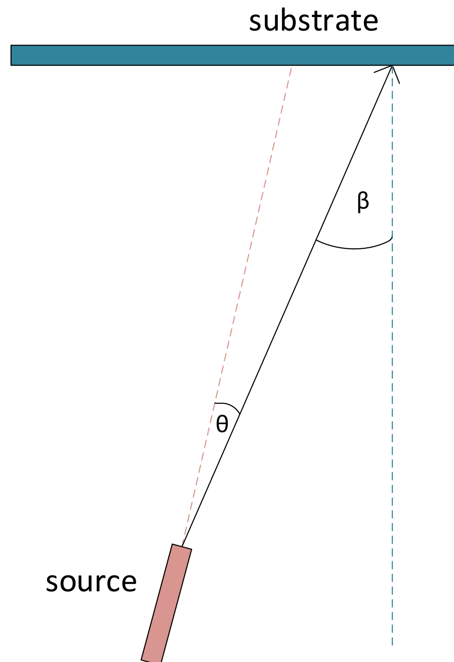

Figure 1: Illustration of the cosine law in a vacuum evaporation arrangement.

When discussing different types of evaporation sources, there are two main aspects to consider: one is the heating method used to transfer energy to the evaporant, the other is a material compatibility issue between the source and the evaporant. Resistance-heated sources are commonly wires or foils in different forms made of refractory metals. Inductively-heated sources are often realized in the form of high-melting or water-cooled crucibles. Electron-beam heated sources have the benefits of high localized power density, and wide range of available evaporation rates, while the source itself is water-cooled. The electron-gun consists of a cathode and an anode, between which a voltage of 10-40 kV is applied. The electron beam is then deflected and focused onto the evaporant source using magnetic fields.

In order to be able to control the thickness and properties of the deposited thin film, different mechanisms are employed to monitor the vapour stream such as ionization gauges, particle impingement rate or ion current monitors, or the deposited mass like microbalances or crystal oscillators [27].

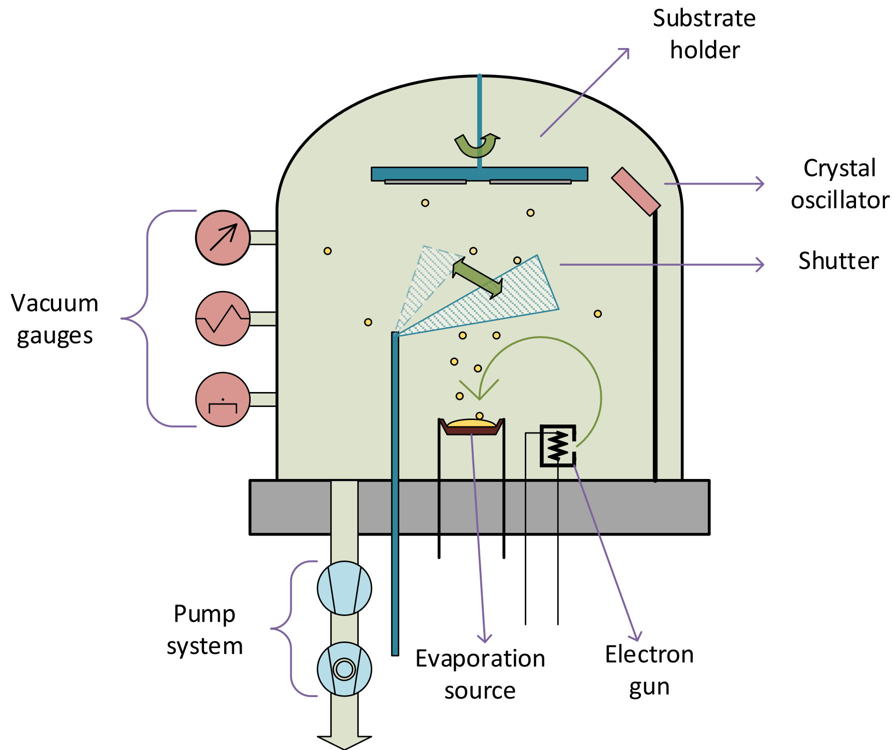

Figure 2: Schematic view of a vacuum evaporation system, featuring a thermal and an e-beam source.

The morphology and microstructure of the deposited thin film is largely dependent on the material class and the substrate temperature, the deposition rate and thickness, the angle of incidence, and the pressure and composition of the ambient gas. A model for the microstructural evolution for single-phase metals, alloys and refractory compounds was first proposed by Movchan and Demischin, later modified by Thornton [29]. The model is based on the temperature-dependent mobility of surface adatoms. As the surface temperature increases, the structural morphology of the deposited thin films changes from a low-density, porous structure (*Zone I*) to tightly packed fibrous grains (*Zone T*). At even higher temperatures, the size of the columnar grains increases (*Zone II*), and finally recrystallization leads to 3-dimensional growth (*Zone III*). The threshold temperatures between the different zones are generally expressed as fractions of the material-specific melting point T_m.

2.1.2. Sputtering

Sputter deposition is a process where atoms of a solid target are ejected due to the bombardment of a target by energetic particles. These are mostly positive ions generated in a (abnormal) glow discharge, using a configuration in which the cathode is the target. The ejected atoms (or clusters) travel to, and precipitate on a substrate, leading to the formation of a thin film [30].

In a conventional sputtering setup, a vacuum chamber is evacuated to a typical base pressure of 10^{-4} Pa or lower using a two-stage vacuum pump system. Then, a noble gas such as Argon (Ar) is introduced to the chamber and the pressure is stabilized, usually in the range of 1-10 Pa. A high voltage is applied between the substrate (anode) and the target (cathode), and an electrical discharge is ignited. This electrical discharge has a current-voltage characteristic, which is dependent on various parameters, such as the pressure and composition of the gas atmosphere, the size and shape of the electrodes and the vacuum enclosure, the inter-electrode distance and the electrode materials. Different regions in the *I-V* characteristics can be identified as the dark (Townsend) discharge, glow (Glimm) discharge and arc discharge regions, as illustrated in Figure 3 from the left to the right [31]. In a sputtering configuration, the value of the load resistor is typically adjusted such that the discharges are in the so-called abnormal glow discharge regime. In this region, the plasma discharge completely covers the surface of the cathode, and the discharge voltage increases with an increasing current density.

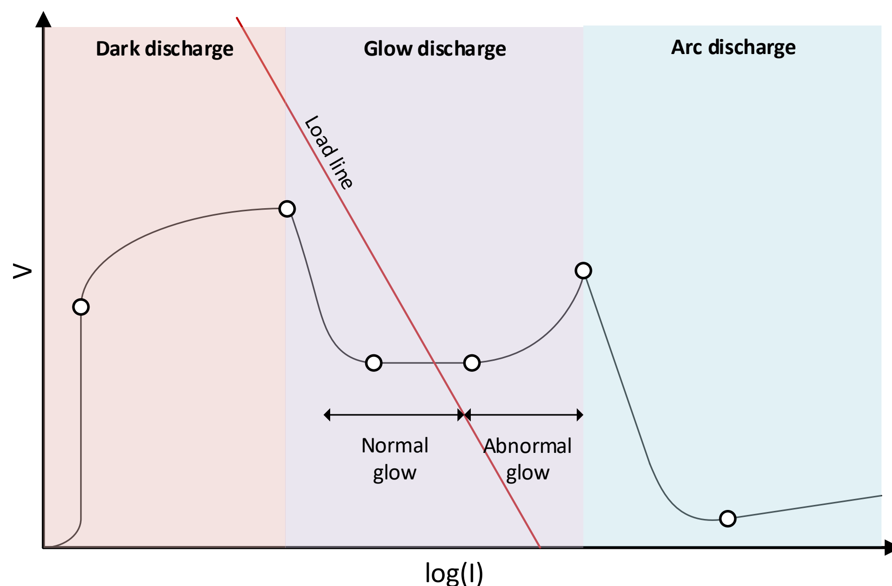

Figure 3: I-V characteristics of an electrical discharge with the most important regions highlighted [32].

The measure for the amount of surface atoms removed from the target per incident energetic atoms is the sputter yield *Y*. While naturally it is a function of the ion and target material, *Y* is also dependent on the ion energy, having a threshold value and exhibiting a maximum [28]. The reason for the material-dependent behaviour is two-fold: the momentum-transfer from the incoming ion to a target atom is dependent on the mass ratio of these two species and the surface binding energy U_s, which is the energy needed to overcome in order to eject an atom from the target. The latter two quantities are characteristic for a given target material and microstructure. Furthermore, it needs to be considered that at higher energies the incident ions will penetrate deeper into the target, thus the

probability of a recoiled target atom escaping will decrease. Several different equations are being used to model the sputter yield as a function of the aforementioned parameters (all having varying grades of empiricism), with some of the most widely-used ones being those developed by Sigmund [33], Yamamura [34] and Mahan [35].

The sputtering system with a glow discharge as described above is from an electrical point of view essentially a diode, in which the movement of the electrons is defined by the electric field, as they move towards the anode and are lost from the discharge upon their arrival. This can have ramifications regarding the self-sustaining ability of the discharge, since the electrons under some circumstances might not be able to produce enough ions during their travel through the plasma. There are several possibilities to overcome this obstacle, such as the utilization of an auxiliary discharge, a hollow cathode configuration, or external magnetic fields. Apparatuses using the latter approach are called magnetrons. They utilize the magnetic field force acting on the moving charge carriers (electrons) to elongate their trajectory and hence, their dwell time inside the plasma, resulting in an increased number of collisions and a higher degree of ionization.

To deposit compound materials (mainly oxides, nitrides and sulphides) by sputter deposition basically two methods exist. In the first approach a compound target has to be used, which will be electrically non-conductive for most cases, which requires powering the discharge using radiofrequency (RF) waves instead of direct current (DC). The other possibility is to use a metallic target, but add a reactive gas such oxygen, nitrogen or hydrogen sulphide to the discharge. This gas will enter a chemical reaction with the sputtered material and form a compound on the substrate. This process is called *reactive sputter deposition*.

As it was mentioned earlier, glow discharges in sputter deposition systems can be driven in DC (i.e. continuous or pulsed operation) or RF mode. In the following sections, their specific attributes and unique features are presented and discussed in detail.

2.1.2.1. DC-sputtering

As stated above, for general considerations a DC powered electrical discharge (see Figure 4) can be viewed as a diode, with very unique current-voltage characteristics, as depicted in Figure 3. The mechanisms which allow the ignition of a self-sustaining glow discharge will be described briefly in the following. A presumption can be made that there are a number of initial free electrons inside the discharge volume. These electrons are accelerated towards the positive electrode (the anode), but undergo collisions with the atoms and molecules in the vacuum chamber. Some of those collisions result in ionization: the generation of a positively charged ion and one or more free electrons. The number of positive ions generated by an electron over a unit distance is the so-called primary

ionization coefficient α_1. The positive ions will, in turn travel to the cathode (the target) and cause the ejection of both γ_i secondary electrons and of target atoms. γ_i is therefore called secondary amplification. Besides this quantity there are also a few additional processes that contribute to the generation of secondary electrons, such as the photo-effect on the cathode or the photo-ionization in the discharge volume. All these effects, including γ_i can be summarized in the 2nd Townsend coefficient γ. The discharge is self-sustaining, if the ions generated by an electron, release one electron from the cathode on average. Given the inter-electrode distance *d*, this relation called the stationary ignition condition can be written as:

$$\gamma_i[exp(\alpha_1 d) - 1] = 1 \quad (2.3)$$

The ignition actually happens if the left-side of the expression is greater than one. Admittedly, the ignition condition using α and γ_i is not very usable in practice, as these quantities are impractical to measure and control. Instead, by using Paschen's law the minimal ignition voltage V_t is calculated as a function of the product of the inter-electrode distance and the chamber back pressure *p* and is also dependent on the gas and electrode materials [36]. This gives the so-called Paschen-curves, which exhibit an absolute minimum, while the necessary ignition voltage increases very rapidly towards low, and steadily towards high $p{\cdot}d$ values. The explanation for these effects is the following: at low back pressure levels or small gap distances between the electrodes, the free electrons are only able to generate fewer ions. In turn, at high pressures the collisions become so frequent that the electrons are rarely able to accumulate sufficient energy to ionize their collision partners.

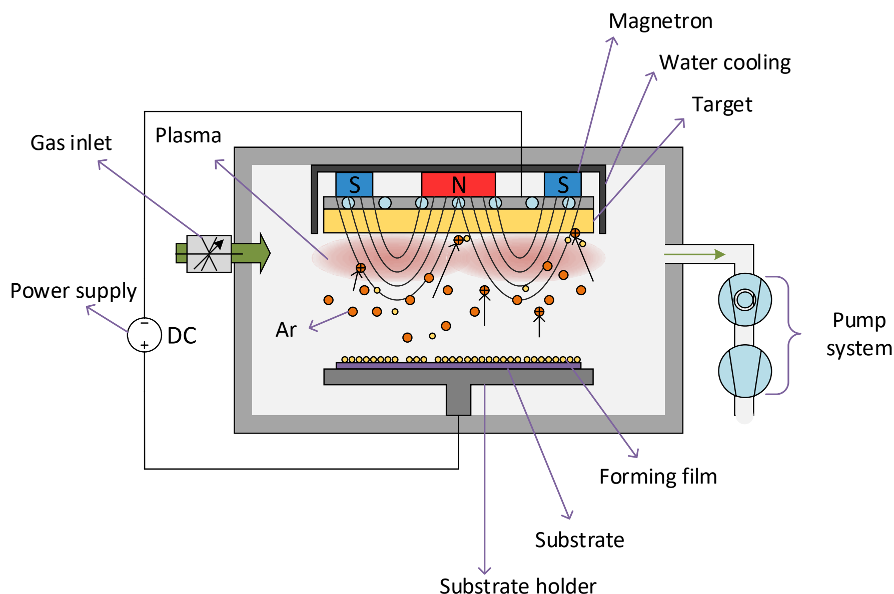

Figure 4: Schematic view of a DC magnetron sputtering system.

The resulting requirements towards the electrical components of the sputtering systems are such that the electromotive force of the DC power supply has to be higher than V_t, and the load resistance has to be chosen in a way that the load curve intersects the *V-I* characteristic at only one point, meaning in the abnormal glow discharge region.

The limitations set to the usage of DC discharges in sputter deposition are direct consequences of their properties. Using either an isolating or poorly conductive target would essentially block the current path, and leads to electrostatic charging of the electrodes resulting in a high arcing probability. Deposition of non-conductive materials although possible, can lead to the formation of a closed non-conductive capping of the anode, thus hindering the electron flow. This is called the disappearing anode effect. To enable sputter deposition under those circumstances, electric discharges powered by radiofrequency waves are utilized.

2.1.2.2. RF-sputtering

Electrical discharges behave differently when driven in varying frequency ranges. This also has an impact on their respective ignition voltages. At low frequencies below 100 kHz, where the ignition time is significantly lower than the half-period of the electrical field, the conditions are similar to the case of DC-discharges, hence V_t will not change. At higher frequencies between 100 kHz and 10 MHz and depending on inter-electrode distance, the ions will not be able to follow the electric field, resulting in fewer ions hitting the cathode, which leads to an increased V_t. At even higher frequencies in the range of tens to hundreds of MHz, electrons will also not be able to reach the electrodes in one half-period, and will be confined in the discharge volume, effectively lowering the ignition voltage. In turn, at very high frequencies in the GHz (microwave) range, electrons will gain too little energy in one half period, to effectively participate in the ionization process, further increasing V_t.

Technologically and practically relevant are the frequency ranges between a few hundred kHz and 40 MHz, as well as microwave-discharges above 900 MHz. There are a few standardized frequency bands allowed for industrial use, e.g. 13.56 MHz and 2.45 GHz that are typically utilized.

Further distinction between the techniques can be made by taking into account the way the radiofrequency power is coupled into the discharge: capacitively and inductively coupled discharges, as well as microwave (electrode-less) discharges at $f > 1$ GHz. There is also a minimal power required for sustaining an RF-discharge, which is dependent on the power coupling method as well as the frequency. The position (i.e. internal or external) and form (i.e. plates or coils) of the electrodes can also vary. In RF sputtering configurations, the target and the substrate holder are used as internal electrodes for capacitive coupling. There is, however, another obstacle hindering the effective coupling of the RF power into the discharge: the difference in the impedance of the plasma and the output

impedance of the RF generator. A tuneable *R-C* matching network is used to adjust both impedances and is in most cases controlled automatically by minimizing the reflected power. Another issue to keep in mind is the large difference in the mobility of electrons (high) and positive ions (low), resulting in a non-linear *I-V* curve. This would lead to a significantly higher electron current in one half-period than the corresponding ion-current in the other half, thus leading to a non-equilibrium state. In order to maintain equilibrium, the potential of the cathode will shift to the so-called self-bias potential. Routinely, a blocking capacitor is also used in these systems, to effectively prevent the DC component passing through, even when conductive targets are used. A schematic representation of an RF sputtering system is pictured in Figure 5.

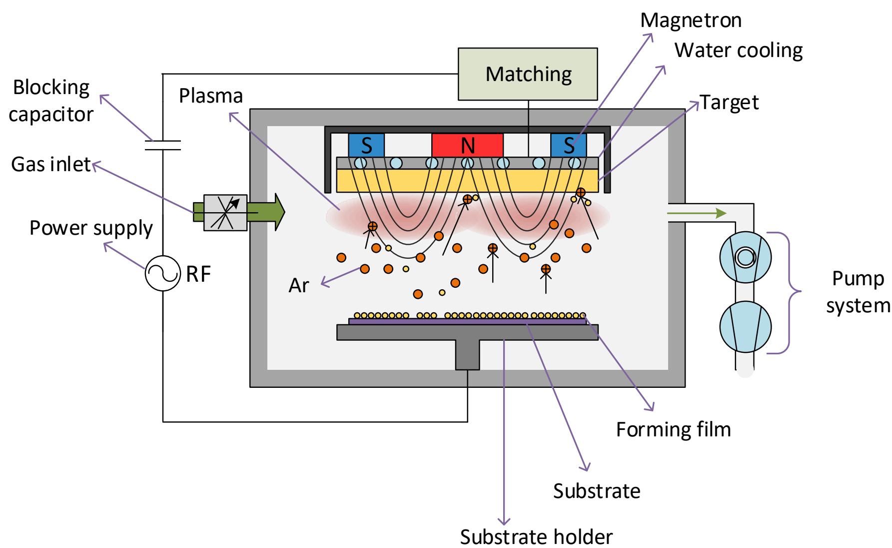

Figure 5: Schematic view on an RF magnetron sputtering system.

For the sputter deposition of silicon nitride and metallic thin films in this work, an *LS730S* sputter plant manufactured by *VON ARDENNE GmbH* was used. The deposition chamber is evacuated by a two stage (rotary vane and turbomolecular) vacuum pump system, providing a base pressure in the range of 10^{-7} mbar. The main deposition chamber houses a carousel with positions for four substrates having a size up to 6 inches in diameter. In one of the positions, substrate heating using a radiative heat source is available. In the upper part of the chamber three positions to fix targets are realized (i.e. two 6 inch and one 4 inch in diameter), as well as an ISE (inverted sputter etching) unit. The targets are held at their respective positions by using machine crews and clamp rings, as well as a graphite foil to ensure good thermal contact to the water cooling system. The sputter equipment features both DC and 13.56 MHz RF plasma generators (Type: *TruePlasma DC 3005* and *PFG 1000 RF* by *Hüttinger Electronic*). The flow of the inert gas Ar, as well as the reactive gases O_2 and N_2 is regulated by mass flow controllers.

2.2. Chemical vapour deposition

Chemical vapour deposition (CVD) is defined as a family of processing techniques, where a thin solid film, powder or single crystal is formed on a (generally heated) substrate by a chemical reaction, with the films constituents provided by gaseous reactants [37]. The variation of the experimental conditions such as the temperature and the substrate material, the partial gas pressures as well as the composition and total flow of the precursor gases enables the deposition of materials possessing a wide range of chemical, mechanical and electrical properties.

A major point of distinction between different CVD processes is the way how the energy necessary for the chemical reactions is fed into the system. In the simplest case, all energy is provided thermally. Techniques that fall into that category are atmospheric pressure CVD (APCVD)[38], low-pressure CVD (LPCVD), and Catalytic CVD [39, 40] (Cat-CVD, also known as hot-wire CVD). Another possibility is to provide part of the energy by means of an electrical gas discharge. These techniques are named either plasma-enhanced CVD (PECVD) or plasma assisted CVD (PACVD). In this work, the former acronym will be used. A third option is to achieve high local energy densities by a focused laser beam, called laser-CVD, enabling area-selective material deposition [41]. In the following discussion, the attention will be focused to LPCVD and PECVD techniques.

Regardless of the above distinction and the differences present in the exact specifics, CVD processes share some general characteristics in the subsequent process steps that are taking place. These steps are the following [42]:

1. Material transport: the gaseous reactants are transported to the surface of the substrate.
2. Adsorption: the reactive species chemically (chemisorption) or by van-der-Waals forces (physisorption) attach to the substrate surface.
3. Heterogeneous chemical reaction, where the desired reaction product and volatile by-products are formed.
4. Surface diffusion: dependant on the surface temperature and material parameters, the reaction products diffuse along the substrate surface to their permanent location.
5. Desorption of volatile by-products.
6. Transport of the by-products away from the substrate.

Although the chemical reactions occurring during CVD processes can exhibit very complex reaction schemes, they can still be classified into some general categories listed below with some examples.

1. Thermal decomposition (pyrolysis): A gaseous compound decomposes to a solid material and a gaseous by-product.

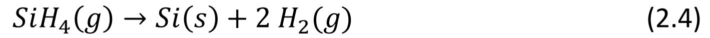

$$SiH_4(g) \rightarrow Si(s) + 2\,H_2(g) \quad (2.4)$$

2. Reduction: molecular hydrogen acts as a reducing agent.

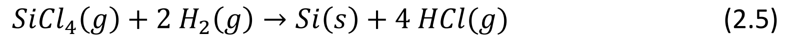

$$SiCl_4(g) + 2\,H_2(g) \rightarrow Si(s) + 4\,HCl(g) \quad (2.5)$$

3. Exchange: an element is replacing another one in a molecule.

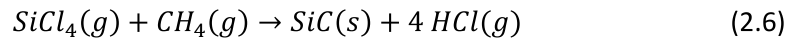

$$SiCl_4(g) + CH_4(g) \rightarrow SiC(s) + 4\,HCl(g) \quad (2.6)$$

4. Disproportionation: the oxidation number of an element changes by the formation of two new reaction products.

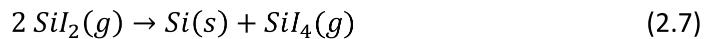

$$2\,SiI_2(g) \rightarrow Si(s) + SiI_4(g) \quad (2.7)$$

5. Coupled reactions: where two different types of the above are coupled together

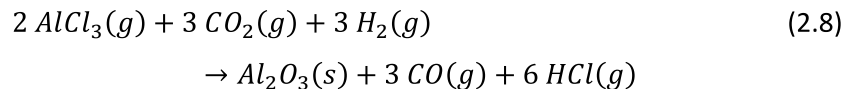

$$2\,AlCl_3(g) + 3\,CO_2(g) + 3\,H_2(g) \rightarrow Al_2O_3(s) + 3\,CO(g) + 6\,HCl(g) \quad (2.8)$$

consisting of a reduction reaction

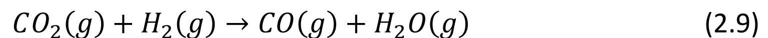

$$CO_2(g) + H_2(g) \rightarrow CO(g) + H_2O(g) \quad (2.9)$$

and an exchange reaction

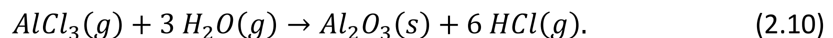

$$AlCl_3(g) + 3\,H_2O(g) \rightarrow Al_2O_3(s) + 6\,HCl(g). \quad (2.10)$$

As the above examples show, in theory a great variety of CVD processes is available for the synthesis of a certain material (e.g. Si). Technically relevant, however, are only few, taking into consideration the required process parameters and their possible ramifications including challenges with respect to the reactor design and material safety aspects. One particular issue is posed by the utilization of potentially hazardous (e. g. toxic, flammable or pyrophoric) materials in CVD processes [43]. These gases must be removed from the exhaust streams of the reactor. Such units are called scrubbers, which can operate on different principles including combustion, thermal decomposition and wet scrubbing depending on the material to be removed.

In the following, the two most prominent types of chemical vapour deposition, LPCVD and PECVD will be covered in more detail.

2.2.1. LPCVD

Low Pressure Chemical Vapour Deposition (LPCVD) is a technique where the deposition process takes place at sub-atmospheric pressure levels. This is achieved by using a vacuum pump system. Regardless of the reactor configuration, gaseous reactants are fed into the process chamber and transported through it by means of forced or free convection. Two distinct types of LPCVD reactor designs are prevalent in practice: *hot* (see Figure 6) and *cold wall* reactors (see Figure 7), which also determine what type of convection is dominant [37]. Cylindrical hot wall reactors are surrounded by a tube furnace, which ensures that the temperature gradients in the reactor are small. In that case, material transport is dominated by forced convection caused by the continuous evacuation of the reactor. Due to the high temperature of the reactor walls, deposition does not only occur on the substrates, but there as well. This can lead to severe problems with thicker deposited layers, especially when the adhesion to the reactor wall is poor, as particles can detach and cause contamination on the substrate. Another source for surface contamination can be a reaction between the reactor wall and the precursor gas.

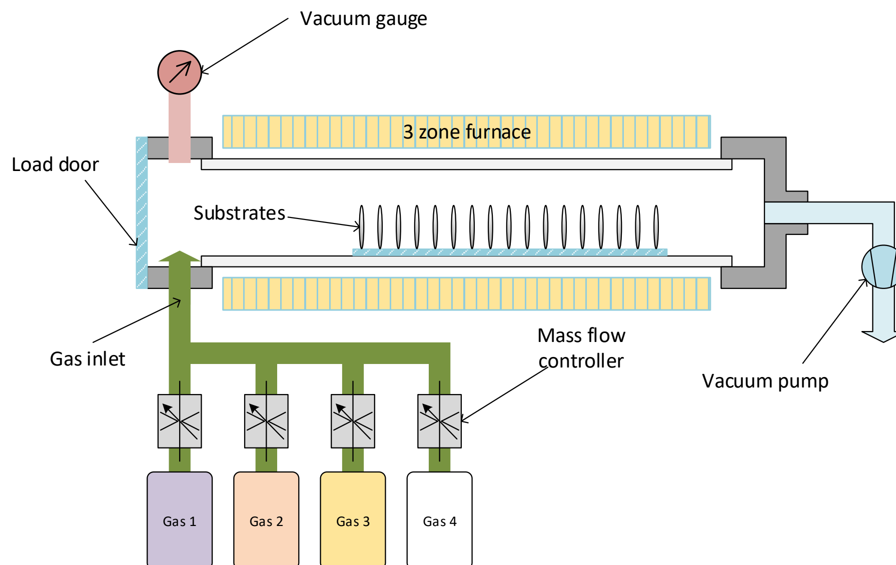

Figure 6: Schematic view of a hot wall LPCVD reactor.

In cold wall reactors, only the substrates are heated (e.g. via radiofrequency electromagnetic heating), leading to large temperature gradients inside the reactor, which itself is a driving force for

free convection that tends to dominate the material transport. Furthermore, the low wall temperature suppresses the deposition and chemical reactions in these areas, eliminating those two sources of contamination. On the other hand, the high temperature gradients also have a negative effect on the uniformity of deposition rates and microstructure across the substrate. All in all, due to its flexibility, especially regarding the increasing wafer sizes in semiconductor industry, the usage of cold wall reactors is becoming more prevalent [43].

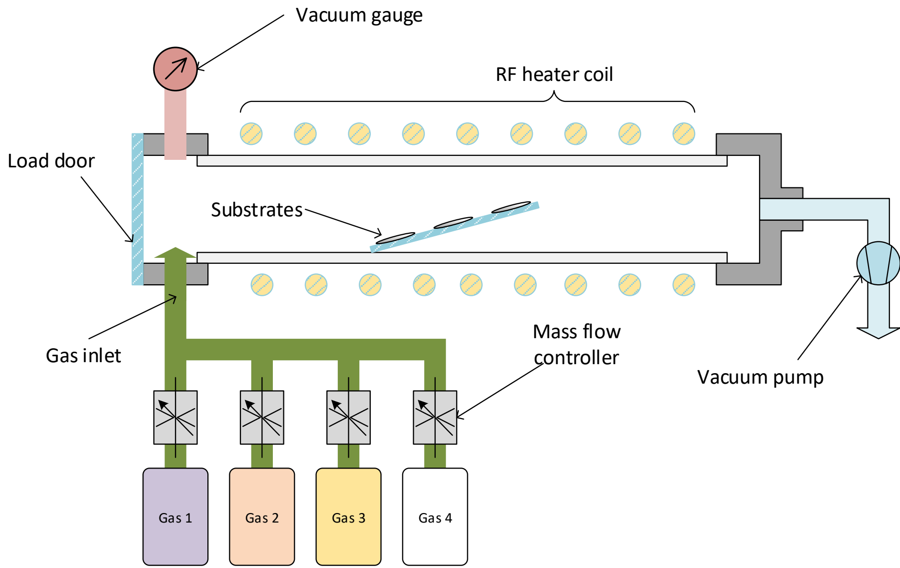

Figure 7: Schematic view of a cold wall LPCVD reactor.

A number of typical LPCVD processes and their characteristics are listed below in Table 1:

Material	Gases	*T* [°C]	Remarks	Ref.
Silicon nitride (SiN_x)	$SiCl_2H_2 + NH_3$	650-750	High diffusion barrier, wear resistant	[44], [45]
	$SiH_4 + NH_3$	700-900		
Polysilicon	SiH_4	580-650	Low stress after annealing	[46]
Silicon oxide (SiO_2)	$Si(OC_2H_5)_4$ (TEOS)	650-750	Low HF etch rate	[47]
	$SiCl_2H_2 + N_2O$	850-900		
Silicon oxynitride (SiO_xN_y)	$SiCl_2H_2 + NH_3 + O_2$	850-1000	Variable refractive index: 1.5-2.0	[48]
Tungsten (W)	$WF_6 + H_2$	200-600	Low resistivity	[47]
Tin oxide (SnO_2)	Dibutyltin diacetate (DBTD)	300-600	High CH_4 sensitivity	[47]

Table 1: Typical LPCVD deposition processes.

The deposition of silicon nitride films by LPCVD processes is common in microelectronics and MEMS. Techniques based on two different gas chemistries (either $SiCl_2H_2$ and NH_3 or SiH_4 and NH_3) are widespread (see Table 1). They are characterized by a uniform composition across the thickness of the film, and a relatively low hydrogen content (<5% according to Yota *et al.* [49], 3-8% according to Stoffel [42]), which originates from both precursor gases [50]. The composition ranges from stoichiometric to silicon rich, resulting in a stress level between +2000 and -200 MPa (highly tensile to slightly compressive, can be influenced by the Si/N ratio or ion implantation) with a Poisson number of 0.25. LPCVD deposited silicon nitride films generally show good etch resistance against hydrofluoric acid (HF), a high breakdown strength (around 10 MV/cm) and a high electrical resistivity at room temperature in the range of 10^{16} Ω·cm [42], with Poole-Frenkel conduction as the dominating leakage mechanism up to 500°C [51]. These properties enable the utilization of silicon nitride thin films deposited by LPCVD in a wide variety of devices for an array of different tasks, such as masking and insulation layers [52], membranes [53], micromotors and resonators, as well as optical coatings [54].

2.2.2. PECVD

Plasma Enhanced Chemical Vapour Deposition (PECVD) is defined as a subset of CVD processes, where part of the energy for the chemical processes taking place during deposition is provided by means of an electrical glow discharge (plasma) [55], as previously pointed out in section 2.2. There are two main advantages to this approach. The first one is the reduction of the necessary reactor and substrate temperature during deposition. This can enable the deposition of certain CVD materials in processes, where the available temperature budget is limited as e.g. the substrate would be damaged or results of previous steps in manufacturing such as doping profiles or metallization layers would be disrupted by using higher temperature processes [43]. The other significant benefit is the added level of control that inherently appears when using a second energy source. This means that different process parameters such as the substrate temperature (also available in LPCVD processes), as well as the plasma power can be independently chosen. Compared to LPCVD processes, in which the density of the different reactive species formed from the precursor gases is mainly determined by the temperature, in PECVD the user has a more direct control. This ultimately allows a more flexible process that can be tailored to the specific application [42]. While the two factors presented above are the distinctive advantages of PECVD processes, there is additional merit to these techniques making them very attractive for practical uses. These – among others – are potentially very robust films due to the tailored plasma-surface interactions, the possibility to deposit graded films in terms of composition and refractive index *n* (e.g. for optical rugate filters) and the comparatively high (1-

10 nm/s [55]) deposition rates. On the other hand, the characteristically lower deposition temperatures compared to LPCVD processes lead to an increased incorporation of hydrogen into the deposit. This phenomenon can have serious ramifications regarding the chemical robustness of the layers.

Common of PECVD deposition systems is that all utilize glow discharges powered by alternating electromagnetic fields. The main distinction between the processes is the actual frequency range in which the system operates, and the method of power coupling into the plasma [43], as already described in section 2.1.2.2. Further distinction can be made (although not customary for PECVD systems) by the position (i.e. internal or external) and shape (i.e. plate or coil) of the electrodes. In PECVD thin film deposition, both capacitively and inductively coupled plasmas are utilized, as well as microwave and ECR (electron cyclotron resonance) reactors. However, capacitively coupled systems are most widespread.

Capacitively coupled PECVD systems (see Figure 8) conventionally feature an internal parallel plate configuration as electrodes, with the substrate placed and electrically connected, in the case of a conductive substrate to the lower electrode. In general, the gas distribution consists of a single inlet, a more advanced showerhead, or the combination of those two depending on the reactor design. The main target is to ensure an acceptable degree of uniformity of electromagnetic field and gas composition over the substrate surface, what is a prerequisite for uniform film deposition [28].

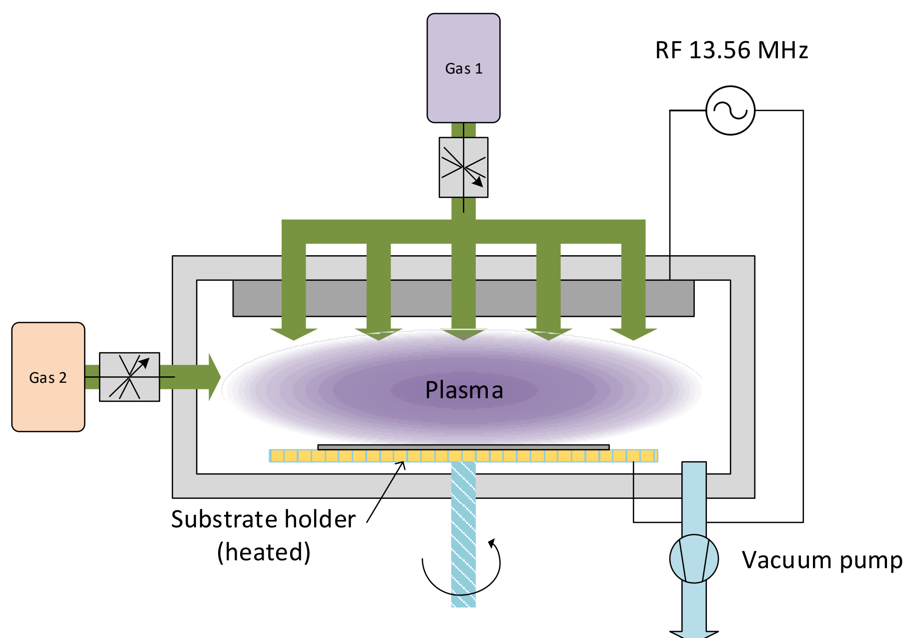

Figure 8: Schematic view of a capacitively coupled PECVD system.

PECVD systems powered by microwave radiation lack electrodes in the conventional sense. Instead they are equipped with (circular or rectangular) waveguides geometrically matched to the frequency and mode of operation. In a regular cavity resonator, however, the spatial extent of the plasma is strongly limited by the wavelength of the microwave. More common are special wave-heated systems such as ECR-CVD (electron-cyclotron resonance). Here, a circular-polarized microwave propagates along a magnetic field line to the so-called resonant zone (see Figure 9), where its energy gets absorbed by a collision-free heating mechanism. The resonance criterion that is necessary for the electrons to follow a circular path is given by:

$$\omega_{ce} = \frac{qB}{\gamma \cdot m_0}, \tag{2.11}$$

$$\text{where } \gamma = \frac{1}{\sqrt{1-(v/c)^2}} \tag{2.12}$$

where ω_{ce} is the angular frequency of the cyclotron motion, q the elementary charge, B the magnetic field, m_0 the rest mass, v the velocity of the particle, and c the speed of light. This equation yields a magnetic field of B = 875 G at f = 2.45 GHz. Some attractive properties of ECR-CVD processes are the wide operating pressure range, a high degree of ionization, and the ability to keep the kinetic energy of the impinging ions low, thus minimizing ion-induced damage [56].

In order to understand the chemical and physical processes taking place in PECVD plasmas, the external process parameters like back pressure in the deposition chamber, gas flow, and plasma power and their influence on the internal parameters of the plasma such as the plasma density, the electron energy density distribution function (EEDF), electric potentials and particle fluxes toward the substrate, have to be considered. In reality, these internal characteristics are affected by the external parameters in a complex way, and is for practical use assessed in an empirical manner. Some general points to be made are that a higher frequency leads to less surface charging and a higher power efficiency in terms of ionization, thus leading to increased dissociation rates and ion fluxes in MW plasmas [57]. Reactions in the gas phase determine the chemical composition of the deposited film, while plasma-surface interactions dominate the microstructure and morphology of the layers.

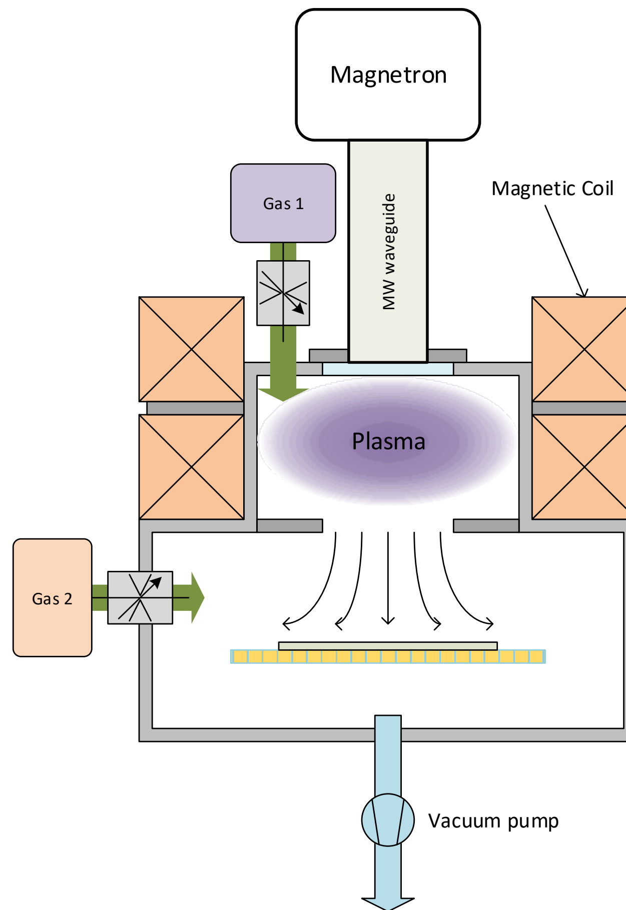

Figure 9: Schematic view of an ECR-CVD system.

Basically, the generation rate of the chemically reactive precursor and energetic species governs the internal parameters of the bulk plasma. The amount of different species existing in even the simplest plasma chemistries is already tremendous, therefore for practical purposes, generalized reaction pathways are considered. The interface between an immersed surface and the bulk of the plasma is called the plasma sheath, which is not electrically neutral. The potential difference between the bulk and the surface of the plasma accelerates ions through the plasma sheath. The kinetic energy that these ions gain is also dependent on the external plasma parameters and the type of ions [58]. The energy spectrum of the ions in a plasma is expressed in the ion energy distribution function (IEDF), in an analogous way to EEDF. The control of ion bombardment by controlling the IEDF has great importance in the deposition of thin films, particularly at low substrate temperatures. Ion bombardment affects nucleation and film growth by introducing interfacial atom mixing, increasing the surface mobility of deposited atoms, resputtering, and forward sputtering. These phenomena generally lead to a densification of the deposited film in agreement with the Movchan-Demischin structure zone model [29]. Some authors propose the existence of critical ion energies and flux ratios (the ratio of ion to neutral flux) that trigger transitions in the microstructure evolution during film

growth [59]. Experimental results indicate that low to intermediate (i.e. in the range of 10-100 eV) ion energies and high ion fluxes generally deliver the highest quality deposits in terms of density, hardness, chemical stability and residual stress. Monte Carlo simulations delivered similar results [60]. In other configurations, especially when organic substances are involved in the process, photon-surface interactions can also have a significant impact on the surface morphology. VUV (Vacuum Ultraviolet, 100 nm $< \lambda <$ 200 nm) photons are able to break chemical bonds. This can be relevant in plasmas which contain hydrogen, oxygen or helium and thus, irradiate in the VUV range (121, 130 and 157 mm).

The PECVD technique is used to deposit – amongst other materials – a range of silicon-based binary, ternary and quaternary thin films, such as:

- Silicon dioxide (SiO_2) and suboxides (SiO_x, x<2)
- Stoichiometric and nonstoichiometric silicon nitrides (Si_3N_4 and SiN_x)
- Silicon carbides (SiC and SiC_x)
- Silicon oxynitride and carbonitride (SiO_xN_y and SiC_xN_y)
- Silicon oxycarbonitride ($SiO_xC_yN_z$)

The composition of the precursor gases as well as the other parameters like plasma power and frequency, deposition temperature and pressure are utilized to tailor the chemical composition and physical properties of the deposited thin film. Criado *et al.* [61, 62] found that by the substitution of the precursor NH_3 with N_2O the composition of the deposit can be tuned from silicon nitride to silicon dioxide. This behaviour is reflected in the decrease of the refractive index *n* and the atomic concentrations measured by RBS (Rutherford backscattering spectroscopy). Other groups made similar observations that the tuning of mechanical properties like hardness, Young's modulus and film stress is possible between the limiting values set by Si_3N_4 and SiO_2, as well as the occurrence of different Si-N bonding groups in PECVD silicon nitride deposits [63]. Thermal annealing of PECVD thin films was also found to be an effective way to tailor their mechanical properties [64]. Silicon nitride thin films deposited by PECVD typically feature a high hydrogen content (10-40 at. %), are significantly less robust against HF based etchants, and have lower Young's moduli and hardness values compared to their LPCVD counterparts. The breakdown strength and film resistivity vary at room temperature over a wide range typically from 1 to 5 MV/cm and from 10^6 to 10^{15} Ω·cm, respectively [42].

Since this deposition technique plays a central role in this thesis, inductively coupled plasma enhanced chemical vapour deposition (ICP-CVD) processes will be discussed separately in the following subsection.

2.2.3 ICP-CVD

Besides from capacitively coupled and microwave discharges, inductively coupled plasmas can also be used for the deposition of thin films. The radiofrequency power is coupled into the system using helical or planar coils [65], either in an adapted LPCVD furnace [66, 67] or a system specifically built for ICP-CVD processing, as illustrated in Figure 10 [65, 68]. Low pressure ICP sources are especially advantageous for single wafer processes, where a high density of ions, electrons, and radicals is needed for a process with good uniformity over the whole wafer area. Inductively coupled plasmas are capable of fulfilling those requirements, while keeping the energies of ions and electrons low enough to limit damage to the wafers and the chamber. By using an ICP source the independent control of particle energy and plasma density becomes possible [69]. The spiral or helical inductor is placed either inside or next to a gas discharge to transfer the energy from the RF source, can operate in a wide range of frequencies, and can be electrostatically shielded or unshielded. Unlike in the case of ECR sources, there is no resonance between the motion of the electrons and the driving frequency.

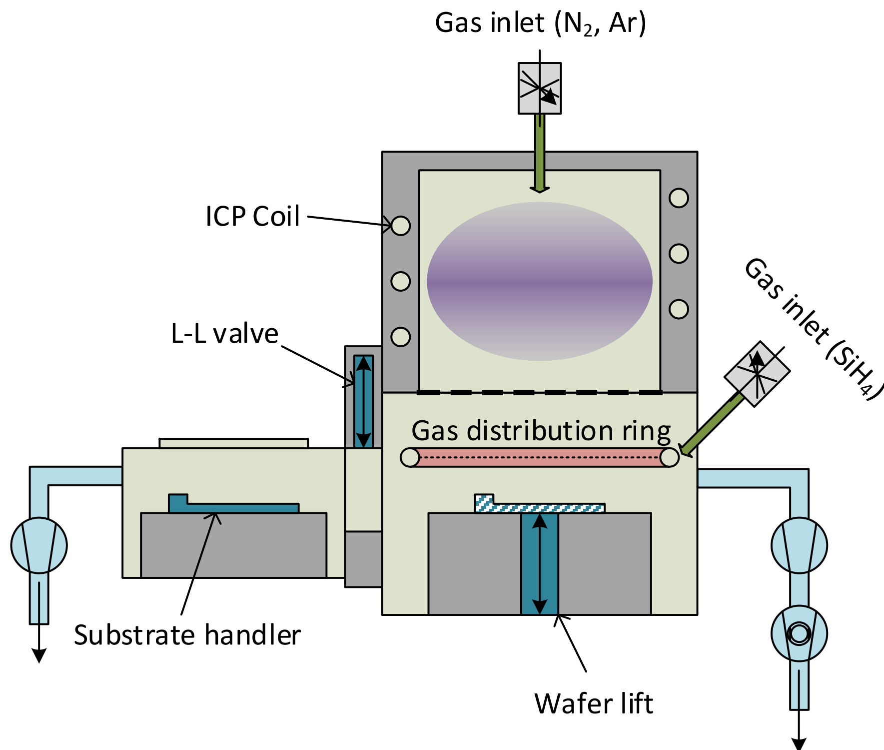

Figure 10: Schematic view of an ICP-CVD system with a load-lock chamber.

At low pressures, it is increasingly difficult to couple the RF power into the plasma, since the reduced number of atoms inside leads to fewer collisions, thus not enough ions and electrons are generated for a self-sustaining discharge. In order to increase the collision cross-section (and thus

probability), an increase of the average electron energy (electron temperature) is necessary. The density of electrons, ions and reactive species is approximately proportional to the power density. The RF coil generates a rotational symmetric RF field and is separated from the plasma by a dielectric wall and in some cases by an electrostatic shield. The RF electromagnetic field does not penetrate the plasma entirely at typical plasma densities and operational frequencies, only in its boundary region, due to the *skin effect*. As a consequence, there is no electromagnetic field inside of the plasma and the motion of charged particles is governed only by diffusion. Thus, the uniformity inside the plasma is controlled by other factors such as the reactor geometry, gas distribution system, temperature gradients and gas composition. Stability of the chamber wall temperature is a critical parameter for processes utilizing ICP plasma, therefore they are often liquid cooled. Electrostatic shielding can be utilized to deliver ions to the substrate having very low kinetic energies, on the other hand it suppresses capacitive coupling. The presence of capacitive coupling is often essential to ignite an inductively coupled discharge. Without it much larger electromagnetic fields are needed.

The deposition of silicon nitride by the ICP-CVD technique can use different gas chemistries: as silicon precursor, mostly silane (SiH_4) and sometimes dichlorosilane ($SiCl_2H_2$) are used. As nitrogen source, either molecular nitrogen (N_2) or ammonia (NH_3) is used, often diluted in either helium (He) or argon (Ar). Adding ICP excitation to an adapted LPCVD furnace for silicon nitride deposition results in a significantly increased deposition rate, since the RF power enables the dissociation of N_2 molecules [66, 67, 70]. The Si/N ratio and residual stress of the deposited film are mainly dependent on the ratio of the different precursor gases. In addition, stoichiometric, low-temperature (80-130°C) ICP-CVD deposited silicon nitride has lower etch rates and hydrogen content compared to conventional PECVD films [71], accompanied by a higher electrical breakdown strength [72]. ICP-CVD deposition generally leads to more favourable results when carried out at higher substrate temperatures, as in this case the deposition takes place at a higher rate, with decreased hydrogen incorporation, resulting in higher refractive indices [73]. In some cases [74], even the formation of β-Si_3N_4 is observed in low temperature, low-stress ICP-CVD silicon nitride films. Those trends are largely transferrable to ICP-CVD silicon oxynitride deposits [67]. Resistivity values of low-temperature ICP-CVD SiN_x and SiO_xN_y films are generally in the range of 10^9-10^{12} Ω·cm [67, 70].

ICP-CVD deposition experiments in this work have been carried out with an *Oxford Plasmalab 100* deposition system. The equipment consists of a reaction and a load-lock chamber, with the former one evacuated by a two-stage (rotary-vane and turbomolecular) pump system, while the latter by a simple rotary-vane pump. The substrate is placed for deposition onto an aluminium chuck. Depending on the deposition temperature, it can be clamped down using a glass ring with an applied helium backflow for improved thermal transfer up to a substrate temperature of 200°C. Alternatively, at higher temperatures the usage of the clamp ring is omitted, and the user can switch to radiative

heating. The process gases are fed into the deposition chamber at two distinct locations: at the top, through a perforated showerhead, and through a gas distribution ring in the vicinity of the substrate, both controlled by mass flow controllers. The system uses two 13.56 MHz plasma sources, both complete with automatically and manually controllable matchboxes. The main source, capable of outputting 200 W of power is connected to a helical ICP coil, while the secondary source (max power: 300 W) is capacitively coupled. The ICP coil and other parts of the chamber are cooled by liquid nitrogen.

2.3. Patterning

The fabrication of micromachined devices often consists of subsequent deposition and transferring a master pattern onto different layers. Processes and techniques in pattern transfer encompass lithographic techniques, by some definition additive techniques (i.e. deposition, already covered in section 2.2.) and etching processes. In the following chapter details about all these techniques will be given and discussed.

2.3.1. Photolithography

Lithography (from the ancient Greek words *λίθος* “stone” and *γράφειν* “to write”) is a pattern transfer method originally used in printing, utilizing a carved master image with an area-selective chemical treatment. The chemical treatment results in areas either being receptive or repellent to ink. [28].

Photolithography (also known as optical lithography) is a process for transferring patterns from a master (called a *photomask*) onto a light-sensitive substance called *photoresist* on the substrate. Depending on the type of the resist (positive or negative), upon exposure to ultraviolet radiation the resist undergoes an irreversible chemical transition, toggling its solubility to a certain solvent. Thus, by selective illumination, the original pattern can be transferred onto the resist. A simple photolithographic process using a positive resist is shown in Figure 11.

The process begins with the pre-treatment of the substrate, consisting of the cleaning of the surface, a bake-out to get rid of adsorbed molecules, and the application of an adhesion promoter. Next the photoresist is applied by using a spin-, a spray-, or an immersion coater. This is followed by a heat-treatment step to evaporate most of the solvent in the resist. The key step in the photolithography process is the exposure, where the mask pattern is transferred onto the substrate

by splitting the sensitizer molecules. Typically, different illumination techniques are utilized, such as contact, proximity or projection illumination [75]. For most of the processes another heat-treatment step follows. It is mainly employed to catalyse the completion of the reactions started. After this, the soluble areas of the exposed resist are removed by a chemical, so-called developing agent. The photolithography is finished by an optional hard-bake, mainly to raise the softening point of the developed resist [76].

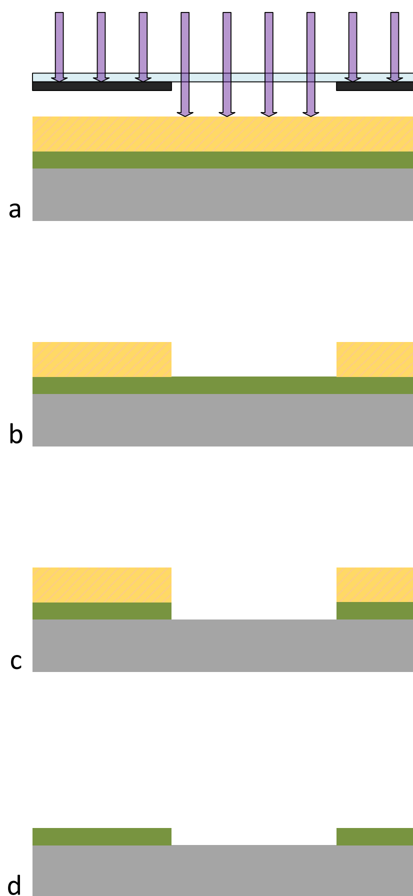

Figure 11: A simplified illustration of a photolithography process featuring a positive photoresist. a: Exposure, b:Development, c: Pattern transfer by etching, d: Resist stripping.

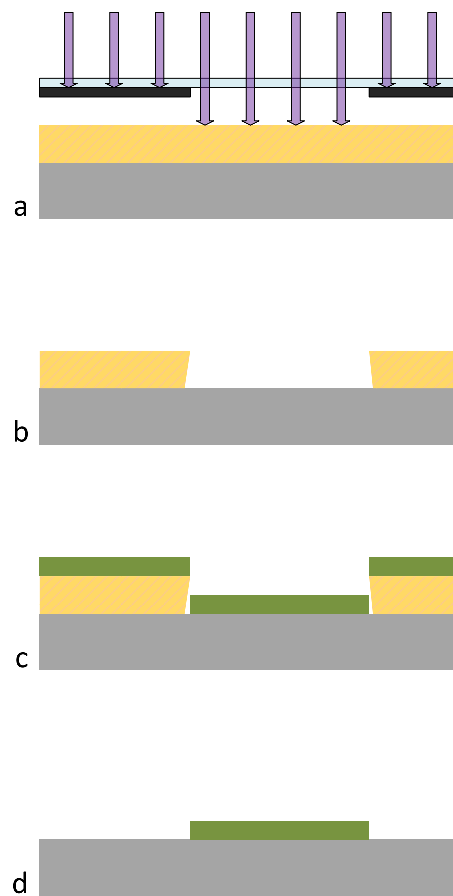

Figure 12: Illustration of the lift-off process, with the following steps: a: Resist exposure, b: Development, c: Thin film deposition, d: Lift-off.

These steps lead to the end-result of the photolithographic process, a substrate covered by a uniform layer of patterned photoresist. This is then utilized to generate patterned functional layers by additive (deposition and lift-off) or subtractive processes (etching).

Lift-off processes, on the other hand, consist of photolithographic patterning of a resist on a substrate followed by deposition of a thin film (usually an evaporated metallic film), and the removal of the resist along with the film on it. This results in a coverage of the substrate with the thin film having the inverted pattern of the photoresist (Figure 12). There are, however, some requirements to be able to perform a successful lift-off process. To ensure the area-selective removability of the thin

film the thickness of the resist has to be significantly larger than that of the film. Moreover, the physical continuity between areas of the deposited film that are to be removed and that are not should be disrupted. This is achieved by creating negatively tapered resist sidewalls (with a special resist, called image-reversal) and by directional thin film deposition (e.g. evaporative deposition).

2.3.2. Etching

Subtractive pattern transfer processes, where material is removed are generally covered by the term *etching*. The term is used in microfabrication and microelectronics for a plethora of different chemical, physical and combined processes having the sole common ground that they are used for material removal.

There are a couple of important characteristics for each etch process and target material combination:

- **Etch rate**: the temporal rate of material removal. Since mostly planar processes are considered (involving planar substrates and thin films), this is expressed in etch depth/time (usually nm/min). Industrial processes have strong preferences for high etch rates.

- **Selectivity** with respect to the mask material (photoresist or a so-called hard mask) or to the substrate material. It is simply the ratio of two etch rates: that of the etched material and that of the mask material. Usually a high selectivity is desired.

- **Isotropy/Anisotropy**: If the etch rate is independent of spatial directions, the etch process is isotropic, in other cases anisotropic. This difference can be dependent on crystallographic orientations or directions with respect to the surface normal. Sometimes a measure for the anisotropy of the process is used, the anisotropy factor $A_f = 1 - {}^{r_L}/_{r_V}$, with r_L and r_V being the lateral and vertical etch rates, respectively. Although fully anisotropic etch processes offer a more accurate pattern transfer, for some applications isotropic techniques are required.

A common point of distinction between etch processes is whether the etchant utilized in the process is gaseous or liquid. In the former case, it is called a *dry etching* technique, in the latter a *wet etching* technique. Dry etching processes are typically plasma processes, and can be purely physical, purely chemical or combined approaches, whereas wet etching techniques always rely on chemical reactions. In the following a brief summary of the most important etch techniques used in MEMS and microelectronics will be given.

Dry etching techniques:

- *Physical etching: sputter etching / ion-beam etching (ion-beam milling)*

  In this case the material removal is achieved by bombarding the surface by inert ions (e.g. Ar^{+}), similarly to the case of sputtering from a target. The momentum transfer from the energetic ions causes ejection of atoms from the bombarded material. The actual process taking place upon the impingement of the ions is highly dependent on their kinetic energy. The optimal energy range for sputtering is roughly between 10 and 1000 eV [28]. Physical dry etching processes share some inherent properties, as the low selectivity with respect to materials, high directional anisotropy, and relatively low etch rates compared to chemical and physical-chemical approaches. A major point of distinction between sputter and ion-beam etching is whether or not the substrate is electrically coupled to the plasma source (sputter etching) or placed on a third electrode in a triode configuration (ion-beam etching). Some undesirable issues that can arise will cause deviation of the sidewall geometry from the ideal vertical profile. These include mask erosion, faceting, trenching and redeposition, as displayed in Figure 13. These effects are described in greater detail in [77].

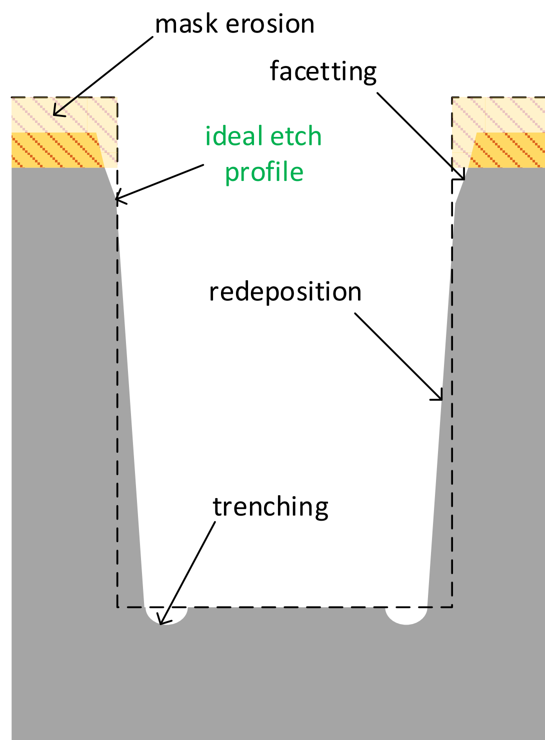

Figure 13: Typical problems in physical dry etching.

- *Vapour phase plasmaless chemical etching*

The chemical xenon difluoride (XeF_2) does not require a plasma to be ignited in order to generate reactive species. XeF_2 has a vapour pressure of approximately 4 Torr at room temperature. As a consequence, a vacuum chamber evacuated to a similar pressure level will contain an atmosphere with a high concentration of gaseous XeF_2, which reacts readily with silicon as described in [78].

Etching of Si with XeF_2 is highly selective against most photoresist and hard mask materials. The etch rate can be as high as 10 µm/min, but is strongly dependent on the opening size.

- *Chemical plasma etching*

In this technique, the plasma has the sole role to supply the reactive species: neutral atoms (Cl or F) or molecules. These reactive species diffuse to the substrate and form volatile products with the surface material in a chemical reaction [79]. The volatile products are then transported away, leading to material removal from the substrate [80]. At typical pressure levels, the velocity vector of radicals will feature a broad angular distribution, leading to an isotropic etch profile. A typical glow discharge for plasma etching is driven at low voltages in order to avoid high-energy ions hitting the substrate. Three reactor configurations are common in plasma etching: barrel, downstream and parallel-plate reactors, each offering different advantages [28].

Since the number of radicals formed in the plasma is in the same order of magnitude as the number of surface atoms to be removed, a so-called *loading effect* can occur if the radicals are depleted during the chemical reaction. This results in an etch rate that is inversely proportional to the opening size in the etch mask, having an adverse effect on the uniformity throughout the wafer.

- *Synergetic physical-chemical plasma etching: (deep) reactive ion etching /(D)RIE*

Both purely physical and purely chemical etch processes have their own shortcomings: poor selectivity and isotropic etch profiles, respectively. These can be overcome by combining physical and chemical component in a single etch process [80]. In physical-chemical plasma etching techniques, the material removal is promoted by ion-surface interactions. In reactive ion etching (RIE), a diode-type parallel-plate reactor is used. In this type of etching, the formation of an anisotropic etch profile is energy-driven, as the substrate is disrupted by the bombardment of energetic ions. The high directionality of the ion bombardment carries through to the surface activations, resulting in an anisotropic etch profile. The achievable etch

rates are also significantly higher than in the case of physical etching, while the selectivity, although lower than for purely chemical etching processes, stays at reasonable levels. The anisotropy in RIE processes can also be driven by inhibitors, if the etch reaction produces a passivating agent that covers the substrate [28]. The ion bombardment removes the passivation from the horizontal surfaces, so the etching can continue in the direction perpendicular to the surface. To some extent, however, the passivated sidewalls are also attacked, resulting in tapered sidewalls. An effective way to manipulate the etch geometry in this case is by altering the ratios of gas mixture used in the process [81].

A slightly different technique for high rate, high aspect ratio etching of silicon using high density plasmas is the deep reactive ion etching (DRIE) process. In this technique two alternating process steps are carried out in a subsequent fashion: a passivation (C_4F_8) and an etching (SF_6) step. While the actual etch mechanism has a low anisotropy factor, the absolute amount of horizontal underetching is reasonably small, given the short etch cycles. This results in a scalloped sidewall profile typical for this technique. Potential problems that could arise in DRIE processes are the formation of *black silicon* and the *microloading* effect, also known as *aspect ratio dependent etching* (ARDE). A useful countermeasure to overcome this effect is increasing the ion flux [82].

Wet etching techniques:

- *Isotropic wet etching*

Isotropic or polishing etchants remove material in all spatial directions (crystallographic orientations for crystalline materials) at an equal rate. Usually, these agents are acidic. A subset of this technique are preferential etch processes [28], where the different etch rates between different materials or structural variations can lead to some slight anisotropy, but the achievable etch rates can be very high. The etchants used are often acids with an additive oxidizing agent. Typical isotropic etch reactions are diffusion limited. Isotropic etchants are employed for a wide range of tasks in microelectronics and MEMS, including the removal of damaged surfaces, rounding of sharp edges and corners, creating planar surfaces, or patterning of single- polycrystalline or amorphous thin films (metals, semiconductors, and isolators alike) [83]. A listing of some common isotropic etchants is to be found in Table 2.

Etchant	Material	Remarks
HF + HNO_3+ CH_3COOH	Si	Planar etch; 5 µm/min @ 25°C
HF	SiO_2	20-2000 nm/min
$HF:NH_4F$ (BHF)	SiO_2	100-500 nm/min @ 25°C
$HF:H_2O_2$	Ti	880 nm/min
H_2O_2	W	20-100 nm/min
HCl + $CeSO_4$ (sol.)	Cr	80 nm/min
HCl + glycerine	Cr	80 nm/min
HCl + HNO_3	Au	25-50 µm/min
KI + I_2 + H_2O	Au	0.5-1 µm/min
KOH + alcohols	Poly-Si	@ 85°C
Acetone	Organics	> 4 µm/min
H_2SO_4	Organics	> 1 µm/min
H_3PO_4	Al	660 nm/min @40-50°C
H_3PO_4	Si_3N_4	5-10 nm/min @160-180°C

Table 2: Common isotropic etch processes in microfabrication [28].

- *Anisotropic wet etching*

This technique is mostly used in the bulk micromachining of single-crystalline silicon. The anisotropy is caused by the different etch rates dependent on crystallographic orientation. Although a wide variety of alkaline aqueous solutions (with the optional addition of alcohol) has been used to perform this task, only a few are commonly used: potassium hydroxide (KOH), ethylenediamine pyrocatechol (EDP), tetramethyl ammonium hydroxide (TMAH), and hydrazine(N_2H_4) (For an overview of processes, see Table 3).

Etch process	Etch rate (100)	Etch rate ratio (100)/(111)	Mask material
KOH (aqu.) 85°C	1.4 µm/min	400	Photoresist, Si3N4, SiO_2
EDP(aqu.) 115°C	1.25 µm/min	35	SiO_2, Si_3N_4, Au, Cr, Ag
TMAH (aqu.) 90°C	1 µm/min	12.5-50	SiO_2, Si_3N_4
N_2H_4 (aqu.) 100°C	2 µm/min	10	SiO_2, most metals

Table 3: Anisotropic silicon wet etching processes [28].

Due to the (relatively) large selectivity between the fast (100) and slow (111) etching crystal planes, the latter are generally regarded as etch-stop planes although in reality the etch process does not actually stop at these planes. As a consequence, anisotropic wet etched structures will have exposed (111) planes. This fact limits the range of achievable structure geometry considerably. An added effect is that the obtainable geometry will also be different for different substrate orientation (i.e. for (100), (110), or (111) wafers). In Figure 14, some typical anisotropic wet etched structures in (100) silicon are shown. A description of the widely-used electrochemical model of KOH etching is described by Seidel *et al.* in [84].

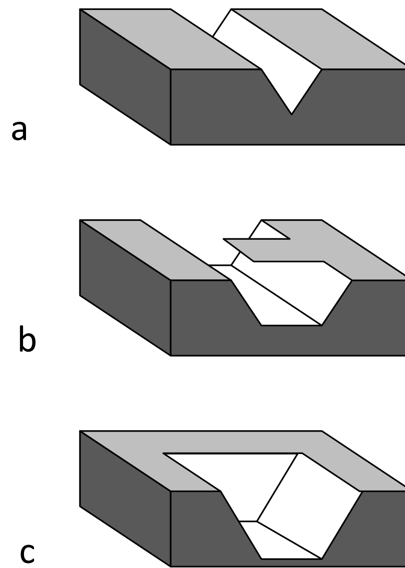

Figure 14: Schematic representation of typical bulk micromachined structures created by anisitropic wet etching of (100) Si. a: V-groove, b: cantilever, c: membrane.

2.4. Summary

Manufacturing functional thin film systems involves a large variety of technical processes. This includes additive techniques, such as physical and chemical vapour deposition, as well as subtractive methods, like lithographic patterning and etch processes. Chapter 2 gives an overview with explanatory notes about a selection of these techniques that are utilized in the latter part of this work for the fabrication of thin films and functional thin film systems based on silicon nitride.

Physical vapour deposition techniques (i.e. electron beam evaporation and magnetron sputter deposition) are used for the deposition of metallization systems and silicon nitride thin films. Inductively coupled plasma enhanced chemical vapour deposition is the technique of choice for depositing amorphous hydrogenated silicon nitride thin films.

Conventional and lift-off lithographic methods are used throughout this thesis in order to fabricate appropriate test structures and functional layers. Wet and dry etch techniques are employed not only for patterning purposes, but also for qualifying the robustness of different silicon nitride deposits against some etchants.

Other than that, it is necessary to assess and measure a wide range of the thin film properties in order to learn more about the deposition process and the influence of different parameters, as well as to evaluate the usefulness of films in certain application scenarios. For that reason, several analysis techniques are applied, which are described in Chapter 3.

Chapter 3: Methods for analysis and characterization of thin films

Thin films and thin film systems, deposited and patterned (see Chapter 2), are integrated for a large variety of different functions into MEMS. Although for some cases a practical approach would dictate to judge their quality solely on how well they perform by evaluating their performance in the corresponding device, experimental techniques are requested to analyse their properties before device integration. In the following chapter a brief overview of the analytical concepts, techniques, and instruments used in this thesis will be given.

3.1. Electron microscopy

Unlike optical microscopy, where electromagnetic waves in the visible light range are utilized to visualize microscopic features of a sample, electron microscopy applies a beam of accelerated electrons for this purpose. The spatial resolution of optical imaging devices is inherently limited by diffraction. This diffraction limit is dependent of the wavelength of the light being used. Accelerated, free electrons also exhibit wave-like behaviour, such as diffraction, and they have a wavelength associated to them, the *de Broglie wavelength*, defined as $\lambda_B = \frac{h}{p_m}$, where p_m is the momentum of the particle and h is the Planck constant. The theoretical diffraction limit resulting from this relation for electrons can be by orders of magnitude smaller, compared to visible light. This opens the possibility for electron optics to have a substantially higher capability in lateral resolution than conventional solutions. Electron microscopy systems are not only utilized to obtain structural and topographic information about the specimen, but in combination of supplementary instruments chemical analysis are possible.

Electron microscopes are generally divided in two categories: Scanning electron microscopes (SEM) and transmission electron microscopes (TEM), both of which will be described in the following sections.

3.1.1. Transmission electron microscopy

Transmission electron microscopes are the original form of electron microscopes, and operate in a largely analogous way with respect to optical microscopes. They utilize an electron beam passing

through a thin specimen to create an image. The electron beam is produced by an *electron gun*, and is accelerated by a high voltage in the range of 100 to 300 kV [85]. Electrostatic and electromagnetic lenses are utilized to focus the beam, and to magnify the image. The image is formed either on a fluorescent or scintillator screen, or is recorded via a charge coupled device (CCD).

Electron guns generate the high-voltage electron beam, as a point-like illumination source for the electron microscope. They consist of several components: the *cathode*, the *Wehnelt* cup, the *anode* and an electric circuit for biasing. Cathodes emit the electrons either thermionically or via field emission (cold cathode). The thermionic cathode is generally either a tungsten filament or a lanthanum hexaboride (LaB_6) crystal. Cold cathodes for electron microscopy are formed from a tungsten cylinder having an extremely sharp tip on one end. The Wehnelt cup, placed beneath the cathode forms a small circular aperture for the electrons to pass through. It is also put on a more negative potential than the cathode. Thus, it acts as an electrostatic lens. The potential difference (the *gun bias*) is adjustable, and controls the number of electrons passing through. At higher bias voltages electrons originating from more peripheral areas cannot pass through, thus lowering the beam intensity. On the other hand, this leads to a smaller diameter of the first crossover, resulting in a higher lateral resolution in imaging [86], by effectively suppressing optical aberrations.

Electromagnetic lenses are applied in the TEM both above (condenser) and beneath (objective, diffraction, and projection lenses) the sample plane. Electromagnetic coils produce a radially symmetric field, acting as a convex lens for electrons. Since the coils are typically under a high voltage, and often carry large current densities, proper insulation and active (water) cooling is employed. The way the specific lenses operate inside a TEM is dependent on the operating mode of the instrument:

- Image mode: High-magnification (HM-TEM) and low-magnification (LM-TEM). In HM-TEM mode, the object lens projects the first magnified image (a 20-40x magnification) at the plane of the *selected area aperture*, on which the imaging lens system (consisting of intermediate and projection lenses) focuses, creating an additionally magnified image on the screen. In LM-TEM mode the objective lens is turned off, and the imaging lens system focuses on the sample, thus generating a far less magnified image on the screen.

- In diffraction mode: The imaging lens system is focused onto the diffraction pattern appearing in the *back focal plane* of the objective lens. It is important to note that since the first magnified image and the diffraction pattern are simultaneously created by the objective lens (albeit in different planes), one can simply switch between HM-TEM and diffraction mode by simply refocusing the imaging lens system.

- Nanoprobe mode: In the previous modes, an (almost) parallel electron beam arrives at the sample (i.e. microprobe mode) while in nanoprobe mode the current in the mini-condenser lens above the sample is reversed, creating a crossover, a very small spot size over the sample. This is then used for STEM (scanning transmission electron microscopy) and for microanalysis purposes.

Transmission electron microscopy studies presented in the later part of this work have been carried out using a *FEI Tecnai F20* microscope, equipped with a field emission gun, under an acceleration voltage of 200 kV, with a stated point resolution of 0.21 nm.

3.1.1.2. Electron energy loss spectroscopy

Electron energy loss spectroscopy (EELS) is an analysis technique, where the specimen is exposed to a monoenergetic electron beam. Part of the electron beam undergoes inelastic scattering upon their interaction with the specimen. An electron spectrometer is used to record the energy distribution of the electron beam after its interaction with the specimen. The amount of energy loss is dependent on the inelastic interaction that has been taken place. These include inter- and intraband transitions, inner shell ionizations, plasmon and phonon excitations and Cherenkov radiation [87]. Some of these interactions (especially inner shell ionizations) are characteristic to the chemical elements being present in the sample, making the technique useful for mapping of the local element distribution.

A typical, schematic loss spectrum is shown in Figure 15. The first peak is the so-called zero-loss peak, representing these electrons that are transmitted through the sample with no or little energy loss, which constitute to the majority of the signal. In the range of about 5 to 50 eV, peaks resulting from inelastic scattering with outer-shell electrons is visible. Although the recorded intensity quickly decreases at higher energies, characteristic features superimposed to this background such as ionization edges are observable when arranged in a semi-logarithmic plot. These ionization edges correspond to different binding energies, and are dependent on the atomic number of the scattering atom. Additionally, both low-loss peaks and ionization edges feature a fine structure from which further assessments towards the microstructure of the specimen can be made.

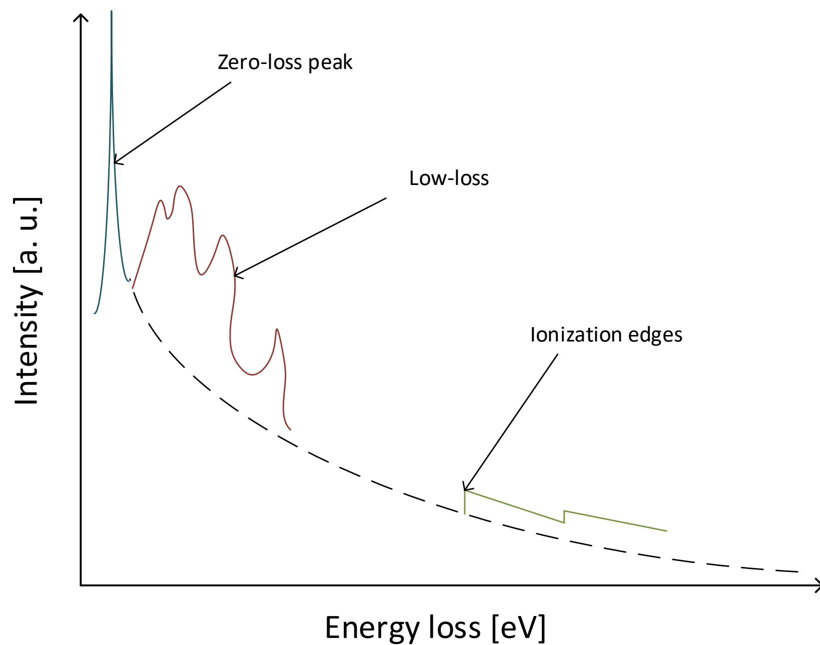

Figure 15: A typical, schematic electron energy loss spectrum (after Egerton et al. [87]).

The EELS measurement in the later chapters of this work have been performed using a *GIF Tridiem* system, manufactured by *Gatan, Inc.* featuring a 5 mm diameter entrance aperture.

3.1.2. Scanning electron microscopy

In a scanning electron microscope (SEM) the surface of the specimen is probed using a focused electron beam. This beam is scanned over a rectangular area using raster scanning. The electron beam interacts with the sample surface, resulting in the emission of secondary electrons and backscattered electrons, as well as electromagnetic radiation (cathode luminescence and X-ray). These signals are recorded using a range of detectors in the vicinity of the sample, and mapped to the raster. The intensity of these signals carries information about the topography and chemical composition of the sample [88]. Since in SEM, the electron beam does not have to pass through the specimen, samples having much larger thickness, and acceleration voltages in the range of 0.5 to 30 keV being much lower than in TEM can be used. As a consequence, the volume of interaction is generally much larger [89], resulting in a significantly lower spatial resolution, as illustrated in Figure 16. By an appropriate positioning of the electron detectors, the secondary and backscattered electron signals can be efficiently separated and evaluated independently. This enables to observe topographic, crystallographic and *Z*-contrast (scattering depending on the atomic number *Z*) from the specimen using the same excitation.

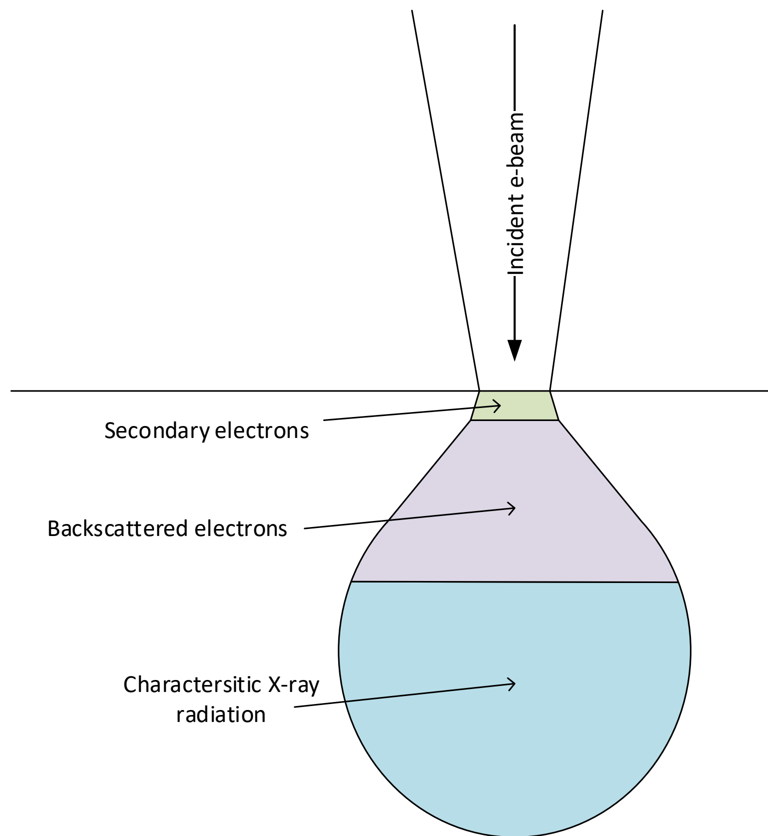

Figure 16: Interaction volume of the incident e-beam and surface-near sample material during SEM probing (after [89]).

The scanning electron micrographs in this work have been recorded using the *SU8030 SEM system* made by *Hitachi, Ltd*. The system features a cold cathode emitter and a beam deceleration function enabling ultra-high-resolution imaging, as well as three secondary electron detectors in a top/upper/lower configuration. Standard accelerating voltages used were around 2-3 keV for imaging and 10-20 keV for EDX (see below) analyses.

3.1.2.1. Energy dispersive X-ray spectroscopy

A frequently used technique for elemental analysis inside a SEM is energy dispersive X-ray spectroscopy (EDX). The emission of characteristic X-ray radiation due to the unique atomic structure of each element is stimulated by a focused beam of high-energy particles, being electrons typically in the 10-30 kV energy range. Electrons of the inner shells can get ejected into higher energy states, and their place will be filled with electrons from higher shells. The energy differences between these states are characteristic for each element [88]. The count and energy of the emitted X-ray photons can be measured using an energy dispersive spectrometer consisting of a detector and pulse processor.

During detection, when an X-ray photon is first absorbed, a high-energy photoelectron will be ejected from the detector silicon. This photoelectron subsequently travels through the detector material, and loses its kinetic energy due to inelastic collisions. These collisions cause electrons to be transferred from the valence into the conduction band, as the rest of the energy leads to the ejection of an Auger electron or an X–ray photon, which will undergo further inelastic scattering, or will be re-absorbed. Ultimately this results in a characteristic number of additional electrons in the conduction band, which is proportional to the energy of the X-ray radiation originating from the sample.

EDX analyses presented in this work were performed using an *X-Max* 50 mm^2 detector made by *Oxford Instruments, Plc*, with a stated energy resolution of 129 eV FWHM (full width at half maximum) for the MnK_{α} peak. Typical acceleration voltages used were 10 to 20 kV, and beam currents in the range of 5 nA.

3.2. X-Ray photoelectron spectroscopy

Another spectroscopic analysis technique for assessing the elemental composition of a specimen is X-ray photoelectron spectroscopy (XPS). When applying this technique, the sample material is irradiated with an X-ray beam under ultra-high vacuum conditions, resulting in the ejection of electrons from the surface typically in a depth up to 10 nm of the sample. The number and energy of these electrons is measured by using an electron monochromator, a detector, and a scan and readout system. By knowing the energy of the X-ray irradiation and the work function of the spectrometer, the core-electron binding energies of the emitted electrons, that are characteristic for each element, can be calculated [90]. Although in principle the detection of every element from the periodic table is possible, conventional XPS systems only effectively detect elements above the atomic number Z = 3 (lithium). The typical detection limits are in the parts per thousand range. The energy resolution of XPS devices enables to investigate the chemical shift present in the bonding energies of atoms. The chemical shift is due to the effect of the valence electrons on the attractive force acting between the nucleus and core-electrons. This effect is dependent on the chemical environment of the atom, thus making XPS a most powerful tool for the determination of even the binding state of the elemental composition [91].

The XPS measurements presented in this work have been carried out using a *Theta Probe XPS system* by *Thermo Fisher Scientific, Inc.* using measurements at a fixed emission angle of 45°. The device features a low-energy Argon (< 500 eV) ion source for sputtering and depth profiling.

3.3. Fourier-transform infrared spectroscopy

When a covalent bond between two atoms is formed, that system can be considered in a first approximation as a simple harmonic oscillator. In molecules, crystalline or amorphous solids, due to the specific spatial configuration of atoms and inter-atomic bonds there exists a range of mechanical vibrating modes such as stretching, rocking, or wagging [91]. As it happens, the frequency of these molecular vibrations falls into the infrared (IR) range of the electromagnetic spectrum, therefore infrared absorption spectroscopy can be applied for detection. Basically, molecular vibrations are grouped into one of the following two complementary categories: Raman or infrared-active. In the first case, the electric polarizability of the molecule must be changed, while in IR-active modes, the electric dipole moment should change. This has the consequence that symmetrical molecular bonds are generally not IR-active, unless they are slightly distorted by their local bonding environment. On a similar note, overtones (i.e. double, triple, quadruple frequencies) and combinations of other modes are sometimes detectable, as are *phonons* (collective lattice vibrations).

Conventional diffractive infrared (DIR) absorption spectroscopy is based on an IR-transparent prism, or a diffraction grating, and a thermocouple detector. The more modern design, the Fourier-transform infrared (FT-IR) spectroscope, is based on a Michelson interferometer, consisting of a beam-splitter, a stationary and a moving mirror (see Figure 17). This design has two main advantages, both increasing the sensitivity compared to the DIR approach. The *Felgett* advantage is caused by the fact that in FT-IR all frequencies across the frequency range are processed at the same time. The consequence of this is that more averaging can be done while maintaining the same measurement time, resulting in a higher signal to noise ratio. The *Jaquinot* advantage is caused by the elimination of the need for a small aperture for a good wavelength resolution. Using a significantly larger aperture leads to an increased sensitivity [92].

The FT-IR technique is widely used to determine hydrogen content in silicon nitride thin films deposited by various CVD techniques[93].

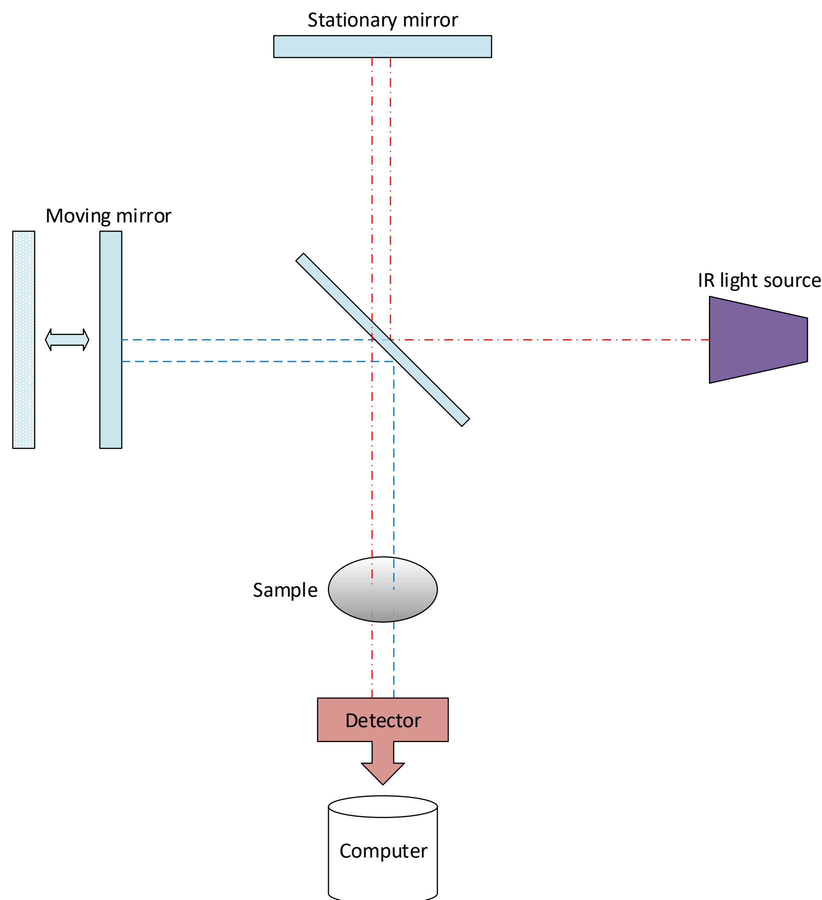

Figure 17: Michelson interferometer in an FTIR spectrometer.

In this work, FT-IR measurement were carried out using a *Tensor 27*, FT-IR spectroscope, manufactured by *Bruker Corp.* The used measurement range was from 400 cm^{-1} to 4000 cm^{-1}, with a resolution of 4 cm^{-1}. The average spectrum from was obtained from 16 scan samples, after the subtraction of the independently recorded background spectrum.

3.4. Mechanical surface profilometry

In order to assess the quality of as-deposited, annealed or etched thin film surfaces, or microstructures during different stages of their fabrication, profilometric methods are employed as standard approach to measure topographic features of the substrate. These methods are typically based on visible light, electron-beam interaction with the sample surface, or are mechanical. The latter group is in focus of this subchapter.

In two- or three-dimensional mechanical profilometer systems a stylus is brought into direct contact with the sample surface, using a constant force, and is scanned along the surface using a linear

motion (2D), raster or radial scan (3D). The vertical displacement of the stylus is converted into an analogue electrical signal by a pickup, is amplified, converted to a digital signal and assigned to the spatial coordinates [94]. The most important factors limiting both the lateral and vertical accuracy of the measurement are the size of the stylus tip, the dynamic behaviour of the stylus, and the accuracy of the moving mechanical stage.

In this work, a *Bruker Dektak* benchtop profilometer was used, mainly to identify and measure etch profiles in a linear mode. The vertical measurement range was set to the lowest limit (20 µm).

Atomic force microscopes (AFM) operate in a way that is largely similar to stylus profilometers, that is the surface of a sample is probed by scanning a tip over it. The core component of an AFM is a microcantilever acting as a soft spring, with an integrated tip ideally ending in a single atom. When the tip comes in close proximity to the sample surface the interaction creates a net force between those two. This force is measured by measuring the deflection or the corresponding feedback signal, and is e.g. kept constant using a feedback loop [95]. As a consequence, when scanning over the sample surface, the tip will follow the surface contour. This mode of operation is called *contact mode*. Another possibility is to excite the cantilever near its resonant frequency using a piezoelectric element. In this mode, the so-called tapping mode, the interaction forces are only present for a short duration of each oscillation period, when the tip comes into sufficient proximity to the sample surface. In this case a piezoelectric actuator is used to adjust vertical position of the cantilever in order to maintain a constant amplitude of oscillation. The AFM image is formed from the measured intermittent forces of tip-sample interaction [96].

3.5. Nanoindentation

Nanoindentation is a destructive analysis technique, where a small, hard tip with precisely known mechanical properties and geometry is pressed into a sample in order to determine its mechanical properties. The tip is inserted into the sample by applying an increasing *load* force P, where the resulting *displacement* d is measured simultaneously. After reaching the maximum load, the applied force is reduced back to zero. The hardness H, as a function of indentation depth is determined by dividing the load P by the indentation area A_r. The indentation area is calculated using an area function that takes both the geometry of the tip and the elastic load during the indentation process into consideration. The reduced Young's modulus is deduced from the slope of the unloading curve, the stiffness $S = \frac{\Delta P}{\Delta d}$ [97]. Given the Poisson's ratio of the material under test, the actual Young's modulus E_f can also be calculated, albeit including influence of the substrate material when

investigating a thin film. A common rule of thumb is to maintain at least a 1:10 ratio of maximal indentation depth and film thickness in order to exclude the substrate influence on the measurement results [98].

For the actual measurements, a *MTS nanoindenter XP* system has been used, with a diamond Berkovich indenter tip: a three-sided pyramid with a half-angle of 65.3°. The specified vertical displacement resolution is 0.02 nm, with a force resolution of 50°nN, and a maximal indentation force of 500 mN. Typical samples thicknesses were in the range of 600-700 nm, with a maximal indentation depth of 300 nm. This seems to be in contradiction with the aforementioned 1:10 rule, but it is important to note, that the range in the measurement data influenced by the substrate can easily be distinguished and discarded during post-processing.

3.6. Spectral reflectometry

Spectral reflectometry is an optical characterization method that is used to determine the thickness, index of refraction and extinction coefficient of a transparent sample by the reflection of electromagnetic radiation (light) [99]. A broadband (white) source of light is focused onto the sample, and the reflected light is separated into its spectral components. The intensity of the reflected light over the available wavelength range is measured. By comparing the measurement results to analytically calculated values by processing, the most matching set of sample parameters can be computed [100]. This, however, requires fairly good initial parameters, e.g. some available information of the expected values of the film parameters given above. A strong limitation is set by the wavelength of the irradiation source, as the measurement accuracy of very thin samples is negatively influenced.

In this work, a *Filmetrics F20* spectral reflectometer was utilized for thickness and refractive index measurement, with the accompanied *FilMeasure* software. The wavelength range for data acquisition was 200-1100 nm.

3.7. Wafer geometry gauge

In MEMS manufacturing, wafer geometry measurement equipment can be extremely useful to determine the actual thickness, total thickness variation (TTV) and bow of individual wafers, as these parameters influence important parameters during processing (e.g. etch times) and the device performance. For the investigation of thin films deposited onto blank wafers, wafer geometry gauges can be utilized to determine the residual stress built up in the film, by measuring the bow of the wafer

prior and subsequent to the thin film deposition. Given the thickness of the film and substrate-related parameters, such as its Young's modulus E_s ,and Poisson ratio v_s, the biaxial film stress is determined using a modified version [101] of Stoney's formula [102]. In practice both optical and capacitive measurement techniques are applied for measuring the curvature of the wafer.

For the wafer-bow measurements throughout this work, an *MX-203* capacitive wafer geometry gauge made by *E+H Metrology GmbH* was used. The biaxial film stress was in turn calculated by using the wafer bow measurements, as well as the film thickness that was determined beforehand.

3.8. Thermal effusion measurement

In a thermal effusion measurement, the chemical composition of gaseous material escaping a heated sample is analysed. Since thin films used in MEMS are often contain several chemical elements, the identity and quantity of the materials that escape are somewhat indicative of its chemical composition. More than that, the exact temperatures the respective species escape the thin film also contains information about the structure of the material under test [103].

Thermal effusion measurements presented in this work were carried out in a custom-made test chamber. The system consists of a vacuum chamber that is evacuated to a base pressure of 10^{-9} mbar for the tests using a two-stage pump setup. The sample is placed on an aluminium nitride rectangular heater plate (*Boralectric HTR1001*), which is heated following a ramp from 15°C to 1000°C over the course of 3 hours, held at 1000°C for 1 hour, and cooled down to room temperature, using a *Textra HC 3500* controller The quantity of materials detected is logged over the whole experiment, by using the appropriate channels of a quadrupole mass spectrometer (*HALO 201 RC residual gas analyser* by *HIDEN, Inc*.), from 1 to 100 amu (atomic mass unit).

3.9. Summary

This chapter introduced a number of electron-optical, spectroscopic, optical, and mechanical methods of instrumental analytics that can be effectively utilized for the assessment of important thin film properties. In the following chapters 4 and 5, these techniques will be applied for the characterization of amorphous silicon nitride thin films, deposited using the ICP-CVD and magnetron sputtering techniques, respectively.

Chapter 4: Physical and microstructural properties of silicon nitride thin films deposited by ICP-CVD

Parts of this chapter have already been published in [104-106].

In section 2.2.3, some information about the basic properties of ICP-CVD deposited SiN films were already presented, based on the work of Zambom [66, 67, 70], Chou [72] and Kshirsagar [74]. In order to gain a deeper understanding about the ICP-CVD deposition of silicon nitride, a systematic study was conducted targeting to tackle essential dependencies between deposition parameters and the resulting physical properties of the SiN layers. The basis for this was provided by carrying out a series of “screening” experiments (see below).

4.1. Experimental details of a-SiN_x:H thin film deposition

The substrates used for the deposition experiments were double-side polished, *n*-type (phosphorous doped,) (100)-oriented single-crystalline silicon wafers, having a resistivity of ρ > 50 Ω·cm. The wafers had a nominal diameter of 4 inches and a thickness of 350±15 µm. Prior to the thin film deposition, the substrates have been cleaned according to the following procedure: they were subsequently rinsed with acetone and isopropyl alcohol, followed by a short (30 s) dip in buffered hydrofluoric acid to remove the native oxide from the wafer surface.

The deposition experiments were performed using an *Oxford Plasmalab 100 System* (See Figure 18) ICP-CVD downstream reactor (for details see chapter 2.2.3). The process chamber was heated to the selected deposition temperature and evacuated to a base pressure of $9 \cdot 10^{-5}$ Pa, before the substrate was loaded, and nitrogen and argon were introduced together with silane (SiH_4) via a gas distribution ring arranged about 5 cm above the substrate electrode. Flow rates of the SiH_4 precursor and the Ar dilution gas during the deposition were kept at constant values of 12 and 48 sccm, respectively. After the introduction of the process gases, the pressure in the deposition chamber was stabilized using an APC (automated pressure control) valve. The ignition sequence starts with the CCP (capacitively coupled plasma) source set to maximum power (300 W), and the ICP source to 1500 W, whereas the latter value being decreased during the silicon nitride deposition process. During two subsequent steps the power of the CCP source was generally tuned down to zero, while that of the ICP source was adjusted to the selected deposition power value. This practice was applied to ensure a smooth transition to a stable ICP discharge and deposition process. After the deposition was completed the plasma sources were turned off, while simultaneously cutting the process gas flows.

Next, the process chamber was purged with pure N_2 gas for a duration of two minutes to remove any process gas residuals. Finally, the chamber was evacuated once again to the base pressure before the coated substrate could be unloaded using the load-lock mechanism.

Figure 18: Photograph of the Oxford Plasmalab 100 System used for the ICP-CVD silicon nitride deposition experiments. A schematic drawing is provided in section 2.2.3.

In order to efficiently investigate the influence of process parameters on the resulting properties of the deposited silicon nitride thin films, a two-stage experimental series was performed. The first experimental stage was designed for screening purposes. Here, the impact of all potential input parameters was investigated on a fundamental level. For this assessment, an appropriate design of experiments (DoE) approach was selected [107]. The list of relevant input variables comprised four quantities: the ICP plasma power P_{ICP}, the pressure p_{dep} in the deposition chamber, the substrate temperature T_s, and the flow rate ratio $R_{N2/SiH4}$ of N_2 and SiH_4. Within the given constraints a two-level full factorial design [108] was chosen including two additional runs with parameters set at the mid-points resulting in 18 deposition runs in total, whereas the details are provided in Table 4. In the case of depositions performed at a substrate temperature of 120°C, the wafers were clamped with a glass

ring to the substrate holder and a He backflow was used for improved heat transfer. At T_s = 350°C, the wafer clamp was removed, as under these conditions the thermo-mechanical stress at such high temperatures induced by the differences in coefficients of thermal expansion would have been too large, so that the heat was transferred solely in a radiative manner. The parameter values used in the experiments were partly based on prior experience with the deposition system, as well as on values reported in literature, especially on the works of Zambom *et al.* [66, 67]. It is worth noting that the different deposition runs at both temperature levels were carried out in a random order, thus eliminating any potential bias of the results. The deposition time was held constant at 15 minutes.

Run #	T_s [°C]	p_{dep} [mTorr]	P_{ICP} [W]	$R_{N2/SiH4}$
1	120	4	500	0.5
2	120	4	500	2
3	120	4	1000	0.5
4	120	4	1000	2
5	120	10	500	0.5
6	120	10	500	2
7	120	10	1000	0.5
8	120	10	1000	2
9	350	4	500	0.5
10	350	4	500	2
11	350	4	1000	0.5
12	350	4	1000	2
13	350	10	500	0.5
14	350	10	500	2
15	350	10	1000	0.5
16	350	10	1000	2
17	120	7	750	1
18	350	7	750	1

Table 4: Deposition parameters of layers synthesized within the screening stage.

The silicon nitride deposits were analyzed in the following manner: at first the thickness *d* and refractive index *n* (at λ = 632.8 nm) of the deposited thin films were determined using the spectral reflectance (SR) method (see chapter 3.6). Given the film thickness, the deposition rate for each parameter set was calculated, as well as the mechanical film stress provided by measurements with a wafer geometry gauge (see Chapter 3.7). The temporal evolution of film stress was monitored by taking repeated measurements at fixed time intervals. The chemical robustness of the silicon nitride deposits was tested by immersing pieces of a coated wafer into a 1:7 mixture of concentrated (50% v/v) hydrofluoric acid (HF) and de-ionized water. The wet etch rates were determined by the surface profilometer measuring the step height at the etch front and by measuring the remaining film thickness using the SR method. Due to the large etch rate variation across the set of samples, given in

the next section, the etch times were adapted accordingly. Chemical analyses of the samples were performed using techniques such as FT-IR (Chapter 3.3) and XPS (Chapter 3.2).

The screening experiments provide a suitable basis for an initial assessment regarding the individual impact of these deposition parameters on the resulting physical, mechanical and chemical properties of the silicon nitride thin films. Based on these results, a second stage of experiments were performed, where the impact of the most influential deposition parameters is scrutinized individually, while keeping all other variables constant.

4.2. Screening experiments and the influence of ICP power, deposition pressure, and substrate temperature on film properties

The average measured values of the deposition rate R_{dep}, refractive index n, film stress σ, and wet etch rate *WER* [104] are presented in Table 5 to illustrate the main effects of the independent variables (i.e. the deposition parameters) on the individual dependent variables (the measured values). As it is apparent from the results, the most significant contrast can be found between the properties of silicon nitride thin films deposited at low (0.5) and high (2) values of $R_{N2/SiH4}$.

All samples		*d [nm]*	R_{dep} *[nm/min]*	*n*	*σ[MPa]*	*WER [nm/min]*
P_{ICP} *[W]*	500	153	10.2	2.20	-380	570
	1000	248	16.5	2.22	-518	865
p_{dep} *[mTorr]*	4	185	12.3	2.12	-530	588
	10	216	14.4	2.30	-368	838
T_s *[°C]*	120	213	14.2	2.19	-398	1055
	350	197	13.1	2.18	-418	410
$R_{N2/SiH4}$	0.5	135	9.0	2.35	-962	5.8
	2	266	17.7	2.07	+11	1429

Table 5: Influence of ICP-CVD deposition parameters on the measured properties of the silicon nitride thin films.

The extreme difference in all measured values of the physical properties of the samples is a strong indicator that the precursor gas ratio is the most influential input parameter in the investigated range of ICP-CVD deposition of silicon nitride thin films, and also shows strong correlation with the deposition rate (as presented in Figure 19, Figure 20, and Figure 21). Moreover, these results suggest splitting the samples into two categories, and investigate the influence of the other parameters beside $R_{N2/SiH4}$ within these categories, rather than globally, thus avoiding that the effect of $R_{N2/SiH4}$ obfuscates the potential impact of P_{ICP}, p_{dep} and T_s. Therefore, within this thesis, the terminology *Type I* will be

introduced for layers synthesized at a high $R_{N2/SiH4}$ values, while *Type II* represents those deposited at low $R_{N2/SiH4}$.

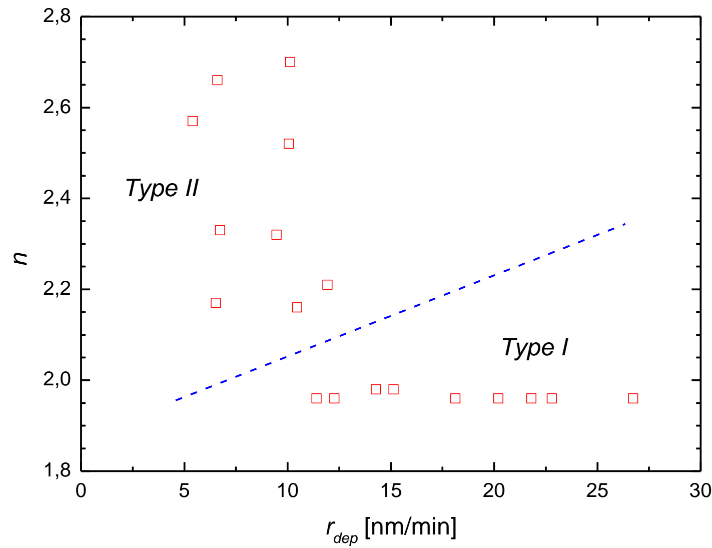

Figure 19: The index of refraction of ICP-CVD silicon nitride thin films versus deposition rate, grouping Type I and Type II samples by the dashed line.

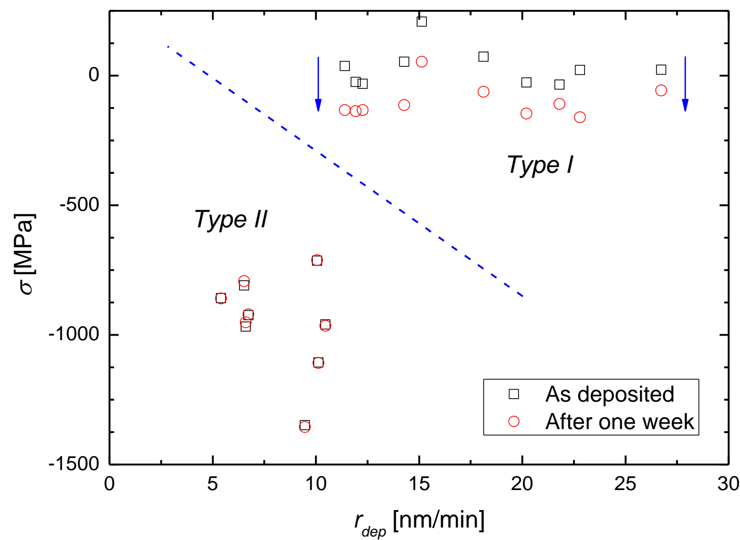

Figure 20: Biaxial film stress of ICP-CVD silicon nitride thin films as a function of the deposition rate, grouping Type I and Type II samples including drift effects indicated by arrows.

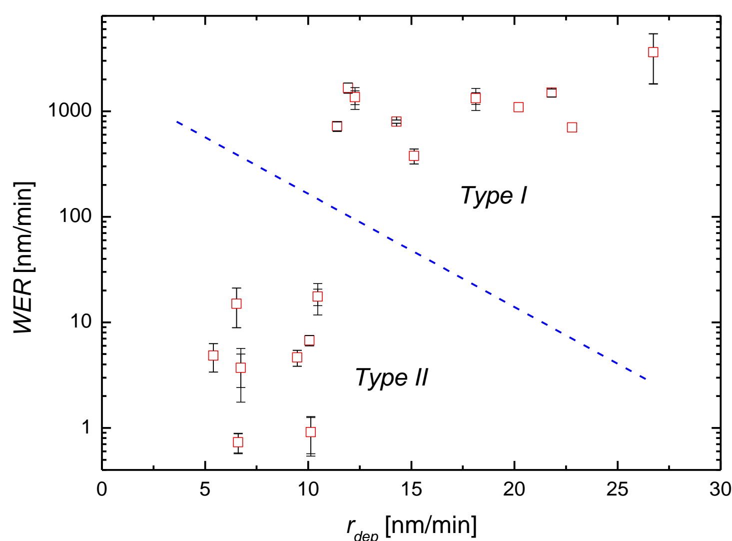

Figure 21: Wet etch rate in hydrofluoric acid of ICP-CVD silicon nitride thin films versus deposition rate, grouping Type I and Type II samples.

The recorded FT-IR absorption spectra also reveal a strong distinction between the characteristics of *Type I* and *Type II* a-SiN_x:H films (see Figure 22) due to four salient differences. Firstly, in the spectra of *Type I* samples there is a very prevalent N-H (Si-NH_2) stretching mode absorption peak at around 3330-3340 cm^{-1} that is practically absent in the case of *Type II* layers [109, 110]. Secondly, the compound Si-H stretching mode absorption peak (at about 2150 cm^{-1}) is clearly observable in spectra of *Type II* samples, but not in those of *Type I*. Thirdly, the appearance of a Si-O absorption peak at 1108 cm^{-1}, which is far more prevalent in the spectra of *Type I* a-SiN_x:H samples than in *Type II*. Since the deposition took place in an oxygen-free environment, the only plausible explanation for this effect is the post-deposition oxidation of the samples. Lastly, the shift of the main Si-N stretching absorption band towards lower wavenumbers of *Type I* (and towards stoichiometric silicon nitride as well, with the theoretical peak at 840 cm^{-1} [111]) with respect to *Type II* is clearly observable. This could theoretically be attributed to two individual factors. The difference in residual stress can lead to different bond lengths and as a consequence, a different frequency of the Si-N stretching mode vibration. The other possibility is, given a difference in the stoichiometry/chemical composition or microstructure of the *Type I* and *Type II* samples, the average local bonding environment of a Si-N bond may statistically be significantly different. This means that the Si-N stretching vibration mode is distorted differently by the neighbouring atoms in the two individual a-SiN_x:H layer types, again leading to a discrepancy in the peak wavenumber of the absorption band. This issue is addressed after analysing in detail the results of the XPS measurements in the following part of this section.

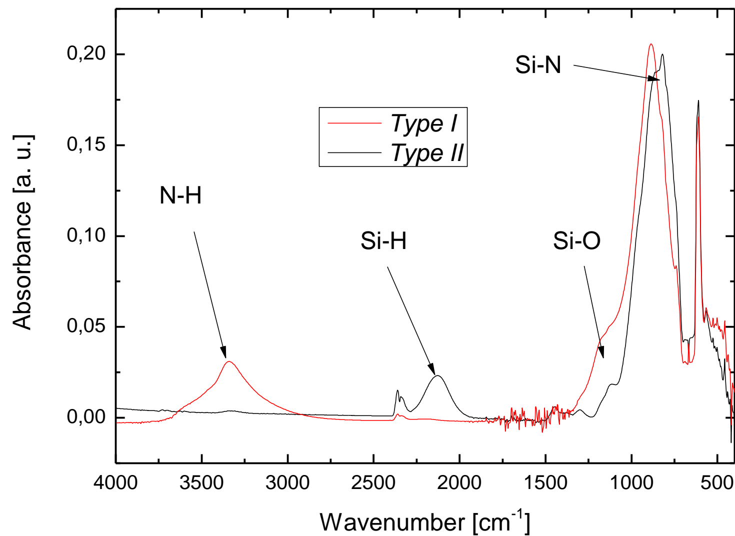

Figure 22 : Comparison of the FTIR spectra of Type I and Type II ICP-CVD silicon nitride thin films with the most prominent absorption peaks highlighted. The peak at ~ 2350°cm^{-1} is attributed to atmospheric CO_2.

The XPS surface scans also reveal a notable difference between the silicon peaks of *Type I* and *Type II* films, as presented in Figure 23. From this point on a simple deconvolution of the peak into three Gaussian peaks associated with pure silicon, silicon nitride and silicon dioxide [112] is performed. This demonstrates some important differences between the two layer types. In *Type I* films, as illustrated in Figure 23a, the majority of the signal originates from electrons of Si-N bonds, and only a small portion is associated with pure silicon. In contrast, as shown in Figure 23b, XPS spectra of *Type II* samples exhibit a relatively large portion related to pure silicon in the Si peak of their XPS spectrum. These observations set a very clear tendency, in which the average number of nitrogen atoms a silicon atom forms a bond with is significantly higher in the case of *Type I* than for *Type II* layers. This result is consistent with the shift of the main Si-N absorption band in the infrared spectra between *Type I* and *Type II* samples. In *Type I* samples, the asymmetric stretching mode Si-N absorption peak at 902 cm^{-1} is dominant, while in the case of *Type II* samples the peak at 870 cm^{-1} typically prevails in near-stoichiometric Si_3N_4 samples [111].

More realistically though, is the assumption that in both cases the observed Si-N absorption band is a compound band, a convolution of the basic Si-N asymmetric stretching mode vibration, perturbed by all the different possible adjacent atoms. The reason for the high portion of Si being in a SiO_2 bonding configuration for both *Type I* and *Type II* samples is that the XPS scans were performed only on sample surfaces, which were prone to oxidation during storage under atmospheric conditions.

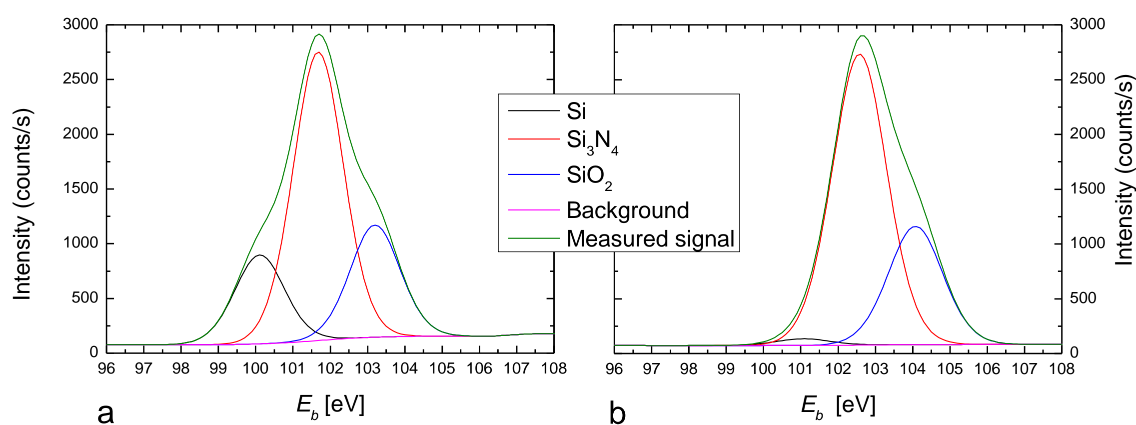

Figure 23: Detailed view on the silicon peak centred at the binding energy E_b of 102 eV of XPS spectra of Type I (a) and Type II (b) ICP-CVD silicon nitride thin films demonstrating the different chemical shift by a deconvolution into Si, Si_3N_4, and SiO_2-related peaks.

Depth profiles of the atomic composition of both *Type I* and *Type II* samples were also recorded, by using the XPS technique (see Figure 24). The average N/Si atomic concentration ratio over the whole thickness of the a-SiN_x:H thin film samples turned out to be in the range of 0.57-0.65 in the case of *Type I* and between 0.35 and 0.52 for *Type II* samples. This means that all the samples are rather silicon-rich, featuring a much lower N/Si ratio compared to both stoichiometric Si_3N_4 and the N/Si atomic ratio of 1 to 4 in the precursor gas mixtures. The reason for these high discrepancies is the dissociation rate of SiH_4 being significantly higher than that of N_2 in the ICP plasma [113]. This leads to a more efficient incorporation of Si atoms into the deposit compared to N, resulting in Si-rich samples. *Type I* samples also exhibit a high concentration of oxygen (in the range of 11.6-17.7 at. %), which remains relatively constant throughout the thickness of the sample, excluding the surface-near region. As pointed out above, the only possible source of the incorporated oxygen is from the atmosphere, in which the sample was stored between deposition and the XPS study. Indeed, there are reports of similar post-deposition oxidation of hydrogenated silicon nitride thin films in standard literature [114]. In contrast to these findings, *Type II* samples do not seem to undergo post-deposition oxidation, excluding the regions close to the surface, as the measured oxygen concentration remains below 2 at. %. It is important to stress that these reported concentrations do not take any impact arising from the hydrogen which is incorporated during film deposition into account, due to the inability of the XPS measurement technique to detect such light elements. That means that the absolute values of the reported atomic concentrations are only valid when considering a silicon/nitrogen/oxygen ternary system, and are only meant to demonstrate the relative frequency of Si, N and O atoms in the samples.

The consequences of the post-deposition diffusion of oxygen-containing species, and their incorporation into the samples are discussed further below.

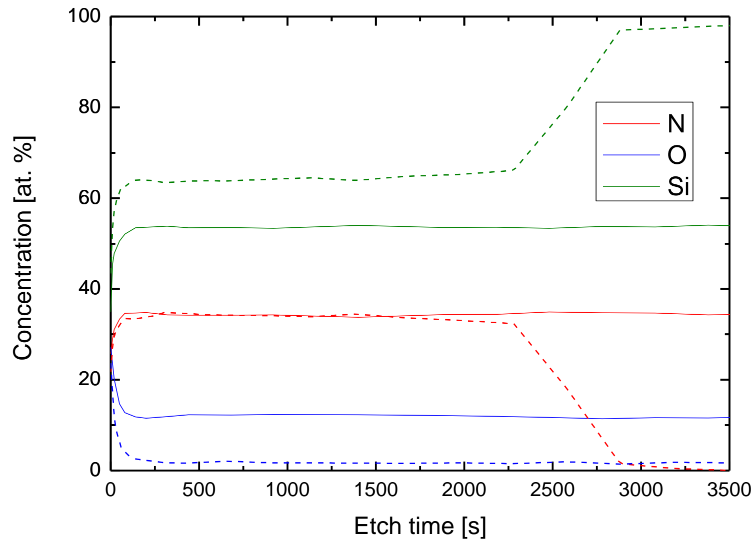

Figure 24: XPS depth profiles showing the apparent concertation of silicon, nitrogen and oxygen throughout the thickness of Type I (continuous line) and Type II (dotted line) ICP-CVD silicon nitride thin films. The sputter etch rate was approximately 0.04 nm/min, as in the case of the Type II sample the silicon substrate is reached.

Another deposition parameter that has a strong impact on the film properties is the ICP plasma power which increases the deposition rate when P_{ICP} is enhanced. This behaviour is expected, due to the following considerations: a higher plasma power level leads to a higher power density in the same reactor volume. This results in enhanced ionization and dissociation of the precursor gases, and hence, in a higher density of reactive species. The higher availability of these species induces higher reaction rates, both on the reactor walls [66, 73] and on the surface of the substrate. In numbers, the average r_{dep} increases from 10.2 to 16.5 nm/min when P_{ICP} is enhanced from 500 to 1000 W. The other significant effect is the decrease of the wet etch rate from an average value of 1045 nm/min to 410 nm/min with the increase of the substrate temperature T_s from 120°C to 350°C. This is predominantly attributed to the increased adatom mobility at higher temperatures enabling adatoms to reach energetically more favourable crystallographic sites during film growth, leading to a denser microstructure [115]. The films with denser microstructures tend to be more robust and resistant against the etchant. The biaxial film stress σ also shows a significant variation depending on the gas flow ratio $R_{N2/SiH4}$. In the case of *Type I* samples, measured immediately after the deposition, σ is found to be in the range of -200 to +100 MPa, demonstrating a low intrinsic stress level. On the contrary, samples of *Type II* SiN_x thin films are with -1350 and -700 MPa under high compressive stress. A more peculiar phenomenon was revealed by the periodic repetition of wafer bow measurements for the

determination of the biaxial film stress over a time period of three weeks after film synthetization. When looking at the temporal evolution of *σ*, the results clearly demonstrate a significant shift to higher compressive values, but only in the case of *Type I* samples. In contrast, for *Type II* samples, *σ* was found to stay constant in the investigated timeframe. This behaviour is illustrated in Figure 25. This gradual change in *σ* after deposition, as well as the significant amount of oxygen bonded with silicon atoms in *Type I* samples (see the FTIR and XPS results above) provide a solid explanation. As already described by other authors [114, 116], diffusion of water vapour (H_2O) and atmospheric oxygen into amorphous hydrogenated silicon nitride thin films can occur even at room temperature. This suggests that these oxygen-containing species penetrate and diffuse into the loosely bonded matrix of *Type I* a-SiN_x:H samples, while getting implemented into the a-SiN_x:H matrix either gaseous or loosely bonded or more strongly by reactions with chemically-active constituents saturating e.g. dangling bonds. Basically, the uptake of this additional material into the a-SiN_x:H matrix causes an increase of compressive stress in the sample, as known from e.g. the thermal oxidation of silicon [117].

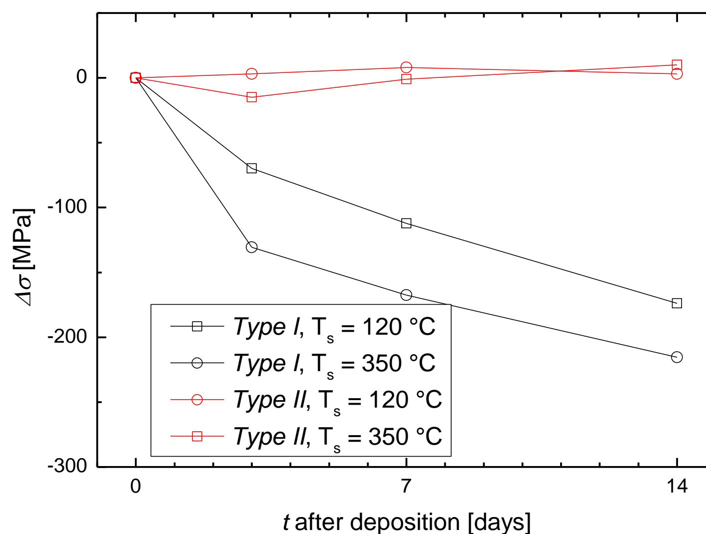

Figure 25: Temporal evolution of the biaxial film stress of Type I and Type II ICP-CVD silicon nitride thin films, deposited at T_s = 120°C and 350°C, respectively.

Although it is apparent from Table 5 that due to the large influence the parameter $R_{N2/SiH4}$ has on film properties further investigations are required which will be presented in section 4.3. Since – as presented by the previous results – the properties of *Type I* and *Type II* samples can differ substantially, it is of utmost importance to investigate the other deposition parameters systematically and in detail. For reasons of clarity, Table 6 and Table 7 summarize the impact of deposition parameters on film properties of *Type I* and *Type II* a-SiN_x:H thin film samples, respectively.

It was found that in the case of *Type I* samples the deposition rate r_{dep} increases almost proportionally with plasma power P_{ICP} from 12.5 to 22.9 nm/min. at 500 and 1000 W, respectively. This finding is fully in line with the explanation presented above, also signifying that under "*Type I* conditions", i.e. when $R_{N2/SiH4}$ = 2, the formation of a-SiN_x:H is only limited by the availability of reactive species. When increasing either the deposition temperature T_s or chamber pressure p_{dep} while keeping the other deposition parameters fixed a slight shift of the biaxial stress σ in the tensile direction results (i.e. from 31 MPa from T = 120°C to 350°C and 32 MPa from p_{dep} = 4 mTorr to 10 mTorr, respectively). Besides that, the stress drift $\Delta\sigma$ measured 7 days after deposition is significantly larger when the deposition temperature is increased ($\Delta\sigma$ = 101 and 158 MPa on average for films deposited at 120°C and 350°C, respectively). Higher deposition temperatures result in a strong reduction of the wet etch rate *WER,* also when specifically considering *Type I* samples (by a factor of about 2.5 from 120°C to 350°C). On the other hand, an increase of P_{ICP} from 500 W to 1000 W or p_{dep} from 4 mTorr to 10 mTorr both give rise to a similar increase in *WER* (by a factor of about 1.6 and 1.5, respectively). These latter effects can be both explained when considering that with higher P_{ICP} or p_{dep}, the deposition rate also increases, and as a result the adatoms may lack sufficient time to diffuse to energetically more favorable positions on the film surface. The consequence is that under these growth conditions the bond matrix of the deposited a-SiN_x:H thin films finally is less dense and more penetrable, by extension less robust against aggressive etch media, such as HF. The density of N-H bonds in *Type I* samples (which corresponds to the area under the N-H (Si-NH_2) peak) is inversely correlated to the deposition temperature (decreases by a factor of 1.54 from 120°C to 350°C), but slightly increases with increasing p_{dep} (by a factor of 1.07 from 4 to 10 mTorr) and increasing P_{ICP} (by a factor of 1.28 from 500 to 1000 W).

Type I		*d [nm]*	*r_{dep} [nm/min]*	*n*	*σ[MPa]*	*WER [nm/min]*
P_{ICP} [W]	500	188	12.5	2.03	+8	1135
	1000	344	22.9	1.96	-5	1868
p_{dep} [mTorr]	4	246	16.4	1.96	-14	1165
	10	284	18.9	2.03	+17	1766
T [°C]	120	273	18.2	2.02	-17	2032
	350	252	16.8	1.97	+15	826

Table 6: Impact of ICP-CVD deposition parameters on the properties of Type I silicon nitride thin films.

In the case of *Type II* samples, a sub-proportional increase of r_{dep} is observed when the plasma power P_{ICP} is increased from 500 W to 1000 W. This indicates that the reaction and hence, the deposition rate, is not only limited by the generation of reactive species, but to some extent also by the availability of precursor gases, in this case N_2. In contrast to *Type I* thin films, the refractive index *n* shows significant variation (between ca. 2.1 and 2.7) in *Type II* samples. This can be correlated to the

variation of the chemical composition (prominently the Si/N ratio) within the sample type, as given by the Lorentz-Lorenz equation [118], which relates the refractive index n to the (composition-dependent) polarizability of the material. Deposition parameters that have an influence are the substrate temperature (Δn = 0.14±0.03 from T_s = 120°C to T_s = 350°C) and the deposition pressure (Δn = 0.36 ± 0.03 from p_{dep} = 4 mTorr to p_{dep} = 10 mTorr). These results suggest major compositional differences between individual *Type II* a-SiN_x:H samples. In contrast to the behavior of n, the biaxial stress σ only shows slight variation between different *Type II* films, where both an increased P_{ICP} and higher T_s values lead to stronger compressive stress. It is important to note, that contrary to *Type I* samples, σ does not show any drift behavior in the case of *Type II* films, and stays constant over any investigated time-frame. Interestingly, the effect of T_s on the wet etch rate of *Type II* samples is very similar to that of *Type I* films, albeit at substantially lower absolute values of *WER*. When increasing the deposition temperature T_s from 120°C to 350°C, the average wet etch rate decreases from 11.0 to 2.5 nm/min (by a factor of 4.4 cf. 2.5 in the case of *Type I*). On the other hand, the increase of the parameter p_{dep} causes *WER* to decrease by a factor of about 3.1, in contrast to the observed increase in *Type I* samples. The negligible observed influence of the increase in P_{ICP} on *WER* indicates that the effect of P_{ICP} on the chemical composition and bonding configuration of *Type II* a-SiN_x:H samples is very minor. Experimental results also indicate that the formation of Si-H bonds in *Type II* a-SiN_x:H is affected by the deposition parameters p_{dep} and P_{ICP} (not shown). The larger p_{dep} and P_{ICP} are, the higher is the measured density of Si-H bonds in the FT-IR spectrum (by a factor of 1.24 between 4 and 10 mTorr and a factor of 1.27 between 500 and 1000 W, respectively). Nevertheless, with increasing p_{dep}, the peak of the Si-H asymmetric absorption band is shifted to lower wavenumbers (average peak positions: 2158 cm^{-1} and 2122 cm^{-1} at 4 and 10 mTorr, respectively). Since this parameter shows only a very slight correlation with the biaxial stress σ of the samples, it can be attributed to changes in chemical composition (cf. the part about the refractive index n). In more detail, this means that the "Si-H" compound absorption band (a convolution of Si_3-Si-H, Si_2-Si-H_2 and Si-Si-H_3 sub-bands) has a larger portion of bonds in a relatively Si-rich configuration. This observation again is coherent with the measured changes in n.

Type II		*d [nm]*	*R_{dep} [nm/min]*	*n*	*σ[MPa]*	*WER [nm/min]*
P_{ICP} [W]	500	95	6.3	2.43	-890	6.1
	1000	152	10.1	2.53	-1032	7.5
p_{dep} [mTorr]	4	125	8.3	2.25	-1010	10.2
	10	122	8.1	2.61	-912	3.3
T [°C]	120	122	8.1	2.36	-835	11.0
	350	123	8.2	2.50	-1087	2.5

Table 7: Impact of ICP-CVD deposition parameters on the properties of Type II silicon nitride thin films.

Based on the deposition temperatures being involved in this study, and on other works [119-121] it is reasonable to assume that the ICP-CVD silicon nitride samples have an amorphous microstructure. To verify this assumption, a sample deposited at $R_{N2/SiH4}$ = 1, T_s = 350°C, P_{ICP} = 750 W and p_{dep} =°7 mTorr was chosen as representative for XRD (X-ray diffraction) analysis as it was deposited at maximum substrate temperature. As illustrated in Figure 26, no characteristic peaks besides that of the substrate are detected excluding the presence of any crystallographic phase in the layer.

As an additional experiment, samples have been deposited using varying substrate temperatures between T_s =120°C and 350°C, while keeping all other parameters constant. The results show almost no impact on r_{dep} (17.6±0.4 nm/min), n (2.02±0.08), and σ (+19±37 MPa), in agreement with the previous results.

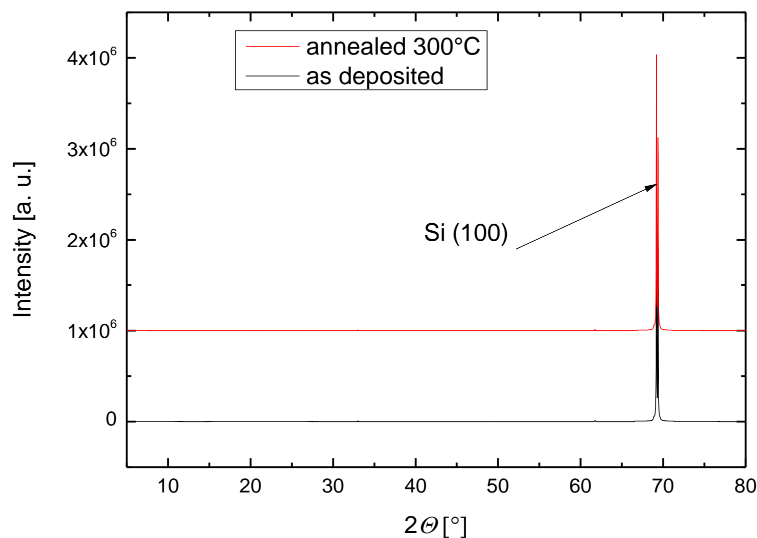

Figure 26: XRD diffractograms of a Type I ICP-CVD deposited silicon nitride sample, "as deposited" and after annealing for 1h at 300°C under atmospheric conditions. The Si(100) peak is associated to the substrate.

Summarizing the results, it can be stated that the above experiments revealed the precursor gas ratio $R_{N2/SiH4}$ to be the most influential parameter affecting the chemical composition and physical properties of ICP-CVD deposited silicon nitride thin films. The significance of this parameter is so dominating that in order to properly scrutinize the influence of other parameters, the samples were put into two distinct categories, based on the used $R_{N2/SiH4}$ value. Samples that have been deposited using $R_{N2/SiH4} \geq 1$ fall in the category *Type I*, while in the case of $R_{N2/SiH4} < 1$ we talk about *Type II* films.

Type I films are characterized by low ($n < 2$) refractive indices, a high *WER* in HF, and low σ, which is prone to significant drift over time by building up additional, compressive stress. In contrast, *Type II* samples have higher ($2.1 < n < 2.7$) refractive indices, are much more resistant against the etchant HF, and have a strong compressive, but stable biaxial stress. These film parameters listed are rather important differences induced only by changing $R_{N2/SiH4}$. But, for device applications, it is most desirable to deposit SiN_x thin films that feature properties like a low film stress in combination with a large temporal stability, so representing a combination of pure *Type I* and *Type II* features. For reaching this goal, a subtler variation of $R_{N2/SiH4}$ than in the screening experiments would lead to a less extreme variation of the physical properties of ICP-CVD deposited a-SiN_x:H thin films. This will be the topic of the next section.

4.3. Influence of the precursor gas flow rate ratio

In order to properly assess the influence of the precursor gas flow ratio $R_{N2/SiH4}$ on the resulting properties of ICP-CVD deposited a-SiN_x:H thin films, a second series of experiments has been performed [105]. In this case the chamber pressure during deposition p_{dep}, the ICP plasma power P_{ICP}, and the substrate temperature T_s were held constant at values of 7 mTorr, 750 W and 350°C, respectively, while $R_{N2/SiH4}$ was gradually changed from 0.5 to 8. A detailed list of the process parameters is provided in Table 8. Due to the limitations set by the mass flow controllers of the deposition system, the maximum flow rate of the gas N_2 was limited to 48 sccm, thus in order to achieve $R_{N2/SiH4} > 4$, the flow rate of silane had to be reduced, from the standard value of 12 sccm. But, as demonstrated in additional pre-experiments, most important is the $R_{N2/SiH4}$ value, not the absolute values of the individual gas flows. The reason for this is that the deposition reaction only consumes a small portion of the gas species delivered into the reaction chamber. This leads to thin film properties being almost independent of the actual flow rates over a large range, and will be affected only by the ratio of partial pressures of the individual precursor gases, being in turn defined by $R_{N2/SiH4}$. Any change in the partial pressure of the inert gas Argon between approximately 2 and 5 mTorr (by changing the Ar flow between 12 and 48 sccm) – as some additional test depositions showed – has no significant influence with respect to the a-SiN_x:H film properties.

In accordance with the results in Section 4.2, a steep increase of r_{dep} was observed between $R_{N2/SiH4} = 0.5$ and 1, from approximately 9 to 18 nm/min (see Figure 27). This is accompanied by a rapid decrease of the refractive index n, from approximately 2.7 at $R_{N2/SiH4} = 0.5$ to about 2.0 at $R_{N2/SiH4} = 1$, as illustrated in Figure 28. These findings again indicate that an increased deposition rate is accompanied with a significant compositional change in the a-SiN_x:H films.

$R_{N2/SiH4}$	r_{SiH4} [sccm]	r_{N2} [sccm]	P_{ICP} [W]	p_{dep} [mTorr]
0.5	12	6	750	7
0.66	12	8	750	7
0.75	12	9	750	7
0.83	12	10	750	7
1	12	12	750	7
2	12	24	750	7
4	12	48	750	7
8	6	48	750	7

Table 8: Overview of the experimental series for the assessment of ICP-CVD deposited a-SiN$_x$:H thin film properties as a function of the precursor gas ratio $R_{N2/SiH4}$. r_{SiH4} and r_{N2} are the flow rates of the nitrogen and silane gas, respectively.

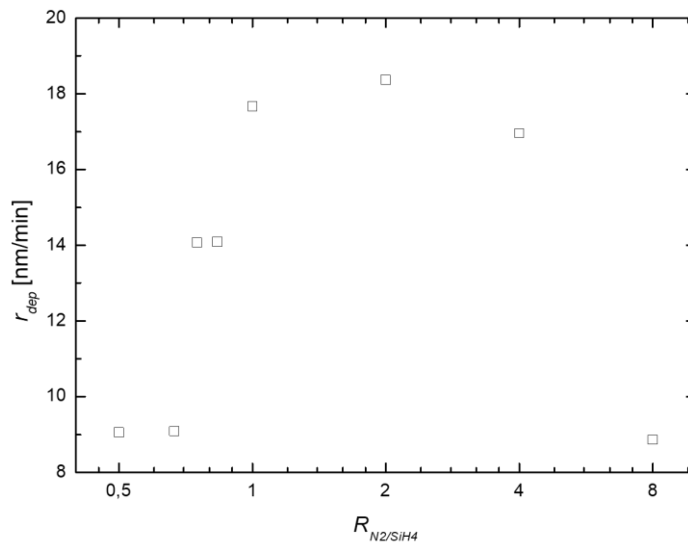

Figure 27: The deposition rate of ICP-CVD silicon nitride thin films as a function of $R_{N2/SiH4}$.

A gradual, but significant change of the biaxial film stress σ is measured over the same range, as shown in Figure 29. At $R_{N2/SiH4}$ = 0.5, σ is in the range of -1000 MPa, which corresponds to a strong compressive stress, while at $R_{N2/SiH4}$ = 1, σ is about +200 MPa (i.e. moderately tensile). The zero-transition can be found at around $R_{N2/SiH4}$ = 0.75. In this range, the stress σ has been found to be stable over time, similar to *Type II* samples. The major difference in this case is, that the variation of the value of $R_{N2/SiH4}$ between 0.5 and 1 leads to far larger discrepancies between the resulting properties of a-SiN$_x$:H samples, than it was found between the typical *Type II* samples of the screening experiments in section 4.2.

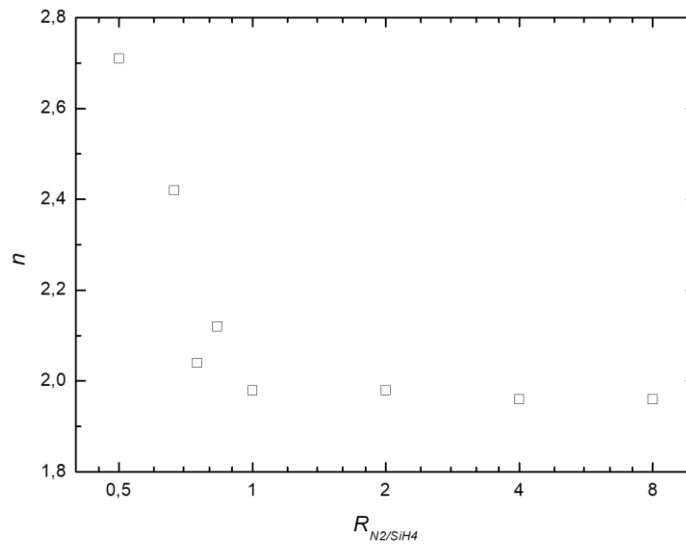

Figure 28: The index of refraction of ICP-CVD silicon nitride thin films as a function of $R_{N2/SiH4}$.

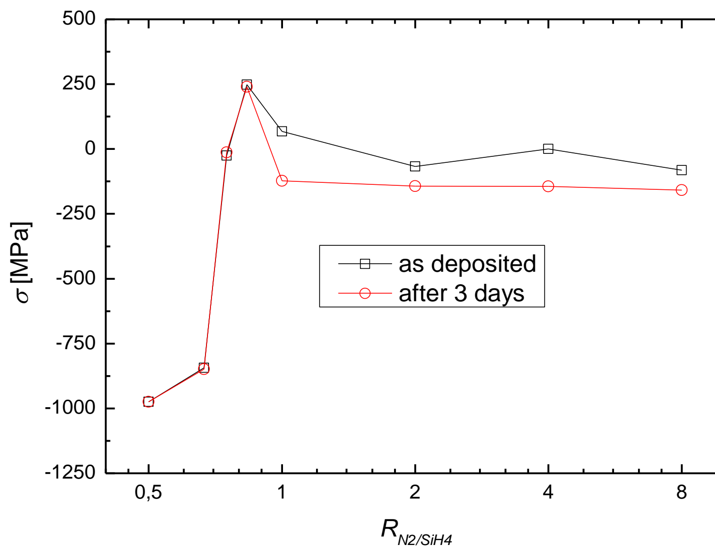

Figure 29: The biaxial film stress of ICP-CVD silicon nitride thin films as a function of $R_{N2/SiH4}$ measured directly and 3 days after the deposition.

In contrast to these results, the a-SiN_x:H samples deposited in the range of $1 \leq R_{N2/SiH4} \leq 8$, show pure *Type I*-like behaviour. Basically, the biaxial film stress σ is low (i.e. in the range of 0 ± 100 MPa) directly after synthetization, but drifts (see Figure 29), as described in section 4.2. The variation in refractive index n (1.96 to 1.99) is, however, relatively low. This indicates that adding surplus N_2 above a critical $R_{N2/SiH4}$ value to the reactive gas mixture does not lead to a higher incorporation of nitrogen into the deposit, due to a saturation effect. On the other hand, at higher $R_{N2/SiH4}$ values a significant

decrease of the deposition rate is observable which is attributed to the oversaturation of the precursor gas mixture with N_2.

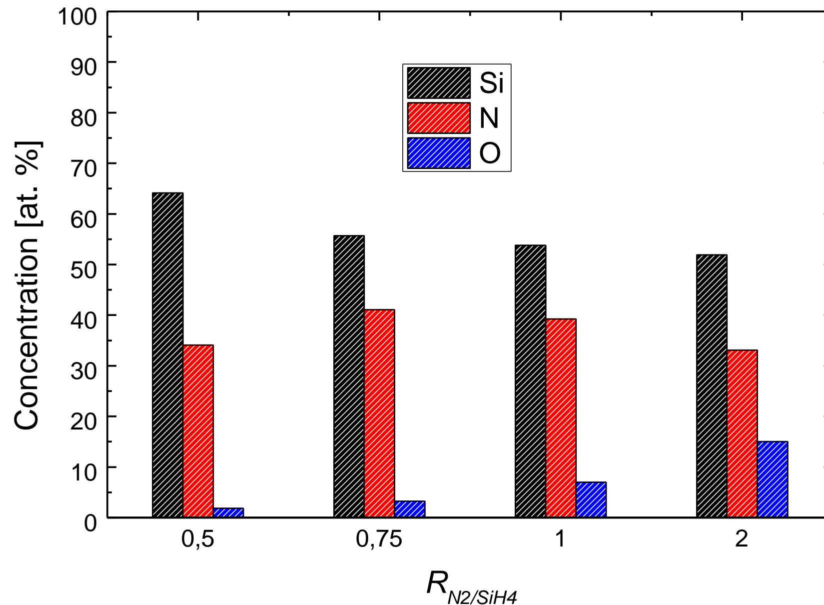

Figure 30: Concentrations of Si, N and O in ICP-CVD silicon nitride thin films measured with XPS as a function of $R_{N2/SiH4}$ values.

The elemental composition of the samples besides hydrogen and argon have been once again measured with XPS technique. This time – in order to avoid measuring the composition of the already highly oxidized surface, which can greatly vary when penetrating deeper into the sample – the measurement was done after *in situ* sputtering cleaning removing about 5 nm from the surface of the sample. The obtained results are presented in Figure 30. It is important to note that while the composition of the samples remains silicon-rich over the whole investigated $R_{N2/SiH4}$ range compared to stoichiometric Si_3N_4 and the apparent silicon concentration steadily decreases from 64 at. % at $R_{N2/SiH4} = 0.5$ to 52 at. % at $R_{N2/SiH4} = 2$, the nitrogen concentration features a maximum of about 41 at. % at $R_{N2/SiH4} = 0.75$. Although exhibiting a higher Si concentration than in Si_3N_4, the latter $R_{N2/SiH4}$ value leads to a composition being closest to the stoichiometric ratio. The measured concentration of oxygen shows a steady increase from < 2 at. % at $R_{N2/SiH4} = 0.5$ up to 15 at. % at $R_{N2/SiH4} = 2$ that is practically silicon oxynitride. The change of the N/Si atomic ratio also causes a chemical shift of the Si-related XPS peak, as illustrated in Figure 31, since with increasing N-content Si atoms in the a-SiN_x:H matrix will have statistically more neighbouring N atoms.

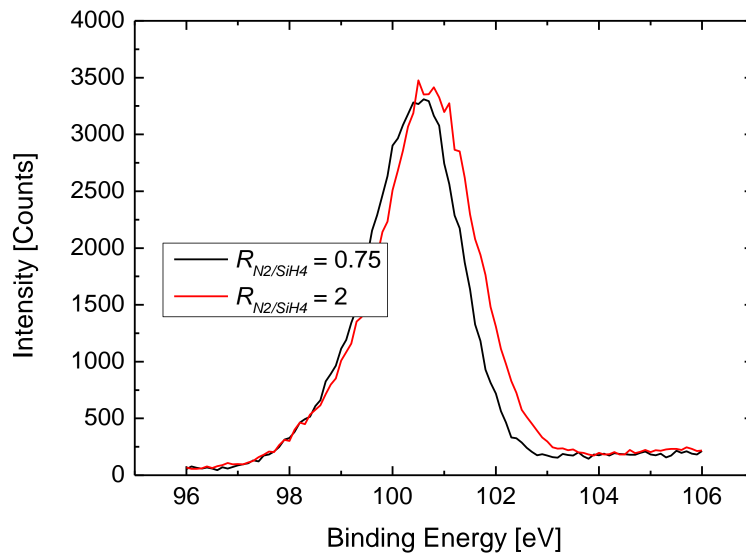

Figure 31: Chemical shift in binding energy of the XPS Si-related peak of ICP-CVD silicon nitride thin films as a result of a change in $R_{N2/SiH4}$.

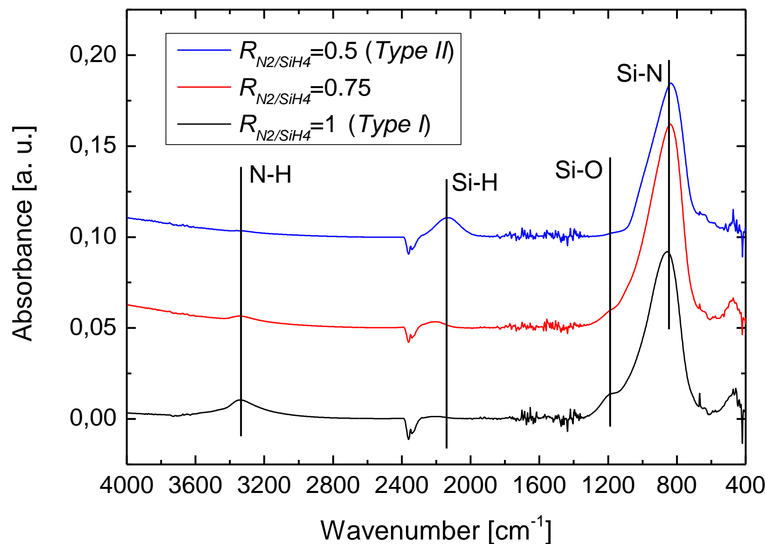

Figure 32: FT-IR spectra of ICP-CVD silicon nitride thin films deposited at selected $R_{N2/SiH4}$ values.

These compositional differences are readily reflected in the observable absorption band characteristics of the samples' FT-IR spectra. The accumulation of oxygen in the a-SiN_x:H samples with increasing $R_{N2/SiH4}$ is displayed by evaluating the Si-O asymmetrical stretching absorption band having its peak at 1108 cm^{-1}. A significant increase in the relative Si-O bond density with increasing $R_{N2/SiH4}$ was confirmed (see Table 9), by a factor of >25 between $R_{N2/SiH4}$ = 0.5 and $R_{N2/SiH4}$ = 1, thus being in good qualitative and quantitative accordance with the results gained from the XPS study. In accordance with the results of section 4.2, the hydrogen in the a-SiN_x:H samples is predominantly present in Si-H bonds when $R_{N2/SiH4}$ is low (< 0.75, *Type II*), or in N-H bonds when $R_{N2/SiH4}$ is high (≥ 0.83). The unique property

is that at about $R_{N2/SiH4}$ = 0.75 both the Si-H and the N-H absorption bands coexist in the sample (see Figure 32).

The relative bond densities as a function of $R_{N2/SiH4}$ are presented in Table 9. Consistently with the results of the XPS study, the Si-N bond density has a maximum at $R_{N2/SiH4}$ = 0.75. In addition, the peak of the Si-N asymmetric absorption band is shifted towards higher frequencies with increasing $R_{N2/SiH4}$, due to the changes in N/Si ratio, as it is displayed in Table 9.

These results indicate that with a careful selection of $R_{N2/SiH4}$, a-SiN_x:H can be deposited that are characterized by a σ that is both low and stable over time as typically requested for MEMS device applications. This is a significant improvement compared to the results gained from the screening experiments.

	Relative bond density [a. u.]			
$R_{N2/SiH4}$	N-H	Si-H	Si-O	Si-N (peak position)
0.5	0.064	1.568	0.008	15.78 (835 cm^{-1})
0.75	0.360	0.132	0.024	24.79 (839 cm^{-1})
1	2.088	0.094	0.211	21.06 (856 cm^{-1})

Table 9: Relative bond densities (calculated from the areas under the corresponding peaks in the FTIR spectra) of some selected absoprtion bands of ICP-CVD silicon nitride thin films extracted from their FT-IR spectra as a function of $R_{N2/SiH4}$.

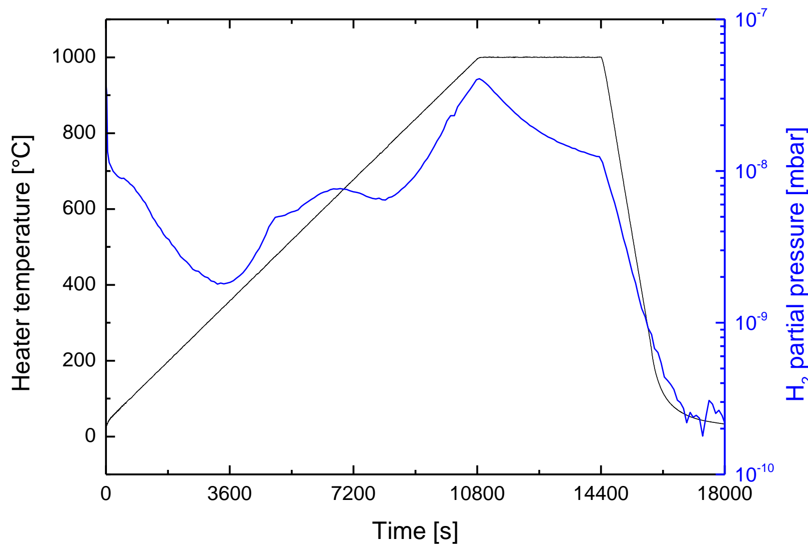

Figure 33: Heater temperature and hydrogen partial pressure as a function of time in the high temperature effusion measurement setup. The sample used was a Type I a-SiN_x:H film with d = 300 nm.

Using the method outlined in Section 3.8, high temperature effusion measurements were performed on selected *Type I* samples. A typical measurement curve showcasing the effusion of

molecular hydrogen from the thin film is presented in Figure 33. The initially high, but rapidly decreasing partial pressure of hydrogen is the result of desorption from the chamber walls at relatively low temperatures. Unsurprisingly, once the temperature increases above the deposition temperature of the samples (350°C in this case) a steep increase in the detected hydrogen partial pressure is observed. This is attributed to the effusion of loosely bonded hydrogen from the easily permeable amorphous matrix. In the temperature range of 600 to 700°C, this process is vanished, as the loosely bound hydrogen is depleted. At temperatures exceeding 800°C, the partial pressure of hydrogen shows a second region of rapid increase. This is likely an effect of the microstructural rearrangement of the amorphous matrix, leading to the expulsive effusion of hydrogen previously stored in form of N-H and Si-H covalent bonds.

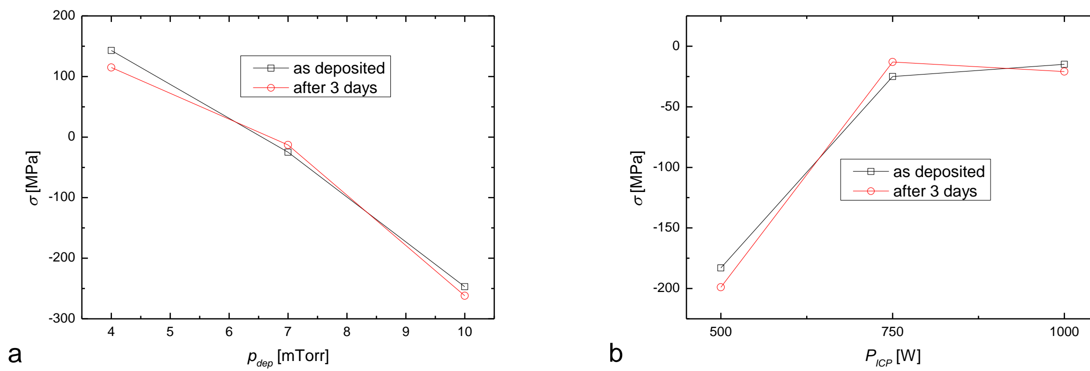

Figure 34: Process parameters enabling to tailor the biaxial film stress of ICP-CVD deposited silicon nitride thin films while preserving its stability. a): The impact of p_{dep}, with T_{dep} = 350°C, $R_{N2/SiH4}$ = 0.75 and P_{ICP} = 750 W b): The impact of P_{ICP}, with T_{dep} =350°C, $R_{N2/SiH4}$ = 0.75 and p_{dep} = 7 mTorr.

In order to assess the potential of the stable, low-stress a-SiN$_x$:H films, a couple of additional deposition runs were performed in which the values of the secondary deposition parameters (in this case p_{dep} and P_{ICP}) have been varied, while maintaining $R_{N2/SiH4}$ at the value of 0.75. The outcome of these experiments clearly demonstrates that as long as $R_{N2/SiH4}$ is kept around 0.75, P_{ICP} and p_{dep} can be varied without sacrificing the long-term stability of the biaxial film stress σ. Moreover, p_{dep} and P_{ICP} can be utilized for tailoring the desired value of σ (see Figure 34). An increase of P_{ICP} from 500 W to 1000 W leads to a shift of σ from approximately -200 MPa (moderately compressive) to about zero. Conversely, when p_{dep} is increased from 4 mTorr to 10 mTorr, σ changes from +150 MPa (tensile) to -250 MPa (compressive). This shows that the reactive gas ratio $R_{N2/SiH4}$ can be effectively used in combination with p_{dep} and P_{ICP} in order to tune the physical properties of ICP-CVD deposited a-SiN$_x$:H thin films. However, there is still another deposition parameter in the ICP deposition process that has large potential in controlling the deposition and resulting properties of a-SiN$_x$:H thin films. This the auxiliary capacitively coupled plasma power P_{RF}, the impact of which will be investigated in detail in the next section.

4.4. Influence of CCP power

As mentioned in Chapter 2.2.3, ICP-CVD deposition systems, such as the *Oxford Instruments Plasmalab 100* used in our experiments, are typically equipped with an ancillary capacitively coupled plasma source. This component is by default only utilized during the initial ignition of the inductively coupled plasma discharge, when starting the deposition process. The capacitive plasma source, however, can also be used as an additional source of energy during the deposition process. Doing so, an independent parameter is made available enabling to control separately the density of the plasma and the bias voltage, respectively. This additional degree of freedom allows a more flexible control over the physical properties of ICP-CVD deposited a-SiN_x:H thin films than other state-of-the-art approaches like LPCVD or conventional capacitively coupled PECVD processes.

In order to study in detail the influence of the capacitively coupled plasma power P_{RF} on film properties, additional deposition experiments were carried out [106]. The substrate materials, as well as the methods of cleaning and pre-treatment were kept identical to those applied and described in the previous sections. For reasons of comparability the deposition conditions were also kept constant to a maximum degree between the individual deposition series. The nominal substrate temperature was kept at 350°C for generally higher quality results, and p_{dep} at the mid-point of 7 mTorr. Since P_{ICP} was found to have only minor influences on the layer properties (beside on the deposition rate) in the previously investigated range of 500 to 1000 W, this parameter was set to 750 W. In the main deposition series, $R_{N2/SiH4}$ was set to the value of 1, while P_{RF} was changed between 0 W and 150 W. Additionally deposition runs with P_{RF} = 150 W and $R_{N2/SiH4}$ = 0.5, 0.75, and 2, were performed, in order to study the impact of an additional capacitively coupled plasma source on the resulting properties of *Type I*, *Type II* and intermediate type a-SiN_x:H thin films. The deposition parameters of these experiments are listed in Table 10.

P_{RF} [W]	P_{ICP} [W]	$R_{N2/SiH4}$	p_{dep} [mTorr]	T_s [°C]
0	750	1	7	350
10	750	1	7	350
20	750	1	7	350
350	750	1	7	350
50	750	1	7	350
100	750	1	7	350
150	750	1	7	350
150	750	0.5	7	350
150	750	0.75	7	350
150	750	2	7	350

Table 10: Overview on the deposition experiments for determining the influence of CCP plasma on ICP-CVD a-SiN_x:H thin film properties.

The effect of P_{RF} on the deposition rate r_{dep} of ICP-CVD silicon nitride is shown in Figure 35. It is immediately apparent that this parameter has a significant influence on r_{dep}. Moreover, the investigated range of P_{RF} from 0 to 150 W can be grouped into two distinct regions. The first one ranges from P_{RF} = 0 W to about P_{RF} = 35 W, while the second covers the range above that value. In the first region r_{dep} increases with increasing P_{RF}, from approximately 19 nm/min to 23 nm/min. On the other hand, between P_{RF} = 35 and 150 W a steady decrease of r_{dep} is observed reaching a value of r_{dep} = 14 nm/min at P_{RF} = 150 W. This contradictory behaviour in the deposition characteristics suggests that the addition of an auxiliary capacitively coupled plasma discharge to the ICP-CVD process facilitates at least two, counteracting effects. Based on the available data and theoretical considerations [43, 59] the following hypothesis is proposed: it is clear that activating the ancillary capacitively coupled RF plasma source provides additional energy to the deposition process, thus increasing r_{dep}. This additional energy can lead to increased excitation, dissociation and ionization of the precursor gases in the plasma. The result of this is twofold, as it appears both in the *quantity* and *quality* of the generated reactive species: compared to a purely ICP discharge, *more* reactive particles and *other types* of reactive particles are produced. This can lead to a significant alteration of the plasma chemistry. Moreover, due to the inherent characteristics of the reactor, the aforementioned reactive species resulting from the CCP discharge appear generally near the substrate surface, further strengthening their impact, resulting in enhanced deposition rates.

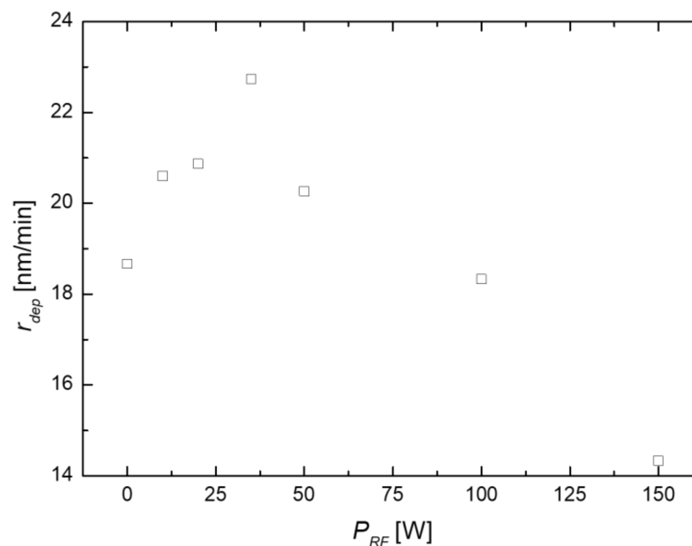

Figure 35: The deposition rate of ICP-CVD silicon nitride thin films as a function of P_{RF}.

The second effect is associated with the vertical electrical field (“bias”) generated by the capacitively coupled RF plasma, being naturally stronger with increasing P_{RF} (see Figure 36). This field accelerates the positive ions (*e.g*. Ar^+) in the plasma discharge towards the substrate surface, leading to an enhanced ion bombardment and an effective reduction of the deposition rate at higher P_{RF} values. Given the boundary conditions and fixed parameters of this experimental series, the value where the ion-bombardment related effect starts to dominate the increased generation of reactive particles is at about P_{RF} = 35 W.

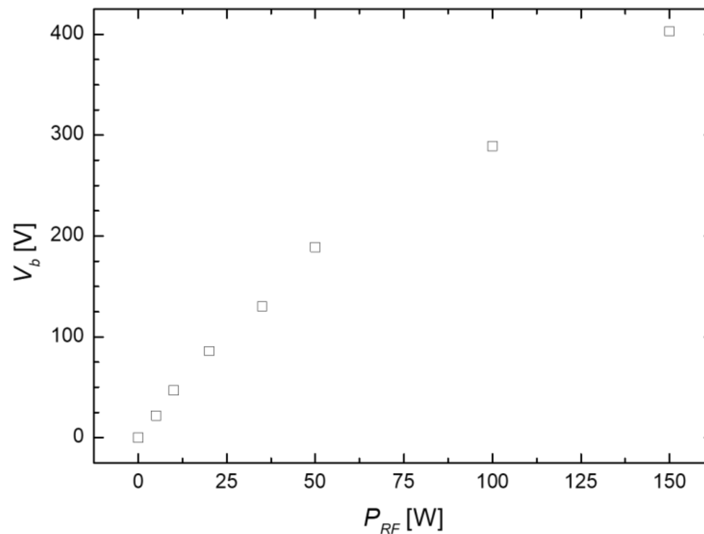

Figure 36: The resulting bias voltage in the ICP-CVD silicon nitride process as a function of P_{RF}.

In contrast to the observed behaviour of the deposition rate, the refractive index *n* tends to steadily increase with increasing values of P_{RF} over the whole investigated range. At P_{RF} = 0 W which is basically a standard *Type* I film, *n* has a value of 1.95, slowly increasing into the range of $2.1 < n < 2.2$ for P_{RF} > 50 W, as shown in Figure 37. Despite *n* being in some cases lower than the value associated with stoichiometric Si_3N_4, these films are still silicon-rich as demonstrated by XPS measurements presented in sections 4.2 and 4.3. This is due to the considerable amount of hydrogen that is stored in the ICP-CVD thin films either as H_2 molecules or in form of Si-H or N-H covalent bonds (thus the prevalent notation a-SiN_x:H, i.e. hydrogenated silicon nitride).

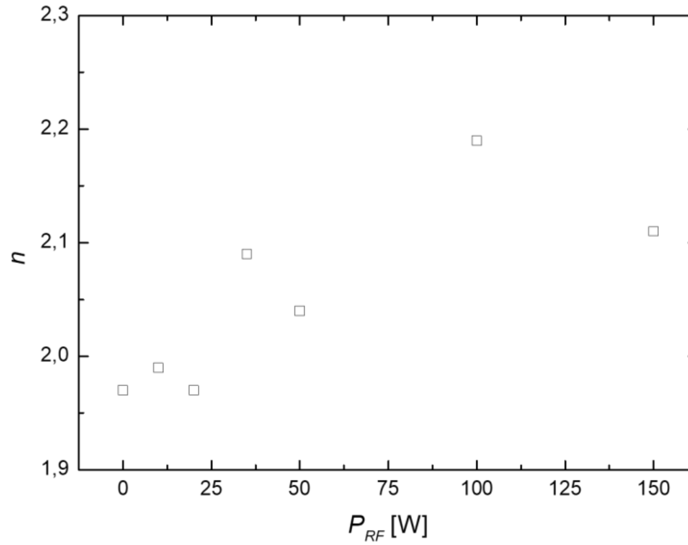

Figure 37: The index of refraction of ICP-CVD silicon nitride thin films as a function of P_{RF}.

Typically, ICP-CVD deposited a-SiN_x:H thin films are amorphous. Because of a large number of structural defects, the amorphous hydrogenated silicon nitride (a-SiN_x:H) matrix has a lower density, and as a consequence, a lower index of refraction compared to crystalline silicon nitride. In combination with the inclusion of hydrogen, the decrease in density and *n* can be significant in contrast to a binary Si-N system. As already pointed out in the previous sections, the change in the weight density ρ_m of the samples can be indirectly linked to the change in the refractive index *n* via the Lorentz-Lorenz (Clausius-Mossotti) equation:

$$\frac{n^2 - 1}{n^2 + 2} = \frac{4\pi}{3} N\alpha \tag{4.1}$$

where *N* is the spatial density of molecules and α is the polarizability [122]. The necessary assumptions are that the sample material is homogeneous, isotropic, with a polarizability α that is constant across the whole sample range. While the first two assumptions can be generally accepted to be true for the samples in this study, the polarizability is certainly affected when the chemical composition of the material changes. When neglecting this a potential error is introduced that needs to be kept in mind when analysing the results. In order to perform the calculations, the samples were weighted (determining the weight of the thin films by measuring the wafers prior to and after the deposition) using an analytical scale by *Sartorius AG*, with a resolution of 0.1 mg. The weight density ρ_m was found to be increasing with increasing values P_{RF}. At P_{RF} = 0 W ρ_m is 2.67 ± 0.01 g/cm^3, at P_{RF} = 35 W ρ_m = 2.85 ± 0.02 g/cm^3, while at P_{RF} = 150 W ρ_m is 2.93 ± 0.03 g/cm^3. In comparison, the theoretical

weight density of stoichiometric Si_3N_4 is around 3.2 g/cm^3 [123], with real-life values depending on the deposition or synthesis method [28]. Given this value, the expected relative change of the refractive index n can be calculated. The resulting values are Δn = 0.09 ± 0.03 from P_{RF} = 0 W to 35 W and 0.15 ± 0.04 for P_{RF} = 0 to 150 W, respectively. This is in reasonable agreement with the measured values of Δn = 0.13 from P_{RF} = 0 W to 35 W and Δn = 0.15 for P_{RF} = 0 to 150 W, especially given the uncertainty of the refractive index measurement with the SR method and the error introduced by a local variation of α. Based on these results it can be stated that the increase of n is the consequence of a change in the chemical composition of the sample deposits to a more Si-rich composition, and/or a decrease of the void volume in the a-SiN_x:H film.

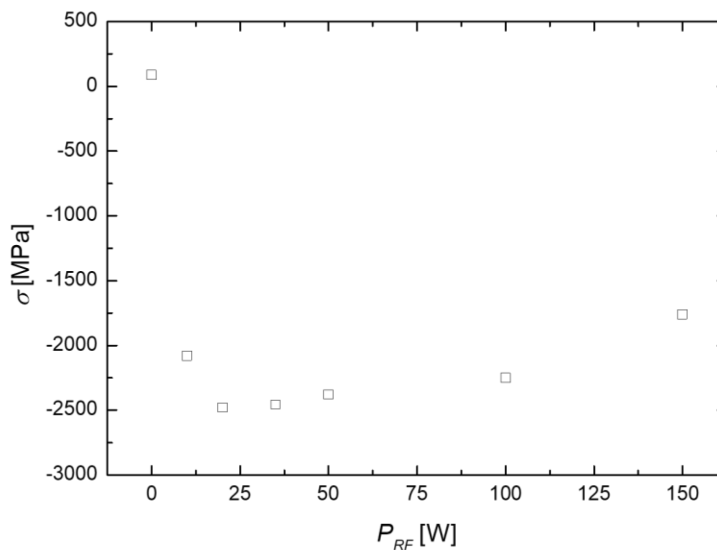

Figure 38: The biaxial film stress of ICP-CVD silicon nitride thin films as a function of P_{RF}.

It was also found that activating the ancillary CCP RF plasma source has a very significant impact on the resulting biaxial stress σ of the deposited a-SiN_x:H thin films, as it is presented in Figure 38. While – as it is a typical *Type I* film – σ is very low at P_{RF} = 0 W, activating the CCP source with a low value of 10 W leads to immense compressive stress, with σ < -2 GPa. It is worth mentioning in this context that although CCP-related discharges with P_{RF} < 10 W could be successfully ignited, down to a minimum of P_{RF} = 5 W, the capacitive discharges at such a low power suffer from instability, leading to inconsistent results. Generally, it can be said, that for 0 W < P_{RF} <10 W, the deposits still exhibit strong compressive stress. When increasing P_{RF} further, the compressive stress reaches its maximum between P_{RF} = 20 W and P_{RF} = 35 W, at a value of approximately σ = -2.5 GPa. At higher values of P_{RF}, a gradual reduction of the compressive stress can be observed, to the value of σ = -1.75 GPa at P_{RF} = 150 W.

Furthermore, the addition of $P_{RF} > 0$ W successfully eliminates the post-deposition drift of σ in compressive direction, that was prevalent in the case of films deposited with similar $R_{N2/SiH4}$ values (basically *Type I* films), without utilizing the CCP RF plasma source. But, the magnitude and the almost abrupt onset of highly compressive stress with the activation of the CCP RF plasma source makes it extremely unlikely that this high stress originates from the mismatch of the *TCE* (temperature coefficient of expansion) between the substrate and the deposit. In turn, it is attributed to substantial changes in the chemical composition or morphology of the a-SiN_x:H thin films. The modest decrease in the absolute value of σ above P_{RF} = 35 W is due to a change in chemical composition induced by the enhanced ion bombardment during deposition.

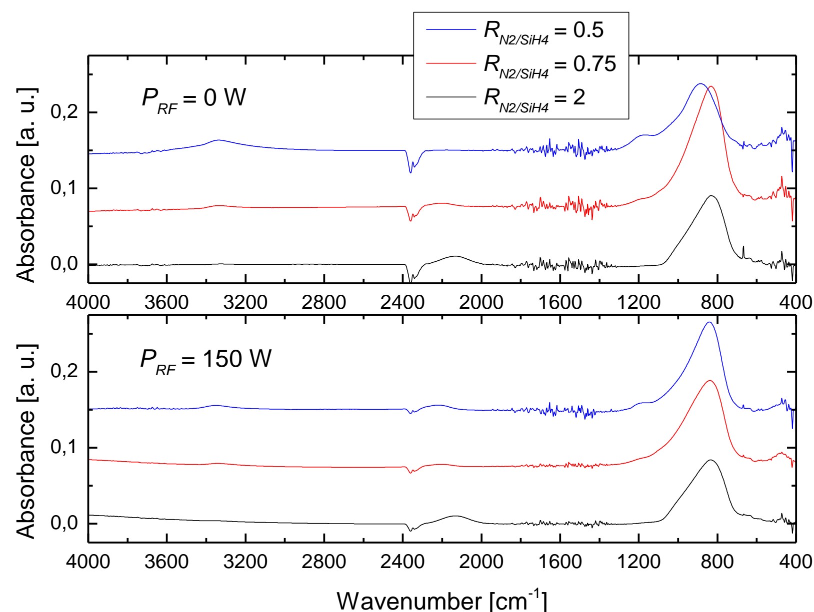

Figure 39: Impact of the auxiliary CCP plasma source on the FT-IR spectra of ICP-CVD silicon nitride thin films deposited using different $R_{N2/SiH4}$ values.

In order to investigate the impact of the ancillary CCP RF plasma discharge on the chemical composition and the morphology of the a-SiN_x:H thin film deposits, samples deposited under an array of different conditions have been analysed using FT-IR. In Figure 39, a comparison of FT-IR spectra of some selected samples synthesized using different $R_{N2/SiH4}$ values, deposited with or without the utilization of the auxiliary CCP RF source is presented. In accordance with the results shown in the previous section, the relative intensity of the main Si-N asymmetric stretching absorption band displays a maximum at $R_{N2/SiH4}$ =0.75, whether or not the deposition was assisted by the CCP RF discharge. The position of the peak of said absorption band is in both cases also shifted towards higher wavenumbers with increasing $R_{N2/SiH4}$. The magnitude of this shift is, however, significantly smaller in the case of CCP-

assisted deposition. (The peak is shifted from 831 to 883 cm^{-1} at P_{RF} = 0 W and from 833 to 854 cm^{-1} at P_{RF} = 150 W, respectively.) The issue of this peak shift was discussed in detail in section 4.2, with the conclusion being that the N/Si ratio x of the a-SiN_x:H thin film has statistically an influence on the number of coexisting Si-N local bonding environments in the a-SiN_x:H matrix, leading to an apparent peak shift of the convoluted Si-N absorption band [124]. A higher N/Si ratio leads to a higher peak wavenumber. The decreased sensitivity of the peak shift when increasing $R_{N2/SiH4}$ in the case of CCP RF-assisted ICP-CVD deposition of a-SiN_x:H leads to the conclusion that the impact of $R_{N2/SiH4}$ on the chemical composition (mainly N/Si ratio) is less pronounced when the CCP RF excitation is activated.

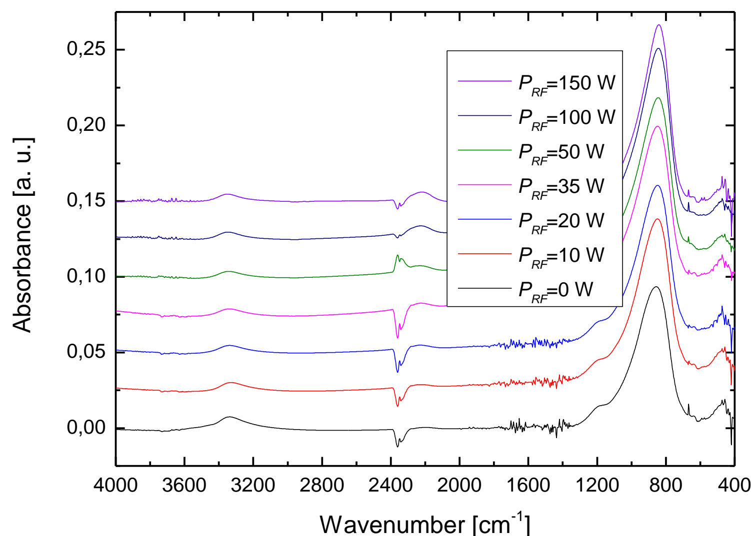

Figure 40: Overview of the FT-IR spectra of ICP-CVD silicon nitride thin films syntesized at different P_{RF} values.

Other features of the FT-IR spectra are observable in samples deposited both with and without additional CCP RF excitation. For example, the N-H bond density, represented by the intensity of the N-H asymmetric absorption band exhibits a significant increase with increasing $R_{N2/SiH4}$ in both cases, although the absolute values in the case where P_{RF} = 150 W are considerably lower. This suggests at least a partial inhibition of the formation of N-H bonds during CCP-RF assisted growth. As the high density of N-H bonds was found to correlate with the drifting behaviour of the biaxial stress σ, this can be seen as an explanation for the stress stability of a-SiN_x:H thin films deposited with P_{RF} > 0 W, even at higher $R_{N2/SiH4}$ values. The intensity of the Si-H absorption band was found to decrease with the increase of $R_{N2/SiH4}$ independent of the activation of the auxiliary CCP RF source. In contrast to the N-H bonds, the formation of this bond type is presumably assisted by the presence of the capacitive discharge, given by the increasing intensities. Additionally, with increasing $R_{N2/SiH4}$, a shift of the band

peak is observed, where the magnitude is roughly the same whether or not the auxiliary discharge was active (i.e. from 2135 to 2200 cm^{-1} at P_{RF} = 0 W and from 2121 to 2179 cm^{-1} at P_{RF} = 150 W, respectively). Basically, this peak shift is an evidence of decreasing Si-concertation with increasing $R_{N2/SiH4}$ value.

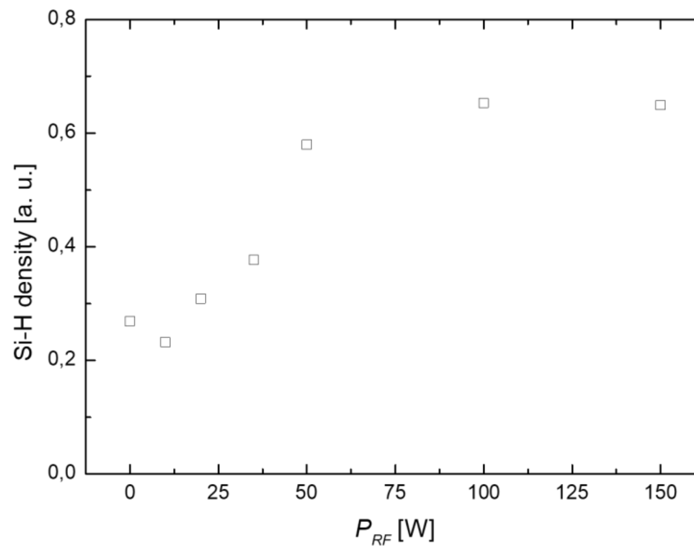

Figure 41: Bond density of the Si-H asymmetric stretching band extracted from the FT-IR spectra of ICP-CVD silicon nitride thin films as a function of P_{RF} in arbitrary units.

Given these results, the effect of P_{RF} on the chemical bonding configuration of the a-SiN_x:H samples was investigated in more detail, while $R_{N2/SiH4}$ was kept constant at the value of 1 and P_{RF} was gradually changed between 0 W and 150 W (see Figure 40). While being in accordance with the previous findings, the results also give some additional insights into the formation process of the a-SiN_x:H thin film during a CCP RF assisted ICP-CVD deposition. The intensity of the Si-H asymmetric absorption band (shown in Figure 41), was found to be steadily increasing with increasing P_{RF} through the whole range. The peak wavenumber has shown only slight variations, as it stays in the range of 2230-2240 cm^{-1}, except for P_{RF} = 0 W. In comparison, the relative intensity of the Si-N compound asymmetric absorption band has also shown a slight trend to increase from P_{RF} = 0 W to P_{RF} = 150 W. In addition, the peak is shifted to lower wavenumbers with increasing P_{RF}, suggesting an increase in the relative Si concentration of the SiN_x deposit (see Figure 42). The N-H absorption band, however, shows a different behaviour compared to those two described above. The N-H bond density decreases abruptly from P_{RF} = 0 W to P_{RF} = 10 W, and decreases further, albeit at a slower rate up to P_{RF} = 50 W. In contrast, from P_{RF} =50 W to P_{RF} = 150 W the N-H bond density shows a slight increase, as it is

displayed in Figure 43. No tendency of shift in the peak position was observed. It is important to point out how some of these changes correlate with other important, film-related parameters such as the deposition rate or the biaxial stress σ.

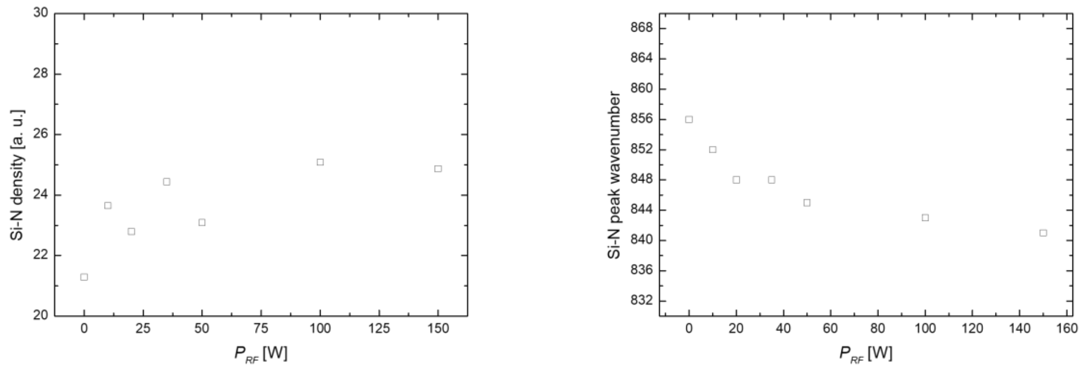

Figure 42: Bond density in arbitrary units (a) and peak shift (b) of the main Si-N asymmetric stretch absorption band extracted from the FT-IR spectra of ICP-CVD silicon nitride thin films as a function of P_{RF}.

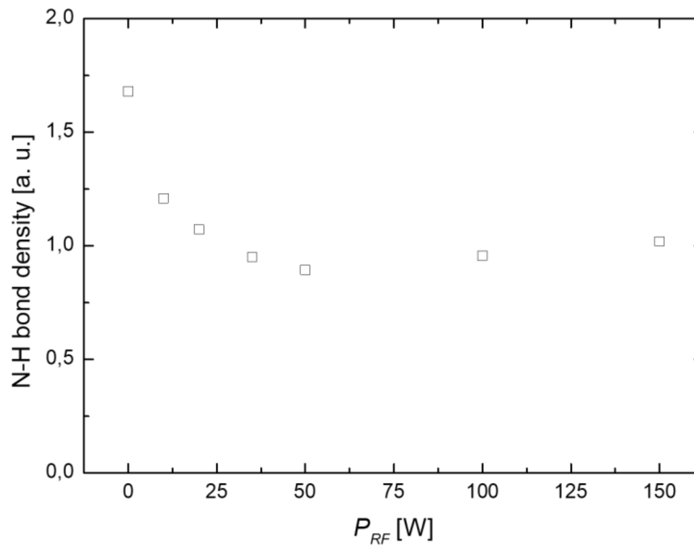

Figure 43: Bond density of the Si-N-H_2 asymmetric absorption band extracted from the FT-IR spectra of ICP-CVD silicon nitride thin films as a function of P_{RF} in arbitrary units.

Based on the presented results, a basic explanation of the dependence of the chemical composition, r_{dep}, and σ as a function of P_{RF} can be proposed. At P_{RF} = 0 W (at least at $R_{N2/SiH4}$ = 1) a standard *Type I* ICP-CVD a-SiN_x:H sample with its corresponding properties is present. A great excess

of hydrogen atoms is incorporated in the film, predominantly in the form of N-H covalent bonds. This leads to a high density of localized defects and inhomogeneities in the a-SiN_x:H network. The high density of these defects impedes the evolution of a high biaxial stress σ, but is also responsible for the drifting behaviour of σ. As a consequence, the film becomes permeable for O_2 and H_2O molecules originating from the surrounding atmosphere, while simultaneously offering many sites which these molecules can easily react with. This leads to an oxidation of the a-SiN_x:H deposit, resulting in a shift of σ in the compressive direction even at room temperature. Activating the CCP RF plasma source changes the plasma chemistry substantially. As a result, between P_{RF} = 0 W and P_{RF} = 35 W the formation of N-H bonds is strongly inhibited, leading to fewer H-saturated defects in the deposited films, which results in a build-up of a strong compressive stress. Simultaneously, the deposition rate slightly increases due to the changed plasma chemistry allowing the formation of more Si-N (and by extension Si-H) bonds. When increasing P_{RF} from 35 to 150 W the ion bombardment of the sample substrate becomes more and more dominating. Apparently, this facilitates the N-H bond formation to a degree, which in an analogous way to the previous points ultimately leads to a partial stress relaxation. On the other hand, as evidenced by the increase in refractive index n and the peak-shift of the Si-N asymmetric stretching absorption band, the composition of the a-SiN_x:H deposit changes to a higher silicon concentration.

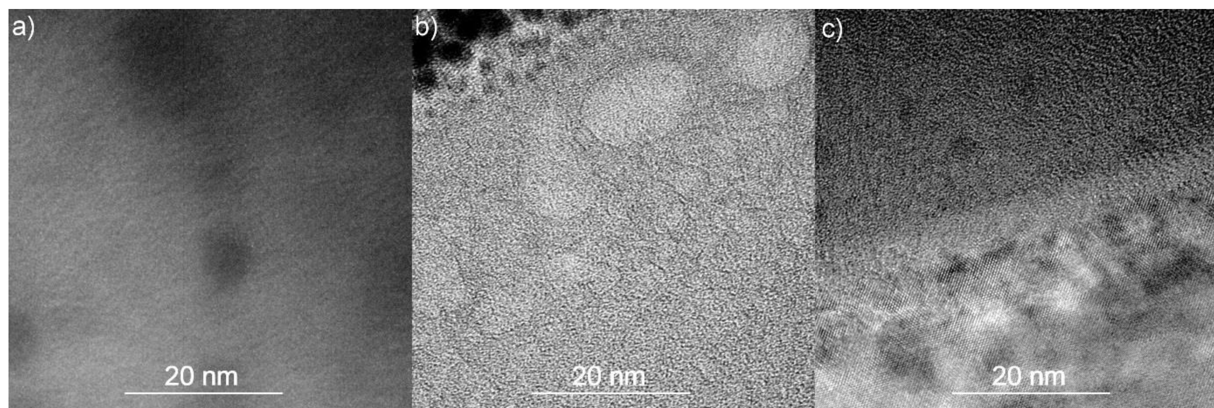

Figure 44: Bright field high-resolution transmission electron micrographs of ICP-CVD silicon nitride films deposited using different values of P_{RF}. a): 0 W b): 35 W c): 150 W.

Thin membranes from a-SiN_x:H thin film samples deposited using different P_{RF} values (0 W, 35 W and 150 W) have been prepared by mechanical thinning and grinding for transmission electron microscope (TEM) investigations. In accordance with the XRD results from section 4.2., an amorphous microstructure was clearly demonstrated in all three samples, as illustrated in Figure 44 and expected from literature [121]. In addition, nano-sized particles have been identified within the a-SiN_x:H host

matrix under bright field conditions, based on their differing contrast. Although for obvious reasons a minimal particle size cannot be reliably stated, the maximal lateral dimension of the particles was around 15 nm, but having a wide size distribution. Further investigations included EELS technique described in Chapter 3 to measure the chemical composition of both the particles and the surrounding matrix. The results of these measurements are indecisive, since no significant difference has been found between the chemical compositions of the two phases in the sample. The ability to differentiate between signals originating from the particles and the matrix was largely limited by the sample geometry, as the minimal achievable samples thickness was several times larger than the size of the particles. Although, in the literature (amorphous and crystalline) silicon nanoparticles embedded in a a-SiN_x:H host matrix are reported [14, 125], it is worth mentioning that the latter samples are generally synthesized at temperatures far exceeding the temperature range ($T < 350°C$) the present samples were exposed to. These facts make the presence of pure silicon nanoparticles in the samples very unlikely. Additionally, the selected area diffraction (SAD) pattern (see Figure 45) indicates that beside the amorphous phase, an ultra-nanocrystalline phase is also present in at least one of the samples (at $P_{RF} = 150$ W), meaning that there are locations in the a-SiN_x:H deposit, where at least locally a crystallographic structure can be found.

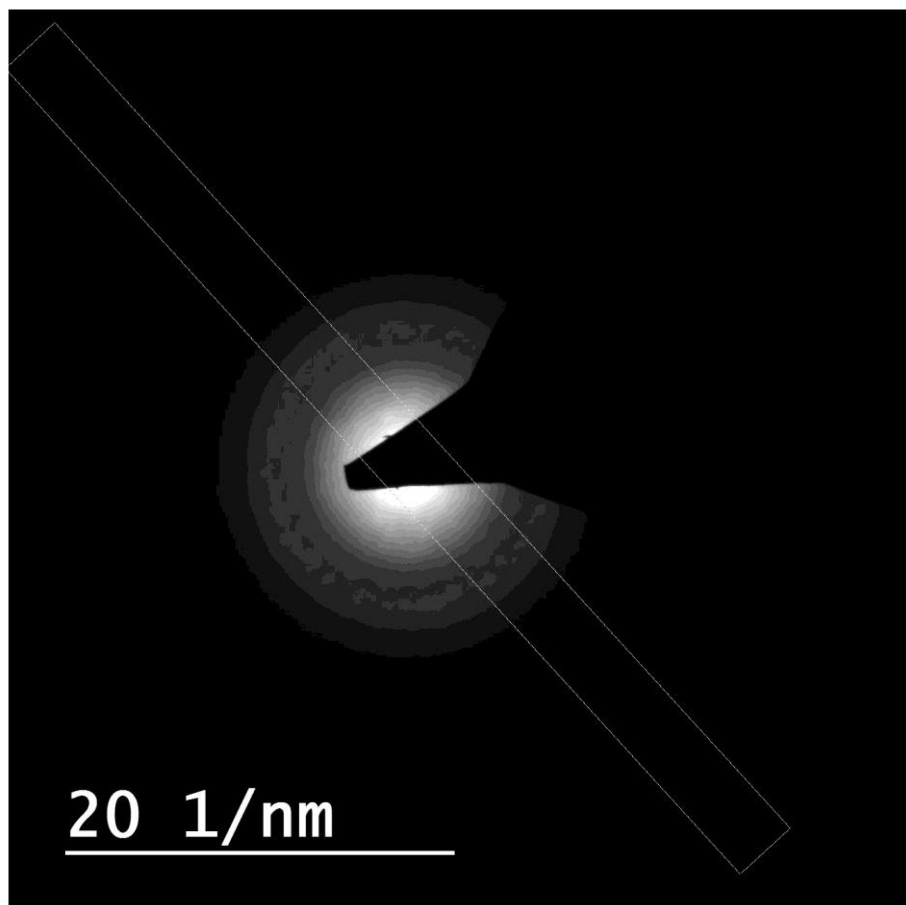

Figure 45: TEM selected area diffraction pattern of an ICP-CVD silicon nitride thin film sample.

To be able to fully compare the performance of ICP-CVD a-SiN_x:H thin films deposited with the aid of a CCP RF discharge to those synthesized without, the same wet etching test has been performed as before. The general reaction that describes the etching of silicon nitride by hydrofluoric acid is as follows [126]:

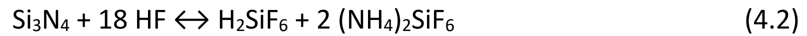

$$Si_3N_4 + 18\ HF \leftrightarrow H_2SiF_6 + 2\ (NH_4)_2SiF_6 \qquad (4.2)$$

Although the main radicals participating in the reaction are monofluorides, HF_2^- also has a substantial role in breaking up the covalent bonds in Si-NH_2 groups that are abundant in most of the samples in this study [127]. The influence of P_{RF} on the wet etch rate *WER* is quite significant, as it is shown in Figure 46. At P_{RF} = 0 W (which again is basically a *Type I* ICP-CVD SiN_x film) *WER* is about 270 nm/min. This is followed by an abrupt decrease with the activation of the CCP RF source (*WER* = 14 nm/in at P_{RF} = 10 W). Still, increasing P_{RF} to higher values leads to a steady increase of the wet etch rate (*WER* = 77 nm/min at P_{RF} = 150 W). This trend correlates well with the N-H bond density over P_{RF} (see above), although the comparison shows that the extremum in the *WER* is reached at a lower value of P_{RF} than in the case of the N-H density. This fact indicates the possible involvement of other factors, such as the total hydrogen amount [128] incorporated into the a-SiN_x:H thin film, as contributors to the observed wet etching behaviour using HF based etch media.

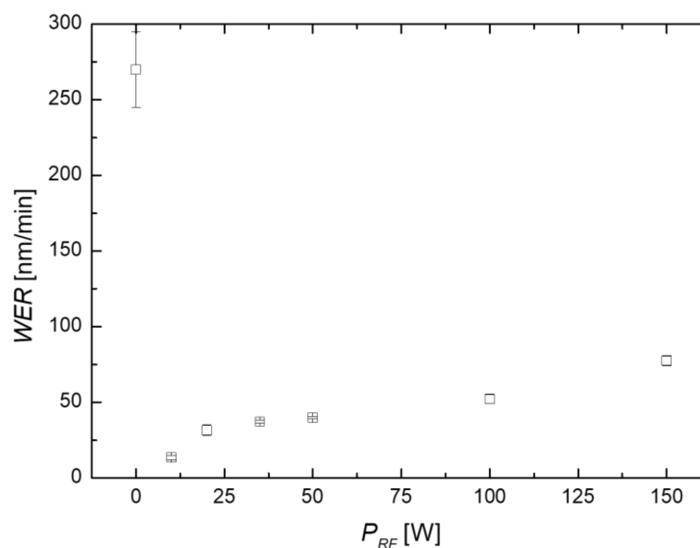

Figure 46: The wet etch rate WER in hydrofluoric acid of ICP-CVD silicon nitride thin films as a function of the capacitively coupled plasma power P_{RF}.

The results of the RIE (See section 2.3.2) dry etching experiments stands in a clear contrast to the experiences from the wet etching tests. For these experiments (and for similar RIE etching

experiments throughout his work) an *STS 320* parallel plate reactor was used. The etch process utilizes a mixture of CF_4 and O_2 gases (a standard gas chemistry for the dry structuring of silicon nitride) and is described in detail in [129]. Figure 47 demonstrates the effect of P_{RF} on the RIE etch rate r_{RIE}. As P_{RF} is increased form 0 W to 150 W, a continuous increase in r_{RIE} is observed from about 150 nm/in to r_{RIE} > 200 nm/min. This behaviour is in good correlation with the increasing Si-content of the a-SiN_x:H deposits with increasing P_{RF}, which is most likely responsible for the observed effect considering the preferential etching of Si by fluorine radicals [129] found in the used etch gas chemistry.

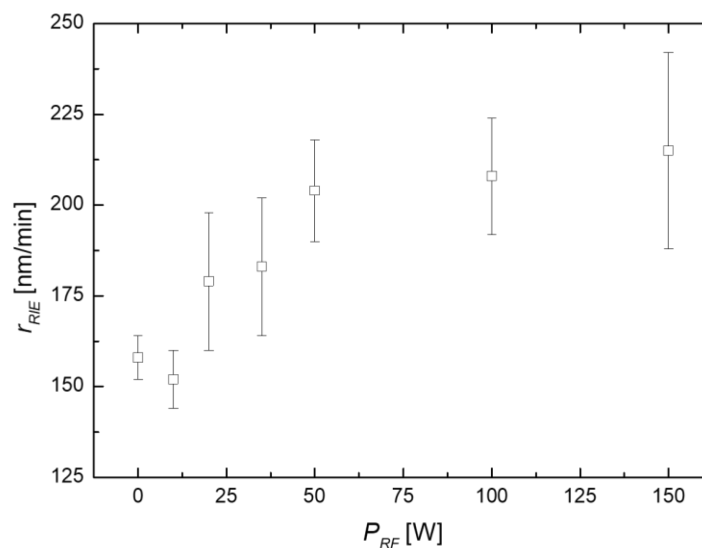

Figure 47: The RIE etch rate r_{RIE} in CF_4:O_2 plasma of ICP-CVD silicon nitride thin films as a function of the capacitively coupled plasma power P_{RF}.

In essence, activating the ancillary capacitively coupled plasma source during the deposition of ICP-CVD silicon nitride has a major effect on the resulting properties of the thin film samples. Using this technique, the drift of the biaxial film stress can be avoided at any precursor gas ratio, albeit at a cost of a strong compressive stress. The main causes for the observed effects are the change of the plasma chemistry and the ion bombardment induced by the CCP discharge. The macroscopically observable effects can be traced back to the changes introduced to the chemical composition of the silicon nitride thin film samples, namely the partial inhibition of the N-H bond formation and the shift to higher Si/N ratios.

4.5. Summary

After evaluation of the state of the art regarding the use of the ICP-CVD technique in the synthesis of amorphous hydrogenated silicon nitride thin films, a detailed experimental approach was designed in order to scrutinize the effect of the individual process variables on the resulting physical properties, microstructure, and chemical composition of the silicon nitride thin films. By using DoE, the first screening stage of experiments revealed the precursor gas ratio $R_{N2/SiH4}$ to be by far the most influential of the investigated process parameters, compared to other variables, such as the substrate temperature T, the deposition pressure p_{dep} and the ICP power P_{ICP} having secondary, but still measurable impact. Due to their remarkably differing qualities, the distinction between *Type I* and *Type II* samples was introduced. A short comparison between those two highlighting the most prominent differences is provided below in Table 11.

	Type I	***Type II***
r_{dep}	low	high
n	≈ 1.95	> 2
σ	Low, drift	Compressive, stable
WER	high	low
Storage of H	N-H bonds	Si-H bonds
Oxidation	yes	no
N/Si ratio	0.57-0.65	0.35-0.52

Table 11: Comparison of Type I and Type II ICP-CVD silicon nitride thin films.

For most MEMS applications, a simultaneous occurrence of a low and stable biaxial stress is desirable. Since neither *Type I* nor *Type II* films were able to fulfil this requirement, the effect of the parameter $R_{N2/SiH4}$ was scrutinized in more detail. As it was found, there exists a process window at about $R_{N2/SiH4} = 0.75$, where low-stress, stable ICP-CVD silicon nitride thin films can be synthesized. Using the process variables p_{dep} and P_{ICP}, the film stress can also be tailored within a wide range to fit the selected application.

The potential to utilize the ancillary CCP RF source to assist the synthesis of silicon nitride thin films was also assessed. This effort resulted in the conclusion that although it is possible to make use of the CCP source in order to influence the properties of the silicon nitride thin films, the resulting high compressive stress very much limits the potential utilization of this technique.

Chapter 5: Mechanical and morphological properties of silicon nitride thin films deposited by magnetron sputtering

Parts of this chapter have already been published in [130] and [131].

Sputter deposition is a well-established technique for the synthesis of pure metallic materials [132], including metal alloys [133], or even non-metallic [134] thin films when targeting their integration in microelectronic [135] or MEMS [28] devices. This is due to attractive features such as a high flexibility, fast process times, cost-effectiveness and low deposition temperatures. In the past decades, different types of sputter deposition techniques (see Section 2.1.2) have been applied for the synthetization of silicon nitride thin films. In the following chapter, a systematic study about the influence of the sputtering mode and process parameters on the resulting physical properties and chemical composition of silicon nitride thin films is presented.

5.1. Experimental details of the SiN_x thin film sputter deposition

The substrates used for the silicon nitride sputter deposition experiments originated from the same source, and had the same properties as those described in Chapter 4. In short, they had a diameter of 100 mm, 350 µm nominal thickness, double side polished surfaces, and made from *n*-type (P-doped) Si, having a bulk resistivity of more than 50 Ω·cm. Prior to the deposition, the process chamber of the sputtering system was evacuated to a base pressure of $<10^{-7}$ mbar. The cleaning routine prior to the deposition was also based on that presented in section 4.1, but was supplemented by an *in-situ* process step. The latter made use of inverted sputter etcher (ISE) integrated in the sputter equipment, so that the wafers were exposed to an Ar-ion bombardment after loading the substrate into the process chamber via a load-lock chamber. The process parameters for this final cleaning step were: a duration of 60 seconds, back pressure of 6 µbar and plasma power of 200 W. The sputter equipment used for the ISE and the silicon nitride deposition experiments was purchased from *Von Ardenne GmbH (LS730S).* A detailed description can be found in section 2.1.2.2. To ensure maximal comparability between different samples and deposition conditions, the same target position was used for all the silicon nitride deposition experiments allowing deposition in either DC or RF (f = 13.56 MHz) mode. All targets had a nominal diameter of 6 inches. After the deposition, the coated substrate was loaded back into the load-lock chamber, which was vented to atmospheric pressure subsequently. Before removing from the load-lock chamber, the substrate was allowed to cool down close to room temperature.

As it was already pointed out in section 2.1.2, several techniques are available to sputter-deposit thin films of silicon nitride, regarding the target material and sputtering mode. In the present case, taking into account the constraints given by the sputter equipment (e.g. pulsed sputtering being not feasible), three different techniques of silicon nitride sputter deposition were investigated. The first one which is the most commonly used technique of the three [136-138] is reactive RF sputtering using a polycrystalline silicon target and a mixture of nitrogen and argon gases. The latter is needed to ignite and sustain the RF discharge. The second approach is reactive DC sputtering using a polycrystalline silicon target in a pure nitrogen atmosphere. The third possible method which is only briefly investigated in this work is the RF sputtering using a compound silicon nitride (Si_3N_4) sintered ceramic target, and pure argon gas.

The sputter deposition experiments at different parameters have been selected by using a DoE approach similarly to the ICP-CVD experiments. While it is undeniable that some deposition parameters, such as the target to substrate distance, the substrate temperature and the gas composition, can influence the properties of the gas discharge, the deposition process and hence, the physical properties of the deposited silicon nitride thin films, the scope of the investigations was mainly restricted to the most influential deposition parameters in the sputter deposition process, being plasma power and back pressure during deposition[30, 136]. The main concerns for selecting the process variables that have been used in the deposition experiments were the following:

1. to ensure maximum comparability between the different samples
2. to deposit high quality (i.e. close to stoichiometric, highly resistive, etc.) layers
3. to take into account the constrains set by the equipment (e.g.: gas flow rates and pressure control).

These issues have been addressed by a careful selection of the deposition parameters, as it is described in the following. Maximal comparability between different deposition runs and samples is achieved by keeping most parameters at a defined constant value, and by using the same range for the investigated parameters. This leads to a default settings of the target-substrate distance d_{ts} = 65 mm being an empirical value from prior experience with the sputter equipment, without the application of external heating, and a nitrogen flow rate of 60 sccm.

External heating during deposition is not chosen, due to the way the heater is regulated inside the sputtering system. Although nominal temperature values are assigned to different power settings on the heater, the actual substrate temperature also strongly depends on the plasma power setting due to the self-heating effect by the impinging particles, the thermal coupling between the substrate and substrate holder during deposition, and is also a function of the sputtering process time. But, a precise measurement of the substrate temperate is not possible in the way the sputter equipment is

designed. Basically, the signal detected by the pyrometer is originating not only from the bottom side of the substrate holder which can have also have a slightly different temperature from the substrate itself, but also from the heater and to some extent the plasma. Thus, the measured temperature is strongly influenced by these parasitic effects, what does not allow an accurate assessment and control of the substrate temperature during deposition. Consequently, it was decided not to use the heating option during the deposition experiments. Although one should be aware of the plasma heating effect on the substrate temperature, the actual working temperatures are estimated to be below 250°C. Given a melting point of silicon nitride in the range of 1900°C [139], a low impact on the microstructure and on the film stress is expected when comparing different samples between each other.

Another critical point is the sputtering gas composition. Given the target material (6 mm thick polycrystalline Si, 99.99% purity bonded to a copper backplate), for the deposition of high quality (preferably close to stoichiometric) silicon nitride, a pure nitrogen atmosphere is desired. This is certainly feasible in DC sputtering mode, but has proven to be difficult when using a RF gas discharge. During RF sputtering the impedance of the RF discharge has to be matched with the output impedance of the RF source in order to be able to ignite and maintain a stable discharge. Unfortunately, in this case the range in which the match-box of the RF can be tuned does not completely overlap with the impedance of the discharge dominated by parameters such as the target material, reactor geometry and gas composition when using a pure nitrogen atmosphere. To be able to ignite and maintain a stable discharge, argon was added to the gas mixture. The minimal flow rate of Ar need to ensure a stable ignition procedure and subsequently a reliable burning of the plasma was 20 sccm, therefore this flow rate was used during the RF sputter deposition experiments. Under these circumstances it is necessary to use argon in the gas mixture, with the disadvantage that the change in the gas composition reduces the partial pressure of N_2 compared to the case of a pure N_2 sputtering gas regulated to the same total pressure, thus influencing the deposition process. In addition, incorporation of Ar atoms into the deposit is expected to some extent. To provide a wide process window, in which the back pressure during deposition can be controlled accurately via opening and closing a butterfly valve, the gas flow rates have to be limited appropriately. A hard, upper limit is the throughput of the installed MFC (mass flow controller units), while a soft limit is defined by the pumping speed of the system.

The deposition times have been selected in such a way, that silicon nitride thin films with comparable thicknesses of about 500 nm are synthesized. The actual deposition times used were based on results of some preliminary experiments and literature values [140-142], by taking also into account [136, 142], that the sputter deposition rate should be proportional to the plasma power in a first approximation. (This turned out to be true in the case of DC sputter deposition, but deviated in the RF case, see below in the results). As a result, a series of deposition times were selected, where the duration of the deposition is in inverse proportion to the DC or RD plasma power.

In order to provide a reasonable coverage of the investigated parameter field, in this case a four-level full factorial experimental design was applied with the two aforementioned process variables: the back pressure during deposition p_{back} and the DC or RF plasma power $P_{plasmaDC}$ or $P_{plasmaRF}$. p_{back} was varied between the values of 3 µbar and 9µbar in equidistant steps, while for $P_{plasmaDC}$ and $P_{plasmaRF}$ the nominal values of 300, 450, 600, and 900 W have been used, corresponding to a power density range of about 1.5 to 4.5 W/cm^2.

The actual deposition rate for each of the parameter sets have been calculated from the measured thickness values of the deposited thin films assuming a constant rate of deposition throughout the whole processing time. This is a reasonable assumption when considering the physical model of sputter deposition, except for very short durations (in the range of tens of seconds), where process transients can be of significant influence. The thicknesses of the silicon nitride deposits have been determined both with the help of a non-destructive and a destructive method: spectral reflectometry, and scanning electron microscopy (see Chapter 3), respectively. In these cases where both measurements have been carried out, the discrepancy between the measurement values was within the expected range of uncertainty of the measurement methods (under ±5%). Due to the characteristics of the sputter deposition process – and in contrast to most CVD processes – the deposition rate is significantly less uniform over the whole 4-inch wafer. Because of the reactor geometry, the deposition rate near the edges of the substrate can decrease by 20 to 25%. For that reason, the thickness of each thin film sample has been measured on multiple locations, both near the middle and the edges, and averaged. Thus, the deposition process (with the given geometric constrains) can be represented by an average deposition rate.

Using the calculated average film thickness, the biaxial film stress can be determined using wafer bow measurements and Stoney's formula, exactly as in the previous chapter for in the case of ICP-CVD samples. The accuracy of the latter calculation is naturally dependant on the uniformity of the sputter deposition rate, as the stress is not determined locally, but across the whole wafer.

In order to test the influence of the sputter deposition parameters on the robustness of the silicon nitride thin films against certain etch media, a range of dry and wet etching tests have been performed. Therefore, SiN_x samples have been placed into a *Xactix e1* xenon difluoride plasmaless etching system. The samples have been etched for 20 and 40 cycles of 30 s, using the parameters described in [129]. RIE etching was performed in an *STS320* parallel plate reactor, using a mixture of CF_4 and O_2 gases, and the parameters reported in [129]. The etch times in the latter case have varied between 2 and 4 minutes. Wet etching tests have been carried out in a 1:7 mixture of 49 % aqueous HF and DI water, for durations ranging from 1 to 30 minutes. The etch rates have been determined by measuring the remaining film thickness after the etch process using the spectral reflectance method.

5.2 RF sputter deposited silicon nitride

The deposition rate r_{dep} – according to initial expectations [142] – increases linearly with RF plasma power for $P_{plasmaRF} \geq 300°W$, as it is presented in Figure 48. Setting the value of $P_{plasmaRF}$ below 300 W, however, results in such a dramatic reduction of the deposition rate, that it becomes negligible and technically irrelevant. According to [30, 143] this result is attributed to the insufficient ionization of the gaseous species being present in the sputtering atmosphere inside the reaction chamber. This is a consequence of the magnitude of the electric field being too low to induce sufficient ionization at these moderate power settings (see Figure 49 for the measured bias voltages at different parameter sets), and is accompanied by the instability of the RF plasma discharge. The essence of these observation is that in the case RF sputtering there is a very real and technically relevant lower threshold limiting the usable range of $P_{plasmaRF}$ for the sputter deposition of silicon nitride.

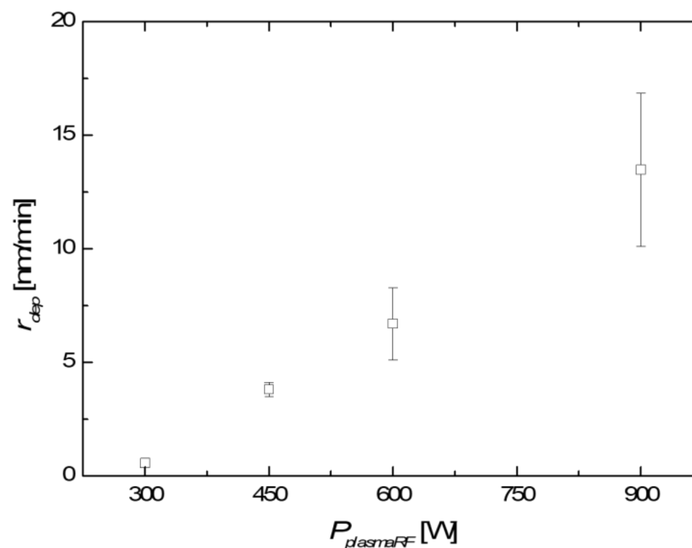

Figure 48: The deposition rate as a function of the plasma power $P_{plasmaRF}$ for RF sputter deposition of silicon nitride thin films.

For the $P_{plasmaRF}$ values at which meaningful deposition of silicon nitride takes place, it is necessary to calculate the deposition rate normalized to the applied power for the sake of comparison, which is presented in Figure 50. There is a measurable decrease of the normalized deposition rate with increasing back pressure during the sputter deposition. This behaviour can be associated to the increased collision rate between the particles ejected from the target and those present in the gaseous atmosphere of the processing chamber.

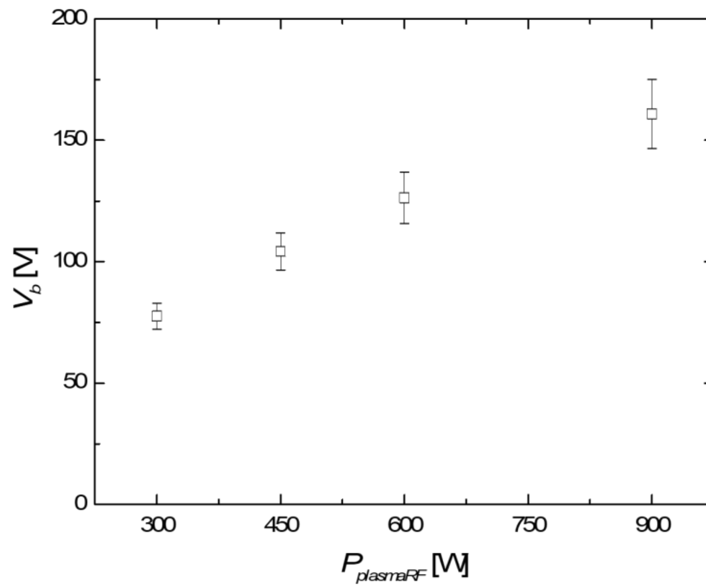

Figure 49: Impact of RF plasma power $P_{plasmaRF}$ on the resulting bias voltage V_b during RF sputter deposition.

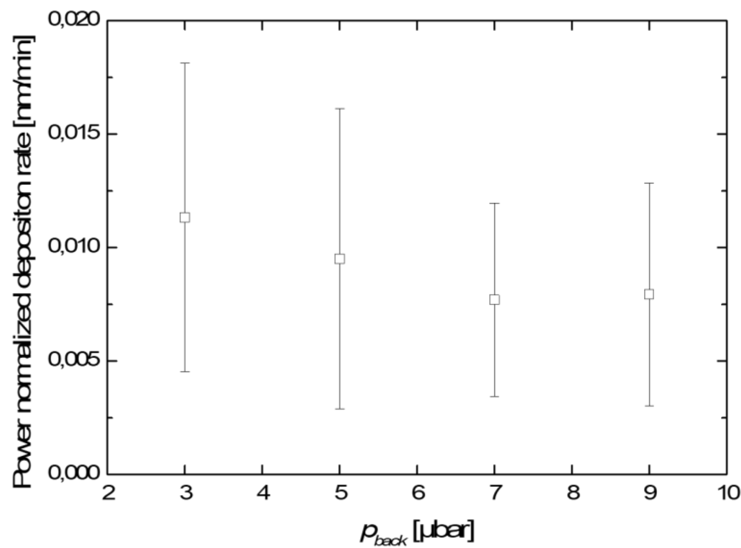

Figure 50: Sputter deposition rate of silicon nitride thin films as a function of the chamber pressure p_{back} normalized by the RF power.

From the spectral reflectometry measurements two important results are derived. The first one is that the refractive indices of RF magnetron reactive sputter deposited silicon nitride thin film samples (See Figure 51) are well above of the characteristic values for stoichiometric silicon nitride ($n \approx 2.01$) samples. This indicates a rather significant compositional difference compared to Si_3N_4. Secondly, despite the somewhat large variation of the individual measured values, neither of the two

investigated deposition parameters seems to have a significant influence on the resulting *n* value, as it was determined using an ANOVA (analysis of variance) approach. The typical significance level was 0.05, and the resulting probability values for $P_{plasmaRF}$ and p_{back} were 0.628 and 0.352, respectively, both much larger than the significance level, which in this case indicates the negligible influence of the input parameters [131]. Taking all samples into account, a mean value of $n = 2.55$ is extracted. Based on Makino *et al.* [144], the apparent N/Si atomic ratio *x* can be derived from the refractive index. In this case, the equation gives an approximate average value of $x = 0.72$, being significantly lower than the expected value of 1.33 in the case of stoichiometric Si_3N_4, indicating a large deficit of nitrogen atoms, in other terms a silicon-rich deposit. The most probable cause for this large discrepancy is the addition of argon into the sputtering atmosphere. As discussed above, this was unavoidable to ensure sufficient process stability. Doing so, however, increases the mean atomic mass in the process gas mixture compared to a pure nitrogen atmosphere, leading to an increased sputter yield from the silicon target. In addition, the partial pressure of N_2 gas in the processing chamber is lower than it would be in the ideal situation operating with pure N_2 as a process gas. Altogether, these two factors contribute to an excess of Si atoms resulting in a low N/Si ratio in the deposit.

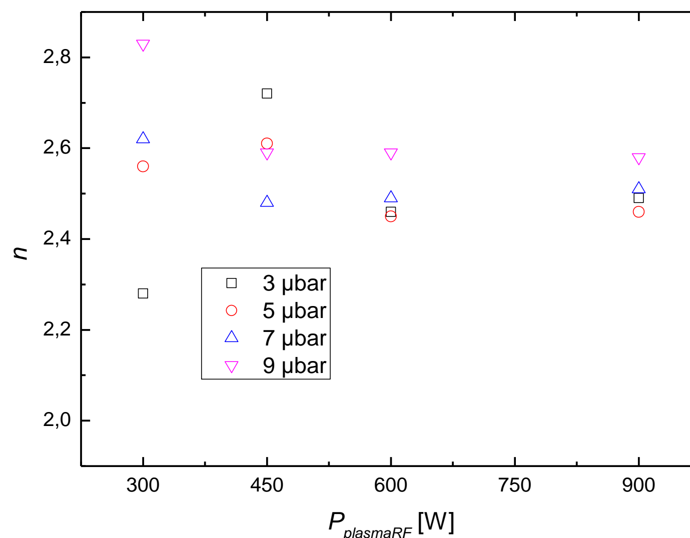

Figure 51: The refractive index n of RF sputter deposited SiN_x thin films as a function of the parameters $P_{plasmaRF}$ and p_{back}.

The average volumetric mass density (ρ_m) values of the silicon nitride thin films lies in the range of 2.9 g/cm^3 (at 300 W) and 3.3-3.4 g/cm^3 (at 450 to 900 W), as it is displayed in Figure 52. The significant reduction of the volumetric mass density at $P_{plasmaRF}$ = 300 W can be attributed to the insufficient ionization at this power level (see above), negatively influencing the layer growth. More interesting are the relatively steady values from $P_{plasmaRF}$ = 450 W to 900 W, being significantly higher

than the density of stoichiometric silicon nitride at 3.0-3.1 g/cm^3. This discrepancy can be fully explained by the assumed increased silicon content in the RF magnetron reactive sputter deposited silicon nitride thin films. Another factor can be the incorporation of gaseous species (such as argon) from the process gas mixture into the deposit.

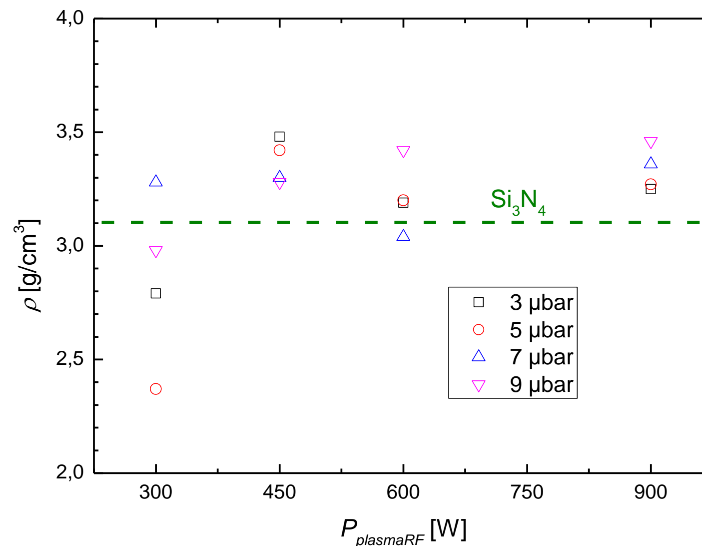

Figure 52: The volumetric mass density ρ_m of RF sputter deposited SiN_x thin films as a function of the parameters $P_{plasmaRF}$ and p_{back}.

In order to verify the above findings about the chemical composition of the RF magnetron sputtered silicon nitride films, XPS was applied for quantitative chemical analysis. Due to a limited access to the equipment, only few samples were analysed (deposited at $P_{plasmaRF}$ = 600 W, using different back pressure values). As illustrated in Figure 53, the differences in the chemical composition across the sample range are low. But, the average N/Si ratio for the investigated samples x=0.85 is in very good accordance with that derived from the refractive indices of the same samples, *i. e.* x = 0.87. The oxygen concentration reaching more than 5 at. % can be attributed to surface oxidation, and is most likely not representative for the whole cross-section of the deposit.

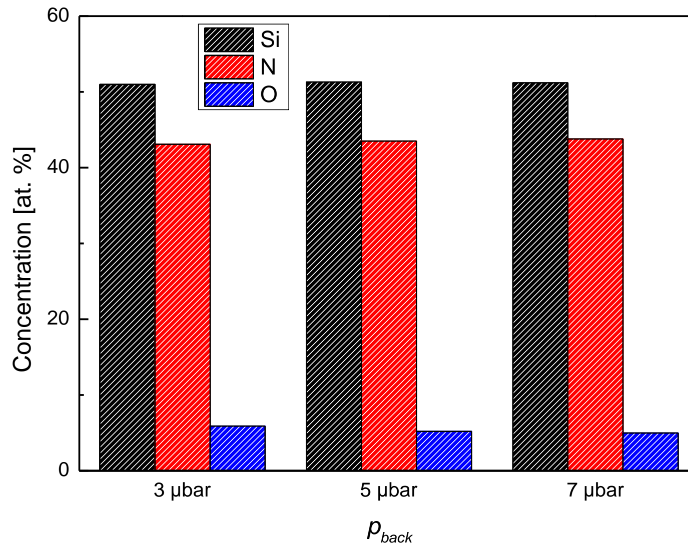

Figure 53: Chemical composition of selected RF sputter deposited (at $P_{plasmaRF}$ = 600 W) SiN_x thin film samples as a function of p_{back}, assuming a ternary system of Si,N,O.

One way to confirm the assumption of the surface-near oxidation is to monitor the biaxial stress σ of the thin film samples over a certain period of time, as post-deposition oxidation would have the potential to cause a significant change in this film parameter, as shown in the previous chapter. Since the biaxial stress values of the RF magnetron sputter deposited samples have been found to be very stable over any investigated timeframe (see in Appendix A), significant post-deposition oxidation except surface-near can be ruled out. Generally, the samples featured strong compressive stress in the range of σ = -1.1 to -1.6 GPa, while the samples deposited at $P_{plasmaRF}$ = 300 W are in the moderate range, compared to those with $P_{plasmaRF} \geq$ 450 W, where a biaxial stress of σ = 1.5 to 1.6 GPa is measured (see Figure 54).

Due to the relatively low deposition temperatures ($T_{max} \approx$ 150°C), and the fact that the mismatch of the thermal coefficients of expansion between silicon (3.5 to 4 $\cdot 10^{-6}$ K^{-1}) and silicon nitride (3 to 3.7 $\cdot 10^{-6}$ K^{-1}) [145] is rather low, the measured stress is mostly intrinsic in nature. This can be attributed to the morphological difference between the single-crystalline silicon substrate and the amorphous silicon-rich silicon nitride deposit. As a supplementary experiment, a range of samples sharing the same deposition parameters ($P_{plasmaRF}$ = 600 W and p_{back} = 5 µbar), but at different elevated temperatures ranging from nominal substrate heater temperature T_{set} = 150°C to 450°C which are not the actual substrate temperatures as mentioned above in the thesis. The results are summarized in Table 12. As one can see, with increasing process temperature a slight reduction of the deposition rate occurs, presumably due to the decreasing sticking coefficients at elevated temperatures. Moreover,

while the refractive index *n* does not show any significant change, a slight increase in the compressive biaxial film stress can be observed. As it is apparent this increase is rather moderate in accordance to the aforementioned assumption that the thermal expansion coefficient mismatch between substrate and thin film is negligible.

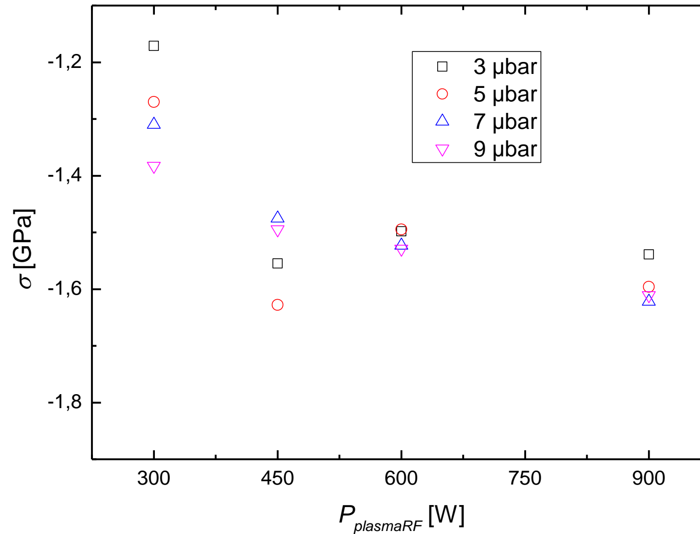

Figure 54: The biaxial film stress σ of RF sputter deposited SiN_x thin films as a function of the parameters $P_{plasmaRF}$ and p_{back}.

Selected samples have been subjected to nanoindentation measurements in order to gain further insight into the mechanical properties of the silicon nitride thin films. The resulting Young`s moduli and indentation hardness values are in the range of E_f =205 to 235 GPa and H = 25 to 27 GPa, respectively. Both values can be considered as typical for such films [98].

T_{set} [˚C]	*σ* [GPa]	*d* [nm]	r_{dep} [nm/min]	*n*
150	-1.25	324	7.20	2.03
250	-1.30	308	6.84	2.08
350	-1.36	304	6.75	2.07
450	-1.43	297	6.60	2.07

Table 12: Effect of elevated substrate temperature during RF magnetron sputter deposition ($P_{plasmaRF}$ =600 W, p_{back} = 5 µbar) on the resulting properties of SiN_x thin films.

As displayed in Figure 55, the FT-IR spectra of RF magnetron sputter deposited silicon nitride thin films have been found to be very similar to each other, regardless of the deposition parameters $P_{plasmaRF}$ and p_{back}. Prominent features in the infrared spectra are the CO_2 absorption peak, caused by

the atmosphere inside the specimen chamber of the FT-IR spectroscope (at around 2360 cm^{-1}), the Si-O asymmetric stretching band at 1180 cm^{-1}, and the broad Si-N "compound" asymmetric stretching band centred at approximately 840 cm^{-1}. To a substantially lower extent, the symmetric stretching mode band at about 490 cm^{-1} is observable. The relative amplitude of the Si-O absorption band significantly decreases with increasing thickness of the silicon nitride deposit, further supporting the assumption, that the oxygen found in the samples is primarily due to post-deposition surface oxidation. The broad nature of the Si-N peak occurs partially due to the amorphous microstructure of the silicon nitride deposit leading to diverse local environments adjacent to Si-N covalent bonds. Traces of the incorporation of H can be found in the appearance of a Si-H wagging mode band at about 660 cm^{-1} [141]. A small amount of H in the Si-N deposit is basically unavoidable, mostly due to the presence of water vapour in the residual gas of the sputtering chamber and adsorbed on the inside walls of the reactor.

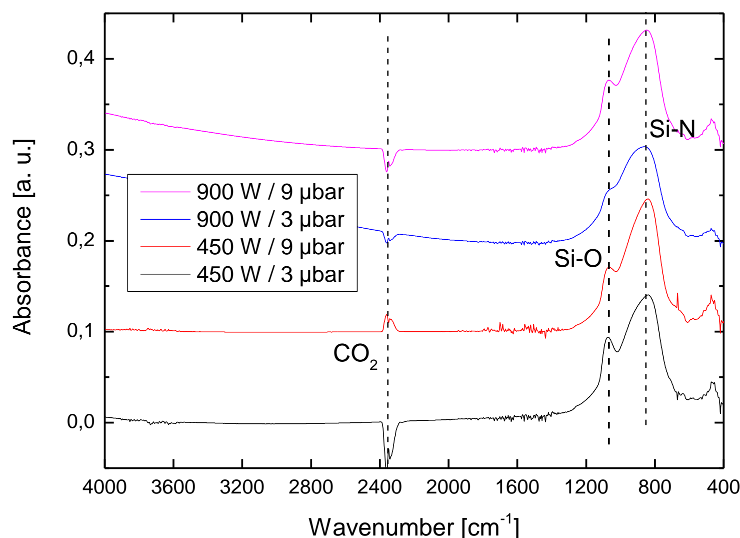

Figure 55: FTIR spectra of RF sputter deposited SiN_x thin films normalized to unit thickness, synthesized using different parameter sets.

In addition, assuming that the Si-N band density has a strong impact on the film properties, it is reasonable to plot the chemical composition/microstructure represented by the peak wavenumber of the main Si-N asymmetric absorption band as a function of the biaxial film stress (see Figure 56). As the graph shows, there is a tendency of σ shifting to a more compressive state as the peak wavenumber increases, indicating that subtle compositional and microstructural differences arise between samples deposited using different parameters. At the same time, it is worth mentioning the significant extent by which σ reacts to these presumably small compositional changes (see the largely consistent composition from XPS measurements).

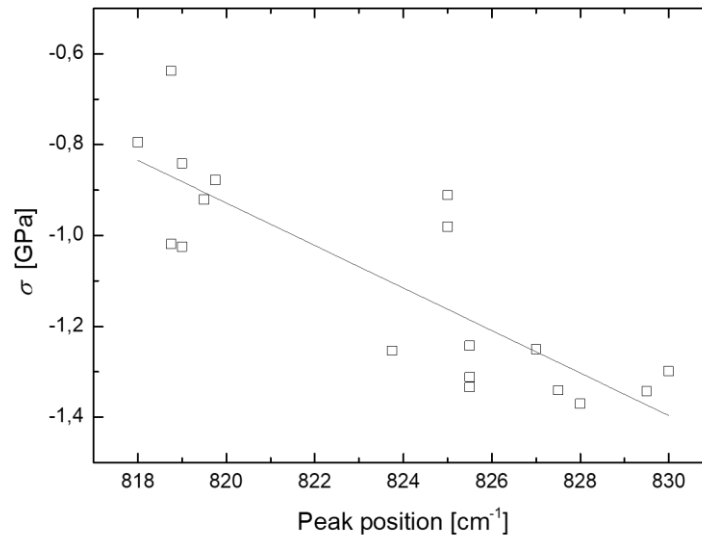

Figure 56: Correlation between the biaxial film stress σ and the peak position of the main Si-N asymmetric stretching absorption band in the RF magnetron sputter deposited SiN_x thin films.

A further issue is the high compressive stress present in the reactive RF magnetron sputter deposited silicon-rich silicon nitride layers. It is obvious that the presence of this high value of σ (roughly 1-1.5 GPa) can be detrimental or even prohibitive to a large number of device applications. Since it is not possible set by the process window of the available equipment to overcome the issue of depositing SiN_x thin films having strong compressive stress, it would be prudent to investigate post-deposition strategies to promote at least partial relaxation of the film stress, such as thermal annealing. Subjecting the samples to elevated temperatures for a given time introduces energy to the system. As a consequence, the atoms in the deposit have an opportunity to rearrange in an energetically more favourable position, or even microstructure, which can in turn lead to (partial) stress relaxation. This may compensate the relatively low substrate temperatures during the process of deposition, where the particles are generally incorporated into the amorphous SiN_x matrix at energetically suboptimal sites during film growth. This brings up an important point though; on some occasions, sputter deposition of silicon nitride thin films is precisely a preferred method over other techniques because of the low substrate temperature. This means that thermal annealing can only be a viable alternative to achieve post-deposition stress relaxation, where no strong limitations regarding the processing temperatures are present.

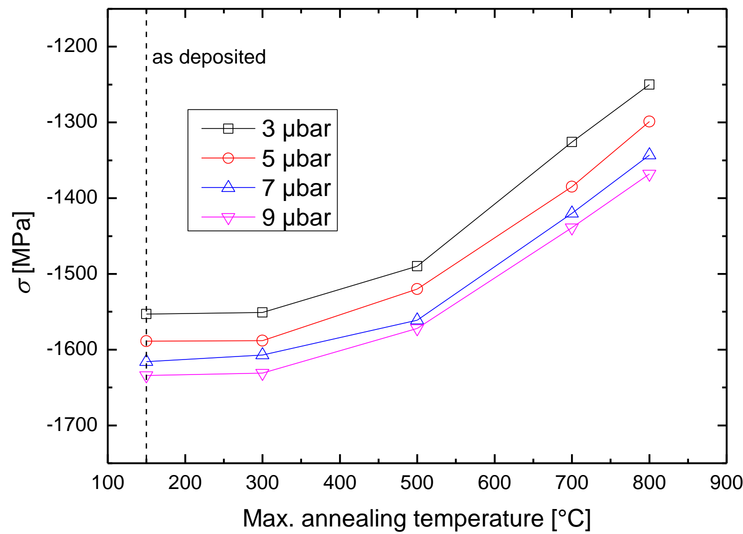

Figure 57: Biaxial film stress σ as a function of the maximum annealing temperature for RF magnetron sputter deposited ($P_{plasmaRF}$ = 900 W) silicon nitride thin films synthesized at different p_{back} values.

In this study, a series of experiments have been carried out to assess the potential of post-deposition thermal annealing for mechanical stress relaxation. The samples have been heated in a muffle furnace (type: *Nabertherm P330*). In order to limit oxidation in the non-hermetically sealed furnace a steady flow of gaseous Argon was introduced, to at least partially replace the air. The samples have been successively heated to 300, 500, 700 and 800°C, and kept at those annealing temperatures for a duration of 1 h. After each annealing step, the samples have been removed from the furnace, thus allowing to cool down to room temperature, and σ was determined using a wafer geometry gauge (see Chapter 3). Subsequently, the samples have been loaded into the furnace once again, ready to be heated to the next temperature level. This also means that the measured effects of annealing at 500°C and above are all cumulative including the effects of all of the previous steps. As a response to the heat treatment, a significant reduction of the compressive biaxial stress σ has been observed in all samples (see Figure 57). Unsurprisingly, the magnitude of the change $\Delta\sigma$ was found to be greatly increasing with increasing annealing temperatures. Moreover, this increase is not linear, but rather quasi-exponential in nature, which is perfectly coherent with the proposed mechanism of thermally activated structural rearrangement in the silicon nitride thin film. The relative reduction in σ is $\Delta\sigma < 5\%$ after exposure to 300°C, $3\% < \Delta\sigma < 10\%$ after 500°C, $10\% < \Delta\sigma < 21\%$ after 700°C, and $15\% < \Delta\sigma < 35\%$ after 800°C, respectively, as illustrated in Figure 58. In addition, very thin samples (d < 100 nm) have shown an increased amount of stress relaxation compared to thicker samples (d > 100 nm), which can be explained by the relatively larger effect of the film surface, where the structural rearrangement of the atoms can happen more easily.

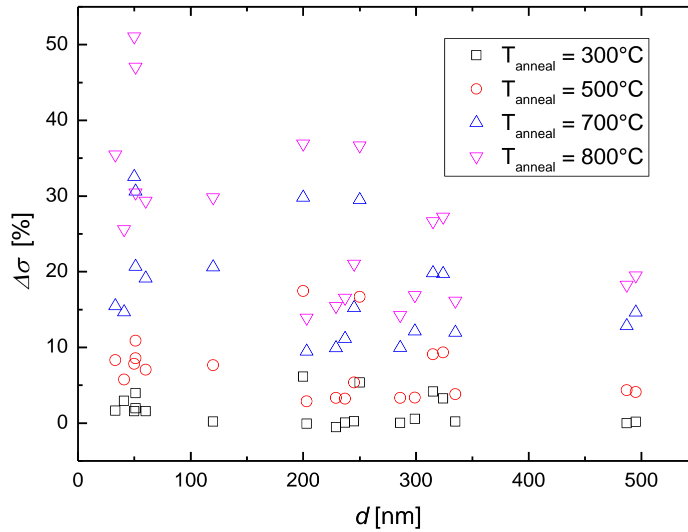

Figure 58: Relative reduction of the biaxial film stress σ as a function of the silicon nitride film thickness for different maximum annealing temperatures.

Another phenomenon that was observed during the annealing experiments in some cases is called *blistering* [146, 147]. Detected only in some thicker (d > 300 nm) samples after annealing at T_{anneal} > 700°C this effect is characterized by the local delamination or complete detachment of the thin film deposit from the substrate surface over a small (approximate diameter of 5-20 µm) circular area, as it is shown in Figure 59. It is caused by the release of stored elastic energy in compressively stressed thin films. Preferred sites for this phenomenon to occur are centred on local surface defects, where there is a decreased degree of adhesion between the substrate and the coating. Other authors have pointed out the potential effect of argon inclusion promoting the observed behaviour [14]. Given this explanation, it also becomes clear why this phenomenon only occurs above certain film thickness values: the stored elastic energy at a given value of σ scales proportionally with the film thickness d, while the adhesive force between the two materials is independent of d. Thus, above a certain threshold the force trying to delaminate the coating exceeds the adhesive force, and blistering occurs.

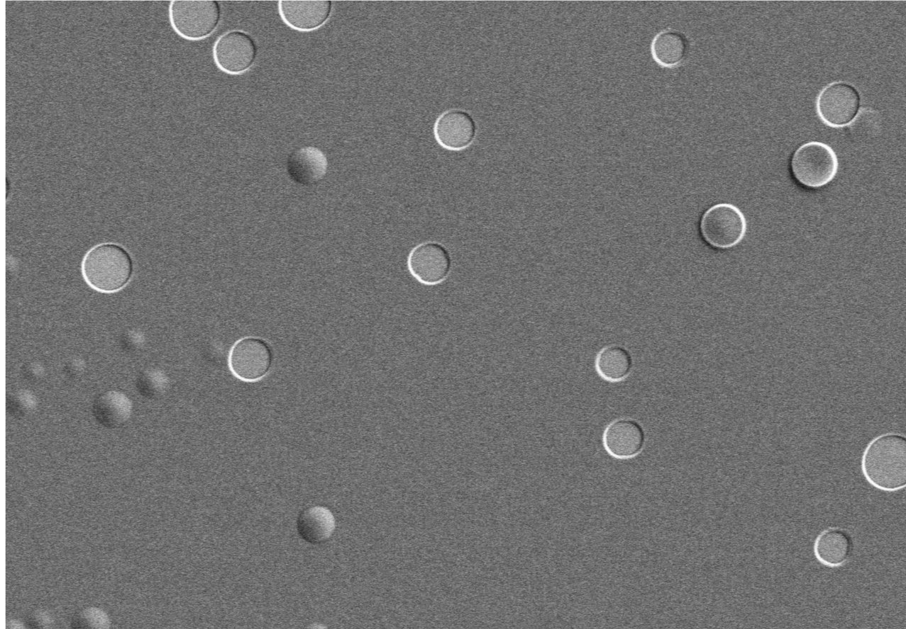

Figure 59: Scanning electron micrograph of an RF magnetron sputter deposited SiN_x thin film, after annealing at 800°C, illustrating the blistering phenomenon.

The quantitative results of the wet etching experiments in hydrofluoric acid are summarized in Figure 60. It was found that changing the parameter $P_{plasmaDC}$ has hardly any influence on the wet etching behaviour of the RF sputter deposited silicon nitride thin film samples. In contrast, the wet etch rate r_{HF} significantly decreases with increasing p_{back} values from an average r_{HF} of 33.7 nm/min to 18.4 nm/min at p_{back} = 3 µbar and 9 µbar, respectively.

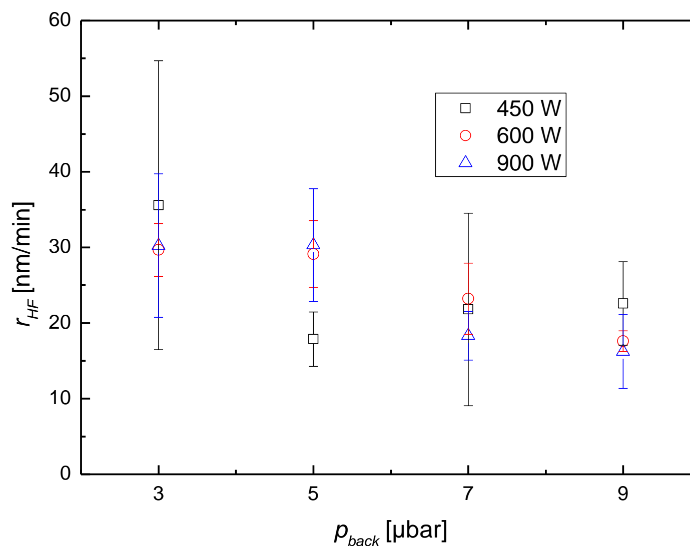

Figure 60: The wet etch rate in HF of RF sputter deposited SiN_x thin films as a function of the deposition parameters $P_{plasmaRF}$ and p_{back}.

This can be explained by the decreasing deposition rate and the resulting increased volumetric mass density at elevated back pressure values, as pointed out earlier in this chapter. The decreased

deposition rate allows more time for desorption of the unbound gaseous molecules (N_2, Ar) that are physisorbed to the growth front of the film surface [131]. This leads to a lower incorporation rate of unbound gaseous impurities into the amorphous matrix during film growth, which ultimately results in a denser, more compact morphology (see the increase of ρ). This results in an increased chemical stability, as in a more densely packed deposit, the etchant has fewer sites per unit volume, where it can disrupt the matrix of the amorphous thin film.

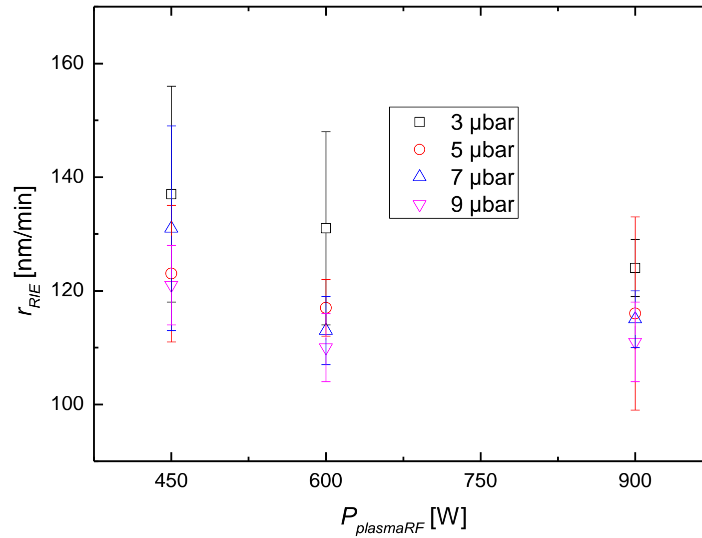

Figure 61: The RIE etch rate of RF magnetron sputter deposited SiN_x thin films as a function of the deposition parameters $P_{plasmaRF}$ and p_{back}.

Similar observations can be made in the case of the CF_4:O_2 reactive ion etching experiments. The etch rate r_{RIE} is generally around 120 nm/min, which is in good agreement with literature values [83]. A decrease of the etch rate with increasing p_{back} is clearly present (see Figure 61), as the average etch rate decreases from r_{RIE} = 138.6 nm/min at p_{back} = 3 µbar to r_{RIE} = 114.0 nm/min at p_{back} = 9 µbar. This behaviour can be again attributed to the densification effect described above. In addition, a weak tendency of decreasing etch rate with increasing $P_{plasmaRF}$ is observed (average r_{RIE} =134.2 nm/min and r_{RIE} =116.8 nm/min at $P_{plasmaRF}$ = 450 W and 900 W, respectively). This change can both be linked to the additional physical component present in RIE etching compared to the purely chemical HF wet etching, as well as to some degree to the densification effect, as samples deposited with higher $P_{plasmaRF}$ feature an increased ρ. Somewhat surprisingly, SEM investigations of both the original and etched SiN_x thin films surfaces has not revealed any significant roughening effect after exposure to RIE plasma etching. This, in turn, means that, despite the highly silicon-rich composition of the samples, the etch process is adequately uniform and homogeneous even on a microscopic scale, as illustrated by the SEM micrographs in Figure 62.

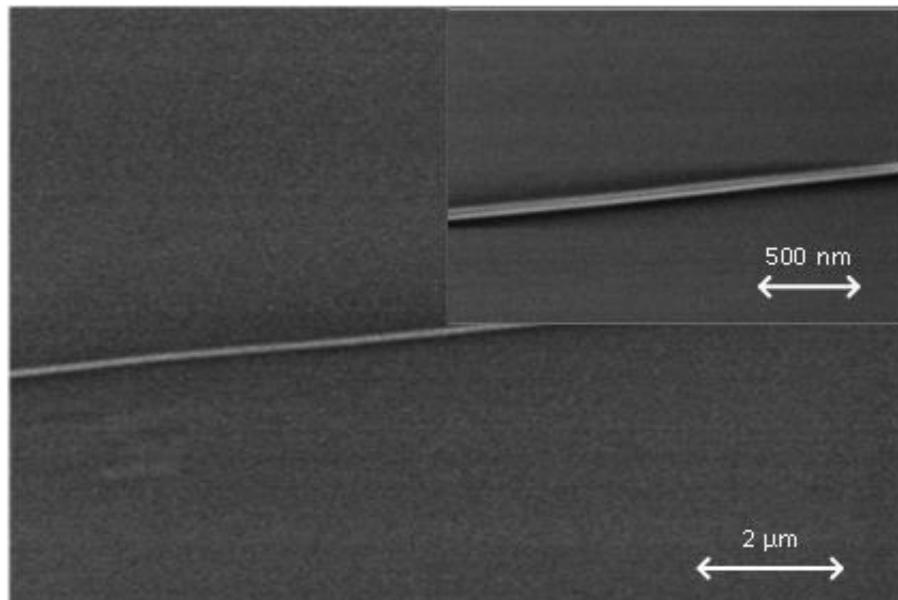

Figure 62: Scanning electron micrograph of RIE etched (bottom part of the images) and as depsoited (top part of the images) RF magnetron sputter deposited SiN_x surfaces.

Finally the plasmaless dry etching tests in XeF_2 have proven that the RF magnetron sputter deposited SiN_x thin films are extremely robust against this etching agent, in good agreement to other studies [129]. This enables the usage of this material as a suitable hard mask for the dry bulk micromachining of silicon. The calculated etch rates are lower than 1 nm/min, and decrease also with increasing etch duration. This suggests that the etchant predominantly attacks the (partially oxidized) sample surface. Upon reaching the deeper, thus oxygen-depleted regions of the thin films, the etch process practically comes to a complete halt. Given the very low etch rates, no significant influence of the sputter deposition parameters can be specified.

5.3 DC sputter deposited SiN_x thin films

Unlike to RF sputtering, the deposition rate r_{dep} of DC sputtered silicon nitride thin films has shown an almost perfectly linear relationship with the DC plasma power, as shown in Figure 63. It is worth noting that DC bias voltage, while reaching significantly higher absolute values than in the case of the RF magnetron sputtering experiments, was far less dependent on the deposition parameters, and stayed in the range of 390 to 410 V, as given in Appendix B. However, after normalization to the plasma power $P_{plasmaDC}$, the influence of back pressure during deposition becomes more apparent, as with the increase of the back pressure p_{back}, the deposition rate tends to decrease (see Figure 64). The most probable cause for this phenomenon is the increased collision rate between the plasma constituents and the ejected target atoms. This results in an increased redistribution of kinetical energy

between the aforementioned species, ultimately leading to a slight decrease in the silicon nitride growth rate. One particular point to note is the increase of the normalized sputter deposition rate by a factor of 1.5 to 2, compared to RF reactive sputter deposited silicon nitride (see earlier in this chapter). This phenomenon is known as the “deposition rate paradox”, and has been described by multiple authors both for reactive and non-reactive sputter deposition processes [143, 148, 149]. The observed large disparity between the deposition rates of DC and RF sputter deposition processes is suggested to be a result of a largely different power distribution in the DC and RF plasma sheaths, respectively.

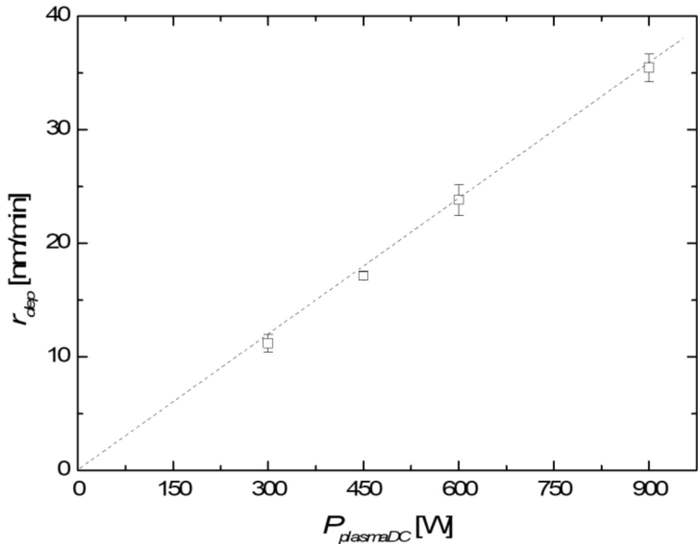

Figure 63: The deposition rate of DC magnetron sputter deposited SiN_x thin films as a function of $P_{plasmaDC}$.

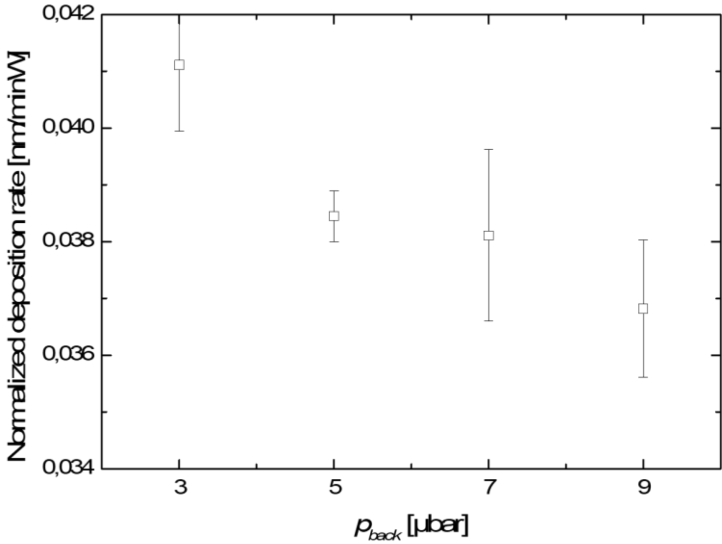

Figure 64: The power normalized deposition rate of DC magnetron sputter deposited SiN_x thin films as a function of p_{back}.

Another noteworthy effect associated with the increased back pressure is a decrease in the refractive index *n*, as illustrated in Figure 65, due to an overabundance of nitrogenous species in the plasma. This enhances the probability that nitrogen atoms are incorporated into the deposit, resulting in a shift of the N/Si atomic ratio *x* to a nitrogen-rich composition. With the refractive indices known, one can apply the relationship between the *x* and *n*, as described by Makino *et al.* [144]:

$$\boldsymbol{n(x)} = \frac{\boldsymbol{n_{Si} + \frac{3}{4}x\left(2n_{Si_3N_4} - n_{Si}\right)}}{\boldsymbol{1 + \frac{3}{4}x}}, \tag{5.1}$$

where n_{Si3N4} = 1.98 is the refractive index of stoichiometric silicon nitride, and n_{Si} = 3.85 that of silicon, respectively. Applying the measured *n* values to the equation, a change of the apparent N/Si atomic ratio is clearly observable, from an average value of *x* = 1.148 at 3 µbar to *x* = 1.291 at 9 µbar (with *x* = 1.333 being the value for stoichiometric silicon nitride).

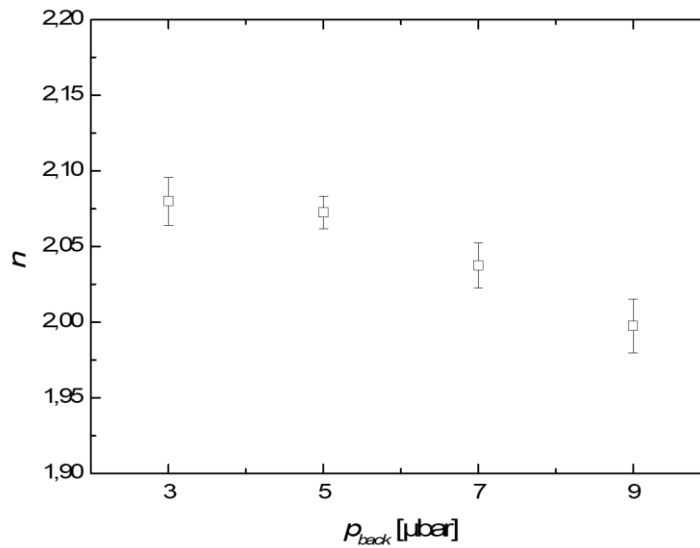

Figure 65: The refractive index n of DC magnetron sputter deposited SiN_x thin films as a function of p_{back}.

In addition, in an analogous manner to the case of ICP-CVD silicon nitride samples, the Lorentz-Lorenz (also known as Clausius-Mossotti) equation can be used to correlate the changes in the refractive indices to the variation of the measured volumetric mass density. As before, a homogeneous, isotropic material with a constant polarizability is assumed. The volumetric mass densities of samples deposited in two extreme cases, when the sputtered particles have either low ($P_{plasmaDC}$ = 450 W, p_{back} = 9 µbar) or high ($P_{plasmaDC}$ = 900 W, p_{back} = 3 µbar) mean kinetic energies are determined to 2.77±0.01 g/cm^3 and 3.04±0.01 g/cm^3, respectively. The corresponding refractive

indices are n = 2.01 and n = 2.12, respectively. Applying the Lorentz-Lorenz equation gives a change of the refractive index by a factor of 1.06±0.02, which is in reasonable agreement with the directly measured increase by a factor of 1.055.

Wafer bow measurements prove that the biaxial film stress σ of DC sputter deposited silicon nitride thin films is dependent both on the plasma power and the back pressure during deposition, as displayed in Figure 66. Basically, σ is compressive, although it does show a great variation in the range of -1300 to nearly 0 MPa. Independent of the other deposition parameters, an increased back pressure level always results in a lowered magnitude of compressive stress. Given the accompanying change of the refractive index n, this behaviour is explained best by the compositional changes resulting from the alteration of the deposition parameters. At increased back pressure levels, the composition of the deposit comes closer to that of stoichiometric silicon nitride film, resulting in a reduction of biaxial stress in the film. Another effect is the increase of compressive stress with increased DC plasma power. This phenomenon is only observable at back pressure levels higher than 3 µbar. These results can be interpreted in a consistent model, which is described in the following. Since at low back pressures, the frequency, that the sputtered particles collide with the constituents of the plasma, is relatively low, so that they arrive on the substrate surface with enhanced kinetic energy. Given this condition, the impact of the DC plasma power on the particle energy and by extension on σ is negligible, as it is seen in the results at p_{back} = 3 µbar. In contrast, with increasing back pressure levels, collisions in the plasma become more frequent, leading to a decrease in the mean kinetic energy of the sputtered particles. This gradually increases the impact of $P_{plasmaDC}$, as the variation between σ values of samples deposited using different $P_{plasmaDC}$ getting larger with increasing p_{back}.

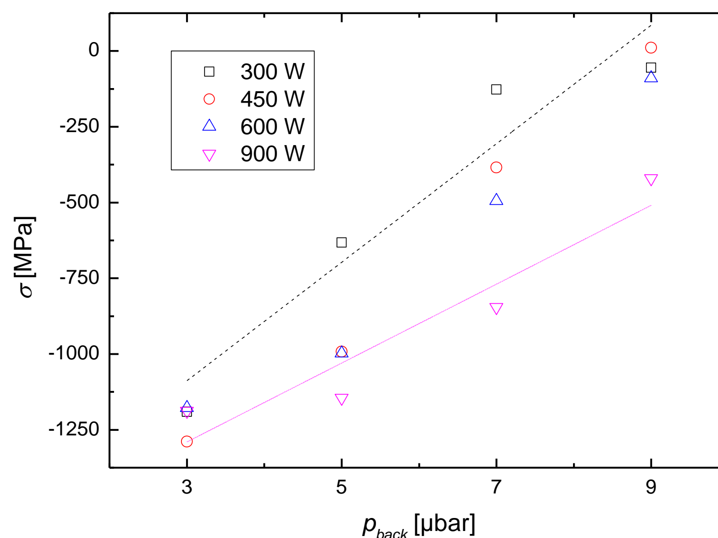

Figure 66: The biaxial film stress σ of DC magnetron sputter deposited SiN_x thin films as a function of the parameters $P_{plasmaDC}$ and p_{back}.

Nanoindentation measurements performed over a selected range of samples have yet again yielded quite typical values for the DC magnetron sputter deposited SiN_x thin films. The indentation hardness values were measured to be in the range of $H = 23$ to 27 GPa, while the Young`s moduli between $E = 220$ and 250 GPa. This is slightly higher than what was found for RF magnetron sputter deposited samples, presumably due to the different chemical composition between the samples deposited using the two techniques. In contrast to the biaxial film stress, the H and E values do not show any considerable influence by the two parameters $P_{plasmaDC}$ or p_{back}.

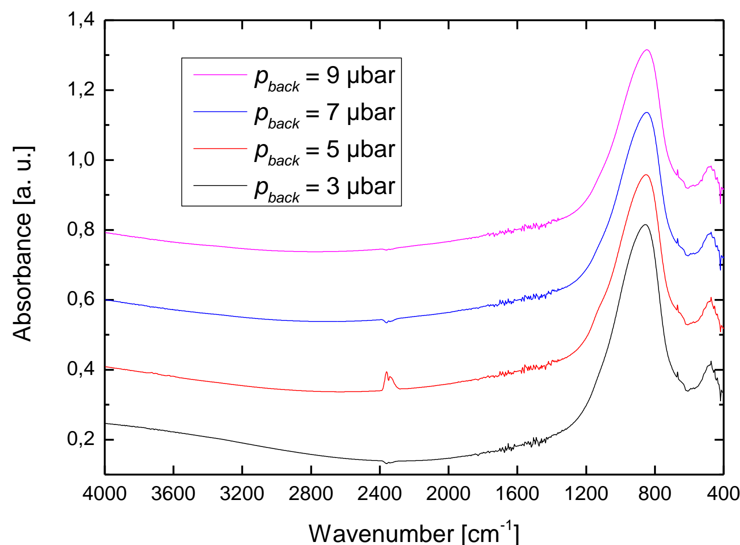

Figure 67: Selected FTIR spectra of DC magnetron sputter deposited ($P_{plasmaDC}$ = 450 W) SiN_x thin films.

As illustrated in Figure 67, Fourier-transform infrared spectroscopy measurements have not shown any significant systematic variation across the investigated sample range, which gives no direct confirmation of any compositional differences between the samples. Independent from the deposition conditions, characteristic absorption bands for amorphous silicon nitride films are clearly observable in the FT-IR spectra. Generally, the main asymmetric stretching mode Si-N band is rather broad, indicating a wide distribution of different Si-N local bonding environments. The peak wavenumber falls in the range of 868 to 872 cm^{-1} with a shoulder band appearing at around 840 cm^{-1}. The features between the wavenumbers of 2360 and 2340cm^{-1} originate from atmospheric CO_2. In contrast to ICP-CVD silicon nitride samples, significant Si-H, N-H, and Si-O bands have not been detected [130]. While the absence of the former two bands was not expected, the latter is remarkable compared to the previously presented findings of RF magnetron sputter deposited SiN_x thin films. This can possibly also mean that the DC sputter deposited SiN_x coatings are more robust against surface oxidation than their RF counterparts.

The results of the different etch tests conducted on the DC magnetron sputter deposited silicon nitride samples are summarized in Table 13. According to the expectations, the etch rates in hydrofluoric acid are significantly lower compared to different types of hydrogenated PECVD silicon nitride thin films [83], especially ICP-CVD films (see Chapter 4). On the other hand, the measured rates are higher than the reported values for LPCVD silicon nitrides [129]. When taking all the results gained so far into consideration, this behaviour is not unexpected due to the following reasons: the vastly lower hydrogen content of the sputter deposited silicon nitride thin films compared to ICP and PECVD samples, and the much lower deposition temperature then those used in LPCVD processes lead to an amorphous structure with a substantially higher density of unsaturated structural defects. Furthermore, a clear influence of the mean kinetic energy of the sputtered particles on the HF etch rate r_{HF} is observable. This results in a reduction of the etch rate in the case of samples deposited using high power (from an average r_{HF} = 37.8 nm/min to r_{HF} = 2.98 nm/min at $P_{plasmaDC}$ = 300 and 900 W, respectively) or low back pressure (average r_{HF} of 2.69 nm/min and 40.3 nm/min at p_{back} = 3 and 9 µbar, respectively), which is a direct consequence of the reduced density of structural defects at these deposition conditions.

$P_{plasmaDC}$ [W]	r_{HF} [nm/min]				r_{RIE} [nm/min]			
	3 µbar	5 µbar	7 µbar	9 µbar	3 µbar	5 µbar	7 µbar	9 µbar
300	3.07±0.31	3.33±0.40	8.35±0.47	136.3±30.9	68.8±4.2	89±7.6	98.3±5.9	100.7±5.2
450	3.31±0.95	2.89±0.08	4.53±0.67	14.8±0.8	80.4±6.4	88±3.8	90.9±2.7	112.8±5.4
600	1.86±1.09	2.8±0.46	3.39±0.77	6.97±1.36	87.6±1.9	80.4±1.2	87.8±5.3	109±7.0
900	2.53±0.13	3.24±0.85	3.03±1.12	3.13±0.41	89.7±9.8	79.2±23.5	98.7±2.2	94.4±0.4

Table 13: Etch rates of DC magnetron sputter deposited SiN_x thin films in HF wet etch (isotropic) and in CF_4:O_2 RIE dry etching as a function of the deposition parameters $P_{plasmaDC}$ and p_{back}.

In comparison, CF_4:O_2 RIE etch rates are, although slightly lower than, but still comparable to the reported etch rates of stoichiometric LPCVD silicon nitride materials when using the same etch mixture [129]. In addition, the etch rates are also significantly lower compared to the applicable values for RF magnetron sputter deposited silicon nitride thin films. This is due to the difference between the chemical compositions of the silicon nitride deposits from the RF and DC technique, where the N/Si atomic concentration ratio x is much higher in the latter case. In addition, it was found that the RIE etching characteristic of DC sputter deposited silicon nitride thin films does not show a highly significant dependence on the investigated deposition parameters. This is in accordance with the preconceived expectations, taking into account an enhanced physical component in the RIE etch process during material removal. The influence of the mean kinetic energy of the sputtered particles is still observable to some extent, as the samples deposited at low power ($P_{plasmaDC}$ = 300 W) exhibit

increased etch rates when deposited using higher back pressures (r_{RIE} =68.8 nm/min and r_{RIE} = 100.7 nm/min at p_{back} = 3 and 9 µbar, respectively). This behaviour can be linked to the changes in the N/Si atomic ratio x in the silicon nitride samples deposited using different parameter sets.

The last etch medium the DC magnetron sputtered silicon nitride thin films were tested against was XeF_2. The results have shown that independent from the DC power and back pressure levels used during the deposition, the etch rates were lower than 2 nm/min (which is – due to the limits of the employed measurement method – the most accurate figure that can be given at this point). These values are far below the etch rates presented above for the other two etch media, but are in good accordance with other reported values [129] for different silicon nitride thin films (including the RF magnetron sputter deposited samples described earlier in this chapter), meaning that the samples can be suitably used as a hard mask in XeF_2 etch processes. This, however, does not mean that the samples are completely unscathed by the etch process, as a shift in the perceived colour of the etched surfaces is clearly observable by the naked eye. Since the magnitude of the perceived colour shift [150] is generally exceedingly large for it to be elicited by the measured thickness reduction, it is presumably caused by the roughening of the surface due to selective etching of the heterogeneous silicon nitride matrix silicon rich sites, by attacking Si-Si bonds.

5.4. Summary

In this chapter, a systematic experimental study was executed in order to assess the influence of the main sputter deposition parameters such as the plasma power and chamber pressure, on the resulting properties of the deposited silicon nitride thin films. Within the technical constrains, the experiments have been designed to ensure a maximum degree of comparability between the RF and DC sputter deposition process.

The deposition rate is in a linear relation to the plasma power in both techniques, however during RF sputtering there is a relatively high threshold limiting the effective range of deposition parameters. Normalized to unit power, the influence of p_{back} is observable in both cases. The refractive index n shows a large difference between the samples synthesized by the two techniques: this is due to the significant difference in the N/Si ratio x. RF sputtered samples are extensively Si-rich, while their DC counterparts are much closer to a stoichiometric composition. This also has consequences regarding the value of the biaxial film stress σ. In the case of RF deposited samples σ is highly compressive (<-1 GPa), thus annealing at high temperatures is necessary to achieve partial stress relaxation. In the DC case, however, while σ is generally still compressive, but a careful variation of the sputter parameters offers the possibility to reduce the film stress close to a stress-free state.

Chapter 6: Electrical characterization of silicon nitride thin films

Parts of this chapter have already been published in [130, 131].

One attractive feature of silicon nitride and related materials such as silicon dioxide or undoped silicon carbide for microelectronics and MEMS is that they are considered to be excellent electrical insulators [25, 151]. The wide range across which the physical and chemical properties of ICP-CVD and magnetron sputter deposited silicon nitride thin films can vary was presented in the previous chapters. Given this knowledge, a significant scatter in their electrical performance is expected when varying the deposition techniques as well as the deposition parameters.

In this chapter, the electrical behaviour of silicon nitride thin films deposited with the aforementioned techniques will be investigated in detail. For this purpose, the samples will be subjected to two standardized, temperature-dependent benchmark measurement routines, assessing their leakage current and dielectric breakdown characteristics in a reproducible and comparable approach.

6.1. Sample preparation and measurement methods

In order to enable the efficient assessment of the electrical performance of various silicon nitride thin films, the design and fabrication of appropriate test structures was inevitable. The consistent usage of a well-thought-out methodology and a controlled environment can ensure that that results of the tests performed remain relevant in real-world applications, and the maximal comparability of the various results.

6.1.1. Sample preparation

The samples for the leakage current (LC) and dielectric breakdown (BD) measurements have been produced in a comparable way. As substrate, single-crystalline silicon wafers, having a diameter of 4", and a nominal thickness of 350 µm have been used. The wafers were *n*-type (phosphorous doped, ρ > 50 Ω·cm) in all cases, ensuring that electrons are the majority charge carriers. In the first step, a silicon nitride thin film was deposited onto the blank substrate. The deposition technique (i.e. ICP-CVD, RF and DC magnetron sputtering), deposition parameters, and film thickness (in the case of sputter deposited samples) have been varied to provide a wide array of samples with different physical properties.

ICP-CVD silicon nitride samples were synthesized using four different parameter sets (see Table 14), varying the parameter $R_{N2/SiH4}$, and in addition the auxiliary CCP RF plasma source, similarly to the processes described in Chapter 4. In Table 14 the details of the deposition runs are listed. For reason of comparison, the deposition times have been adjusted such to achieve a nominal sample thickness of 100 nm. The constant process parameters p_{dep} = 7 mTorr and T = 350°C ensure maximal reliability of the process, while a samples thickness of 100 nm is the most representative for real-life application scenarios.

Shorthand	P_{ICP} [W]	P_{CCP} [W]	p_{dep} [mTorr]	T [°C]	$R_{N2/SiH4}$
Type I	750	0	7	350	2
Type II	750	0	7	350	0.5
Type RF	750	150	7	350	1
Intermediate	750	0	7	350	0.75

Table 14: Parameter sets for the synthesis of ICP-CVD silicon nitride thin films used in the leakage current and dielectric breakdown measurements.

Sputter deposition experiments of SiN_x samples, on the other hand, have been carried out in a sequential manner, shortly breaking the vacuum to readjust the mask covering three quarters of the substrate wafer, which allowed for a more wafer-efficient fabrication procedure. The practice of changing the deposition parameters in between the individual runs resulted in wafers covered by films deposited using all four different parameter sets, while the position of the wafer flat was used to provide unambiguous identification of the individual samples.

RF and DC sputter deposited silicon nitride samples have both been synthesized using a two-level full factorial design, with the input parameters being the plasma power $P_{plasmaRF}$ or $P_{plasmaDC}$, and the chamber pressure p_{back}. The low and high levels used for the deposition runs were 450 W and 3 µbar, and 900 W and 9 µbar, respectively. The deposition runs have been repeated three times with the only variation in the duration of the process, in order to produce samples with nominal thickness values of 40 nm, 100 nm, and 300 nm, respectively.

The electrical contact pads have been designed specifically to be used with the existing measurement setup (see further below). To provide an enhanced electrical contact to the wafer chuck, all of the samples have been fully coated with an aluminium backside metallization having an approximate thickness of 800 nm using the DC magnetron sputtering, subsequently to the silicon nitride deposition. On the front side of the wafer, the MIS (metal – insulator – semiconductor) stack was completed by the electron-beam evaporation of a 10 nm thin film of chromium serving as an adhesion promoter and 200 nm of gold as the contact layer. The front-side metallization was patterned

using lift-off technique (i.e. *AZ nLOF 2070* resist), in order to obtain an array of separated electrodes suited for multiple measurements. A photomask specially designed for this purpose (see Figure 68) has been utilized for the realization of circular disc shaped electrodes, thus avoiding any peaks in the (rotationally symmetric) electric field distribution. The diameters ranged from 250 µm to 1000 µm to evaluate the impact of any size effect. As a closing step, the wafers complete with contacts were split into smaller samples for individual measurements.

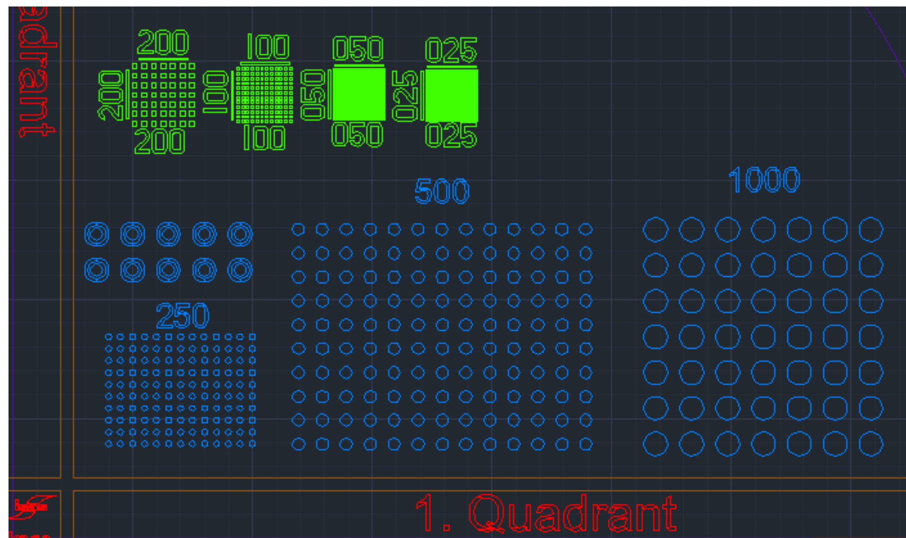

Figure 68: Detailed view of the front-side metallization mask for the LC and BD experiments, prepared with the software AutoCAD.

6.1.2. Measurement setup and methods

Leakage current and dielectric breakdown measurements were both carried out on a temperature-controlled wafer probe station (*PM 8* from *Süss Microtec AG*). Samples were securely held on their place using a vacuum chuck (*ATT systems*, model *A200* with an external controller), featuring an integrated heater. The substrate temperatures for the temperature-dependent measurements were set between room temperature (25°C) and 300°C in air. The deviation between the nominal and the actual temperature on the sample surface are taken into account using a temperature correction curve (see Appendix C). Ample electrical backside contact to the sample was also provided by the vacuum chuck. On the other hand, the front-side pads have been contacted individually using a tungsten needle brought into position by a three-axis micro-linear actuator. The accurate positioning of the contact needle was ensured by performing the operation under an optical microscope. The front and back electrodes were connected to an *Agilent B2911A Precision Source / Measure Unit* using coaxial wires having an impedance of 50 Ω. The heater and the Source/Measure

Unit were both controlled using a personal computer equipped with the software *LabVIEW* through the *IEEE 488 (GPIB)* interface. An optical photograph showing the measurement setup is provided in Figure 69, while a schematic is presented in Figure 70.

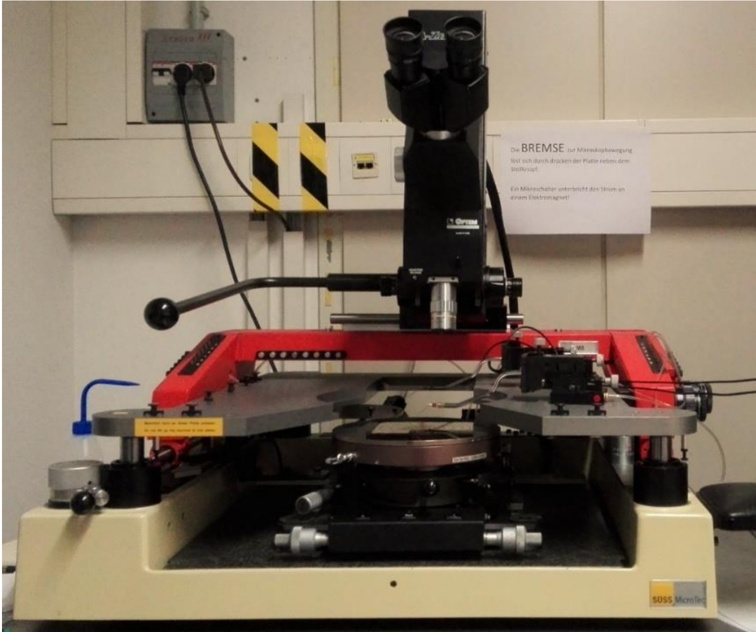

Figure 69: Optical photograph of the wafer probe station used for the LC and BD measurements.

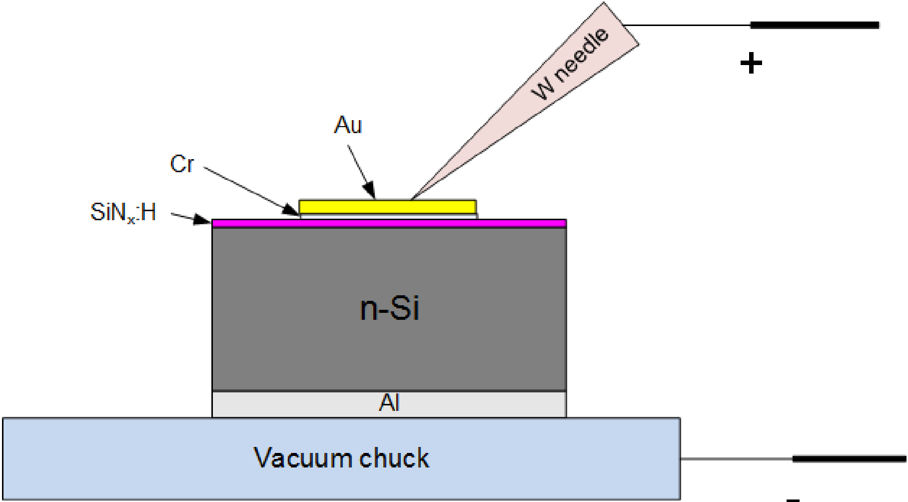

Figure 70: Cross-sectional schematic of the LC and BD measurement setup.

While the fundamental methodology of the leakage current and the dielectric breakdown measurements was largely the same (applying a voltage between the electrodes, and simultaneously recording the current flowing between them), there were also some important differences between the two types of experiments, as explained in the following:

The leakage current (LC) measurements were carried out using the largest (1000 µm diameter) contact pads, since this would provide a higher absolute current at the relatively low electrical fields, leading to a higher signal-to-noise ratio in contrast when using the smaller contact pads. Since the voltage drop across the substrate was neglected due to a parasitic resistance being in the range of 200 Ω, the field across the SiN_x dielectric thin film can be easily calculated as $E = V/d$, where d is the film thickness and V the applied voltage. The maximum applied field in the LC measurements was $E = 0.5$ MV/cm.

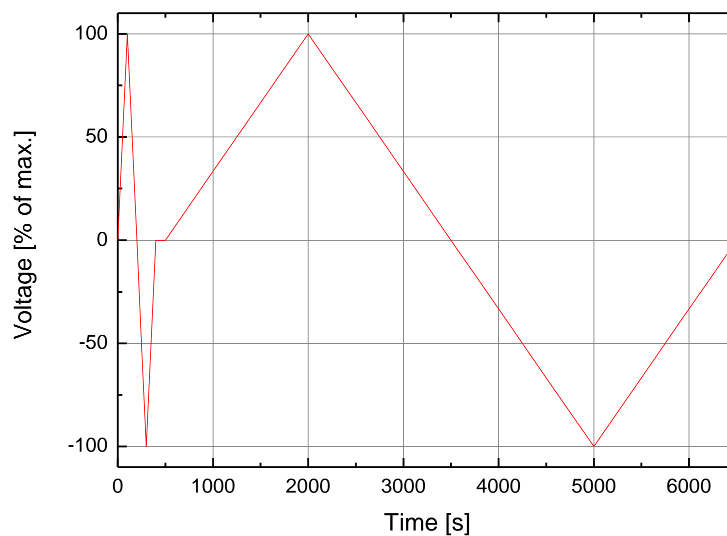

Figure 71: Standard load over time characteristics for the leakage current measurements.

A measurement routine consisting of two distinct regions was used in all cases (see Figure 71), whereas both regions included stepped voltage ramps. These ramps started from 0 V reaching to the maximum voltage in the positive bias direction (meaning that the top contact was brought to the highest potential), going back to 0 V, and then repeating the same pattern in the opposite, negative bias direction. The first, “stabilization” section – which was also used to filter out defective samples – consisted of voltage steps with an amplitude of 10% of the maximum voltage, and a hold time of 10 s for each step. In the second part, during the actual measurement, however, voltage steps of 2% with respect to the maximum voltage level were applied, accompanied by a hold time of 30 s, allowing the attenuation of transient currents and relaxation effects arising from the voltage jumps. In the standard measurement routine, this procedure was repeated for each sample at each temperature step from 25°C up to the maximum temperature of 300°C (with the intermediate measurement temperatures being: 60°C, 120°C, 180°C, and 240°C). The recorded data were analysed with respect to the

dependence of the leakage current on the applied electric field *E* and sample temperature *T*, in order to identify the physical mechanisms governing the leakage current through the thin films, and to quantify physical parameters such as the activation energy.

The dielectric breakdown (BD) measurements have been carried out using the same physical sample and probe configuration as used for the LC, with the only difference that in this case the circular pads with a diameter of 500 µm were used. The reasons for choosing samples of less diameter were the much higher applied electrical fields compared to the LC measurements, resulting in increased values of leakage current density (which increases the signal-to-noise ratio *SNR* even when using smaller contact pads) and the decreased probability of structural defects causing premature breakdown. The latter means that the breakdown can occur with higher probability at the intrinsic breakdown strength value of the material, assuming an equal density of structural defects, since the absolute number of structural defects is lower.

During these measurements, a time-zero measurement approach was implemented by applying a voltage ramp to the sample. It is important to note, that the voltage ramp was generally only applied in the positive bias direction, meaning in this configuration that a space-charge region did not form at the semiconductor-insulator interface. The source/measure unit was set to drive a voltage ramp from 0 V to its maximum output voltage (V_{max} = 200 V), or until a set compliance current limit (generally I_{limit} = 1 mA) of the leakage current was reached. The standard ramp speed was dV/dt = 500 mV/s, with a measurement taken at every voltage step of 80 mV. Given the generally destructive nature of the test, a set of about 20 samples have been measured at each temperature step. This measure helped in gaining a meaningful insight into the evolution of the leakage current at higher field strengths than during the LC measurements, and allowed a statistical evaluation of the maximum dielectric strength of the materials under test.

6.1.3. On the electrical conduction and dielectric breakdown in insulators

While an *ideal* insulator is characterized by having an electrical conductance of exactly zero [152], this assumption does not hold true for a *real* MIS (metal-insulator-semiconductor) capacitor. A certain degree of conduction, *i.e.* a transport of charge carriers through the insulating film is measurable, given a sufficiently high temperature *T* and electrical field *E*. This behaviour can be an effect of one or more of several distinct physical mechanisms, which are shortly explained in the following, while their dependence on the values of *T* and *V* are presented in Table 15.

Conduction mechanism	Full expression for current density	*V* and *T* dependence
Tunnel emission	$J \propto E_i^2 exp\left[-\frac{4\sqrt{2m^*}(q\Phi_B)^{3/2}}{3q\hbar E_i}\right]$	$J \propto V^2 exp\left(\frac{-b}{V}\right)$
Schottky emission	$J = A^{**}T^2 exp\left[\frac{-q\left(\Phi_B - \sqrt{qE_i/4\pi\varepsilon_i}\right)}{kT}\right]$	$J \propto T^2 exp\left[\frac{q}{kT}\left(a\sqrt{V} - \Phi_B\right)\right]$
Frenkel-Poole emission	$J \propto E_i exp\left[\frac{-q\left(\Phi_B - \sqrt{qE_i/\pi\varepsilon_i}\right)}{kT}\right]$	$J \propto V exp\left[\frac{q}{kT}\left(2a\sqrt{V} - \Phi_B\right)\right]$
Ohmic conduction	$J \propto E_i exp\left(\frac{-\Delta E_{ac}}{kT}\right)$	$J \propto V exp\left(\frac{-c}{T}\right)$
Ionic conduction	$J \propto \frac{E_i}{T} exp\left(\frac{-\Delta E_{ai}}{kT}\right)$	$J \propto \frac{V}{t} exp\left(\frac{-d'}{T}\right)$
Space-charge limited	$J = \frac{9\varepsilon_i \mu V^2}{8d^3}$	$J \propto V^2$

Table 15: Conduction mechanisms in insulators according to [152]. The symbols used in the expressions above are: A^{**} = the effective Richardson constant, Φ_B = barrier height, ε_i = permittivity of the insulator, E_i = electric field in the insulator, m^* = effective mass, d = thickness of the insulator, ΔE_{ac} = electron activation energy, ΔE_{ai} = ion activation energy, while a, b, c, and d' are constants.

When the electrical field *E* is very high (and generally the film thickness *d* very low), tunnel emission is often the dominant conduction mechanism. *Tunnelling* is a quantum mechanical phenomenon where the electron wave function penetrates through the potential barrier. This behaviour has a very strong dependence on the applied electrical field, but is from the pure theoretical point of view independent of temperature. In the case of direct tunnelling the charge carriers pass through the whole potential barrier, while in the case of *Fowler-Nordheim* [153] tunnelling only through a partial width of a barrier which is strongly bended by the external field.

The *Schottky emission* process occurs when the main source of carrier transport is the thermionic emission of electrons over the insulator-semiconductor barrier [154]. When plotting $ln(J/T^2)$ over $1/T$, a straight line in principal indicates by the sign of Schottky emission which charge transport mechanism dominates through the insulator. In the case of *Frenkel-Poole emission*[155], trapped electrons are emitted into the conduction band by means of thermal excitation. The barrier height in this case is the depth of the potential well associated with the trap. *Ohmic conduction* [152] can dominate at relatively low fields and high temperatures, where thermally excited electrons are transported by hopping form one isolated state to another. The leakage current characteristics are exponentially dependent on temperature *T*.

Ionic conduction processes [156] have a very characteristic dynamic that can be observed when applying a stationary electric field. Since ions generally cannot be injected or extracted from the

insulator, positive and negative charges will accumulate at the interfaces after loading with a DC voltage. This manifests itself in the gradual decrease of the initially high apparent conductivity through the insulator layer. Additionally, remaining internal fields can lead to charges flowing back once the external excitation is removed, visible as hysteresis in the *I-V* characteristics. Space-charge-limited conduction [157] is a result of carriers being injected into either a semiconductor that is lightly doped, or an insulator, without the presence of compensating charges. In a unipolar, trap-free setup, the current is proportional to V^2, since in insulators, the mobility μ is usually very low, this conduction mechanism is typically not dominating.

The *dielectric breakdown strength* is an important parameter when assessing the performance and quality of thin insulating films, and is a common concern for device reliability reasons. Thus, it is critically important to provide a most detailed explanation of the mechanisms taking place during breakdown. As it is presented above, at elevated temperatures and sufficiently high electric fields, leakage current flows through a real insulator. Under these circumstances energetic carriers contribute to the formation of structural defects in the bulk of the insulator film. Once the density of these defects reaches a critical level, a non-reversible event called *catastrophic breakdown* will occur. A common, microscopic-level explanation offered for this behaviour is the so-called *percolation theory*. This theory assumes a random distribution of the structural defects generated by the energetic carriers passing through the dielectric thin film [158]. As soon as the density of the defects is high enough to form a continuous string through the insulator also known as the percolation path, an effective conduction path is created [159] leading to the catastrophic, irreversible breakdown of the insulator. In addition, thermally generated instabilities generally reduce the dielectric breakdown strength of materials at elevated temperatures [151].

The statistical nature of probability of breakdown events does not only necessitate a sufficient number of samples to be measured for meaningful results, but also an ample statistical method for evaluating the measured values. This work uses a method based on the work of W. Weibull [160], applied for the evaluation of dielectric breakdown strength of thin films, similar to [161]. The cumulative failure distribution function *F* provides the percentage of failure (breakdown) events at a given field *E*.

In the following sections, the LC and BD measurement results accompanied by their analysis and the conclusions drawn from those will be presented for each individual investigated SiN_x thin film type [152].

6.2. ICP-CVD deposited a-SiN_x:H thin films

As already mentioned above, leakage current and dielectric breakdown measurements have been carried out on four different types of ICP-CVD deposited silicon nitride thin films, which have been selected based on the results presented in Chapter 3. The nominal film thickness in these tests was typically 100 nm. In the following, the findings gained from each individual type will be presented and discussed.

6.2.1. *Type I* films

The measured typical leakage current characteristics for *Type I* a-SiN_x:H thin films are displayed in Figure 72. There are two remarkable features of the *J-E* characteristics that are worth mentioning, as they deviate significantly from the expected behaviour as given in [151] and [162] for a MIS (metal-insulator-semiconductor) capacitor with a silicon nitride insulating layer.

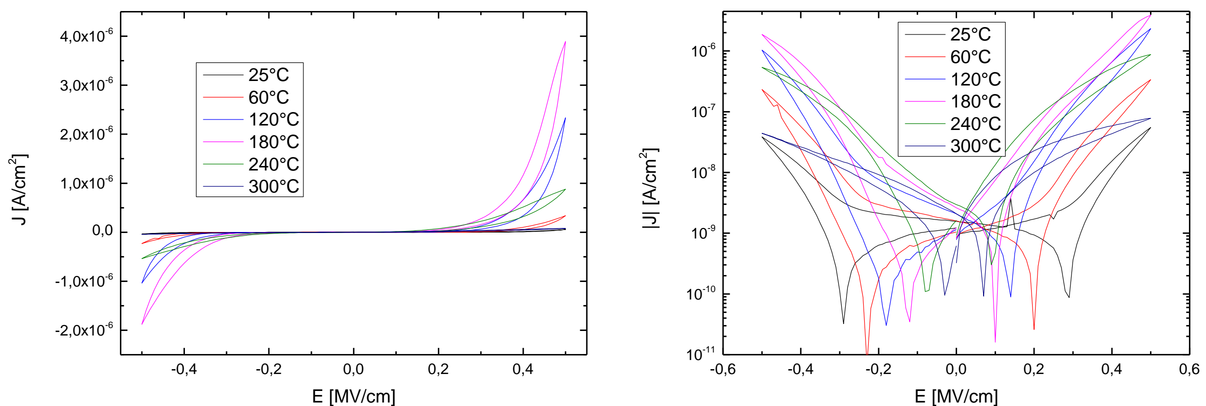

Figure 72: Leakage current density characteristics of a Type I ICP-CVD a-SiN_x:H sample recorded between 25°C and 300°C.

First, field hysteresis occurs as a significant discrepancy between the recorded leakage current values when increasing and decreasing the load voltage gradually, as illustrated in Figure 72. This is accompanied by the shift of the zero-transition point to the negative or positive bias direction depending whether the load was increasing or decreasing during that part of the measurement routine (see Figure 72). While the physical cause for this phenomenon remains to be discussed further below, the technical reason becomes apparent when the measurement is recorded: each voltage step is accompanied by an abrupt change in the leakage current in the corresponding direction, but is followed by a quasi-exponential decay of the signal towards an equilibrium value, during the 30 seconds of hold time (see Figure 73). The amplitude of this decay can be comparable to or even exceed that of the amplitude resulting from the voltage jump. Since the presented leakage current values are

averaged values over the complete hold time of each individual voltage step, the results can exhibit a strong dependence on the direction of the load voltage ramp.

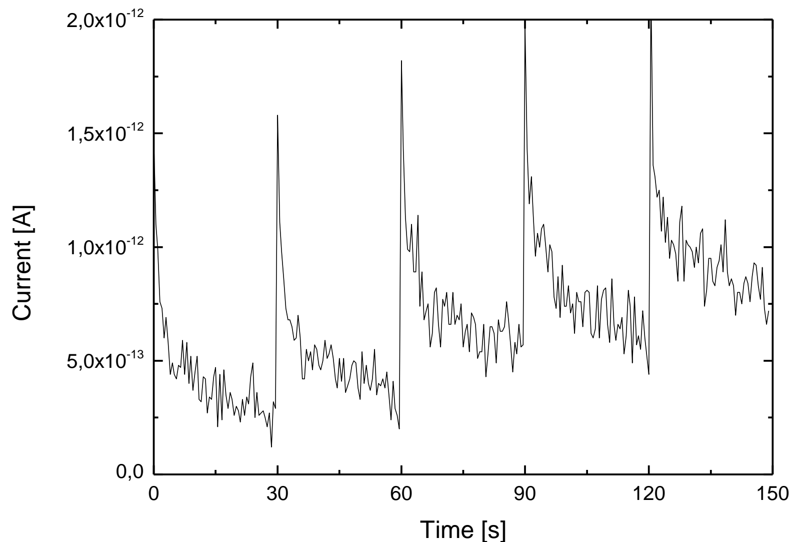

Figure 73: Transients of the leakage current when changing the load voltage levels.

The second anomaly is related to the temperature-dependence of the leakage current characteristics. While from 25°C to 120°C, the leakage current increases at comparable electric field values in accordance with the expectations, increasing the temperature to 180°C and above does not have the same effect (see Figure 72). In contrast, the increase in temperature above $T = 180°C$ is accompanied by the opposite effect: a significant decrease of the leakage current, reaching almost room temperature levels at $T = 300°C$. As an example, the film resistivity values are 10^{13} Ω·cm, $2{\cdot}10^{11}$ Ω·cm, and $5{\cdot}10^{12}$ Ω·cm at $T = 25°C$, 180°C, and 300°C at an electric field of 0.5 MV/cm, respectively. This is indeed in contrary to the expectations from the simple models of physical conduction mechanisms through insulating materials, presented in section 6.1.3.

This unexpected behaviour especially regarding the impact of elevated temperatures on the leakage current characteristics raises a few questions. First, the fact whether or not the occurrence is repeatable using the same sample when measuring multiple times would provide essential information about the physical mechanisms behind this observation. With the intention of answering this question, the initial, now "annealed" samples were subjected to the measurement routine for a second time, again successively from 25°C up to 300°C. The results were found to be vastly different from the initial characteristics obtained when measuring the "as deposited" samples (see Figure 74). For the entirety of the considered temperature range, the measured leakage current values were by orders of magnitude lower than during the first measurement routine, while the leakage current density

basically increased with increasing temperature. These observations indicate that during the first-time measurements of *Type I* ICP-CVD silicon nitride samples at elevated temperatures above 120°C irreversible changes occur that are readily reflected in the leakage current characteristics. Now, film resistivity values for the annealed samples are $5 \cdot 10^{14}$ Ω·cm, $5 \cdot 10^{14}$ Ω·cm, and $5 \cdot 10^{12}$ Ω·cm, for the lowest temperature $T = 25$°C, the turning point 180°C, and the maximum measurement temperature 300°C at an electric field of 0.5 MV/cm, respectively. These findings suggest that the elevated temperatures and/or the applied electric load induce modifications in the material. This hypothesis draws an interesting parallel with the *Type I* ICP-CVD silicon nitride material's apparent instability with respect to film stress (see Chapter 4), however it needs extensive further investigations.

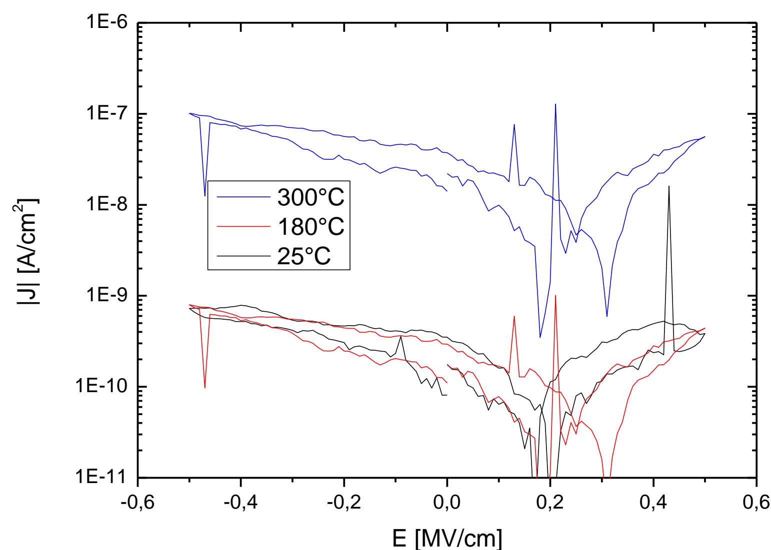

Figure 74: Typical leakage current density characteristics between T = 25°C and T = 300°C of a Type I ICP-CVD a-SiN$_x$:H sample after exposure to elevated temperatures up to 300°C in air.

First of all, the possible influence of an external factor, such as ambient light, needs to be addressed. Ultraviolet (UV) light can potentially generate carriers inside the device under test [163], thus affecting the measurement results. For this reason, two different measurements, both only at room temperature (25°C, in order to somewhat suppress the strongly temperature-dependent carrier generation processes.) have been performed, where one of the samples was subjected to ultraviolet light from a table-top photolithographic illumination source for a duration of five minutes, while the reference sample was kept under standard conditions, meaning under light shielded conditions. Since the measured values (not shown) indicate within the measurement accuracy that leakage current characteristics were not affected by the ultraviolet light irradiation, this factor can be safely ruled out.

Sources for inducing the non-reversible shift in the leakage current behaviour of *Type I* ICP-CVD silicon nitride thin films may be due to the repeated electrical load that the material exposed to

during the measurements, as well as the thermal load from the actual and even the previous measurement cycles performed at increasing temperature levels. In order to prove this assumption, a second set of experiments have been carried out, where three subsequent full leakage current measurement cycles were taken at each temperature step starting from 25°C up to 300°C. For each temperature step, a new measurement pad was used, thus each sample has experienced the electric load cycle three times. The pads, however, were located on a singular die, thus the samples measured at the later stages of the experiment have been subjected to the thermal loading arising from the prior temperature steps. An example of the described three-cycle leakage current measurement (taken at T =60°C) is presented below in Figure 75. (For the rest of the available data, see Appendix D).

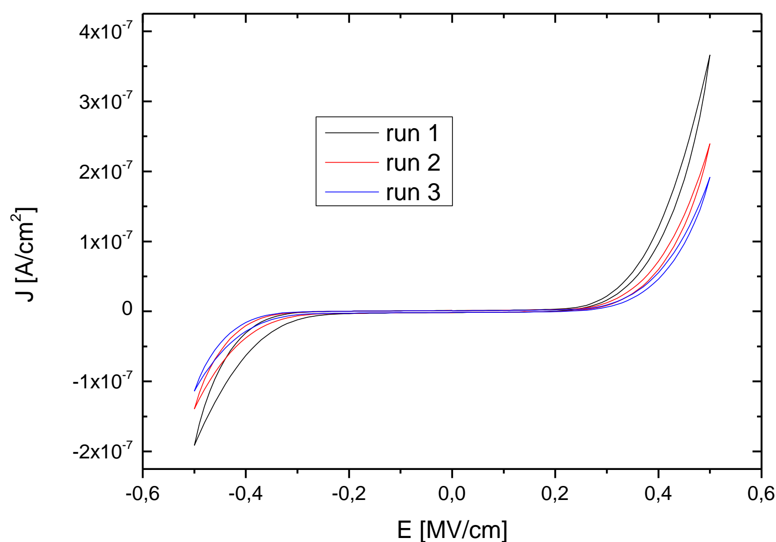

Figure 75: Evolution of leakage current characteristics of Type I ICP-CVD deposited a-SiN$_x$:H samples. The measurements have been cyclically repeated 3 times at T = 60°C.

Apparently – even at relatively low temperatures, where the results of the original experiments did not significantly deviate from the expectation (i.e. a quasi-exponential increase of the leakage current density with the temperature) – the repetition of the measurement cycle affects the recorded leakage current characteristics. As it is illustrated, with each subsequent iteration, the measured leakage current density decreases over the whole range of applied voltages.

Additionally, as illustrated in Figure 76, the variation between the maximum leakage current values recorded during the three subsequent measurement cycles at each temperature step became increasingly larger when increasing the temperature. Therefore, it is reasonable to assume that during the measurements at elevated temperatures, the impact of electrical and thermal load causes the irreversible reduction in conductivity of the silicon nitride thin film. The results also clarified one further issue: The present test method (partly due to the cumulative thermal load on the samples),

however, does not provide a suitable approach to separate the influence of these two parameters for a more precise analysis.

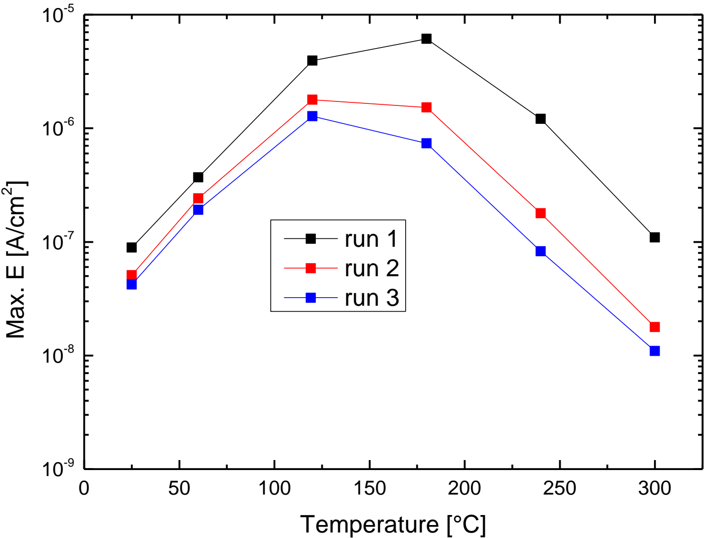

Figure 76: Maximal leakage current values measured at E = 0.5 MV/cm of Type I ICP-CVD deposited a-SiN_x:H samples. The graph shows the dependence and evolution of the leakage current on the measurement temperature and repetition count at the respective temperature.

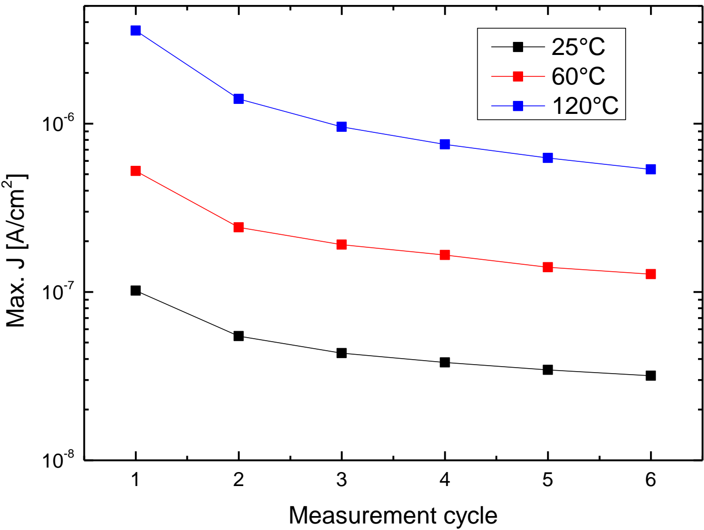

Figure 77: Evolution of the maximum leakage current measured at E = 0.5 MV/cm of Type I ICP-CVD a-SiN_x:H samples at different temperatures as a function of the measurement cycle.

In order to mitigate some of the parasitic issues outlined above, the next experiments utilized a slightly different, improved method. Here - with the goal of minimizing the impact of the elevated temperatures – the maximal measurement temperature was limited to 120°C since the hysteresis

effect was found to start dominating at temperatures above, while the samples for each temperature were kept on different dies, allowing to investigate the effect of the pure cyclical electrical field load. The samples have been put through six consecutive measurement cycles, whereas the results are summarized in Figure 77.

As the results show, even at room temperature there is still a significant decrease by a factor of 3 of the maximum leakage current value after six measurement cycles. Furthermore, the change of the maximal leakage current (each at E = 0.5 MV/cm) between consecutive measurement cycles does increase with increasing temperature, suggesting that the influence of the thermal load cannot be decoupled from the experiments in its entirety.

In order to obtain additional information about the transient behaviour in leakage current of *Type I* ICP-CVD silicon nitride thin film samples, a set of samples were subjected to constant field load at different temperatures. The test procedure started by placing the sample on the pre-heated chuck. Given the relatively small nominal thickness of the samples, the actual temperature value converged to the equilibrium temperature within a minute. Thus, after that amount of time, the leakage current through the samples was monitored and recorded for a duration of 1 hour. The resulting graphs are illustrated in Figure 78.

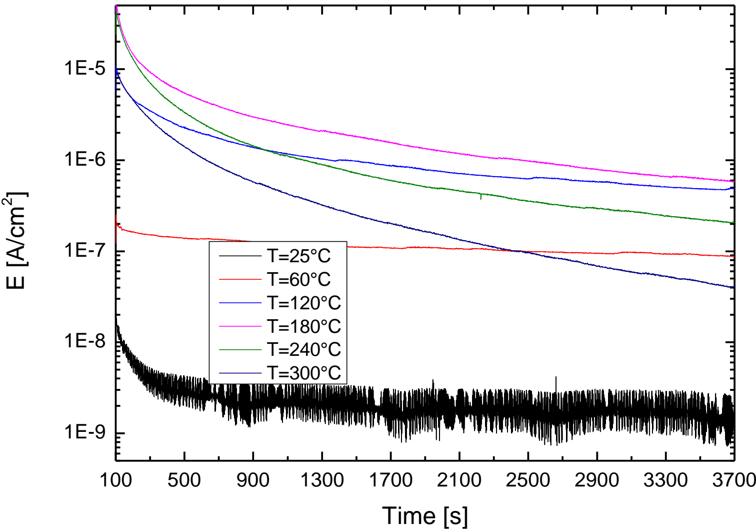

Figure 78: Leakage current through a 100 nm thin Type I ICP-CVD a-SiN$_x$:H sample under a constant load of E = 0.5 MV/cm at temperatures ranging from T = 25°C to 300°C.

The results are in accordance with the results gained so far, and serve to illustrate the three main characteristic points about the leakage current behaviour of the *Type I* ICP-CVD silicon nitride. The first is the maximum leakage current increasing with the temperature up to a critical temperature

level being in this case at 180°C, but decreasing above. The second feature is the presence of a remarkable decay of the leakage current as a function of time independent of temperature. The third is the significant temperature-dependence of this transient behaviour, as with increasing temperature the decay curves become increasingly steeper.

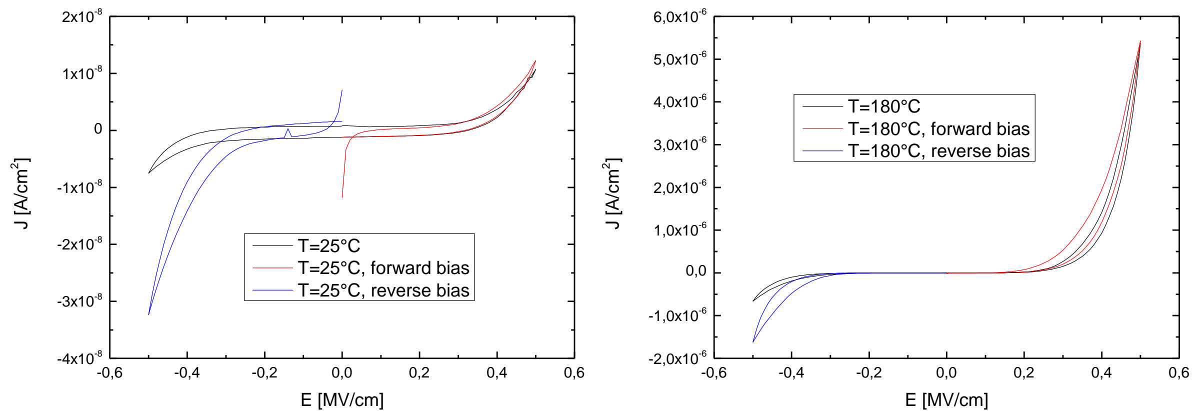

Figure 79: The dependence of the leakage current characteristics of a Type I ICP-CVD a-SiN$_x$:H sample as a function of the bias direction it was first measured. The measurements were performed at T = 25°C (left side) and T = 125°C (right side).

A further point to discuss is the apparent asymmetry on the leakage current characteristics in the first measurement cycle when being biased in forward and in reverse direction. In order to assess the source for this behaviour of the *Type I* ICP-CVD silicon nitride, some additional measurements have been carried out. Figure 79 compares the results of the default measurement cycle with those of two truncated measurements, where only forward, or alternatively only reverse bias was applied at T = 25°C and T = 180°C, respectively. As clearly displayed by both figures, the measured leakage current curves under reverse bias in the default measurement cycle have been significantly influenced by the other half of the measurement cycle performed directly in advance. Considering the factor of leakage current decay under constant field load as presented above, this is an expected behaviour. On the other hand, even after cancelling out the effect of time-dependent leakage current decay, a significant degree of remnant asymmetry is still observed at elevated temperatures (see Figure 79).

Current-voltage characteristics recorded during the time-zero dielectric breakdown (BD) tests at different temperatures are provided in Figure 80. In a similar fashion to the "as deposited" leakage current characteristics, the BD curves have proven to be very significantly affected by the measurement temperature. At low temperatures (i.e. 25°C and 60°C), the current flowing through the insulator also shows a monotonous increase with increasing voltage, although with regimes having different slopes that can be associated with different dominating conduction mechanisms, until finally breakdown occurs.

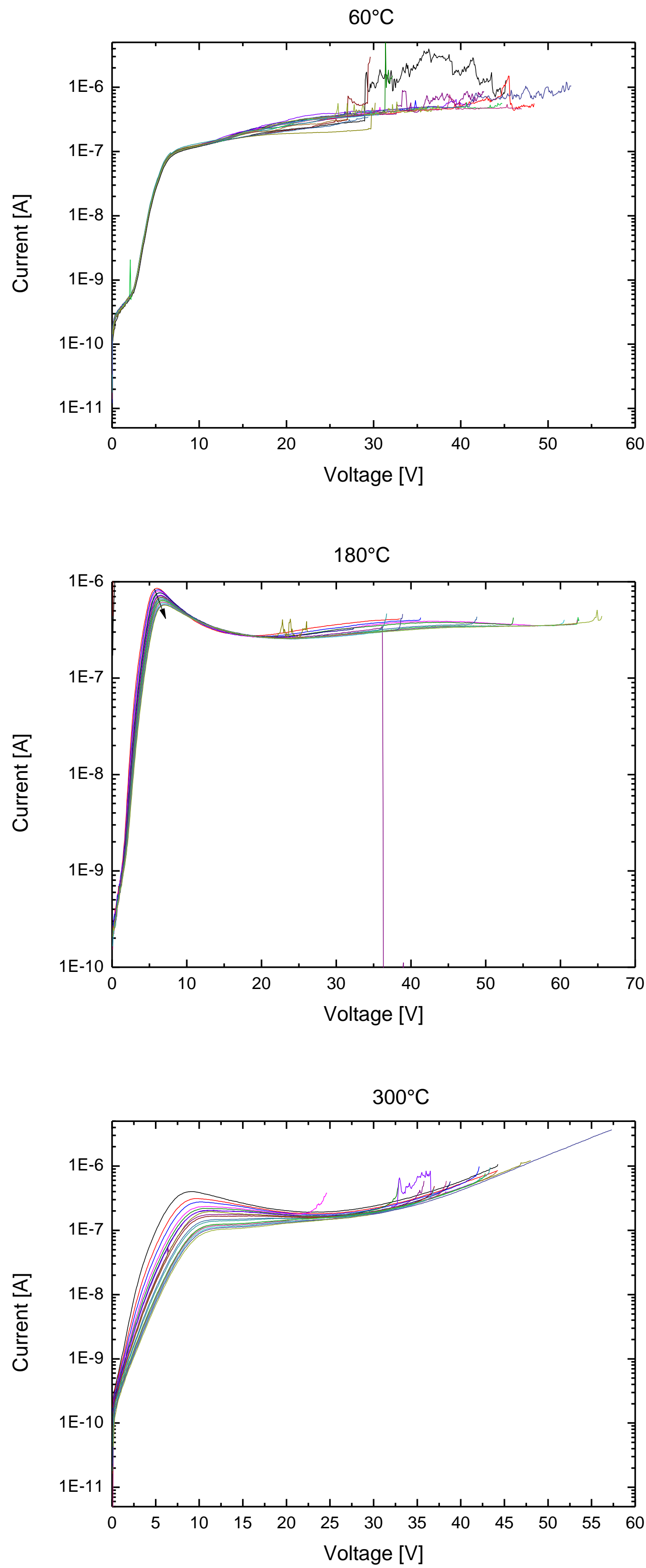

Figure 80: Typical breakdown characteristics of "as deposited" Type I ICP-CVD a-SiN_x:H samples measured at different temperatures using 500 µm diameter pads. The curves at each temperature level have been recorded in direct sequence to each other.

Increasing the measurement temperature to 120°C and above has a profound effect, as a bulge in the characteristics appears, resulting in the decrease of the leakage current while increasing the load voltage (see the second and third graph in Figure 80). The appearance of this negative differential resistance regime is more than unexpected from a passive MIS device, and is indicative of *in-situ* modifications of the insulating material during the measurement cycle especially at elevated temperatures.

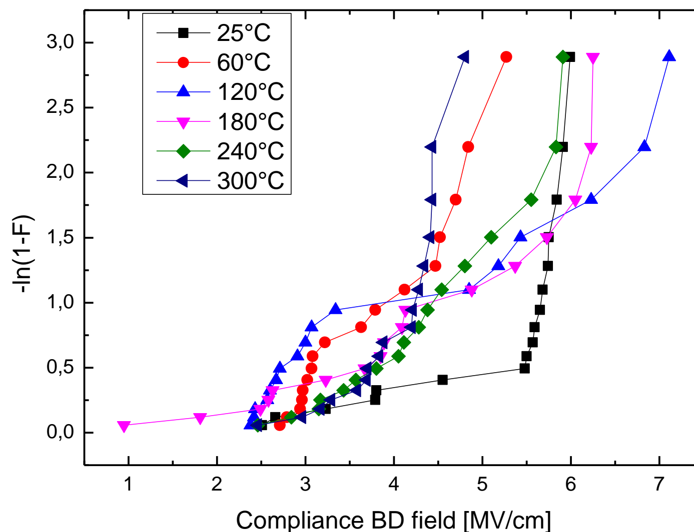

Figure 81: Weibull plot showing the breakdown strength of "as deposited" 100 nm thin Type I ICP-CVD a-SiN_x:H films.

Another important observation is that both the position of this local maximum in the current-voltage characteristics, as well as its absolute value and the shape of the "bulge" characteristics in the vicinity are modified with changing the measurement temperature or subjecting the samples to the same temperature for increased durations. Analysis of the recorded *I-V* curves reveals the following: the curve shapes of the consecutively measured samples shift in a coherent way, by lowering the value of the local maximum, and shifting it to higher voltages. This transformation can only be induced by the thermal load the samples have been subjected to, since during the BD measurements each MIS capacitor is measured only once, yet the shape of the "bulge" changes from sample to sample with a clear trend. Comparison of the results at a measurement temperature of 180°C and the curves recoded at 300°C shows that the latter exhibit a far more prominent change between the first and the last recorded *I-V* curves in a comparable timeframe. This confirms that at higher temperatures the impact of the thermal load is larger and that it becomes apparent more quickly. Altogether it can be stated that in both cases the successively measured *I-V* curves are asymptotically approaching an "ideal" *I-V* characteristics without a local maximum, and thus regimes without negative differential resistance.

The breakdown field values representing the field at which –according to the criterion used in this thesis–the leakage current reaches the compliance of the measurement equipment are summarized in a Weibull-plots at different temperature levels (see Figure 81). Straightforward expectations according to basic theory [151, 164] would predict that the breakdown strength of the material would decrease with increasing temperature, what is only partially true for the samples investigated. While at room temperature the intrinsic breakdown strength appears to be about 6 MV/cm, increasing the temperature to 60°C results in a decrease to approximately 5.3 MV/cm. At T = 120°C this figure increases again to 7.1 MV/cm followed by a steady decrease at higher temperatures, eventually reaching 4.9 MV/cm at 300°C. It is also important to note that the criterion used in this study to determine the breakdown strength of the silicon nitride thin film samples is not necessarily equivalent with the maximum dielectric strength in the referred publications due to different BD criterions being used by various sources.

A straightforward explanation for the observed irregularities of the BD *I-V* characteristics as well as the low-field LC behaviour is due to the abundance of hydrogen in *Type I* ICP-CVD deposited a-SiN_x:H thin films (see Chapter 4). As the high-temperature effusion measurements have shown, at temperatures higher than the deposition temperature (typically 350°C), substantial amounts of atomic and molecular hydrogen start to escape out of the thin film. Therefore, the presence of a significant amount of H^+ ions in the *Type I* silicon nitride thin film sample can be assumed. These H^+ ions are indeed influenced by both the external field and the measurement temperature. When an external field is applied, they will be drawn to the cathode, and with increasing temperature, the mobility and diffusion coefficient of the ions increase accordingly. This leads to an increased contribution from ionic conduction to the total leakage current at elevated temperatures.

On the other hand, unlike electrons that can be reintroduced through the electrodes, the amount of H^+ ions available in the sample is limited. As time progresses, through drift and diffusion more and more H^+ ions reach the cathode-insulator interface, or get trapped at negatively charged defect states, and are lost for current transport. This leads to a reduction of the leakage current over time, despite the increasing electrical load. The loss of some of these charge carriers over time at elevated temperatures due to diffusion also explains the successively lower absolute value of the local maximum in the BD *I-V* characteristics. Additionally, the difference in the total charge (which is proportional to the area under the *I-V* curve) between two successive measurements at the same temperature increases at higher temperatures, since more H^+ ions are lost due to diffusion to the interface in the same time interval. These assumptions also indicate why the local leakage current maximum is observed at lower field values when enhancing the temperature: this phenomenon dependent mostly only on the elapsed time, rather than on the electrical field load.

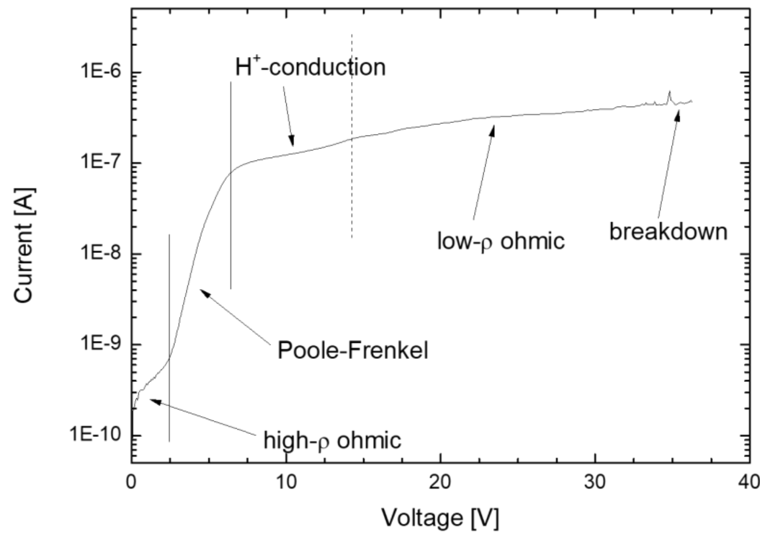

Figure 82: Voltage sections leading to different dominating conduction mechanisms in "as deposited" Type I SiN_x:H thin films.

Given this model, one can identify different field ranges in the BD current-voltage characteristics, which are dominated by different conduction mechanisms (see e.g. measurements at 60°C and 180°C in Figure 80). It is important to note, however, that the exact values greatly depend on different parameters, such as the film thickness, measurement temperature, and ramp speed (see further below). The general behaviour is illustrated in Figure 82. At very low loads ($V < 5$ V), ohmic conduction is dominating, while under higher bias conditions (5 V < V < 10 V), Poole-Frenkel emission dominates indicated by an exponential increase of the current, before going into saturation. At even higher electric field loads the conduction via H^+ ions takes over, characterized by a load voltage which has almost no impact on the leakage current. Further increasing the load leads either to a catastrophic breakdown, or the further increase of the leakage current in linear proportion to the load voltage, suggesting that ohmic conduction through the modified sample is the dominating conduction mechanism. This diffusion model of H^+ ions through the *Type I* silicon nitride thin film samples at elevated temperatures offers an explanation for the very specific leakage-current characteristics even at low electric fields. During the standard measurement routine, at elevated temperatures, H+ ions present in the sample contribute more and more to the leakage current, but are also bounded to negatively charged trap states and at the interfaces.

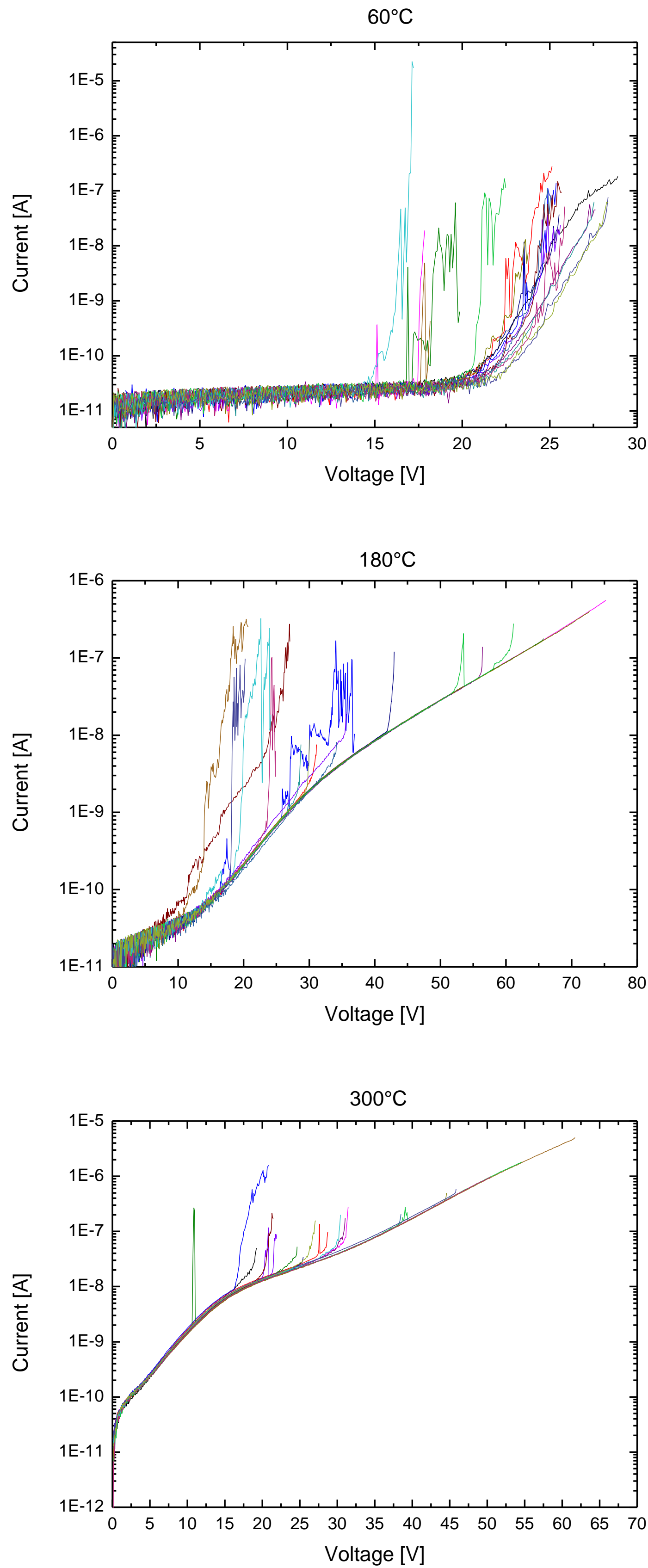

Figure 83: Typical breakdown characteristics of 100 nm thin Type I ICP-CVD a-SiN$_x$:H after exposure to temperatures up to 300°C using pads of 500 µm diameter. The individual samples at each temperature have been measured in direct sequence to each other.

At low field values of $E < 0.5$ MV/cm, the first effect increases the leakage current significantly up to 180 C, but at higher temperatures the second effect becomes more relevant. As fewer ions are available, the leakage current drops, despite the increasing temperature. The loss of mobile H^+ ions over time at elevated temperatures and under electrical load due to diffusion and drift effects also explains the apparent asymmetry between the positive and negative bias sides of the LC characteristics, as well as the different current fall-off curves (see Figure 78) under constant load at different temperatures.

Since the leakage current measurements have shown a very significant difference between the performances of "as deposited" and "annealed" *Type I* ICP-CVD silicon nitride samples, the dielectric breakdown tests have been repeated, this time using samples that have been exposed to thermal loadings up to 300°C before characterization. The corresponding current-voltage characteristics are presented in Figure 83. Comparing these with those from "as deposited" samples given in Figure 80, it is immediately apparent that the conduction mechanisms of *Type I* samples drastically changed after exposing the material to such elevated temperatures. In the case of "annealed" samples, none of the specific characteristics described above are present. The *I-V* curves have a monotonously increasing slope without any local maxima, until the point of a catastrophic breakdown. Subsequent measurement curves at the same (elevated) temperatures do not show any shift when comparing both characteristics. This is attributed due to the absence of mobile H^+ ions in the samples after being subjected to elevated temperature for an extended period of time.

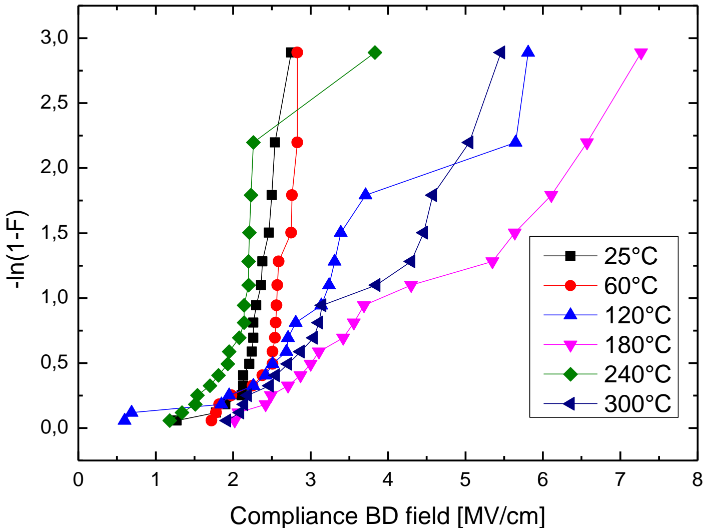

Figure 84: Weibull plot showing the breakdown strength of "annealed" (@ 300°C) 100 nm thin Type I ICP-CVD a-SiN_x:H films.

As illustrated by the Weibull-plot, presented in Figure 84, the breakdown strength of the *Type I* ICP-CVD silicon nitride material has not improved significantly after thermal loading. Generally, it can be stated that there is no clear trend of the intrinsic breakdown strength changing in either direction upon increasing the measurement temperature. While some sample sets (at the temperatures of *T* = 120°C, 180°C, and 300°C) are characterized by higher apparent dielectric strengths between 5 and 7 MV/cm, others (at 25°C, 60°V, and 240°C) only reach significantly lower values of 3-4 MV/cm. On the other hand, it is important to note that at a higher measurement temperature and at a given electric field value the leakage current will indeed increase, as given by the measurement results shown in Figure 83. At this point it cannot be confidently stated if the generally low measured dielectric strength of the samples at some temperature levels actually corresponds to their respective intrinsic breakdown strength, or alternatively is a statistical anomaly due to the low sample size and a high occurrence of early failures.

The findings of the additional dielectric breakdown measurements performed at 50 nm and 300 nm thin samples are in accordance with the theory based on the results of the 100 nm thin samples. Both the thinner and the thicker samples feature a local maximum in their respective current-voltage characteristics at elevated temperatures (see supplementary figures in Appendix E). The position and the magnitude of the local maximum is subject to the same influences as it was in the case of the 100 nm thin samples, despite quantitative differences stemming from the different length of diffusion paths in films having different thickness values.

The apparent dielectric breakdown strength of “as deposited” 50 nm thin *Type I* samples is in the range of 5-6 MV/cm, without any clear dependence on the measurement temperature. This is due to the thermally induced diffusion process of the H^+ ions taking place during the measurements, leading to a continuous modification of the material under test. In the case of the annealed 50 nm samples on the other hand, an effect if the measurement temperature is clearly observed, as the apparent breakdown strength shows a significant decrease from about 7 MV/cm to approximately 5 MV/cm, when increasing the measurement temperature from 25°C to 300°C.

The ability to determine the breakdown strength of 300 nm thin *Type I* silicon nitride samples is greatly limited by the maximum output voltage of the equipment (200 V). It appears, that even at 300°C, some samples do not reach the point of catastrophic breakdown, thus only a lower estimate of this parameter at about 6.7 MV/cm can be given. It is noteworthy though, that most early failures happen in the range of 4-5 MV/cm independent of the temperature level.

One further notable aspect of the dielectric breakdown tests is the extensive mechanical damage that often accompanies the event of a catastrophic breakdown. Figure 85 below serves as a telling illustration of the phenomenon. As it is clearly visible in the scanning electron micrographs, the

front-side electrode pad was locally destroyed, and delaminated from the substrate. This results in the disruption of the continuity and delamination of both the dielectric thin film and the front-side metallization, and is most probably caused by the localized extreme current and field densities at the point of catastrophic breakdown inducing a significant rise in the local temperature, and hence, large temperature gradients.

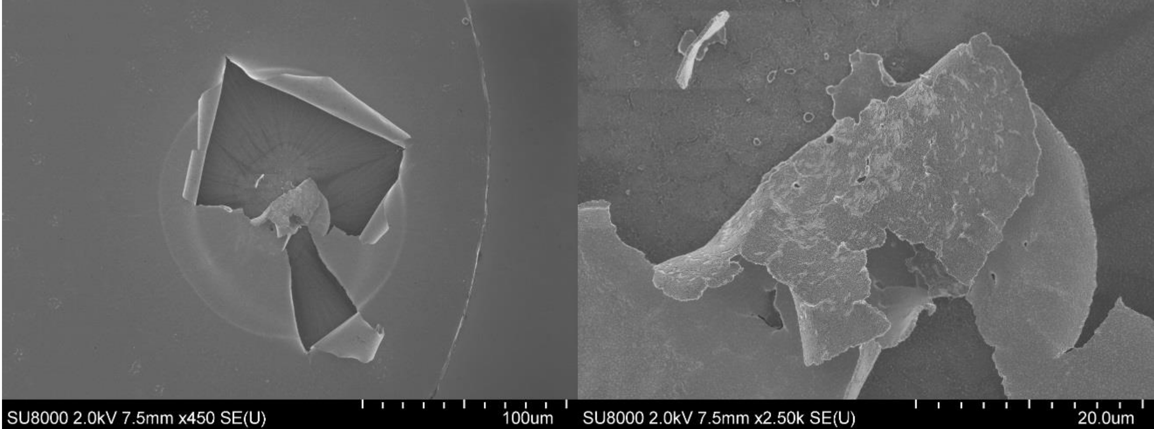

Figure 85: Scanning electron micrographs showing the effect of catastrophic breakdown on an MIS sample with an ICP-CVD deposited a-SiN_x:H dielectric layer. The images are representative to the catastrophic breakdown of all sample types.

Moreover, as it is displayed in Figure 86, it can also be noted that the delamination does not appear to be separating the silicon nitride insulator film from either the bulk silicon substrate or the front-side metallization. The failure plane, however, is found inside the dielectric, as the electron micrographs illustrate, since both the delaminated and the remaining surfaces are characterized by the same distinct microstructure (as presented on the bottom of the rolled-up electrode on the left, and on the substrate on the right). This microstructure strongly differs from that of the typical metallic front-side electrode visible on the left upper part of the right-hand side picture.

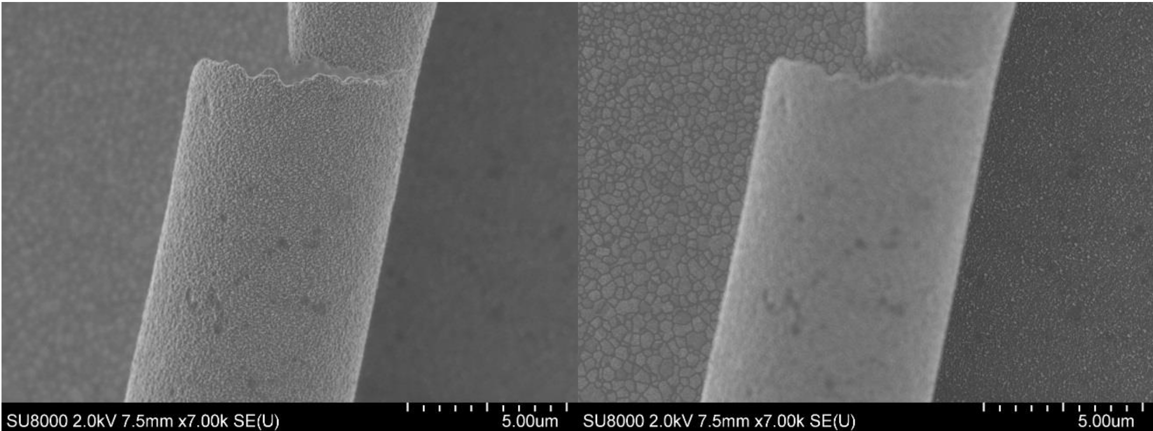

Figure 86: Scanning electron micrographs displaying a detailed view on the effect of catastrophic breakdown.

An additional test has been performed in order to evaluate the dynamic behaviour of the *Type I* ICP-CVD silicon nitride dielectric thin films during the time-dependent dielectric breakdown measurements. The effect of changing the ramp speed on the current-voltage characteristics has been studied. This was done to assess the possible influence of the ramp speed in the occurrence and characteristics of the local maximum “bulge” in leakage current curve. Figure 87 shows current-voltage characteristics of 100 nm thin *Type I* samples recorded at a measurement temperature of 180°C. The only factor that is different between the individual samples is the ramp speed, which has been varied in a wide range from 5 to 500 mV/s.

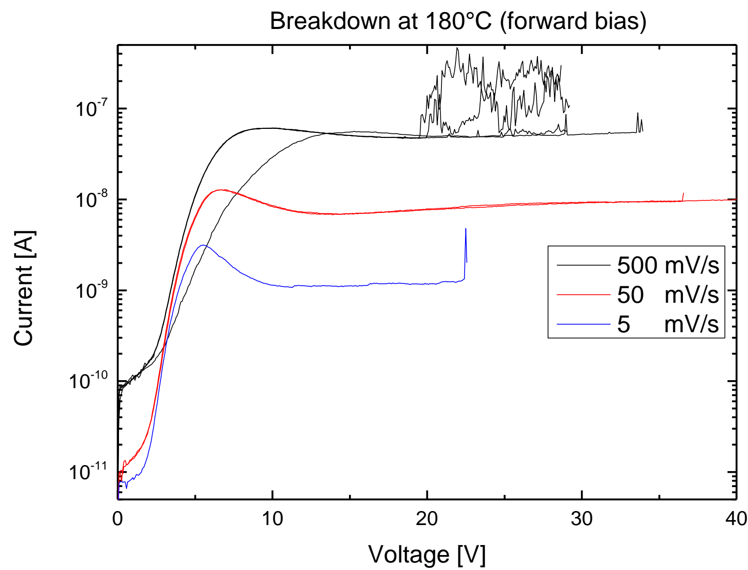

Figure 87: Impact of ramp speed between 5 mV/s and 500 mV/s on the characteristic BD curve of Type I ICP-CVD a-SiN$_x$:H thin film samples in the time-zero dielectric breakdown test with a pad diameter of 500 µm.

As the graph clearly presents, there is a rather significant influence of the ramp speed, regarding both the local maxima and the overall characteristics. While the main qualitative features of the current-voltage curves remain unaffected at all three ramp speeds, there are strong quantitative differences pointing in the same direction. With increasing ramp speed, the leakage current increases significantly over almost the whole voltage range, and in an interesting way approximately proportionally to the increase in ramp speed itself. Additionally, the position of the local peak shifts to higher voltage values, and the peak height decreases with increasing ramp speed. This behaviour, consisting of a substantial increase of leakage current with rapidly changing electrical load, correlates indeed with the previously observed transient effects in the leakage current measurements. These are also most likely to be responsible for the apparent difference in leakage current values at comparable conditions between the LC and BD measurements (cf. the effective ramp speed of ≈3 mV/s during the LC tests).

6.2.2 *Type II* films

In contrast to *Type I* samples, *Type II* ICD-CVD silicon nitride shows significantly different leakage current characteristics, as presented in Figure 88. The samples are characterized both by a highly asymmetric *J-E* characteristics depending on the direction of the loading bias, and by relatively low resistivity values, especially under forward bias, when compared to standard resistivity values of silicon nitride [165] ranging up to 10^{16} Ω·cm, as well as *Type I* samples having values of around 10^{13} Ω·cm at room temperature. As a consequence, this low film resistivity resulted in leakage current density values being high enough at elevated temperatures to cause self-heating. This, in turn, gave rise to events of catastrophic breakdown even at moderate electric field values when performing leakage current measurements, rendering those impractical. Thus, leakage current measurements of *Type II* ICP-CVD silicon nitride thin films above a temperature of 120°C were not possible.

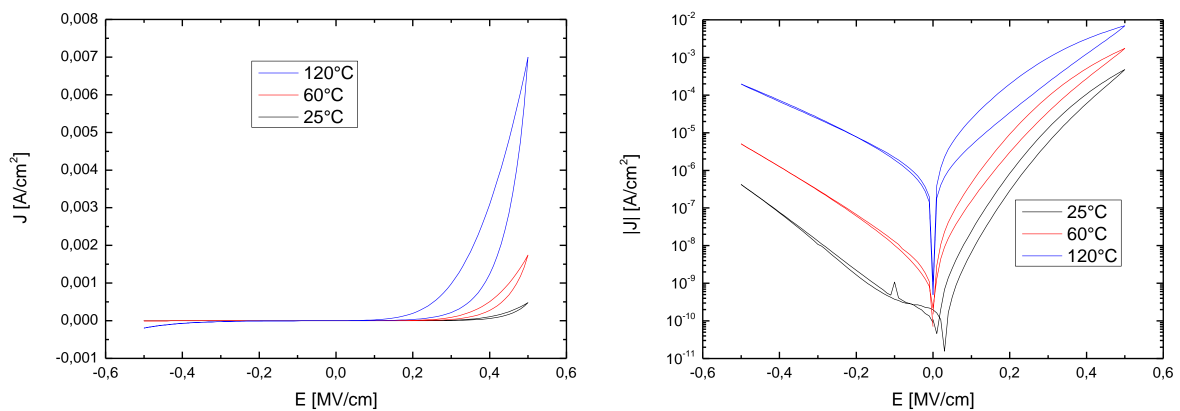

Figure 88: Leakage current density characteristics of a 100 nm thin Type II ICP-CVD a-SiN_x:H sample between T = 25°C and 120°C, on a linear (left) and semi-logarithmic (right) scale

The asymmetry of the leakage current at $E = 0.5$ MV/cm between both load directions can amount at room temperature to a factor of over 1000 decreasing to approximately 35 at 120°C. Additionally, in strong contrast to the *Type I* samples, no evidence of an annealing or other hysteresis effect similar to those documented in the case of *Type I* samples was found. This leads to the conclusion that the morphology and chemical composition of *Type II* samples does not change given the measurement conditions.

Regarding the dielectric breakdown performance of the MIS devices with a *Type II* ICP-CVD silicon nitride dielectric, it is reasonable to assume that at least some of the characteristics that were present in the leakage current measurements are present at higher electric loading conditions as well.

Due to the lack of a distinct point where the current through the insulator increased in an abrupt manner both in forward and in reverse direction, the criterion for stopping the measurement were revised, and the compliant limit was raised to 0.1 A. This allowed for a more detailed observation of the *I-V* characteristics under high electric field loads.

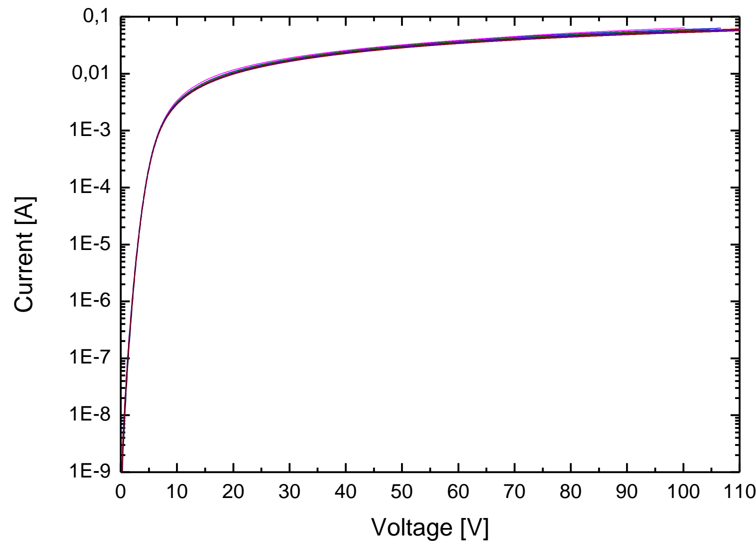

Figure 89: Typical high-load I-V characteristics of 100 nm thin Type II ICP-CVD a-SiN_x:H samples measured at T = 60°C in forward bias condition and a pad diameter of 500 µm.

Especially noteworthy is the strong contrast between the *I-V* characteristics under forward and reverse bias conditions. Under forward bias (see Figure 89) the initial exponential increase of the leakage current is followed by a quasi-saturation at higher voltages. In this regime, the leakage current increases almost linearly with the applied voltage, and the material is essentially behaving as an ohmic conductor. In contrast, under reverse bias conditions as illustrated in Figure 90 one can identify several more distinct regimes of the current-voltage characteristics. At lower fields, up to 2 MV/cm (which corresponds to *V* = 20 V for 100 nm thick samples) the same two regions of exponential leakage current growth and saturation as in the case of forward bias appear, although with significantly lower absolute current values. When further increasing the reverse bias, another region of quasi-exponential increase occurs. The characteristics conclude in catastrophic breakdown at a reverse bias field of approximately 10 MV/cm. Referring to *Chapter 4*, it has been proven that *Type II* ICP-CVD silicon nitride has a N/Si atomic concentration ratio which can be as low as 0.35, far below that of stoichiometric Si_3N_4. As it is apparent from the measurement results, this makes the material a poor insulator, with resistivity values as low as 10^9 Ω·cm at 25°C and $7{\cdot}10^7$ Ω·cm at 120°C at 0.5 MV/cm in forward bias direction. For comparison, the values under reverse bias are 10^{12} and 10^9 Ω·cm, respectively.

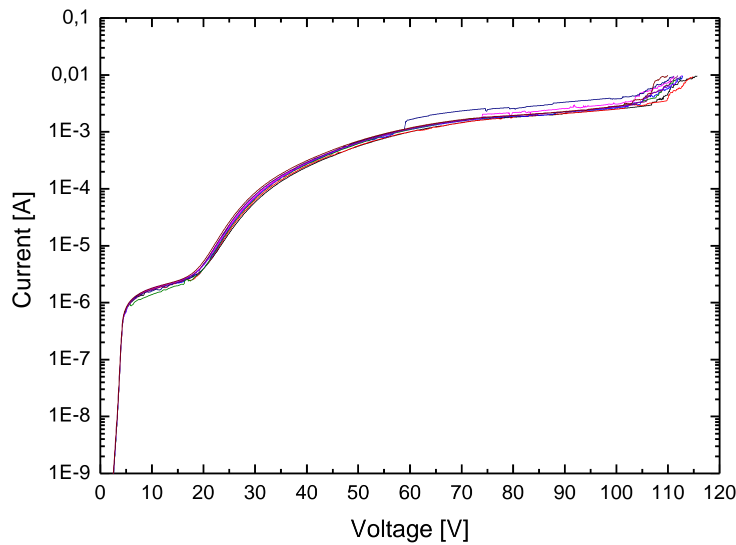

Figure 90: Typical breakdown characteristics of 100 nm thin Type II ICP-CVD a-SiN$_x$:H samples measured at T = 60°C in reverse bias direction using 500 µm diameter pads.

Basically, the material needs to be considered as an extremely poor amorphous silicon layer from the electrical performance point of view. This approach offers some explanation for the remarkably asymmetric, diode-like current- voltage characteristics of the *Type II* samples.

6.2.3. Intermediate Type films

The *Intermediate Type* ICP-CVD silicon nitride thin films showed distinctively different characteristic leakage current behaviour than either the *Type I* or *Type II* samples. As a reminder, these samples are synthesized using a N_2 to SiH_4 flow ratio being in between those used during the deposition of the other two types, resulting in a material with outstanding mechanical properties (see Chapter 4). But, the electrical behaviour of these samples does not simply fall in line with the previous two sample types.

The first straight-forward observation is the very low absolute value of the leakage current. For this reason, the measurement range was extended to 1.0 MV/cm for this type of material. Additionally, it was found that the increase in the measurement temperature has basically no influence on the leakage current characteristics, at least up to 240°C, as shown in Figure 91. In contrast, the leakage current curves do display an effect when increasing the temperature at higher bias values, as it was evidenced during the dielectric breakdown tests (see Figure 92). This apparent insensitivity of

the leakage current with temperature, however, needs to be addressed. One explanation would be that at the measurement conditions the dominating conduction processes are insensitive to temperature. The former would indicate some sort of tunnelling process (see above in section 6.1.3), although the conditions (relatively high film thickness of 100 nm, relatively low field values) make this highly unlikely. The latter parameters could suggest ohmic conduction to be dominating, which is definitely possible at the given field values, despite the fact that even in this case more pronounced temperature-dependence characteristics were to be expected. Another – much more probable – explanation is that the measured values in the given field and temperature range are ultimately limited, not by the conduction mechanics of the samples but by the leakage current signal being below the noise floor of the measurement setup.

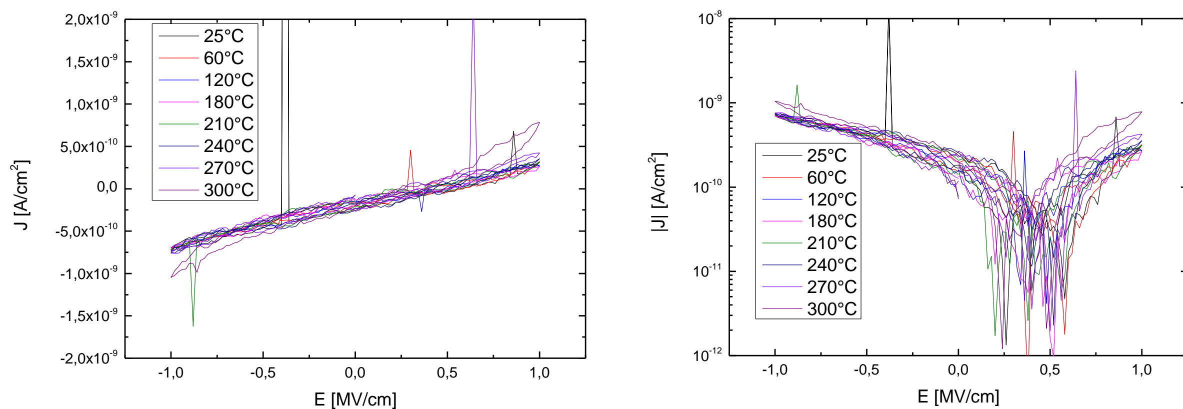

Figure 91: Leakage current characteristics of an Intermediate Type 100 nm thin a-SiN_x:H sample between T =25°C and 300°C on a linear (left) and semi-logarithmic scale (right).

Although in this case the precise determination of the leakage current characteristics is not achieved, an upper limit of the conductance value under the tested circumstances can be calculated. This leads to the rather impressive film resistivity values of $7\cdot10^{15}$ Ω·cm and $4\cdot10^{15}$ Ω·cm at 0.5 and 1.0 MV/cm at 25°C, and of $3\cdot10^{15}$ Ω·cm and $1\cdot10^{15}$ Ω·cm at 300°C, respectively.

In contrast to particularly *Type II* samples, no significant amount of asymmetry of the leakage current amplitude was observed with respect to the loading direction. As it is visible on the semi-logarithmic representation in Figure 91, however, the leakage current characteristics are shifted by about 0.2 to 0.4 MV/cm to the positive bias direction. This, in combination with the exceptionally low measured values is further evidence suggesting a significant portion of the measured values affected by artefacts originating from the limitations of the setup, rather than an actual feature of the sample material. This means that the resistivity values given above are only lower bounds for the actual values.

As an additional important point of distinction, *Intermediate Type* samples do not suffer from the temperature- and field induced irreversible hysteresis effects like *Type I* samples.

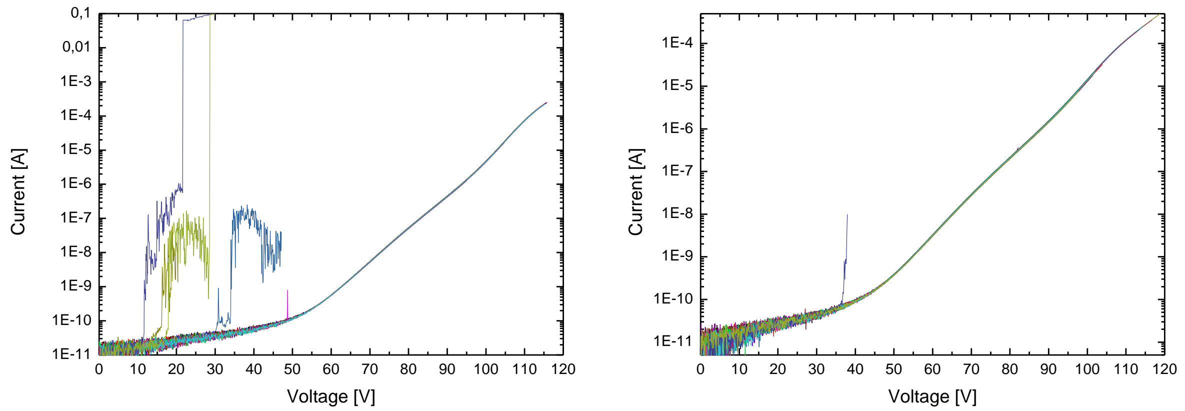

Figure 92: Dielectric breakdown characteristics of 100 nm thin Intermediate Type a-SiN$_x$:H samples measured at T = 25°C (left) and T = 120°C (right) with a pad diameter of 500 µm. The 18 samples in each graph have been measured in direct sequence to each other.

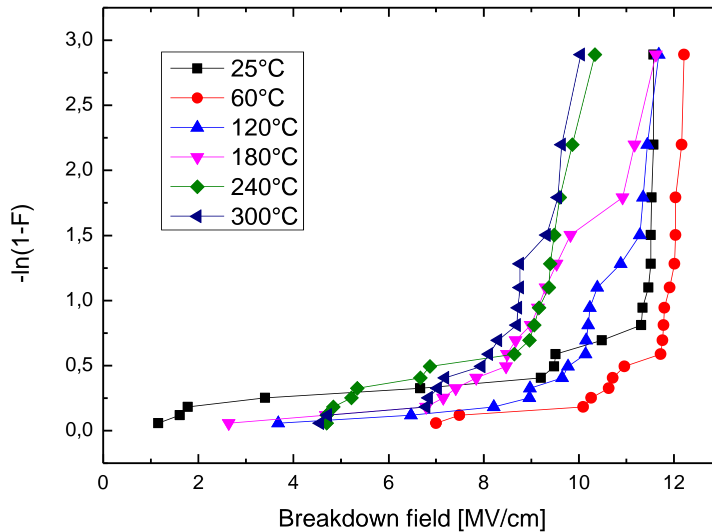

Figure 93: Weibull-plot showing the dielectric breakdown strength of 100 nm thin Intermediate Type ICP-CVD a-SiN$_x$:H thin film samples.

The dielectric breakdown measurements have also revealed the leakage current characteristics of the *Intermediate Type* ICP-CVD silicon nitride samples, although using much higher ramp speeds of 500 mV/s then in the case of the LC measurements (effectively 2-10 mV/s), making a direct comparison between the two measurements difficult. It can be stated, however, that the recorded *I-V* characteristics at higher electric fields are in stark contrast to the *Type I* and *Type II* samples. The leakage current as a function of the load voltage shows a strictly monotonous increase, while following a smooth quasi-exponential curve characteristic for Frenkel-Pole type emission, up to the point of breakdown indicated by a steep increase, as displayed in Figure 92. As the statistical

analysis shows (see the Weibull-plot in Figure 93) the intrinsic dielectric breakdown strength of the intermediate type material is relatively high at 9-12 MV/cm compared to *Type I* and *Type II* materials, and comparable to textbook examples of sputter-deposited samples [151]. Additionally, the decrease of the dielectric strength at temperatures above 60°C is clearly observable.

6.2.4. Type RF films

The leakage current characteristics of 100 nm thick *Type RF* ICP-CVD silicon nitride samples show a great degree of similarity to those measured at the *Intermediate Type* samples. This includes the apparent insensitivity of the leakage current to temperature (see Figure 94), accompanied by the shift of the minimum of the curve in forward bias direction up to 240°C.

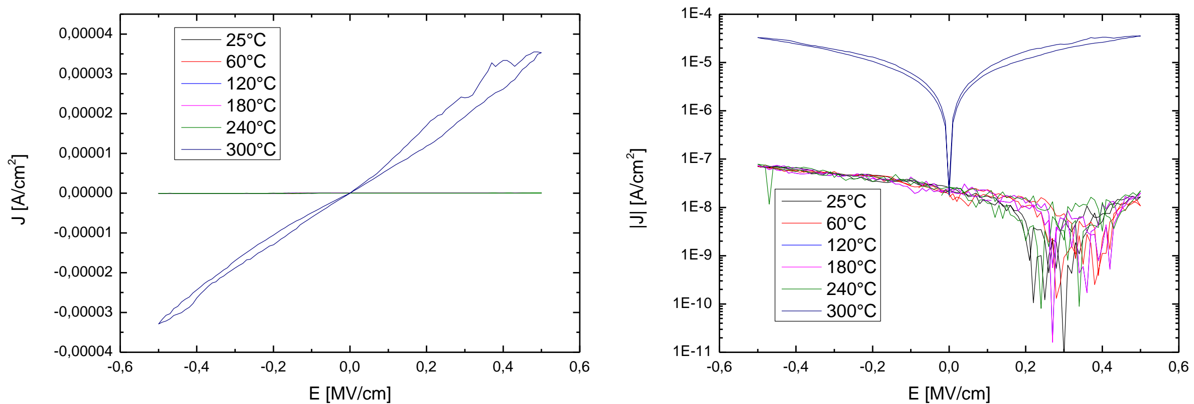

Figure 94: Leakage current characteristics of a Type RF 100 nm thin a-SiN_x:H sample between T =25°C and 300°C in a linear(left) and a semi-logarithmic (right) scale.

On the other hand, a significant discrepancy between the two silicon nitride sample types is the substantially higher increase of the measured leakage current density above 240°C, compared to the *Intermediate Type*. This information acts as a further proof that the negligible impact of temperature on the leakage current characteristics, as well the shift in the curves are –as suggested above– caused by the limitations of the instrumentations, rather than being inherent properties of the material under test. Given this assumption, the recorded leakage current characteristics up to 240°C may be interpreted as upper limits.

Given the measured data, the calculated resistivity of the 100 nm thin Type RF samples at an electric field load of 0.5 MV/cm is about $1\cdot10^{13}$ Ω·cm at 25°C and about $2\cdot10^{10}$ Ω·cm at 300°C, respectively. Although these values are somewhat inferior compared to the film resistivity of

Intermediate Type samples, the high potential of *Type RF* insulators, at least at moderate temperatures is demonstrated.

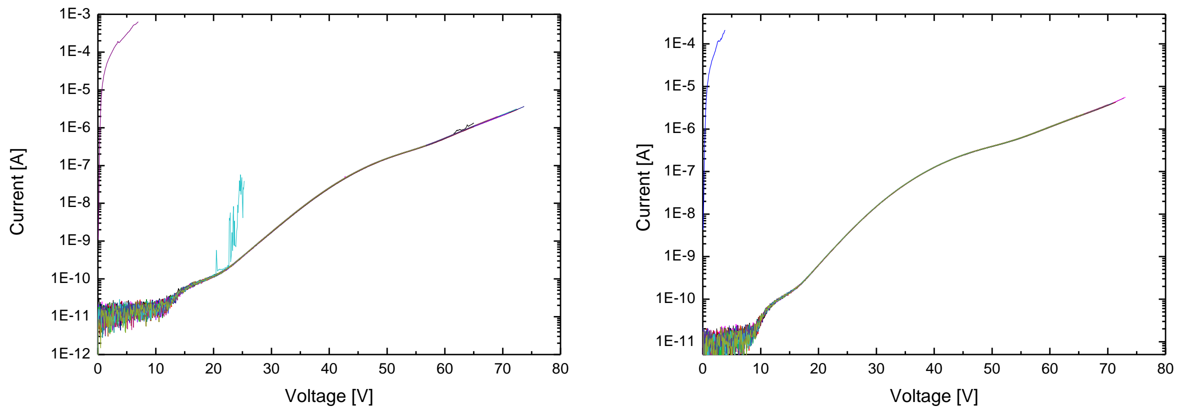

Figure 95: Dielectric breakdown characteristics of 100 nm thin Type RF a-SiN$_x$:H samples measured at T°= 25°C (left) and T = 120°C (right) with a pad diameter of 500 µm. The curves in each figure were recorded in direct sequence to each other.

By increasing the bias field during the dielectric breakdown tests– again in a similar approach as done at the *Intermediate Type* samples – the current passing through the insulating thin film increases to a measurable level. Additionally, the temperature-dependence of the measured leakage current values with increasing temperature becomes apparent. It is important to note that the shapes of the *I-V* characteristics are notably different than in the previous section, by having defined regimes with different slopes, as illustrated in Figure 95.

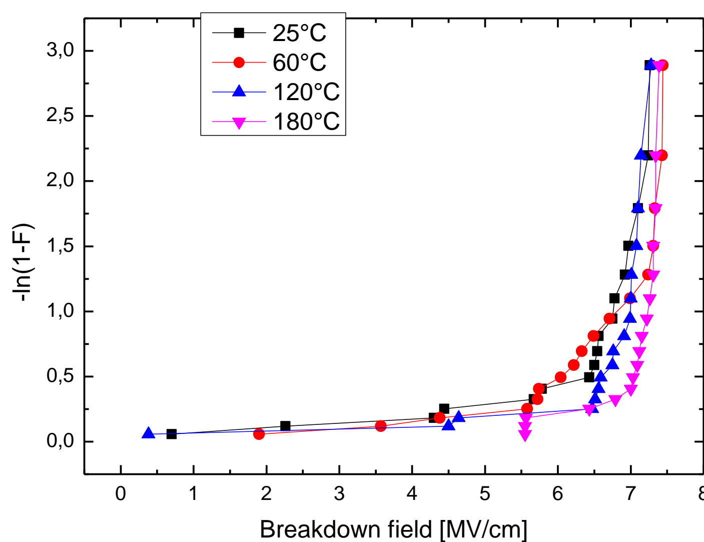

Figure 96: Weibull-plot showing the dielectric breakdown strength of 100 nm thin Type RF ICP-CVD a-SiN$_x$:H samples.

This suggests that when the electric field at the device changes, different conductions mechanisms can dominate the leakage current behaviour. Despite this difference, the measured characteristics are characterized by the expected strictly monotonous increase in leakage current with increasing load voltage, until a sudden increase of several orders of magnitude occurs, thus exceeding the compliance limit. This terminates the measurement, indicating that dielectric breakdown has been reached.

Regarding the intrinsic dielectric strength of 100 nm thin *Type RF* ICP-CVD silicon nitride samples, it can be stated that the substrate temperature does not have a strong effect on it, contrary to what was observed in the case of *Intermediate Type* samples. Between 25°C and 180°C the intrinsic breakdown strength of the material under test was found to be in the range of 6.5 to 7 MV/cm, as it is presented in Figure 96. At temperatures above T =180°C, the breakdown measurements have proven to be unreliable for this type of samples (meaning that the amount of exceedingly early failures rendered the results statistically unusable), and are thus omitted from the presented results. These values are comparable with the dielectric strength of *Type I*, but superior to *Type II* samples. Despite being appropriate for many applications, *Type RF* samples are still clearly inferior to the properties of the *Intermediate Type* material when comparing film resistivity and intrinsic dielectric strength.

6.3. RF sputtered a-SiN_x thin films

In contrast to ICP-CVD deposited a-SiN_x:H thin films, magnetron sputter deposited silicon nitride has by orders of magnitude lower concentrations of incorporated hydrogen (see Chapter 5). This fact alone makes RF and DC sputter deposited SiN_x materials very interesting candidate for improved electrical insulating performance compared to their ICP-CVD counterparts. As mentioned above, sputter deposited silicon nitride samples have been prepared with three thickness values: 40, 100 and 300 nm. In Figure 97 typical leakage current characteristics of 100 nm thin RF magnetron sputter deposited silicon nitride samples (with the deposition parameters $P_{plasmaRF}$ = 900 W and p_{back} = 9 µbar) are illustrated. Qualitatively, these characteristics are representative for the complete set of samples sputter deposited in RF mode. (For more examples, refer to Appendix F.)

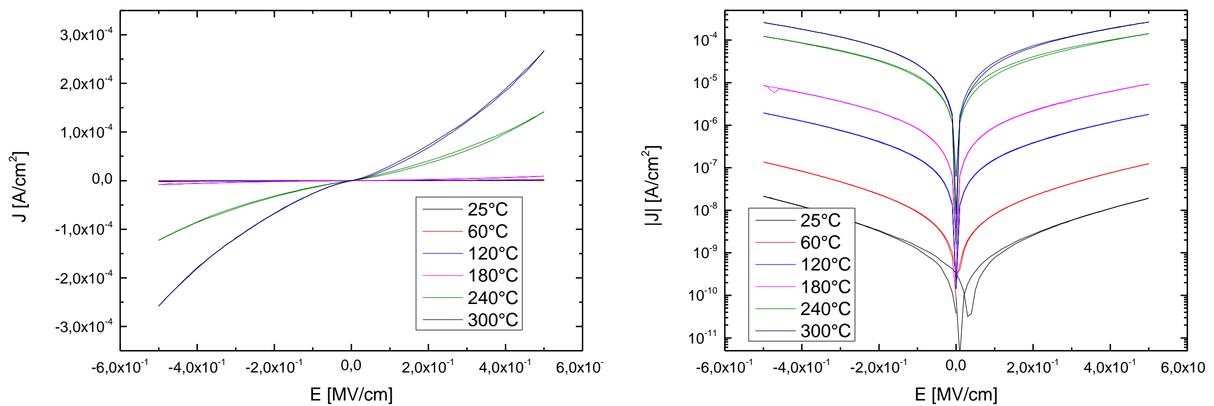

Figure 97: Leakage current characteristics of a RF magnetron sputter deposited 100 nm thin SiN_x sample in the temperature range of T =25°C and 300°C on a linear (left) and a semi-logarithmic (right) scale.

Contrary to the previously discussed ICP-CVD deposited samples, these results are comparable to those published in literature [151, 166, 167]. The most important features represented here are the large symmetry of the leakge current characterisitcs with respect to both bias directions and the exponantial increase of the leakage current with increasing temperature across the investigated temperature range. Given these basic features, a few assumptions can be made regarding the dominating leakage current mechanisms under different measurement conditions. This allows for a quanititative analysis of the results, which will be described below.

For the purpose of comparison the resistance values at an electric field of E = 0.5 MV/cm have been determined for different temperatures and for samples syntehsized using different parameter sets. In the case of 40 nm and 100m thick samples, the average resitivity is in the range of $\rho = 10^{13}$ Ω·cm

at 25°C and 10^9 Ω·cm at 300°C, while the corresponding value at room temperature increases to 10^{14} Ω·cm for 300 nm thin films.

In the investigated field and temperature range, the most influential conduction mechanisms considered to contribute to the leakage current through sputter deposited silicon nitride thin films are ohmic conduction and Poole-Frenkel emission [151, 152]. Ohmic conduction is generally dominating at low bias fields, while Poole-Frenkel emission at higher loads. As a first step, the validity of these assumptions for the material under test must be checked. This is done by a fitting procedure using a simple linear regression model and a variable width for the fitting window based on the equations presented in Table 15. Once the correlation factor exceeds a pre-defined value of 0.995, the fit is considered adequate enough. With this procedure, three distinct regions can be identified between 0 to 0.5 MV/cm. From $E = 0$ to 0.1 MV/cm, ohmic conduction is dominating, while for $E \geq 0.3$ MV/cm Poole-Frenkel emission describes the leakage current best. Additionally, between those two values, a transition region exists, where both aforementioned mechanisms contribute to the leakage current to a significant degree. For the subsequent calculations, the recorded *I-V* curves are transformed into *J-E* plots for direct data analyses.

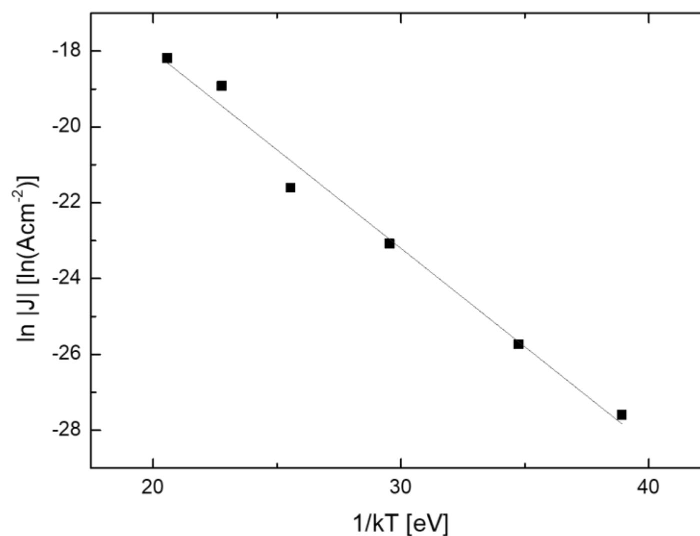

Figure 98: Arrhenius plot illustrating the temperature-dependency of a leakage current density of 100 nm thin RF sputter deposited SiN_x thin film sample.

Next, in an Arrhenius plot the natural logarithm of the leakage current density J is fitted to $1/k_BT$, where k_B is the Boltzmann constant, combining the data from measurements performed at different temperatures. The slope of the linear fit yields the effective activation energy E_A. This is done for every value of the electric field E, resulting in E_A as a function of E.

The activation energy for Poole-Frenkel emission is given by the following equation, as a function of the electric field E:

$$E_{A,PF}(E) = q\Phi_B - \beta\sqrt{E} \tag{6.1}$$

This can be fitted to the calculated $E(E_A)$ function in the appropriate range of $|E| \geq 0.3$ MV/cm, yielding an initial value for the determination of the barrier height Φ_B.

In addition, the measured leakage current density J is fitted to the equation describing ohmic conduction (See Table 15) using linear regression on the range of $0 \leq E \leq 0.1$ MV/cm. This gives a value for the ohmic activation energy $E_{A,\Omega}$ and conductivity σ_Ω. With these two values, the contribution of the ohmic conduction mechanism to the leakage current – J_Ω – can be calculated.

Based on the assumption that the impact of conduction mechanisms other than ohmic conduction and Poole-Frenkel emission is negligible, the contribution of the latter mechanism can be calculated in a straightforward approach by subtracting the ohmic current density from the total measured current density: $J_{PF} = J - J_\Omega$.

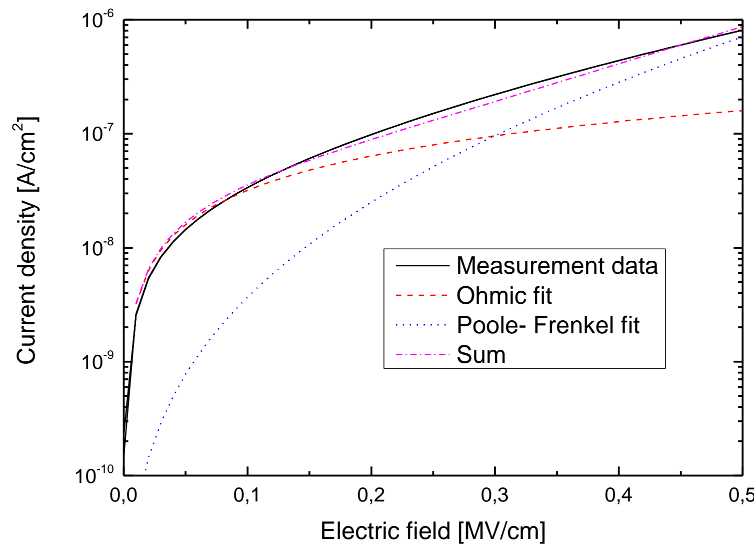

Figure 99: Illustration of the data fitting process of the recorded leakage current data to identify different charge transport mechanisms.

Again with a linear fit J_{PF} is fitted to the appropriate equation from Table 15 (also known as the Poole-Frenkel equation), using the pre-determined value of Φ_B as an initial value, in the range of $0.3 \leq E \leq 0.5$ MV/cm. Assuming an electron mobility value [168] of $\mu = 5 \cdot 10^{-12}$ m²/V·s, the final Poole-Frenkel barrier height Φ_B and the volumetric defect density n_0 are extracted.

As it is shown in Figure 99, the sum of J_{PF} and J_{Ω} gives a very good approximation of the actual measure date for the entirety of the measurement range. This validates the assumptions made and the fitting process.

For the determination of the impact that the various input parameters such as film thickness, chamber pressure and plasma power, have on the values of $E_{A,\Omega}$, σ_{Ω}, Φ_B and n_0, multivariate statistical analysis (MANOVA [169]) was used [131].

The results strongly indicate that the chamber pressure p_{back} has no significant effect on any of the investigated electrical parameters. These findings are in good accordance with the results presented in Chapter 5.2, where it was shown that both the chemical composition and biaxial film stress of the RF magnetron sputter deposited silicon nitride thin films were found to be unaffected by the parameter p_{back}. In contrast, the sputter power $P_{plasmaRF}$ has a measurable impact on the parameters describing ohmic conduction ($E_{A,\Omega}$ and σ_{Ω},), but not on the effective barrier height. The film thickness d, however, has a significant influence on $E_{A,\Omega}$, σ_{Ω}, and Φ_B.

	***d* [nm]**	**$P_{plasmaRF}$ [W]**	
		450	900
$E_{A,\Omega}$ [meV]	40	417.2±23.3	394.7±64.1
	100	426.9±38.5	408.1±65.0
	300	491.6±36.6	417.8±52.2
σ_{Ω} [µS/m]	40	64.8±2.6	67.3±3.8
	100	63.7±4.2	65.8±7.2
	300	56.5±4.0	64.7±5.8
Φ_B [meV]	40	635.8±7.1	
	100	691.6±12.6	
	300	748.5±9.3	
n_0 [10^{21} cm^{-3}]	40	1.19±0.83	
	100		
	300		

Table 16: Electrical parameters of RF magnetron sputter deposited SiN_x thin films. Φ_B is averaged over $P_{plasmaRF}$, and n_0 is averaged over both $P_{plasmaRF}$ and d values.

In addition, it can be stated that the volumetric defect density n_0 has not shown any significant dependence on any of the input parameters. Due to a number of assumptions necessary for determining this value, a large uncertainty is associated with these values. Thus, the calculated n_0 values should only be regarded as rough estimate indicating the order of magnitude.

A summary of the extracted parameters is presented in Table 16. It is worth noting that the ohmic activation energy $E_{A,\Omega}$ is significantly lower than the effective Poole-Frenkel barrier height Φ_B. This indicates that the leakage current contributed by ohmic conduction is dominated by the effect of shallow defect states. These are electrically active at comparatively low values of E. On the contrary, J_{PF} is predominantly influenced by deep defect states, which become electrically active only when a higher electric field or temperature is applied.

The ohmic activation energy and the effective Poole-Frenkel barrier height both show a measurable increase with increasing thickness of the insulator, which ultimately results in a decrease of the leakage current. This can be explained by a size effect connected to the scaling of the silicon nitride thin film from 40 nm to 300 nm. This may be caused by defect-rich regions as present at both the metal-insulator and the insulator-silicon interface, thus having a comparatively larger contribution to the overall film properties in thinner samples. The result of this effect is an effective decrease of $E_{A,\Omega}$ and Φ_B.

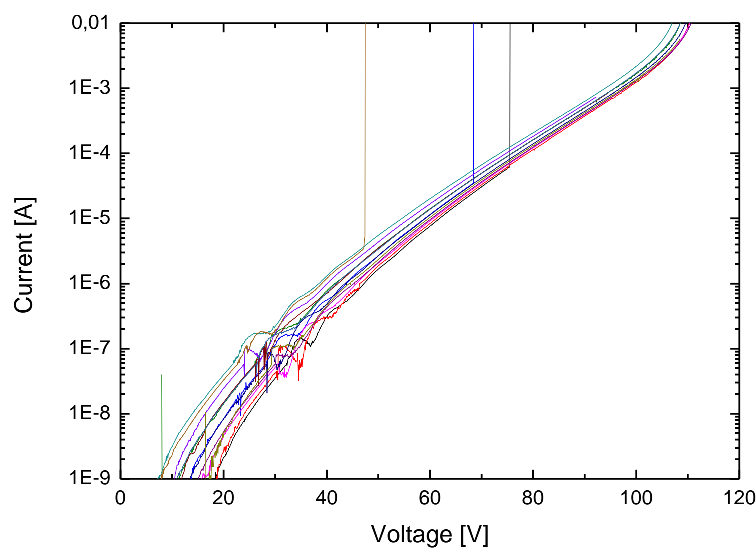

Figure 100: Typical current-voltage characteristics of 100 nm thin RF magnetron sputter deposited (450 W and 3 µbar) SiN_x samples during a time-zero dielectric breakdown measurement performed at T = 120°C, using 500 µm diameter pads.

Some typical high-load current voltage characteristics of 100 nm thin RF magnetron sputter deposited silicon nitride thin films are presented in Figure 100 and Figure 101. (Further examples are provided in Appendix G.) As it is clearly visible the *I-V* characteristics within a sample set of 18 samples at a given temperature level show a high degree of uniformity. Also, independent of the deposition conditions (e.g. low or high values of the parameters $P_{plasmaRF}$ and p_{back}), the samples exhibit a very similar behaviour among each other. Common features are the rather smooth *I-V* curves, showing an

exponential increase of the leakage current right until reaching the compliance limit. The occurrence of “early failures”, signified by an abrupt increase of the leakage current occurs with low probability. Additionally, a significant decrease of the breakdown strength with increasing temperature is observed, starting from 8-9 MV/cm at 60°C down to 5-6 MV/cm at 300°C. Interestingly, the samples measured at room temperature, while the general characteristics of the *I-V* curves are the same, seem to deviate from this trend. This is most probably due to the more frequent premature failure events that took place, and distorted the statistics at the given sample count. This is attributed to the fact that the room temperature measurements have been performed first during the measurement routine, so these samples are more susceptible to settle-in effects, which also have been observable in the other SiN_x sample types.

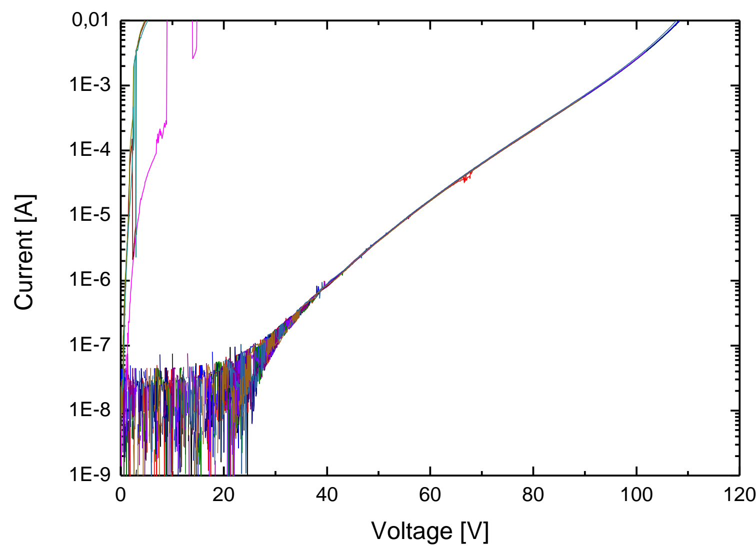

Figure 101: Typical current-voltage characteristics of 100 nm thin RF magnetron sputter deposited (450 W and 9 µbar) SiN_x thin film samples (a total of 18 samples) during a time-zero dielectric breakdown measurement performed at T = 120°C using 500 µm diameter pads.

A comparison between the dielectric breakdown strength of RF magnetron sputtered samples deposited using different parameter sets is shown in Figure 102. Some quantitative differences, however, are detectable from the data: while samples deposited at $P_{plasmaRF}$ = 450 W have a maximum breakdown strength of about 10 MV/cm, samples synthesized at $P_{plasmaRF}$ =900 W reach only lower values between 8 and 9 MV/cm. The effect of the increasing measurement temperature on the dielectric breakdown strength shows a significant variation between the different sample sets. The breakdown strength reaches values >8 MV/cm at 450 W@3 µbar, but <5 MV/cm at 900 W.

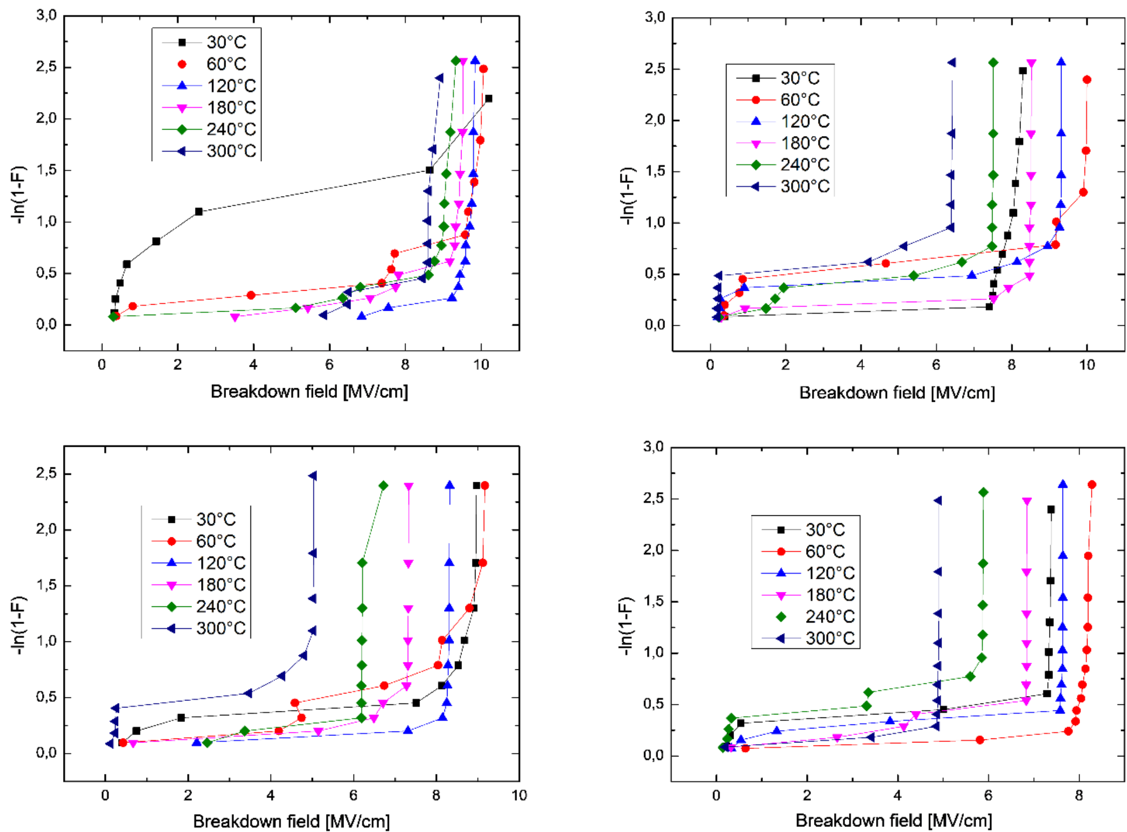

Figure 102: Weibull-plots of the dielectric breakdown strength of 100 nm thin RF magnetron sputter deposited SiN_x samples synthesized using the following parameter sets from top left to bottom right: 450 W and 3µbar; 450 W and 9 µbar; 900 W and 3 µbar; 900 W and 9 µbar.

Extending the investigation to 40 nm thin samples yields similar results. (Example *I-V* curves as well as Weibull plots are provided in Appendix G). The *I-V* characteristics are generally still characterized by a smooth, exponential increase of the leakage current. The probability of early failures is, however, increased compared to the 100 nm thin samples. In addition, in some characteristics, a quantization effect is observable. This consists of multiple abrupt steps in the – otherwise smooth – *I-V* curve. The reason for this is regarded due to the formation of individual percolation paths through the isolator film under increased electrical load, whose occurrence is more probable in thinner samples. Breakdown strength values are found in the range of 10-14 MV/cm at 60°C to 4-6 MV/cm at 300°C.

The ability to measure the breakdown strength of 300 nm thin RF magnetron sputter deposited silicon nitride samples is inherently limited by the maximum output voltage of 200 V of the source/measure unit. This means that breakdown strengths larger than 6.7 MV/cm cannot be measured. Qualitatively, the *I-V* characteristics are rather similar to those measured at thinner samples (see Appendix G), with occasional failures and abrupt jumps at very high loads. The samples deposited using a $P_{plasmaRF}$ value of 450°W have up to 240°C a higher dielectric breakdown strength than

detectable by the measurement limit and barely below that measured at 300°C (i.e. 6.4 and 6.2 MV/cm for 3 and 9 µbar, respectively). The samples deposited at $P_{plasmaRF}$ = 900 W, however, reach T = 240°C already values of 4.9 and 4.5 MV/cm for p_{back} = 3 µbar and 9 µbar, respectively.

In summary, while the electrical performance of RF magnetron sputter deposited silicon nitride thin films does not reach the level of *Intermediate Type* ICP-CVD deposited samples in terms of resistivity at a load of 0.5 MV/cm and dielectric breakdown strength, this does not pose a relevant limitation for real-life applications. At room teperature the high resistivity of 10^{13} Ω·cm and breakdown strength of > 10 MV/cm compare favourably with both literature values [151] and *Type I*, *Type II* and *Type RF* samples, which makes the material a good candidate as an electrical isolator. The leakage current through the RF sputter deposited silicon nitride samples can also be modelled well by ohmic conduction dominating at low fields, and Poole-Frenkel emission under higher loads, while the electrical performance shows only a low sensitivity to the deposition parameters.

6.4. DC sputtered a-SiN_x thin films

The DC magnetron sputter deposited silicon nitride samples having a thickness of 40 nm, 100 nm, and 300 nm have been subjected to the same measurement procedure, including leakage current and dielectric breakdown, as the samples synthesised in RF mode. Leakage current characteristics of a 100 nm thin specimen deposited using the parameters $P_{plasmaRF}$ = 450 W and p_{back} = 3 µbar are shown in Figure 103. The showcased characteristics are representative for the samples deposited under different conditions as well.

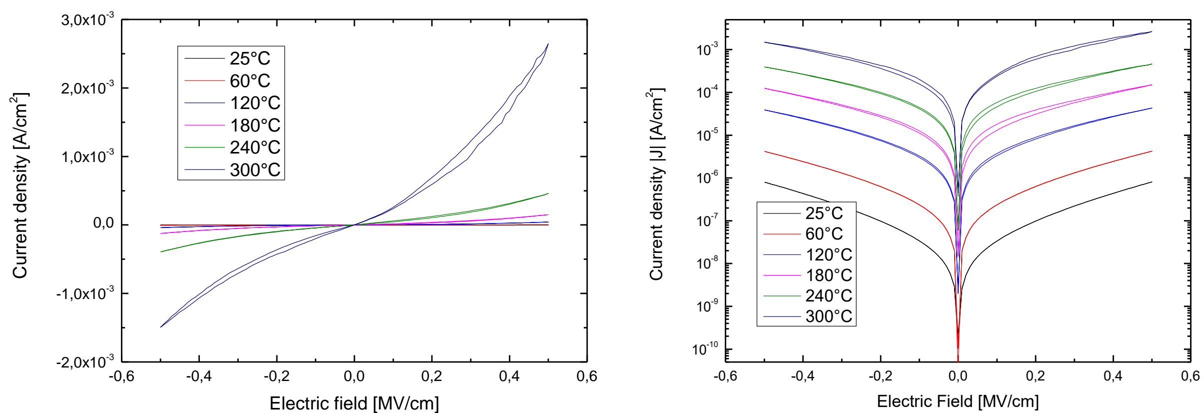

Figure 103: Leakage current characteristics of a DC magnetron sputter deposited 100 nm thin SiN_x sample in the temperature range between 25°C and 300°C on a linear (left) and a semi-logarithmic (right) scale.

The resistivity values at an electric field of 0.5 MV/cm show significant dependence on the deposition parameters, and range from $5 \cdot 10^{11}$ Ω·cm at 25°C and $2 \cdot 10^{8}$ Ω·cm ($P_{plasmaDC}$ =900 W, p_{back} = 3 µbar) to $2 \cdot 10^{13}$ Ω·cm at 25°C and $2 \cdot 10^{9}$ Ω·cm ($P_{plasmaDC}$ =450 W, p_{back} = 9 µbar). The latter numbers are comparable to the corresponding values of RF sputter deposited samples.

In addition, similarly to the RF sputtered samples, the leakage current characteristics of DC magnetron sputter deposited silicon nitride thin films are characterized by a high degree of symmetry with respect to the bias directions, as well as an exponential increase of the leakage current with increasing measurement temperature. This, together with other published results [170], leads to the assumption, that the dominating conduction mechanisms contributing to the leakage current are again ohmic conduction at low fields, and Poole-Frenkel emission under higher electric loads.

When applying the same evaluation procedure as done at the RF sputter deposited samples, the numerical field ranges are in rather good agreement, as shown in Figure 104. Up to 0.1 MV/cm, ohmic conduction dominates, whereas under electric loads higher than 0.3 MV/cm, Poole-Frenkel emission contributes most to the leakage current. This is true for all investigated film thickness values.

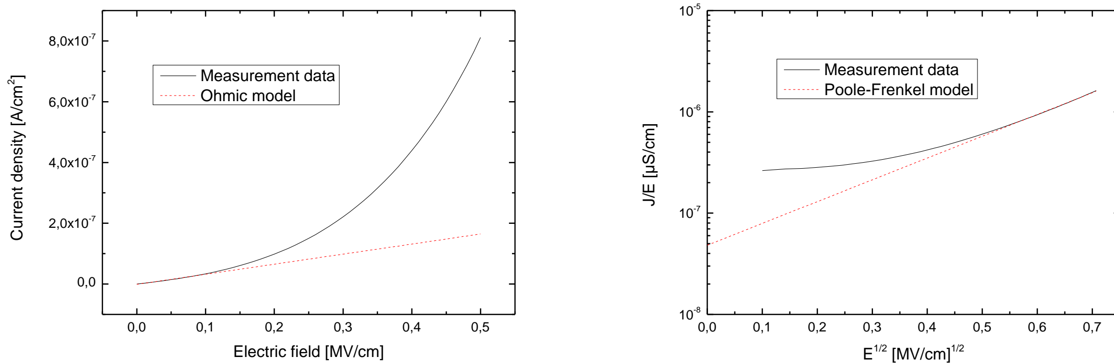

Figure 104: Identification of ohmic and Poole-Frenkel dominated field regimes in the leakage current measurements of DC sputter deposited silicon nitride thin films.

The rest of the fitting procedure and parameter extraction process followed exactly as it was described in Chapter 6.3. A summary of the extracted parameters for the ohmic conduction ($E_{A,\Omega}$, σ_{Ω}) and Poole-Frenkel emission (Φ_B, n_0) is provided in Table 17. It is apparent, that the former two are largely independent of both the film thickness, and the deposition conditions. In contrast, the Poole-Frenkel barrier height increases significantly with increasing film thickness. This behaviour can be explained by the same size effect that was already present in the RF sputter deposited samples. In short, the relatively enhanced contribution of the interface regions at thinner films lowers the effective barrier height.

	d [nm]	$P_{plasmaRF}$ = 450 W		$P_{plasmaRF}$ = 900 W	
		p_{back} =3 µbar	p_{back} =9 µbar	p_{back} =3 µbar	p_{back} =9 µbar
$E_{A,\Omega}$ [meV]	40	407±52	349±31	298±29	364±30
	100	340±26	438±21	341±21	365±16
	300	347±29	414±16	460±11	411±19
σ_{Ω} [µS/m]	40	6.59±0.58	7.24±0.35	7.81±0.32	7.06±0.34
	100	7.33±0.3	6.25±0.23	7.32±0.24	7.05±0.18
	300	6.95±0.33	6.51±0.17	6.00±0.13	6.54±0.21
Φ_B [meV]	40	611±34	478±36	464±39	488±39
	100	552±11	636±8	538±10	531±3
	300	598±5	603±23	609±8	593±5
n_0 [10^{20} cm^{-3}]	40	1.19±0.28	0.97±0.08	0.98±0.05	0.95±0.07
	100	7.65±4.19	6.49±2.25	3.63±1.58	1.98±0.59
	300	10.6±3.7	2.22±0.72	1.62±0.50	4.02±1.09

Table 17: Leakage current parameters for ohmic conduction and Poole-Frenkel emission in 100 nm thin RF magnetron sputter deposited silicon nitride films in dependence of the deposition parameters.

Additionally, there is a strong correlation between the volumetric defect density n_0 and the kinetic energy of the sputtering particles which, in turn, are influenced by the deposition parameters. When comparing the two extreme parameter combinations, 450 W@9 µbar and 900 W@3 µbar, the samples deposited with a higher average particle energy and as a consequence having a lower N/Si atomic concentration ratio (see Chapter 5) exhibit a significantly lower volumetric defect density. The calculated defect density values also compare favourably with those of RF magnetron sputtered samples.

Furthermore, it is noteworthy, that the variation of the extracted barrier height through the whole measurement temperature range is relatively small. This observation implies that the Poole-Frenkel type defect hopping mechanism utilizes the same defect type, with a low impact arising from temperature.

Typical current voltage characteristics under high load and a ramp speed of 500 mV/s of DC magnetron sputter deposited, 100 nm thin silicon nitride thin films recorded during the dielectric breakdown measurements are presented in Figure 105 and Figure 106. (For additional graphs, refer to Appendix H.) As it is apparent, despite the qualitative similarities between different sample sets, statistically viewed, there are significant differences, dependent on the deposition conditions.

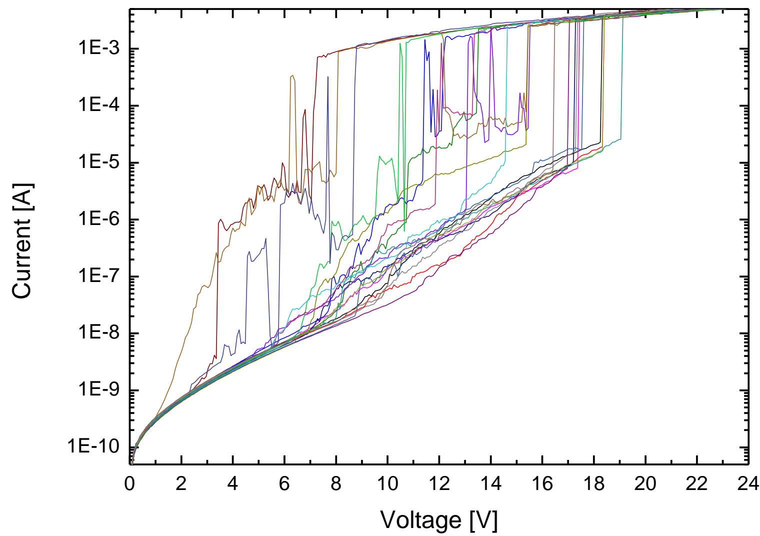

Figure 105: Current-voltage characteristics of 100 nm thin DC magnetron sputter deposited (450 W and 3 µbar) SiN_x samples during a time-zero dielectric breakdown measurement performed at T = 120°C using 500 µm diameter pads.

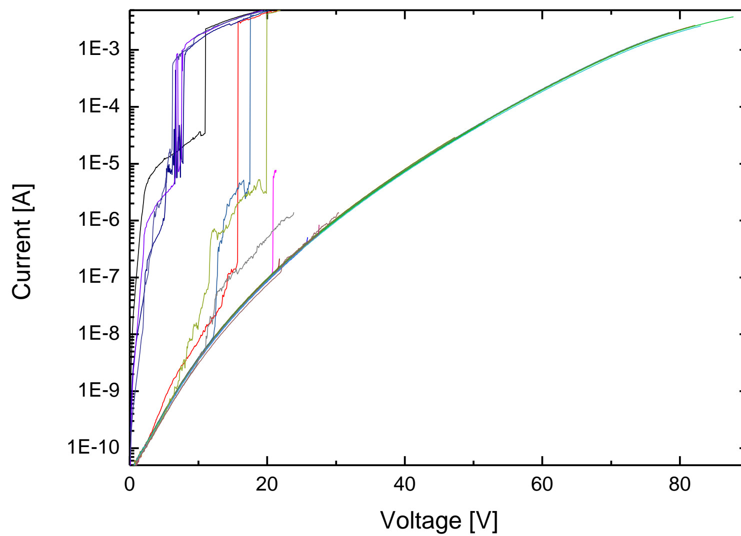

Figure 106: Current-voltage characteristics of 100 nm thin DC magnetron sputter deposited (450 W and 9 µbar) SiN_x samples during a time-zero dielectric breakdown measurement performed at T = 120°C using 500 µm diameter pads.

In general, though, the *I-V* characteristics within any singular sample set are superimposable up to the point of breakdown. (Here, under breakdown, the point where an erratic or abrupt change of the leakage current begins, is meant; rather than the formal breakdown requirement of the leakage current reaching the compliance limit.) The initial smooth, exponential increase of the leakage current is followed by an optional region, where the current changes in an erratic way, or increases in an abrupt manner over multiple orders of magnitude. This behaviour is likely to be a sign of the formation of a

percolation path through the insulator. If after the formation of said percolation path the leakage current does not reach the compliance limit of 1 mA, it increases in a linear fashion, as the material at this point is essentially a (very poor) ohmic conductor. This behaviour is clearly visible in Figure 105. Alternatively, if no percolation path is formed, the leakage current can often increase up to (and beyond) the compliance limit in a continuous fashion, as shown in Figure 106. As the difference in the two graphs shows, the relative frequency of the formation of a percolation path before reaching the compliance limit is largely dependent on the deposition conditions of the DC magnetron sputtered films.

The difference is even more apparent in the respective Weibull-plots (see Figure 107.) The relative frequency of the "early failures" is significantly higher in samples deposited using p_{back} =°3 µbar. This indicates that the average particle energy during deposition has also an influence, as it contributes to the defects that are necessary to the formation of a percolation path. This effect also has a significant influence on the apparent dielectric breakdown strength of the material.

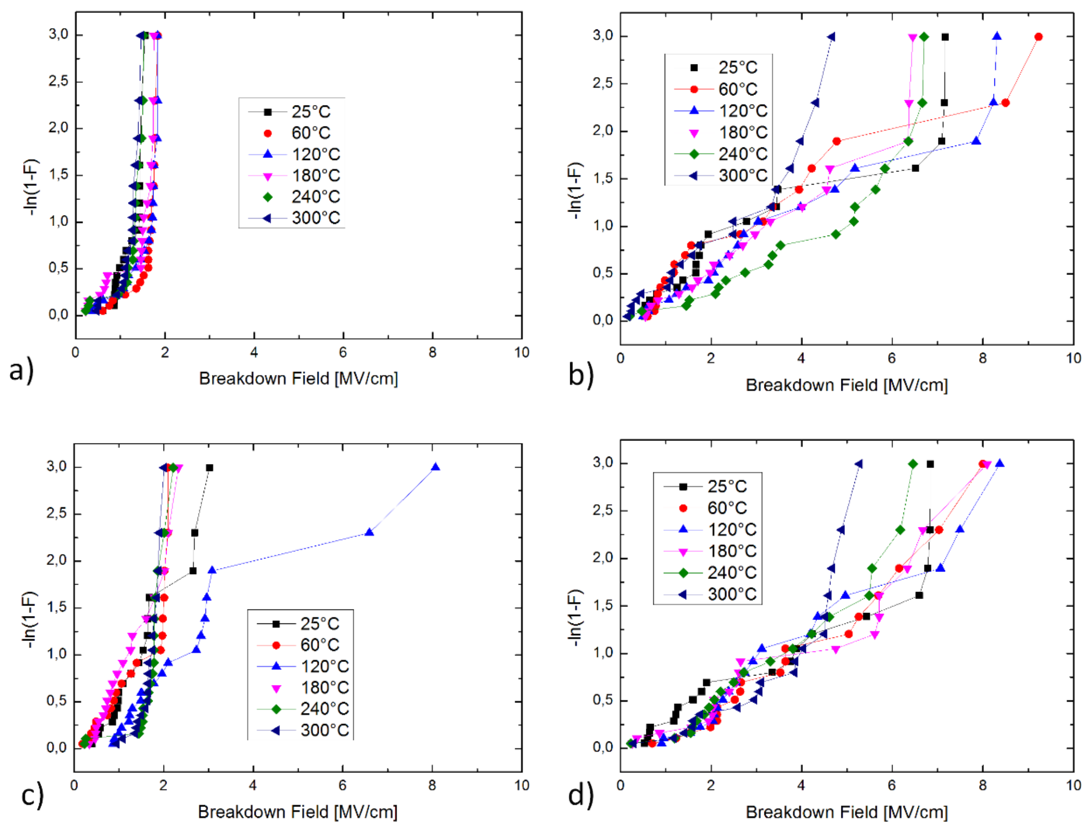

Figure 107: Weibull-plots of the dielectric breakdown strengths of 100 nm thin DC magnetron sputter deposited SiN_x samples synthesized using the following parameter sets: a) 450 W and 3µbar; b) 450 W and 9 µbar; c) 900 W and 3 µbar; d) 900 W and 9 µbar.

In the case of 100 nm thin samples the apparent dielectric breakdown strength only reaches values between 2 and 3 MV/cm, when p_{back} = 3 µbar, with the measurement temperature not being a significant factor. In contrast, when, p_{back} =9 µbar, the apparent breakdown strength is in the range of 8-9 MV/cm at room temperature, but decrease to 4-5 MV/cm at 300°C. This effect is both due to the increased leakage current in general (leading to I reaching the compliance limit at a lower value of V), and the increased frequency of early failures caused by formation of a percolation path.

In case of 40 nm thin films, practically all of the breakdown events can be categorized as early failures. This is due to the fact that the length of the percolation path that need to be formed is significantly reduced. In addition, there is no significant difference in the apparent dielectric breakdown strength based on the deposition conditions. The measurement temperature, on the other hand, has a measurable effect, with the average breakdown strength being 2.5-3 MV/cm at 25°C, and 1.5-2 MV/cm at 300°C.

The determination of the breakdown strength of 300 nm thin samples is once again limited by the output voltage of 200 V, thus 6.7 MV/cm can be given as a lower estimate. It is noteworthy though, that the probability of early failures is again significantly increased compared to the RF sputtered counterparts. Additional graphs about the BD measurements of 40 nm and 300 nm thin samples are provided in Appendix H.

In summary, it can be said that the DC magnetron sputter deposited silicon nitride thin films are capable of high electrical performance, when sufficient care is taken at the selection of deposition conditions. Generally, the leakage current is dominated by ohmic conduction at low fields, and by Poole-Frenkel defect hopping under increased loads. Resistivity values larger than 10^{13} Ω·cm can be reached at room temperature. Breakdown strengths of 9 MV/cm are obtainable with 100 nm thin samples.

6.5 Summary

In this chapter, the leakage current characteristics, as well as the dielectric breakdown of ICP-CVD deposited, RF magnetron sputtered, and DC magnetron sputtered amorphous silicon nitride thin films have been extensively studied, using a variety of deposition conditions and film thickness values. The experiments have been designed to ensure direct comparison of the results and to deliver concise information on the material performance as an electrical insulator in MEMS devices.

By far, the largest variation of the results has been observed within the group of different ICP -CVD deposited a-SiN_x:H types. *Type I* materials shows an irreversible thermally-electrically induced effect, where H^+ ions present within the thin films diffuse through the sample, contributing to the leakage current, until captured by defect states. This behaviour makes the *Type I* material quite unusable for most applications, despite special cases, where the hysteresis might be desirable such as using the irreversible resistivity change for non-volatile ROM or temperature monitoring applications. *Type II* materials, due to their high Si/N ratio are very poor insulators, and prone to a highly asymmetric, diode-like current-voltage characteristic, making them rather unsuitable for any demanding electrical application. *Intermediate type* samples exhibit very high resistivity (> 10^{15} Ω·cm) and breakdown strength (> 12 MV/cm) values, making the material a prime candidate for demanding applications. *Type RF* samples, although slightly inferior to the *Intermediate type*, still have high potential, due to their high resistivity (> 10^{13} Ω·cm) and breakdown strength (> 8 MV/cm).

The conduction through sputter deposited samples is proven to be dominated by ohmic conduction at very low fields and by Poole-Frenkel emission at higher loads. *RF magnetron sputter deposited* samples are characterized by their excellent resistivity (10^{13} to 10^{14} Ω·cm) and breakdown strength (6-10 MV/cm) at room temperature, with very little effect from the deposition conditions. While *DC magnetron sputter deposited* samples are capable of reaching similar or better figures, the appropriate control of deposition conditions is imperative. The reason for this is that the electrical performance of DC magnetron sputtered silicon nitride is dependent on the average particle energy during sputtering.

As an additional conclusion, it was shown that the maximal dielectric strength of SiN_x materials – both ICP-CVD and sputter deposited – are in good agreement with reported values for silicon nitride materials [113, 151], but do not reach the maximal capabilities of the benchmark thin film isolator for microelectronics and MEMS, namely thermally grown SiO_2, where dielectric strengths exceeding 15 MV/cm have been reported [164, 171].

Chapter 7: Summary and Outlook

7.1. Summary

In this work, the potential of silicon nitride thin films deposited either by ICP-PECVD or sputtering, has been investigated for the tailored realization of key components in MEMS devices such as cantilevers, membranes or passivation layers. The goal was to gain deeper insight into the way that different deposition methods and parameters influence the chemical composition, microstructure, as well as physical properties of such films such as film stress or leakage current behaviour.

A review of relevant thin film deposition and patterning techniques (given in Chapter 2) provides a solid basis for the subsequent experimental chapters in this thesis. The specific characteristics of physical and chemical vapour deposition techniques were discussed, with an emphasis on the commonly used methods for the deposition of silicon nitride thin films. Together with the theoretical explanations of the corresponding deposition processes (including vacuum evaporation, DC and RF sputter deposition, and a variety of CVD techniques), technical considerations about the used instrumentation and equipment were also provided. Different etching techniques typically used for patterning and qualification of silicon nitride thin films were also discussed.

For the determination of the physical and chemical properties of thin film samples different analytical techniques are applied. An overview of those used within the subsequent chapters was given in Chapter 3. Transmission electron microscopy and related techniques is used for microstructural and compositional studies of silicon nitride thin films, while scanning electron microscopy is an advantageous technique for the investigation of topographical features. Optical methods such as spectral reflectometry and Fourier-transform infrared spectroscopy are valuable, non-destructive analytical tools for the measurement of thickness and the index of refraction, as well as for the determination of the chemical composition. For the latter purpose, X-ray techniques, such as energy-dispersive X-ray spectroscopy, and X-ray photoelectron spectroscopy are also applied. For the determination of important mechanical properties such as film stress, Young`s modulus and hardness, measurements with a wafer geometry set-up and a nanoindenter were performed.

One of the more flexible techniques for the synthesis of amorphous hydrogenated silicon nitride thin films – regarding the range of deposition parameters that can be effectively utilized – is inductively coupled plasma chemical vapour deposition (ICP-CVD). A multi-stage experimental series (covered in Chapter 4) was used to determine the most influential process variables that contribute to the resulting properties of the silicon nitride thin films, and the effects of those variables were

scrutinized individually. By far, the most dominant deposition parameter was found to be the ratio of the precursor gas flows $R_{N2/SiH4}$. Through this single parameter, the chemical composition of the resulting a-SiN_x:H thin films can be varied to a large degree. The corresponding change in the chemical composition of the sample leads to significant shift in virtually all of the physical properties investigated in this thesis. At high values of $R_{N2/SiH4}$, the resulting films are slightly silicon-rich, compared to stoichiometric Si_3N_4. The hydrogen in the film is predominantly stored in N-H bonds, and the microstructure of the films becomes permeable to oxygen and water vapour. This leads to a post-deposition oxidation of the samples. This effect has serious ramifications. First, these samples lose the robustness of silicon nitride against wet HF as know when deposited with LPCVD. Second, the long-term stability of the biaxial film stress is lost, as the incorporation of oxygen in the a-SiN_x:H matrix builds up compressive stress. These attributes make the films deposited with a high ratio of $R_{N2/SiH4}$ unsuitable for MEMS applications.

Conversely, a too low $R_{N2/SiH4}$ results in a-SiN_x:H samples that are highly silicon rich. Under these conditions, hydrogen is confirmed to be mainly stored in Si-H bonds. While these films are considerable more robust against HF etchants, and resistant to post-deposition oxidation, the strong compressive biaxial film stress up to -1.0 GPa and the severe non-stoichiometric composition disqualifies them from a broad range of applications.

There is, however a certain range of $R_{N2/SiH4}$, at about 0.75, where a-SiN_x:H films can be synthesized allowing a combination of the most beneficial material properties. This results in samples closer to the stoichiometric composition than those two types discussed above, while maintaining a low, long-term stable biaxial stress, which can even be tailored with other process parameters such as the plasma power and back pressure, without any measurable impact due to post-deposition oxidation. While the robustness in HF etchants is compromised by increase etch rates compared to using lower $R_{N2/SiH4}$ values, it remains at an acceptable level.

Another approach is the utilization of an auxiliary capacitively coupled plasma source during the ICP-CVD a-SiN_x:H deposition. This causes an immediate change in the plasma chemistry and a gradually increasing intensity of ion bombardment of the substrate, whereas both effects directly lead to compositional changes in the a-SiN_x:H deposit. These effects make the samples significantly less permeable to oxygen and water vapour, thus preventing post-deposition oxidation and drift of the biaxial film stress even when using high $R_{N2/SiH4}$ values This comes at the cost of extreme compressive stress (in the range of -1.7 to 2.5 GPa), which significantly limits the possible application field for this material.

Magnetron sputter deposition of silicon nitride thin films was also studied, using both DC and RF plasma power sources. Here, the main process variables were the plasma powers $P_{plasmaDC}$ and

$P_{plasmaRF}$, and the deposition pressure p_{back}. A very important fundamental difference was found in the chemical composition of RF and DC sputter deposited SiN_x films. While the former were found to be distinctively silicon-rich, the latter had a N/Si ratio substantially closer to a stoichiometric composition (x = 0.85…0.97 for RF, and x = 1.15…1.29 for DC samples, respectively). Even more important especially for MEMS device applications this led to a strong compressive biaxial film stress in RF sputter deposited films (> 1 GPa), strongly limiting their potential applicability as typically low-stress layers are required in MEMS. Stress relief is possible to some extent (up to 35%) by post-deposition thermal annealing up to 800°C. However, structural damage may occur resulting in delamination and blistering phenomena. DC sputter deposited SiN_x films are characterized by significantly lower values of biaxial stress between 0 to -1.3 GPa, which can also be appropriately tuned using the available process variables to the desired value. Both DC and RF magnetron sputter deposited films have shown high robustness against an HF etching solution.

Silicon nitride thin films are not only used in MEMS devices due to their mechanical properties, but also for their advantageous electrical features. The two most important quantities are low leakage currents under normal operating voltages, and a high dielectric breakdown strength, which both have been investigated for film thicknesses in the 40 to 300 nm range. These electrical properties have shown a large variation, especially in the case of ICP-CVD deposited a-SiN_x:H samples, depending on the specific deposition conditions.

Samples deposited using a high $R_{N2/SiH4}$ suffer from irreversible modification under elevated temperatures or electrical fields, which makes them unsuitable for most applications. Conversely, films deposited with a $R_{N2/SiH4}$ that is too low were found to be poor insulators, thus fulfilling only moderate electrical requirements. Samples synthesized using an intermediate precursor gas ratio, however, have excellent electrical characteristics, comparable to standard LPCVD SiN_x materials. Films deposited with the help of an auxiliary CCP excitation have also shown high potential, although not fully reaching the same performance level.

Sputter deposited silicon nitride thin films have shown a significantly smaller variation regarding their electrical characteristics, than their ICP-CVD deposited counterparts. Leakage current through these samples is dominated by ohmic conduction at low fields and Poole-Frenkel emission under higher electrical loads. RF magnetron sputter deposited samples reach very impressive resistivity (> 10^{13} Ω·cm) and breakdown strength (> 9MV/cm) values at room temperature, with low impact of the deposition parameters. With DC sputtered samples a similar performance is reached, but they are susceptible to variations depending on the kinetic energy of the particles during the sputter deposition process, meaning plasma power and/or chamber pressure.

7.2. Application Scenario and Outlook

An important prospective, and intended application field of the silicon nitride thin films scrutinized throughout this work was their utilization as structural, as well as capping passivation layers in all-electric AFM (atomic force microscopy) cantilevers for *in-situ* investigation of biological samples. This application would involve the immersion of the device into a PBS (phosphate buffered saline) solution. This creates an electrically conductive, and potentially corrosive environment from which the electrically functional parts of the device need to be protected, in order to ensure proper functionality and to avoid premature failure. For evaluation purposes test structures were designed and fabricated as well as a specific test setup was designed and built.

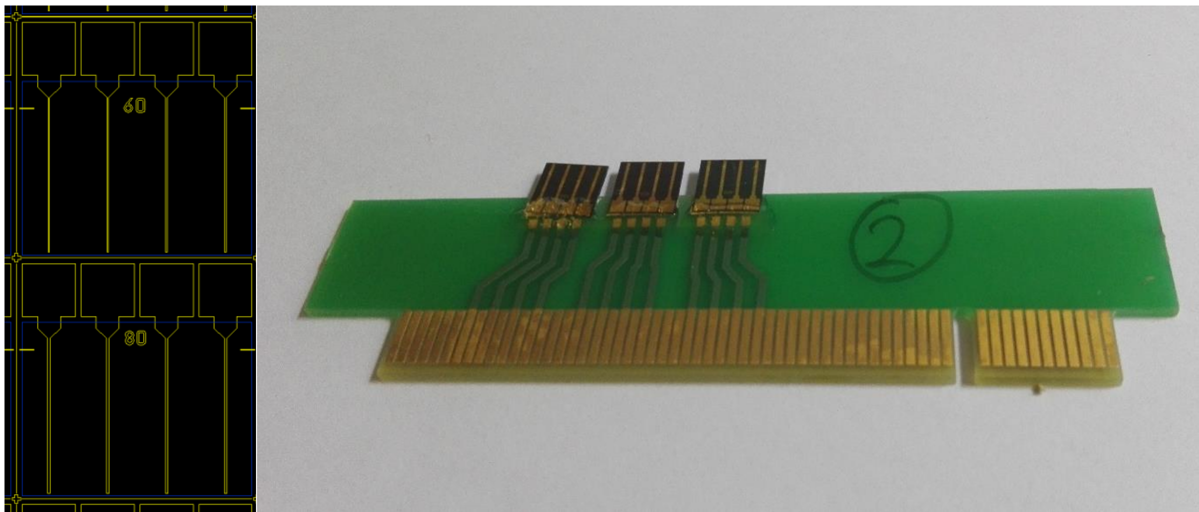

Figure 108: Layout (left) and realization (right) of the test devices for long-term performance testing of silicon nitride passivation layers in electrically conductive, liquid environments.

The test structures shown as schematic in Figure 108 are designed in such a way that they mimic the layer order of an actual device so the application scenario of the passivation layer can be simulated to a reasonable degree. The test structures were realized on silicon dies having a size of 8.4 by 8.4 mm, using the deposition techniques discussed earlier in this work, and photolithography. First, the silicon substrate was fully covered with a 300 nm thick sputter deposited silicon nitride film. In the next step, electrodes were deposited by e-beam evaporation of 10 nm chromium and 100 nm of gold, and patterned by using lift-off technique. The wafers were cut into rectangular dies using a wafer saw, and the electrodes were covered by capping passivation layers consisting of sputter deposited silicon nitride having thicknesses of 25 and 50 nm, as well as reference samples without any capping passivation. Topographical features of the samples, especially step coverage have been investigated

using SEM (See Figure 109), and it was ascertained that even the 25 nm thick passivation layers offered continuous coverage over the edges of the electrodes.

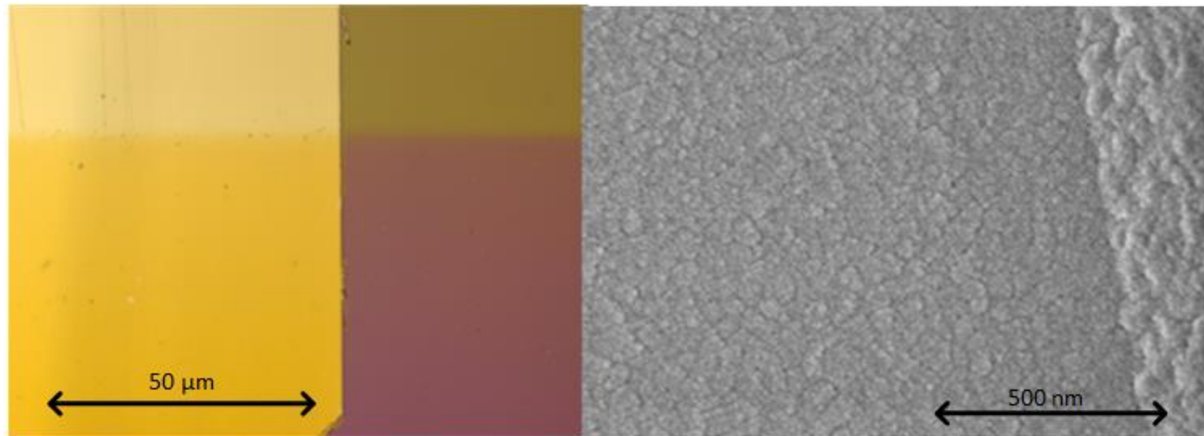

Figure 109: Optical (left) and scanning electron micrographs (right) of the edge coverage of 25 nm (left) and 50 nm (right) thin sputter deposited SiN_x films.

The test samples have been glued to custom-made PCB (printed circuit board) cards equipped with a standard PCI interface, while electrical contact was created by wire-bonding. The gold bonding wires have been encapsulated with epoxy resin for protection against electrical short-cuts. On each card three dies can be placed, each of them comprising of four test structures, thus making a simultaneous testing of 12 samples possible. The cards can be inserted to another custom-made PCB, which routed the signals from the PCI interface to 16 individual BNC outputs. Those were in turn connected through a computer-controlled multiplexer to a source/measure unit. The samples were partially immersed into a 1x PBS solution in a sealed container, in order to ensure a constant concentration by suppressing the evaporation of water. The excitation voltage was applied to a counter-electrode – an immersed unpassivated gold-plated die of the same size as the samples. A *Keithley 707A Switching Matrix* unit was used to switch between the samples every set period of time, where the current through the particular sample was measured by a *Keithley 2400 Sourcemeter*. Since the excitation signal was applied on the counter-electrode, it was present for all samples during the whole duration of the measurement cycle, accomplishing a quasi-simultaneous measurement of all samples. The recording of the measurement data, as well of the control of the equipment was performed using a *LabViEW* program.

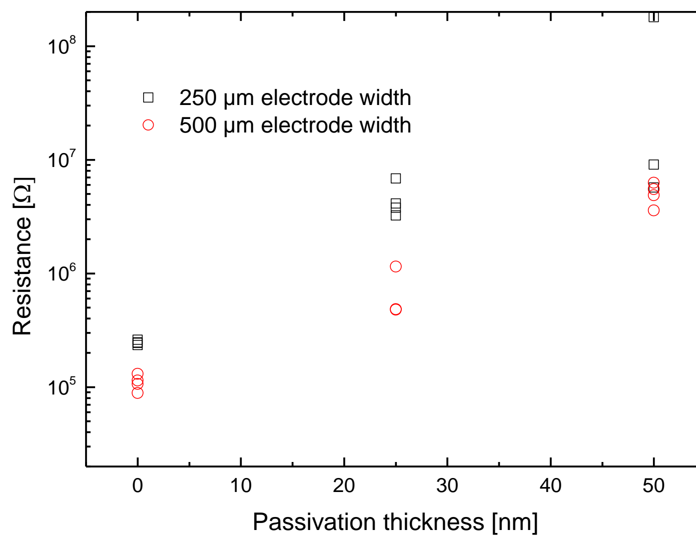

Figure 110: Resistance values in the test setup as a function of passivation thickness after a duration of 24h.

The samples having different electrode widths from 100 to 500 µm were exposed for a duration of one week apiece, applying excitation voltages ranging from 100 mV to 2000 mV. Even though SEM investigations have shown the presence of saline deposits on the sample surface after the measurement cycle was finished, significant degradation of the insulating performance during the test period which exceeds the intended lifespan in an AFM by far was not observed. What is more important, that the application of even a 25 nm thin passivation layer leads to the decrease of the leakage current by an order of magnitude compared to the unpassivated case. Increasing the passivation thickness results in an appropriate increase of the insulating performance (see Figure 110). Given these results one can make a more detailed decision about the appropriate thickness of applied passivation for an optimized performance.

Although the investigations concerning both ICP-CVD and magnetron sputter deposited amorphous silicon nitride thin films have led to significant novel insights into the tailoring of amorphous SiN_x film properties, there are a couple of new research directions promising to further deepen the understanding of their synthetization and the inner structure, as well as a few methods for a more effective application-oriented tuning of their material properties. The usage of sensor elements placed *in-situ* the deposition chamber such as Langmuir-probes and spectrometric tools could offer significant insight into the plasma chemistry during deposition, especially as function of the specific deposition parameters.

A further approach to increase the tunability of the thin film properties would be the usage of tertiary and quaternary material systems instead of pure silicon nitride. Especially the ICP-CVD method

offers a large variation of possibilities in the form of SiO_xN_y [61, 172], SiC_xN_y [173]and $SiO_xC_yN_z$ material systems [174], which can be easily realized with the introduction of N_2O and CH_4 precursor gases into the system. In the case of magnetron sputtering SiO_xN_y [98] materials can be deposited by simply adding O_2 to the sputtering gas mixture. Both of these methods offer a new dimension in parameter control, and are promising areas of future research.

Another promising approach that would optimally use the existing processes to deposit engineered thin films is the gradual tuning of process parameters during deposition [175]. This would allow to synthesize films with set stress-profiles for MEMS and refractive index profiles for optical applications. Another possibility would be to change the composition near the end of the deposition process to gain a chemically resistant surface layer, while the bulk of the material could have significantly different properties. These techniques are readily realizable given the capabilities of both the ICP-CVD and sputter deposition systems.

Bibliography

[1] G. Roos, MEMS market: Steady Growth, lower ASPs Ahead, Accessed 2016.06.14.
[2] Yole Dèvelopment, The MEMS industry: desperately seeking a second wind, Accessed 2016.04.25.
[3] C.J. Brown, J.M. Cheng, Electronic cigarettes: product characterisation and design considerations, Tobacco control, 23 (2014) ii4-ii10.
[4] J. Guidez, Y. Ribaud, O. Dessornes, C. Dumand, Micro engines for micro-drones propulsion, in: 4th European Micro UAV Meeting, Toulouse, France, September, 2004, pp. 15-17.
[5] J. Gubbi, R. Buyya, S. Marusic, M. Palaniswami, Internet of Things (IoT): A vision, architectural elements, and future directions, Future generation computer systems, 29 (2013) 1645-1660.
[6] W.H. Ko, Trends and frontiers of MEMS, Sensors and Actuators A: Physical, 136 (2007) 62-67.
[7] D. Manners, Consumer and mobile MEMS market in decline, in, 2016.
[8] S.h.P. Won, W.W. Melek, F. Golnaraghi, A Kalman/Particle Filter-Based Position and Orientation Estimation Method Using a Position Sensor/Inertial Measurement Unit Hybrid System, IEEE Transactions on Industrial Electronics, 57 (2010) 1787-1798.
[9] S. Gonseth, F. Rudolf, C. Eichenberger, D. Durrant, P. Airey, Miniaturized high-performance MEMS accelerometer detector, CEAS Space Journal, 7 (2015) 263-270.
[10] R.R. Syms, S. Wright, MEMS mass spectrometers: the next wave of miniaturization, Journal of Micromechanics and Microengineering, 26 (2016) 023001.
[11] P. Pitchappa, M. Manjappa, C.P. Ho, R. Singh, N. Singh, C. Lee, Active control of electromagnetically induced transparency analog in terahertz MEMS metamaterial, Advanced Optical Materials, 4 (2016) 541-547.
[12] J.G. Noel, Review of the properties of gold material for MEMS membrane applications, IET Circuits, Devices & Systems, 10 (2016) 156-161.
[13] C.H. Ng, K.W. Chew, S.F. Chu, Characterization and Comparison of PECVD Silicon Nitride and Silicon Oxynitride Dielectric for MIM Capacitors, IEEE Electron Device Letters, 24(8), (2003) 506-508.
[14] S.S. Sandeep, K. Warikoo, A. Kottantharayil, Optimization of ICP-CVD silicon nitride for Si solar cell passivation, in: Photovoltaic Specialists Conference (PVSC), 2012 38th IEEE, 2012, pp. 001102-001104.
[15] A. Khan, J. Philip, P. Hess, Young's modulus of silicon nitride used in scanning force microscope cantilevers, Journal of Applied Physics, 95 (2004) 1667-1672.
[16] K.S. Rao, M.D. Prakash, L.N. Thalluri, Cantilever and circular disc structure based capacitive shunt RF MEMS switches, in: 2016 International Conference on Electrical, Electronics, Communication, Computer and Optimization Techniques (ICEECCOT), 2016, pp. 336-338.
[17] A.A. Vasiliev, A.V. Pisliakov, A.V. Sokolov, N.N. Samotaev, S.A. Soloviev, K. Oblov, V. Guarnieri, L. Lorenzelli, J. Brunelli, A. Maglione, A.S. Lipilin, A. Mozalev, A.V. Legin, Non-silicon MEMS platforms for gas sensors, Sensors and Actuators B: Chemical, 224 (2016) 700-713.
[18] J. Geerlings, E. Sarajlic, J.W. Berenschot, M.H. Siekman, H.V. Jansen, L. Abelmann, N.R. Tas, Design and fabrication of in-plane AFM probes with sharp silicon nitride tips based on refilling of anisotropically etched silicon moulds, Journal of Micromechanics and Microengineering, 24 (2014) 105013.
[19] J.-W. Zhang, H. Fang, J.-W. Wang, L.-Y. Hao, X. Xu, C.-S. Chen, Preparation and characterization of silicon nitride hollow fiber membranes for seawater desalination, Journal of Membrane Science, 450 (2014) 197-206.
[20] M. Yuan, M.A. Cohen, G.A. Steele, Silicon nitride membrane resonators at millikelvin temperatures with quality factors exceeding 108, Applied Physics Letters, 107 (2015) 263501.
[21] W. Kühnel, G. Hess, A silicon condenser microphone with structured back plate and silicon nitride membrane, Sensors and Actuators A: Physical, 30 (1992) 251-258.
[22] M.P. Hughey, R.F. Cook, Stress development in plasma-enhanced chemical-vapor-deposited silicon nitride films, Journal of Applied Physics, 97 (2005) 114914.

[23] K.B. Gavan, H.J.R. Westra, E.W.J.M. van der Drift, W.J. Venstra, H.S.J. van der Zant, Size-dependent effective Young's modulus of silicon nitride cantilevers, Applied Phyiscs Letters, 94 (2009) 233108.
[24] Y. Yee Chia, L. Qiang, L. Wen-Chin, K. Tsu-Jae, H. Chenming, W. Xiewen, G. Xin, T.P. Ma, Direct tunneling gate leakage current in transistors with ultrathin silicon nitride gate dielectric, Electron Device Letters, IEEE, 21 (2000) 540-542.
[25] F.L. Riley, Silicon Nitride and Related Materials, J. Am. Ceram Soc., 83(2) (2000), 245-265.
[26] M.R. Stephen, Physical Vapor Deposition, in: Handbook of Semiconductor Manufacturing Technology, Second Edition, CRC Press, 2007, pp. 15-11-15-27.
[27] S.I. Shah, G.H. Jaffari, E. Yassitepe, B. Ali, Chapter 4 - Evaporation: Processes, Bulk Microstructures, and Mechanical Properties, in: P.M. Martin (Ed.) Handbook of Deposition Technologies for Films and Coatings (Third Edition), William Andrew Publishing, Boston, 2010, pp. 135-252.
[28] M.J. Madou, Fundamentals of Microfabrication: The Science of Miniaturization, Second Edition, Taylor & Francis, 2002.
[29] A. Anders, A structure zone diagram including plasma-based deposition and ion etching, Thin Solid Films, 518 (2010) 4087-4090.
[30] D. Depla, S. Mahieu, J.E. Greene, Chapter 5 - Sputter Deposition Processes, in: P.M. Martin (Ed.) Handbook of Deposition Technologies for Films and Coatings (Third Edition), William Andrew Publishing, Boston, 2010, pp. 253-296.
[31] Infrared Characterization for Microelectronics, W. S. Lau (Ed.) World Scientific (1999).
[32] C.F. Gallo, Corona-A Brief Status Report, Industry Applications, IEEE Transactions on, IA-13 (1977) 550-557.
[33] P. Sigmund, Theory of Sputtering. I. Sputtering Yield of Amorphous and Polycrystalline Targets, Physical Review, 184 (1969) 383-416.
[34] Y. Yamamura, H. Tawara, Energy Dependence of Ion-Induced Sputtering Yields from Monatomic Solids at Normal Incidence, Atomic Data and Nuclear Data Tables, 62 (1996) 149-253.
[35] J.E. Mahan, A. Vantomme, A simplified collisional model of sputtering in the linear cascade regime, Journal of Vacuum Science & Technology A, 15 (1997) 1976-1989.
[36] K.T.A.L. Burm, Calculation of the Townsend Discharge Coefficients and the Paschen Curve Coefficients, Contributions to Plasma Physics, 47 (2007) 177-182.
[37] J.-O. Carlsson, P.M. Martin, Chapter 7 - Chemical Vapor Deposition, in: P.M. Martin (Ed.) Handbook of Deposition Technologies for Films and Coatings (Third Edition), William Andrew Publishing, Boston, 2010, pp. 314-363.
[38] M. Matsuura, Y. Hayashide, H. Kotani, H. Abe, Film Characteristics of APCVD Oxide Using Organic Silicon and Ozone, Japanese Journal of Applied Physics, 30 (1991) 1530.
[39] H. Matsumura, H. Umemoto, A. Masuda, Cat-CVD (hot-wire CVD): how different from PECVD in preparing amorphous silicon, Journal of Non-Crystalline Solids, 338–340 (2004) 19-26.
[40] S.B. Patil, A. Kumbhar, P. Waghmare, V. Ramgopal Rao, R.O. Dusane, Low temperature silicon nitride deposited by Cat-CVD for deep sub-micron metal–oxide–semiconductor devices, Thin Solid Films, 395 (2001) 270-274.
[41] H. Chang, L.J. Lee, R. Li Hwang, C.T. Yeh, M.S. Lin, J.C. Lou, T.H. Hseu, T.B. Wu, Y.-J. Chen, C.-P. Tang, Physical and chemical properties of the cylindrical rods SiCx (x = 0.3−1.2) grown from Si(CH3)2Cl2 by laser pyrolysis, Materials Chemistry and Physics, 44 (1996) 59-66.
[42] A. Stoffel, A. Kovacs, B. Müller, LPCVD against PECVD for micromechanical applications, J. Micromech. Microeng. 6 (1996) 1.
[43] X. Li-Qun, C. Mei, Chemical Vapor Deposition, in: Handbook of Semiconductor Manufacturing Technology, Second Edition, CRC Press, 2007, pp. 13-11-13-87.
[44] P.R. Scheeper, J.A. Voorthuyzen, P. Bergveld, PECVD silicon nitride diaphragms for condenser microphones, Sensors and Actuators B: Chemical, 4 (1991) 79-84.
[45] D. Smith, A. Alimonda, C. Chen, S. Ready, B. Wacker, Mechanism of SiNxHy Deposition from NH3-SiH4 Plasma, Journal of The Electrochemical Society, 137 (1990) 614-623.

[46] A. Benitez, J. Bausells, E. Cabruja, J. Esteve, J. Samitier, Proceedings of Eurosensors VIStress in low pressure chemical vapour deposition polycrystalline silicon thin films deposited below 0.1 Torr, Sensors and Actuators A: Physical, 37 (1993) 723-726.
[47] S. Wolf, R.N. Tauber, Chemical Vapor Deposition (CVD) of Amorphous & Polycrystillane Films, in: Silicon Processing for the VLSI Era, Lattice Press, Sunste Beach, CA, 2000.
[48] D. Peters, K. Fischer, J. Müller, Integrated optics based on silicon oxynitride thin films deposited on silicon substrates for sensor applications, Sensors and Actuators A: Physical, 26 (1991) 425-431.
[49] J. Yota, J. Hander, A. Saleh, A comparative study on inductively-coupled plasma high-density plasma, plasma-enhanced, and low pressure chemical vapor deposition silicon nitride films, Journal of Vacuum Science & Technology A, 18 (2000) 372-376.
[50] F.H.P.M. Habraken, R.H.G. Tijhaar, W.F. van der Weg, A.E.T. Kuiper, M.F.C. Willemsen, Hydrogen in low-pressure chemical-vapor-deposited silicon (oxy)nitride films, Journal of Applied Physics, 59 (1985) 447-453.
[51] R.M. Tiggelaar, A.W. Groenland, R.G.P. Sanders, J.G.E. Gardeniers, Electrical properties of low pressure chemical vapor deposited silicon nitride thin films for temperatures up to 650 °C, Journal of Applied Physics, 105 (2009) 033714.
[52] M.J. Powell, Charge trapping instabilities in amorphous silicon-silicon nitride thin-film transistors, Applied Physics Letters, 43 (1983) 597-599.
[53] P. Eriksson, J.Y. Andersson, G. Stemme, Thermal characterization of surface-micromachined silicon nitride membranes for thermal infrared detectors, Microelectromechanical Systems, Journal of, 6 (1997) 55-61.
[54] J.G.E. Gardeniers, H.A.C. Tilmans, C.C.G. Visser, LPCVD silicon-rich silicon nitride films for applications in micromechanics, studied with statistical experimental design*, Journal of Vacuum Science & Technology A, 14 (1996) 2879-2892.
[55] L. Martinu, O. Zabeida, J.E. Klemberg-Sapieha, Chapter 9 - Plasma-Enhanced Chemical Vapor Deposition of Functional Coatings, in: P.M. Martin (Ed.) Handbook of Deposition Technologies for Films and Coatings (Third Edition), William Andrew Publishing, Boston, 2010, pp. 392-465.
[56] T. Ono, H. Nishimura, M. Shimada, S. Matsuo, Electron cyclotron resonance plasma source for conductive film deposition, Journal of Vacuum Science & Technology A, 12 (1994) 1281-1286.
[57] M. Moisan, C. Barbeau, R. Claude, C.M. Ferreira, J. Margot, J. Paraszczak, A.B. Sá, G. Sauvé, M.R. Wertheimer, Radio frequency or microwave plasma reactors? Factors determining the optimum frequency of operation, Journal of Vacuum Science & Technology B, 9 (1991) 8-25.
[58] B. Chapman, Glow discharge processes: sputtering and plasma etching, Wiley-Interscience, 1980.
[59] L. Martinu, J.E. Klemberg-Sapieha, O.M. Küttel, A. Raveh, M.R. Wertheimer, Critical ion energy and ion flux in the growth of films by plasma-enhanced chemical-vapor deposition, Journal of Vacuum Science & Technology A, 12 (1994) 1360-1364.
[60] A. Amassian, M. Svec, P. Desjardins, L. Martinu, Interface broadening due to ion mixing during thin film growth at the radio-frequency-biased electrode in a plasma-enhanced chemical vapor deposition environment, Journal of Vacuum Science & Technology A, 24 (2006) 2061-2069.
[61] D. Criado, I. Pereyra, M.I. Alayo, Study of nitrogen-rich silicon oxynitride films obtained by PECVD, Materials Characterization, 50 (2003) 167-171.
[62] D. Criado, M.I. Alayo, I. Pereyra, M.C.A. Fantini, Structural analysis of silicon oxynitride films deposited by PECVD, Materials Science and Engineering B, 112 (2004) 123-127.
[63] X. Xu, L. Zhang, L. Huang, Q. He, T. Fan, Z. Yang, Y. Jiang, Zhanping, A comparison of structures and properties of SiN_x and SiO_x films prepared by PECVD, Journal of Non-Crystalline Solids,(2012) 99-106.
[64] M.S. Haque, H.A. Naseem, W.D. Brown, Post-deposition processing of low temperature PECVD silicon dioxide films for enhanced stress stability, Thin Solid Films, 308-309 (1997) 68-73.
[65] S.H. Lee, I. Lee, J. Yi, Silicon nitride films prepared by high-density plasma chemical vapor deposition for solar cell applications, Surface and Coatings Technology, 153 (2002) 67-71.
[66] L. da Silva Zambom, R.D. Mansano, R. Furlan, Silicon nitride deposited by inductively coupled plasma using silane and nitrogen, Vacuum, 65 (2002) 213-220.

[67] L. da Silva Zambom, P. Verdonck, Deposition of silicon oxynitride at room temperature by Inductively Coupled Plasma-CVD, Thin Solid Films, 515 (2006) 596-598.
[68] K. Warikoo, S.S. Sandeep, A. Kottantharayil, Optimization of ICP-CVD Silicon Nitride for SI Solar Cell Passivation, Proceedings ofthe 38th IEEE Photovoltaic Specialist Conference 2012.
[69] W.L. Johnson, 3 - Electrostatically-Shielded Inductively-Coupled RF Plasma Sources, in: O.A. Popov (Ed.) High Density Plasma Sources, William Andrew Publishing, Park Ridge, NJ, 1996, pp. 100-148.
[70] L.S. Zambom, R.D. Mansano, R. Furlan, P. Verdonck, LPCVD deposition of silicon nitride assisted by high density plasmas, Thin Solid Films, 343-344 (1999) 299-301.
[71] R. Wolf, K. Wandel, B. Gruska, Low-temperature ICPECVD of silicon nitride in SiH_4-NH_3-Ar discharges analyzed by spectroscopic ellipsometry and etch behavior in KOH and BHF, Surface and Coatings Technology, 142-144 (2001) 786-791.
[72] Y.C. Chou, R. Lai, G.P. Li, P. Nam, R. Grundbacher, M. Barsky, H.K. Kim, Y. Ra, A. Oki, D. Streit, Innovative nitride passsivation of 0.1 µm InGaAs/InAlAs/InP HEMTs using high-density inductively coupled plasma CVD (HD-ICP-CVD), IPMP, 14 (2002) 315-318.
[73] S.-S. Han, B.-H. Jun, K. No, B.-S. Bae, Preparation of a a-SiN_x Thin Film with Low Hydrogen Content by Inductively Coupled Plasma Enhanced Chemical Vapor Deposition, J. Electrochem. Soc., 145 (1998) 652-658.
[74] A. Kshirsagar, P. Nyaupane, D. Bodas, S.P. Duttagupta, S.A. Gangal, Deposition and characterization of low temperature silicon nitride films deposited by inductively coupled plasma CVD, Applied Surface Science, 257 (2011) 5052-5058.
[75] E.F. Gene, Optical Lithography, in: Handbook of Semiconductor Manufacturing Technology, Second Edition, CRC Press, 2007, pp. 18-11-18-50.
[76] Photolithography: Theory and Application of Photoresists, Etchants and Solvents, in: Microchemicals GmBH (Ed.), 2012.
[77] R.E. Lee, Microfabrication by ion-beam etching, Journal of Vacuum Science & Technology, 16 (1979) 164-170.
[78] F.I. Chang, R. Yeh, G. Lin, P.B. Chu, E.G. Hoffman, E.J. Kruglick, K.S.J. Pister, M.H. Hecht, Gas-phase silicon micromachining with xenon difluoride, in, 1995, pp. 117-128.
[79] R.G. Poulsen, Plasma etching in integrated circuit manufacture—A review, Journal of Vacuum Science & Technology, 14 (1977) 266-274.
[80] L.G.V. Peter, R. Shahid, S. Terry, Plasma Etch, in: Handbook of Semiconductor Manufacturing Technology, Second Edition, CRC Press, 2007, pp. 21-21-21-69.
[81] J. Henri, G. Han, B. Meint de, E. Miko, F. Jan, A survey on the reactive ion etching of silicon in microtechnology, Journal of Micromechanics and Microengineering, 6 (1996) 14.
[82] A.A. Ayón, R. Braff, C.C. Lin, H.H. Sawin, M.A. Schmidt, Characterization of a Time Multiplexed Inductively Coupled Plasma Etcher, Journal of The Electrochemical Society, 146 (1999) 339-349.
[83] K.R. Williams, R.S. Muller, Etch rates for micromachining processing, Journal of Microelectromechanical Systems, 5 (1996) 256-269.
[84] H. Seidel, L. Csepregi, A. Heuberger, H. Baumgärtel, Anisotropic Etching of Crystalline Silicon in Alkaline Solutions: I . Orientation Dependence and Behavior of Passivation Layers, Journal of The Electrochemical Society, 137 (1990) 3612-3626.
[85] R.F. Egerton, Choice of operating voltage for a transmission electron microscope, Ultramicroscopy, 145 (2014) 85-93.
[86] L. Reimer, Transmission electron microscopy: physics of image formation and microanalysis, Springer, 2013.
[87] R. Egerton, Electron energy-loss spectroscopy in the electron microscope, Springer Science & Business Media, 2011.
[88] J. Goldstein, D.E. Newbury, P. Echlin, D.C. Joy, A.D. Romig Jr, C.E. Lyman, C. Fiori, E. Lifshin, Scanning electron microscopy and X-ray microanalysis: a text for biologists, materials scientists, and geologists, Springer Science & Business Media, 2012.
[89] G.E. Lloyd, Atomic number and crystallographic contrast images with the SEM: a review of backscattered electron techniques, Mineralogical Magazine, 51 (1987) 3-19.

[90] W.E. Swartz, X-ray photoelectron spectroscopy, Analytical Chemistry, 45 (1973) 788a-800a.
[91] D.A. Skoog, J.J. Leary, Instrumentelle Analytik: Grundlagen-Geräte-Anwendungen, Springer-Verlag, 2013.
[92] Introduction to INfrared Sepctroscopy, in: Infrared Characterization for Microelectronics, pp. 1-13.
[93] The Characterization of Silicon Dioxide and Silicon Nitride Thin Films, in: Infrared Characterization for Microelectronics, pp. 55-85.
[94] Part II - Instruments and measurement techniques of three-dimensional surface topography, in: K.J. Stout, L. Blunt (Eds.) Three Dimensional Surface Topography, Butterworth-Heinemann, Oxford, 2000, pp. 19-94.
[95] G. Binnig, C.F. Quate, C. Gerber, Atomic Force Microscope, Physical Review Letters, 56 (1986) 930-933.
[96] N.A. Geisse, AFM and combined optical techniques, Materials Today, 12 (2009) 40-45.
[97] B. Poon, D. Rittel, G. Ravichandran, An analysis of nanoindentation in linearly elastic solids, International Journal of Solids and Structures, 45 (2008) 6018-6033.
[98] Y. Liu, X.Z. I.-Kuan Lin, Mechanical properties of sputtered silicon oxynitride films by nanoindentation, Materials Science and Engineering A, 489 (2008) 294-301.
[99] Spectral reflectometry, in: Nova. Ltd. (Ed.), Download date: 2015.11.24.
[100] P. Hlubina, J. Luňáček, D. Ciprian, R. Chlebus, Spectral interferometry and reflectometry used to measure thin films, Applied Physics B, 92 (2008) 203-207.
[101] P.H. Townsend, D.M. Barnett, T.A. Brunner, Elastic relationships in layered composite media with approximation for the case of thin films on a thick substrate, Journal of Applied Physics, 62 (1987) 4438-4444.
[102] G.G. Stoney, The tension of metallic films deposited by electrolysis, Proceedings of the Royal Society of London. Series A, Containing Papers of a Mathematical and Physical Character, 82 (1909) 172-175.
[103] C. Wild, P. Koidl, Thermal gas effusion from hydrogenated amorphous carbon films, Applied Physics Letters, 51 (1987) 1506-1508.
[104] D. Dergez, J. Schalko, A. Bittner, U. Schmid, Fundamental properties of a-SiN_x:H thin films deposited by ICP_PECVD for MEMS applications, Applied Surface Science, 284 (2013) 348-353.
[105] D. Dergez, A. Bittner, J. Schalko, U. Schmid, Low-stress and long-term stable a-SiN<inf>x</inf>:H films deposited by ICPPECVD, Procedia Engineering, 2014, pp. 100-103.
[106] D. Dergez, J. Schalko, S. Löffler, A. Bittner, U. Schmid, Impact of auxiliary capacitively coupled plasma on the properties of ICP-CVD deposited a-SiNx:H thin films, Sensors and Actuators, A: Physical, 224 (2015) 156-162.
[107] J.A. Jacquez, Design of experiments, Journal of the Franklin Institute, 335 (1998) 259-279.
[108] J. Chen, D. Sun, C. Wu, A catalogue of two-level and three-level fractional factorial designs with small runs, International Statistical Review/Revue Internationale de Statistique, (1993) 131-145.
[109] Q. Xu, Y. Ra, M. Bachman, G.P. Li, Characterization of low-temperature silicon nitride films produced by inductively coupled plasma chemical vapor deposition, J. Vac. Sci. Technol. A, 27 (2009) 145-156.
[110] Z. Lu, P. Santos-Filho, G. Stevens, M.J. Williams, G. Lucovsky, Fourier transform infrared study of rapid thermal annealing of a-Si:N:H(D) films prepared by remote plasma-enhanced chemical vapor deposition, J. Vac. Sci. Technol. A, 13 (1995) 607-613.
[111] W.S. Lau, Infrared Characterization for Microelectronics, World Scientific, Singapore, 1999.
[112] M. Matsuoka, S. Isotani, W. Sucasire, L.S.Z. amd K. Ogata, Chemical bonding and composition of silicon nitride films prepared by inductively coupled plasma chemical vapor deposition, Surface and Coatings Technology, 204 (2010) 2923-2927.
[113] H. Dun, P. Pan, F.R. White, R.W. Douse, Mechanisms of Plasma-Enhanced Silicon Nitride Deposition Using SiH4 / N 2 Mixture, Journal of The Electrochemical Society, 128 (1981) 1555-1563.
[114] W.-S. Liao, S.-C. Lee, Water-Resistant Coating on Low Temperature Amorphous Silicon Nitride Films by a Thin Layer of Amorphous Silicon Hydrogen Alloy, J. Electrochem. Soc., 144 (1997) 1477-1481.

[115] H. San, Z. Deng, Y. Yu, G. Li, X. Chen, Study on dielectric charging in low-stress silicon nitride with the MIS structure for reliable MEMS applications, Journal of Micromechanics and Microengineering, 21 (2011) 125019.
[116] W.S. Liao, C.H. Lin, S.C. Lee, Oxidation of silicon nitride prepared by plasma-enhanced chemical vapor deposition at low temperature, Applied physics letters, 65 (1994) 2229-2231.
[117] E. Kobeda, E.A. Irene, In situ stress measurements during thermal oxidation of silicon, Journal of Vacuum Science & Technology B: Microelectronics Processing and Phenomena, 7 (1989) 163-166.
[118] A.K. Sinha, E. Lugujjo, Lorentz-Lorenz correlation for reactively plasma deposited Si-N films, Applied Physics Letters, 32 (1978) 245-246.
[119] J. Bandet, B. Despax, M. Caumont, Nitrogen bonding environments and local order in hydrogenated amorphous silicon nitride films studied by Raman spectroscopy, Journal of Apllied Physics, 85 (1999) 7899-7904.
[120] W.L. Warren, F.C. Rong, E.H. poindexter , G.J. Geraldi, J. Kanicky, Structural identification of the slicon and nitrogen dangling-bond centeres in amorphous silicon nitride, Journal of Applied Physics, 70 (1991) 346-354.
[121] K.T. Butler, M.P.W.E. Lamers, A.W. Weeber, J.H. Harding, Molecular dynamics studies of the bonding properties of amorphous silicon nitride coatings on crystalline silicon, Journal of Applied Physics, 110 (2011) 124905.
[122] P.V. Rysselberghe, Remarks concerning the Clausius-Mossotti Law, The Journal of Physical Chemistry, 36 (1931) 1152-1155.
[123] G. Ziegler, J. Heinrich, G. Wötting, Relationships between processing, microstructure and properties of dense and reaction-bonded silicon nitride, Journal of Materials Science, 22 (1987) 3041-3086.
[124] M.K. Gunde, M. Macek, The relationship between the macroscopic properties of PECVD silicon nitride and oxynitride layers and the characteristics of their networks, Applied Physics A, 74 (2001) 181-186.
[125] R.-Y. Tsai, L.-C. Kuo, F.C. Ho, Amorphous silicon and amorphos silicon nitride films preapred by a plasma-enhanced chemical vapor deposition process as optical coating materials, Applied Optics, 32 (1993) 5561-5566.
[126] K.B. Sundaram, R.E. Sah, H. Baumann, K. Balachandran, R.M. Todi, Wet etching of silicon nitride thin films deposited by electron cyclotron resonance (ECR) plasma enhanced chemical vapor deposition, Microelectronic Engineering, 70 (2003) 109-114.
[127] D.M. Knotter, T.D. Denteneer, Etching mechanism of silicon nitride in HF-based solutions, Journal of The Electrochemical Society, 148 (2001) F43-F46.
[128] W. Lanford, M. Rand, The hydrogen content of plasma-deposited silicon nitride, Journal of Applied Physics, 49 (1978) 2473-2477.
[129] K.R. Williams, K. Gupta, M. Wasilik, Etch rates for micromachining processing-Part II, Journal of Microelectromechanical Systems, 12 (2003) 761-778.
[130] D. Dergez, M. Schneider, A. Bittner, U. Schmid, Mechanical and electrical properties of DC magnetron sputter deposited amorphous silicon nitride thin films, Thin Solid Films, 589 (2015) 227-232.
[131] D. Dergez, M. Schneider, A. Bittner, N. Pawlak, U. Schmid, Mechanical and electrical properties of RF magnetron sputter deposited amorphous silicon-rich silicon nitride thin films, Thin Solid Films, 606 (2016) 7-12.
[132] K.-F. Chiu, M.G. Blamire, Z.H. Barber, Microstructure modification of silver films deposited by ionized magnetron sputter deposition, Journal of Vacuum Science & Technology A, 17 (1999) 2891-2895.
[133] P.P. Ferguson, A.D.W. Todd, M.L. Martine, J.R. Dahn, Structure and Performance of Tin-Cobalt-Carbon Alloys Prepared by Attriting, Roller Milling and Sputtering, Journal of The Electrochemical Society, 161 (2014) A342-A347.
[134] L. Stöber, J.P. Konrath, S. Krivec, F. Patocka, S. Schwarz, A. Bittner, M. Schneider, U. Schmid, Impact of sputter deposition parameters on molybdenum nitride thin film properties, Journal of Micromechanics and Microengineering, 25 (2015) 074001.

[135] M. Wittmer, Properties and microelectronic applications of thin films of refractory metal nitrides, Journal of Vacuum Science & Technology A, 3 (1985) 1797-1803.
[136] H. Liang, Q.Z. an Feng Gao, W. Yuan, Y. Dong, Effect of RF Sputtering Power on the Structural, Optical and Hydrophobic Properties of SiN_x Thin Film, Advanced Materials Research.
[137] G. Xu, P. Jin, M. Tazawa, K. Yoshimura, Optical investigation of silicon nitride thin films deposited by r. f. magnetron sputtering, Thin Solid Films, 425 (2003) 196-202.
[138] F. Gao, Q. Zhao, X. Zhao, Influence of Substrate Temperature on Silicon Nitride Films Deposited by R.F. Magnetron Sputtering, Advanced Materials Research, 150-151 (2011) 1391-1395.
[139] W.M. Haynes, CRC handbook of chemistry and physics, CRC press, 2014.
[140] M.A. Signore, A. Sytchkova, D. Dimaio, A. Capello, A. Rizzo, Deposition of silicon nitride thin films by RF magnetron sputtering: a material and growth process study, Optical Materials.
[141] M.A. Signore, A. Sytchkova, D. Dimaio, A. Cappello, A. Rizzo, Deposition of silicon nitride thin films by RF magnetron sputtering: a material and growth process study, Optical Materials, 34 (2012) 632-638.
[142] P.S. Nayar, Refractive index control of silicon nitride films prepared by radio-frequency reactive sputtering, J. Vac. Sci. Technol. A, 20 (2002) 2137-2139.
[143] A.R. Nyaiesh, L. Holland, The dependence of deposition rate on power input for dc and rf magnetron sputtering, Vacuum, 31 (1981) 315-317.
[144] T. Makino, Composition and Structure Control by Source Gas Ratio in LPCVD SiN x, Journal of The Electrochemical Society, 130 (1983) 450-455.
[145] L. Wen, H. Howard, Silicon Materials, in: Handbook of Semiconductor Manufacturing Technology, Second Edition, CRC Press, 2007, pp. 3-1-3-78.
[146] G. Gioia, M. Ortiz, Delamination of Compressed Thin Films, Advances in Applied Mechanics, 33 (1997) pp. 120-188.
[147] J.W. Hutchinson, Mechanics of thin films and multilayers: Course Notes, in, Technical University of Denmark, 1996.
[148] S. Maniv, A comparison of deposition rates and temperature measurements for dc and rf diode sputtering, Journal of Applied Physics, 69 (1991) 8411-8413.
[149] G. Este, W.D. Westwood, A quasi-direct-current sputtering technique for the deposition of dielectrics at enhanced rates, Journal of Vacuum Science & Technology A, 6 (1988) 1845-1848.
[150] J. Henrie, S. Kellis, S.M. Schultz, A. Hawkins, Electronic color charts for dielectric films on silicon, Opt. Express, 12 (2004) 1464-1469.
[151] S.M. Sze, Current Transport and Maximum Dielectric Strength of Silicon Nitride Films, Journal of Apllied Physics, 38 (1967) 2951-2956.
[152] S.M. Sze, K.K. Ng, Physics of semiconductor devices, John wiley & sons, 2006.
[153] M. Lenzlinger, E. Snow, Fowler-Nordheim tunneling into thermally grown SiO2, Journal of Applied physics, 40 (1969) 278-283.
[154] S. Pollack, Schottky field emission through insulating layers, Journal of Applied Physics, 34 (1963) 877-880.
[155] P. Rottländer, M. Hehn, A. Schuhl, Determining the interfacial barrier height and its relation to tunnel magnetoresistance, Physical Review B, 65 (2002) 054422.
[156] H.L. Tuller, Ionic conduction in nanocrystalline materials, Solid State Ionics, 131 (2000) 143-157.
[157] A. Rose, Space-Charge-Limited Currents in Solids, Physical Review, 97 (1955) 1538-1544.
[158] M. Ohring, Materials science of thin films, Academic press, 2001.
[159] J. Stathis, Percolation models for gate oxide breakdown, Journal of applied physics, 86 (1999) 5757-5766.
[160] W. Weibull, A statistical distribution function of wide applicability, Journal of Applied Mechanics, 18 (1951) 293-297.
[161] M. Schneider, A. Bittner, A. Klein, U. Schmid, Impact of film thickness and temperature on the dielectric breakdown behavior of sputtered aluminum nitride thin films, Microelectronic Engineering, 140 (2015) 47-51.

[162] J.-S. Yoo, J.-S. Cho, J.-H. Park, S.-K. Ahn, K.-S. Shin, K.-H. Yoon, J. Yi, Electrical characterization of MIS devices using PECVD SiN x :H films for application of silicon solar cells, Journal of the Korean Physical Society, 61 (2012) 89-92.
[163] T.E. Hansen, Silicon UV-Photodiodes Using Natural Inversion Layers, Physica Scripta, 18 (1978) 471.
[164] N. Klein, H. Gafni, The maximum dielectric strength of thin silicon oxide films, IEEE Transactions on Electron Devices, ED-13 (1966) 281-289.
[165] C.R. Cleavelin, C. Luigi, N. Hiro, P. Sylvia, M.V. Eric, Oxidation and Gate Dielectrics, in: Handbook of Semiconductor Manufacturing Technology, Second Edition, CRC Press, 2007, pp. 9-1-9-37.
[166] M. Vila, C. Prieto, R. Ramirez, Electrical behavior of silicon nitride sputtered thin films, Thin Solid Films, 459 (2004) 195-199.
[167] M. Vila, E. Roman, C. Prieto, Electrical conduction mechanism in silicon nitride and oxy-nitride-sputtered thin films, Journal of Applied Physics, 97 (2005) 113710.
[168] S.A. Awan, R.D. Gould, S. Gravano, Electrical conduction proceses in silicon nitride thin films prepared by rf magnetron sputtering using nitrogen gas, Thin Solid Films, 355-356 (1999) 4556-4460.
[169] K.P. Weinfurt, Multivariate analysis of variance, (1995).
[170] K. Mokeddem, M. Aoucher, T. Smail, Hydrogenated amorphous silicon nitride deposited by DC magnetron sputtering, Superlattices and Microstructures, 40 (2006) 598-602.
[171] C.M. Osburn, E.J. Weitzman, Electrical Conduction and Dielectric Breakdown in Silicon Dioxide Films on Silicon, Journal of The Electrochemical Society, 119 (1972) 603-609.
[172] A.E.T. Kuiper, S.W. Koo, F.H.P.M. Habraken, Y. Tamminga, Deposition and composition of silicon oxynitride films, J. Vac. Sci. Technol. B, 1 (1982) 62-66.
[173] V.I. Ivashchenko, A.O. Kozak, O.K. Porada, L.A. Ivashchenko, O.K. Sinelnichenko, O.S. Lytvyn, T.V. Tomila, V.J. Malakhov, Characterization of SiCN thin films: Experimental and theoretical investigations, Thin Solid Films, 569 (2014) 57-63.
[174] S.C. Hamm, J. Waidmann, J.C. Mathai, K. Gangopadhyay, L. Currano, S. Gangopadhyay, Characterization and versatile applications of low hydrogen content SiOCN grown by plasma-enhanced chemical vapor deposition, Journal of Applied Physics, 116 (2014) 104902.
[175] A. Tarraf, J. Daleiden, S. Irmer, D. Prasai, H. Hillmer, Stress investigation of PECVD dielectric layers for advanced optical MEMS, Journal of Micromechanics and Microengineering, 14 (2004) 317.

List of Figures

Figure 1: Illustration of the cosine law in a vacuum evaporation arrangement. 6
Figure 2: Schematic view of a vacuum evaporation system, featuring a thermal and an e-beam source. 7
Figure 3: I-V characteristics of an electrical discharge with the most important regions highlighted [32]. 8
Figure 4: Schematic view of a DC magnetron sputtering system. 10
Figure 5: Schematic view on an RF magnetron sputtering system. 12
Figure 6: Schematic view of a hot wall LPCVD reactor. 15
Figure 7: Schematic view of a cold wall LPCVD reactor. 16
Figure 8: Schematic view of a capacitively coupled PECVD system. 18
Figure 9: Schematic view of an ECR-CVD system. 20
Figure 10: Schematic view of an ICP-CVD system with a load-lock chamber. 22
Figure 11: A simplified illustration of a photolithography process featuring a positive photoresist. a: Exposure, b:Development, c: Pattern transfer by etching, d: Resist stripping. 25
Figure 12: Illustration of the lift-off process, with the following steps: a: Resist exposure, b: Development, c: Thin film deposition, d: Lift-off. 25
Figure 13: Typical problems in physical dry etching. 27
Figure 14: Schematic representation of typical bulk micromachined structures created by anisitropic wet etching of (100) Si. a: V-groove, b: cantilever, c: membrane. 31
Figure 15: A typical, schematic electron energy loss spectrum (after Egerton et al. [87]). 35
Figure 16: Interaction volume of the incident e-beam and surface-near sample material during SEM probing (after [89]). 36
Figure 17: Michelson interferometer in an FTIR spectrometer. 39
Figure 18: Photograph of the Oxford Plasmalab 100 System used for the ICP-CVD silicon nitride deposition experiments. A schematic drawing is provided in section 2.2.3. 44
Figure 19: The index of refraction of ICP-CVD silicon nitride thin films versus deposition rate, grouping Type I and Type II samples by the dashed line. 47
Figure 20: Biaxial film stress of ICP-CVD silicon nitride thin films as a function of the deposition rate, grouping Type I and Type II samples including drift effects indicated by arrows. 47
Figure 21: Wet etch rate in hydrofluoric acid of ICP-CVD silicon nitride thin films versus deposition rate, grouping Type I and Type II samples. 48
Figure 22 : Comparison of the FTIR spectra of Type I and Type II ICP-CVD silicon nitride thin films with the most prominent absorption peaks highlighted. The peak at ~ 2350°cm^{-1} is attributed to atmospheric CO_2. 49
Figure 23: Detailed view on the silicon peak centred at the binding energy E_b of 102 eV of XPS spectra of Type I (a) and Type II (b) ICP-CVD silicon nitride thin films demonstrating the different chemical shift by a deconvolution into Si, Si_3N_4, and SiO_2-related peaks. 50
Figure 24: XPS depth profiles showing the apparent concertation of silicon, nitrogen and oxygen throughout the thickness of Type I (continuous line) and Type II (dotted line) ICP-CVD silicon nitride thin films. The sputter etch rate was approximately 0.04 nm/min, as in the case of the Type II sample the silicon substrate is reached. 51
Figure 25: Temporal evolution of the biaxial film stress of Type I and Type II ICP-CVD silicon nitride thin films, deposited at T_s = 120°C and 350°C, respectively. 52
Figure 26: XRD diffractograms of a Type I ICP-CVD deposited silicon nitride sample, "as deposited" and after annealing for 1h at 300°C under atmospheric conditions. The Si(100) peak is associated to the substrate. 55

Figure 27: The deposition rate of ICP-CVD silicon nitride thin films as a function of $R_{N2/SiH4}$. 57
Figure 28: The index of refraction of ICP-CVD silicon nitride thin films as a function of $R_{N2/SiH4}$. 58
Figure 29: The biaxial film stress of ICP-CVD silicon nitride thin films as a function of $R_{N2/SiH4}$ measured directly and 3 days after the deposition. 58
Figure 30: Concentrations of Si, N and O in ICP-CVD silicon nitride thin films measured with XPS as a function of $R_{N2/SiH4}$ values. 59
Figure 31: Chemical shift in binding energy of the XPS Si-related peak of ICP-CVD silicon nitride thin films as a result of a change in $R_{N2/SiH4}$. 60
Figure 32: FT-IR spectra of ICP-CVD silicon nitride thin films deposited at selected $R_{N2/SiH4}$ values. 60
Figure 33: Heater temperature and hydrogen partial pressure as a function of time in the high temperature effusion measurement setup. The sample used was a Type I a-SiN_x:H film with d = 300 nm. 61
Figure 34: Process parameters enabling to tailor the biaxial film stress of ICP-CVD deposited silicon nitride thin films while preserving its stability. a): The impact of p_{dep}, with T_{dep} = 350°C, $R_{N2/SiH4}$ = 0.75 and P_{ICP} = 750 W b): The impact of P_{ICP}, with T_{dep} =350°C, $R_{N2/SiH4}$ = 0.75 and p_{dep} = 7 mTorr. 62
Figure 35: The deposition rate of ICP-CVD silicon nitride thin films as a function of P_{RF}. 64
Figure 36: The resulting bias voltage in the ICP-CVD silicon nitride process as a function of P_{RF}. 65
Figure 37: The index of refraction of ICP-CVD silicon nitride thin films as a function of P_{RF}. 66
Figure 38: The biaxial film stress of ICP-CVD silicon nitride thin films as a function of P_{RF}. 67
Figure 39: Impact of the auxiliary CCP plasma source on the FT-IR spectra of ICP-CVD silicon nitride thin films deposited using different $R_{N2/SiH4}$ values. 68
Figure 40: Overview of the FT-IR spectra of ICP-CVD silicon nitride thin films syntesized at different P_{RF} values. 69
Figure 41: Bond density of the Si-H asymmetric stretching band extracted from the FT-IR spectra of ICP-CVD silicon nitride thin films as a function of P_{RF} in arbitrary units. 70
Figure 42: Bond density in arbitrary units (a) and peak shift (b) of the main Si-N asymmetric stretch absorption band extracted from the FT-IR spectra of ICP-CVD silicon nitride thin films as a function of P_{RF}. 71
Figure 43: Bond density of the Si-N-H_2 asymmetric absorption band extracted from the FT-IR spectra of ICP-CVD silicon nitride thin films as a function of P_{RF} in arbitrary units. 71
Figure 44: Bright field high-resolution transmission electron micrographs of ICP-CVD silicon nitride films deposited using different values of P_{RF}. a): 0 W b): 35 W c): 150 W. 72
Figure 45: TEM selected area diffraction pattern of an ICP-CVD silicon nitride thin film sample. 73
Figure 46: The wet etch rate WER in hydrofluoric acid of ICP-CVD silicon nitride thin films as a function of the capacitively coupled plasma power P_{RF}. 74
Figure 47: The RIE etch rate r_{RIE} in CF_4:O_2 plasma of ICP-CVD silicon nitride thin films as a function of the capacitively coupled plasma power P_{RF}. 75
Figure 48: The deposition rate as a function of the plasma power $P_{plasmaRF}$ for RF sputter deposition of silicon nitride thin films. 81
Figure 49: Impact of RF plasma power $P_{plasmaRF}$ on the resulting bias voltage V_b during RF sputter deposition. 82
Figure 50: Sputter deposition rate of silicon nitride thin films as a function of the chamber pressure p_{back} normalized by the RF power. 82
Figure 51: The refractive index n of RF sputter deposited SiN_x thin films as a function of the parameters $P_{plasmaRF}$ and p_{back}. 83
Figure 52: The volumetric mass density ρ_m of RF sputter deposited SiN_x thin films as a function of the parameters $P_{plasmaRF}$ and p_{back}. 84
Figure 53: Chemical composition of selected RF sputter deposited (at $P_{plasmaRF}$ = 600 W) SiN_x thin film samples as a function of p_{back}, assuming a ternary system of Si,N,O. 85

Figure 54: The biaxial film stress σ of RF sputter deposited SiN_x thin films as a function of the parameters $P_{plasmaRF}$ and p_{back}. 86
Figure 55: FTIR spectra of RF sputter deposited SiN_x thin films normalized to unit thickness, synthesized using different parameter sets. 87
Figure 56: Correlation between the biaxial film stress σ and the peak position of the main Si-N asymmetric stretching absorption band in the RF magnetron sputter deposited SiN_x thin films. 88
Figure 57: Biaxial film stress σ as a function of the maximum annealing temperature for RF magnetron sputter deposited ($P_{plasmaRF}$ = 900 W) silicon nitride thin films synthesized at different p_{back} values. 89
Figure 58: Relative reduction of the biaxial film stress σ as a function of the silicon nitride film thickness for different maximum annealing temperatures. 90
Figure 59: Scanning electron micrograph of an RF magnetron sputter deposited SiN_x thin film, after annealing at 800°C, illustrating the blistering phenomenon. 91
Figure 60: The wet etch rate in HF of RF sputter deposited SiN_x thin films as a function of the deposition parameters $P_{plasmaRF}$ and p_{back}. 91
Figure 61: The RIE etch rate of RF magnetron sputter deposited SiN_x thin films as a function of the deposition parameters $P_{plasmaRF}$ and p_{back}. 92
Figure 62: Scanning electron micrograph of RIE etched (bottom part of the images) and as depsoited (top part of the images) RF magnetron sputter deposited SiN_x surfaces. 93
Figure 63: The deposition rate of DC magnetron sputter deposited SiN_x thin films as a function of $P_{plasmaDC}$. 94
Figure 64: The power normalized deposition rate of DC magnetron sputter deposited SiN_x thin films as a function of p_{back}. 94
Figure 65: The refractive index n of DC magnetron sputter deposited SiN_x thin films as a function of p_{back}. 95
Figure 66: The biaxial film stress σ of DC magnetron sputter deposited SiN_x thin films as a function of the parameters $P_{plasmaDC}$ and p_{back}. 96
Figure 67: Selected FTIR spectra of DC magnetron sputter deposited ($P_{plasmaDC}$ = 450 W) SiN_x thin films. 97
Figure 68: Detailed view of the front-side metallization mask for the LC and BD experiments, prepared with the software AutoCAD. 102
Figure 69: Optical photograph of the wafer probe station used for the LC and BD measurements. 103
Figure 70: Cross-sectional schematic of the LC and BD measurement setup. 103
Figure 71: Standard load over time characteristics for the leakage current measurements. 104
Figure 72: Leakage current density characteristics of a Type I ICP-CVD a-SiN_x:H sample recorded between 25°C and 300°C. 108
Figure 73: Transients of the leakage current when changing the load voltage levels. 109
Figure 74: Typical leakage current density characteristics between T = 25°C and T = 300°C of a Type I ICP-CVD a-SiN_x:H sample after exposure to elevated temperatures up to 300°C in air. 110
Figure 75: Evolution of leakage current characteristics of Type I ICP-CVD deposited a-SiN_x:H samples. The measurements have been cyclically repeated 3 times at T = 60°C. 111
Figure 76: Maximal leakage current values measured at E = 0.5 MV/cm of Type I ICP-CVD deposited a-SiN_x:H samples. The graph shows the dependence and evolution of the leakage current on the measurement temperature and repetition count at the respective temperature. 112
Figure 77: Evolution of the maximum leakage current measured at E = 0.5 MV/cm of Type I ICP-CVD a-SiN_x:H samples at different temperatures as a function of the measurement cycle. 112
Figure 78: Leakage current through a 100 nm thin Type I ICP-CVD a-SiN_x:H sample under a constant load of E = 0.5 MV/cm at temperatures ranging from T = 25°C to 300°C. 113

Figure 79: The dependence of the leakage current characteristics of a Type I ICP-CVD a-SiN_x:H sample as a function of the bias direction it was first measured. The measurements were performed at T = 25°C (left side) and T = 125°C (right side)........ 114
Figure 80: Typical breakdown characteristics of “as deposited” Type I ICP-CVD a-SiN_x:H samples measured at different temperatures using 500 µm diameter pads. The curves at each temperature level have been recorded in direct sequence to each other........ 115
Figure 81: Weibull plot showing the breakdown strength of “as deposited” 100 nm thin Type I ICP-CVD a-SiN_x:H films. 116
Figure 82: Voltage sections leading to different dominating conduction mechanisms in “as deposited” Type I SiN_x:H thin films. 118
Figure 83: Typical breakdown characteristics of 100 nm thin Type I ICP-CVD a-SiN_x:H after exposure to temperatures up to 300°C using pads of 500 µm diameter. The individual samples at each temperature have been measured in direct sequence to each other. 119
Figure 84: Weibull plot showing the breakdown strength of “annealed” (@ 300°C) 100 nm thin Type I ICP-CVD a-SiN_x:H films. 120
Figure 85: Scanning electron micrographs showing the effect of catastrophic breakdown on an MIS sample with an ICP-CVD deposited a-SiN_x:H dielectric layer. The images are representative to the catastrophic breakdown of all sample types........ 122
Figure 86: Scanning electron micrographs displaying a detailed view on the effect of catastrophic breakdown........ 122
Figure 87: Impact of ramp speed between 5 mV/s and 500 mV/s on the characteristic BD curve of Type I ICP-CVD a-SiN_x:H thin film samples in the time-zero dielectric breakdown test with a pad diameter of 500 µm........ 123
Figure 88: Leakage current density characteristics of a 100 nm thin Type II ICP-CVD a-SiN_x:H sample between T = 25°C and 120°C, on a linear (left) and semi-logarithmic (right) scale 124
Figure 89: Typical high-load I-V characteristics of 100 nm thin Type II ICP-CVD a-SiN_x:H samples measured at T = 60°C in forward bias condition and a pad diameter of 500 µm. 125
Figure 90: Typical breakdown characteristics of 100 nm thin Type II ICP-CVD a-SiN_x:H samples measured at T = 60°C in reverse bias direction using 500 µm diameter pads. 126
Figure 91: Leakage current characteristics of an Intermediate Type 100 nm thin a-SiN_x:H sample between T =25°C and 300°C on a linear (left) and semi-logarithmic scale (right). 127
Figure 92: Dielectric breakdown characteristics of 100 nm thin Intermediate Type a-SiN_x:H samples measured at T = 25°C (left) and T = 120°C (right) with a pad diameter of 500 µm. The 18 samples in each graph have been measured in direct sequence to each other. 128
Figure 93: Weibull-plot showing the dielectric breakdown strength of 100 nm thin Intermediate Type ICP-CVD a-SiN_x:H thin film samples. 128
Figure 94: Leakage current characteristics of a Type RF 100 nm thin a-SiN_x:H sample between T =25°C and 300°C in a linear(left) and a semi-logarithmic (right) scale. 129
Figure 95: Dielectric breakdown characteristics of 100 nm thin Type RF a-SiN_x:H samples measured at T°= 25°C (left) and T = 120°C (right) with a pad diameter of 500 µm. The curves in each figure were recorded in direct sequence to each other. 130
Figure 96: Weibull-plot showing the dielectric breakdown strength of 100 nm thin Type RF ICP-CVD a-SiN_x:H samples. 130
Figure 97: Leakage current characteristics of a RF magnetron sputter deposited 100 nm thin SiN_x sample in the temperature range of T =25°C and 300°C on a linear (left) and a semi-logarithmic (right) scale. 132
Figure 98: Arrhenius plot illustrating the temperature-dependency of a leakage current density of 100 nm thin RF sputter deposited SiN_x thin film sample. 133

Figure 99: Illustration of the data fitting process of the recorded leakage current data to identify different charge transport mechanisms. 134
Figure 100: Typical current-voltage characteristics of 100 nm thin RF magnetron sputter deposited (450 W and 3 µbar) SiN_x samples during a time-zero dielectric breakdown measurement performed at T = 120°C, using 500 µm diameter pads. 136
Figure 101: Typical current-voltage characteristics of 100 nm thin RF magnetron sputter deposited (450 W and 9 µbar) SiN_x thin film samples (a total of 18 samples) during a time-zero dielectric breakdown measurement performed at T = 120°C using 500 µm diameter pads. 137
Figure 102: Weibull-plots of the dielectric breakdown strength of 100 nm thin RF magnetron sputter deposited SiN_x samples synthesized using the following parameter sets from top left to bottom right: 450 W and 3µbar; 450 W and 9 µbar; 900 W and 3 µbar; 900 W and 9 µbar. 138
Figure 103: Leakage current characteristics of a DC magnetron sputter deposited 100 nm thin SiN_x sample in the temperature range between 25°C and 300°C on a linear (left) and a semi-logarithmic (right) scale. 139
Figure 104: Identification of ohmic and Poole-Frenkel dominated field regimes in the leakage current measurements of DC sputter deposited silicon nitride thin films. 140
Figure 105: Current-voltage characteristics of 100 nm thin DC magnetron sputter deposited (450 W and 3 µbar) SiN_x samples during a time-zero dielectric breakdown measurement performed at T = 120°C using 500 µm diameter pads. 142
Figure 106: Current-voltage characteristics of 100 nm thin DC magnetron sputter deposited (450 W and 9 µbar) SiN_x samples during a time-zero dielectric breakdown measurement performed at T = 120°C using 500 µm diameter pads. 142
Figure 107: Weibull-plots of the dielectric breakdown strengths of 100 nm thin DC magnetron sputter deposited SiN_x samples synthesized using the following parameter sets: a) 450 W and 3µbar; b) 450 W and 9 µbar; c) 900 W and 3 µbar; d) 900 W and 9 µbar. 143
Figure 108: Layout (left) and realization (right) of the test devices for long-term performance testing of silicon nitride passivation layers in electrically conductive, liquid environments. 149
Figure 109: Optical (left) and scanning electron micrographs (right) of the edge coverage of 25 nm (left) and 50 nm (right) thin sputter deposited SiN_x films. 150
Figure 110: Resistance values in the test setup as a function of passivation thickness after a duration of 24h. 151
Figure 111: Bias voltage during DC magnetron sputtering from a poly-Si target, as a function of the inter-electrode distance and DC power, with a gas flow of 60 sccm Ar, with back pressures of 10, 6, and 2 µbar from top to bottom. 176
Figure 112: Bias voltage during DC magnetron sputtering from a poly-Si target, as a function of the inter-electrode distance and DC power, with a gas flow of 40 sccm Ar, 20 sccm N_2, with back pressures of 10, 6, and 2 µbar from top to bottom. 177
Figure 113: Bias voltage during DC magnetron sputtering from a poly-Si target, as a function of the inter-electrode distance and DC power, with a gas flow of 620 sccm Ar, 40 sccm N_2, with back pressures of 10, 6, and 2 µbar from top to bottom. 178
Figure 114: Bias voltage during DC magnetron sputtering from a poly-Si target, as a function of the inter-electrode distance and DC power, with a gas flow of 60 sccm N_2, with back pressures of 10, 6, and 2 µbar from top to bottom. 179
Figure 115: Measurements on the sample surface using a PT-100 resistance thermometer and a Type K thermocouple for the determination of the temperature correction curve for the wafer probe station. 180
Figure 116: Evolution of the leakage current of 100 nm thin Type I ICP-CVD deposited a-SiN_x:H samples. The measurements have been cyclically repeated 3 times at T = 180°C (left side) and T = 300°C (right side). 180

Figure 117: Evolution of the leakage current at the maximum load of ±0.5 MV/cm (on the left) and the zero-transition point of the leakage current characteristics (on the right) of Type I ICP-CVD deposited a-SiN_x:H samples. The measurements have been repeated 3 times. 180
Figure 118: Weibull plot showcasing the breakdown strength of “as deposited” (on the left) and “annealed” (on the right) 50 nm thin Type I ICP-CVD a-SiN_x:H samples, with F being the cumulative distribution function... 181
Figure 119: Weibull plot showcasing the breakdown strength of “as deposited” 300 nm thin Type I ICP-CVD a-SiN_x:H samples, with F being the cumulative distribution function. 181
Figure 120: Breakdown characteristics of 50 nm thin “as deposited” Type I ICP-CVD a-SiN_x:H samples measured at temperatures of 60°C, 180°C and 300°C (top to bottom) using 500 µm diameter pads. The curves in each group have been recorded in immediate succession after each other................ 182
Figure 121: Breakdown characteristics of 50 nm thin annealed Type I ICP-CVD a-SiN_x:H samples measured at temperatures of 60°C, 180°C and 300°C (top to bottom) using 500 µm diameter pads. The curves in each group have been recorded in immediate succession after each other................ 183
Figure 122: Breakdown characteristics of 300 nm thin “as deposited” Type I ICP-CVD a-SiN_x:H samples measured at temperatures of 60°C, 180°C and 300°C (top to bottom) using 500 µm diameter pads. The curves in each group have been recorded in immediate succession after each other................ 184
Figure 123: Leakage current characteristics of 40 nm thin RF sputtered SiN_x samples between T =25°C and 300°C. Deposition parameter sets from top left to bottom right: 450 W / 3µbar; 450 W / 9 µbar; 900 W / 3 µbar; 900 W / 9 µbar. 185
Figure 124: Leakage current characteristics of 100 nm thin RF sputtered SiN_x samples between T =25°C and 300°C. Deposition parameter sets from top left to bottom right: 450 W / 3µbar; 450 W / 9 µbar; 900 W / 3 µbar; 900 W / 9 µbar.. 186
Figure 125: Leakage current characteristics of 300 nm thin RF sputtered SiN_x samples between T =25°C and 300°C. Deposition parameter sets from top left to bottom right: 450 W / 3µbar; 450 W / 9 µbar; 900 W / 3 µbar; 900 W / 9 µbar.. 186
Figure 126: Leakage current characteristics of 40 nm thin DC sputtered SiN_x samples between T =25°C and 300°C. Deposition parameter sets from top left to bottom right: 450 W / 3µbar; 450 W / 9 µbar; 900 W / 3 µbar; 900 W / 9 µbar. 187
Figure 127: Leakage current characteristics of 100 nm thin DC sputtered SiN_x samples between T =25°C and 300°C. Deposition parameter sets from top left to bottom right: 450 W / 3µbar; 450 W / 9 µbar; 900 W / 3 µbar; 900 W / 9 µbar.. 188
Figure 128: Leakage current characteristics of 300 nm thin DC sputtered SiN_x samples between T =25°C and 300°C. Deposition parameter sets from top left to bottom right: 450 W / 3µbar; 450 W / 9 µbar; 900 W / 3 µbar; 900 W / 9 µbar.. 188
Figure 129: Current-voltage characteristics of 100 nm thin RF magnetron sputter deposited SiN_x thin film samples during a time-zero dielectric breakdown measurement performed at T = 120°C using 500 µm diameter pads. The deposition parameters were: 450 W/ 9 µbar (top right), 900 W/ 3 µbar (bottom left), and 900 W/ 9 µbar (bottom right), respectively. 189
Figure 130: Weibull-plots of the dielectric breakdown strengths of 40nm thin DC magnetron sputter deposited SiN_x samples. Deposition parameters were (from top left to bottom right): 450 W/ 3µbar; 450 W/ 9 µbar; 900 W/ 3 µbar; 900 W/ 9 µbar.. 190
Figure 131: Current-voltage characteristics of 40 nm thin RF magnetron sputter deposited SiN_x samples during a time-zero dielectric breakdown measurement performed at T = 120°C using 500 µm diameter pads. Deposition parameter sets were (from top left to bottom right):450 W and 3µbar; 450 W and 9 µbar; 900 W and 3 µbar; 900 W and 9 µbar. 190
Figure 132: Current-voltage characteristics of 300 nm thin RF magnetron sputter deposited (450 W and 3 µbar) SiN_x samples during a time-zero dielectric breakdown measurement performed at

T = 120°C using 500 µm diameter pads. Deposition parameter sets were (from top left to bottom right): 450 W and 3µbar; 450 W and 9 µbar; 900 W and 3 µbar; 900 W and 9 µbar. 191
Figure 133: Current-voltage characteristics of 100 nm thin DC magnetron sputter deposited SiN_x samples during a time-zero dielectric breakdown measurement performed at T = 120°C using 500 µm diameter pads. The deposition parameters were: 450 W and 3 µbar (top left), 900 W and 3 µbar (bottom left), and 900 W and 9 µbar (bottom right), respectively. 192
Figure 134: Weibull-plots of the dielectric breakdown strengths of 40 nm thin DC magnetron sputter deposited SiN_x samples. Deposition parameters were (from top left to bottom right): 450 W/ 3µbar; 450 W/ 9 µbar; 900 W/ 3 µbar; 900 W/ 9 µbar.. 193
Figure 135: Current-voltage characteristics of 40 nm thin DC magnetron sputter deposited SiN_x samples during a time-zero dielectric breakdown measurement performed at T = 120°C using 500 µm diameter pads. Deposition parameter sets were (from top left to bottom right): 450 W/ 3 µbar; 450 W/ 9 µbar; 900 W/ 3 µbar; 900 W/ 9 µbar.. 193
Figure 136: Current-voltage characteristics of 300 nm thin DC magnetron sputter deposited SiN_x samples during a time-zero dielectric breakdown measurement performed at T = 60°C using 500 µm diameter pads. Deposition parameter sets were (from top left to bottom right): 450 W and 3µbar; 450 W and 9 µbar; 900 W and 3 µbar; 900 W and 9 µbar. 194

List of Tables

Table 1: Typical LPCVD deposition processes. 16
Table 2: Common isotropic etch processes in microfabrication [28]. 30
Table 3: Anisotropic silicon wet etching processes [28]. 30
Table 4: Deposition parameters of layers synthesized within the screening stage. 45
Table 5: Influence of ICP-CVD deposition parameters on the measured properties of the silicon nitride thin films. 46
Table 6: Impact of ICP-CVD deposition parameters on the properties of Type I silicon nitride thin films. 53
Table 7: Impact of ICP-CVD deposition parameters on the properties of Type II silicon nitride thin films. 54
Table 8: Overview of the experimental series for the assessment of ICP-CVD deposited a-SiN_x:H thin film properties as a function of the precursor gas ratio $R_{N2/SiH4}$. r_{SiH4} and r_{N2} are the flow rates of the nitrogen and silane gas, respectively. 57
Table 9: Relative bond densities (calculated from the areas under the corresponding peaks in the FTIR spectra) of some selected absoprtion bands of ICP-CVD silicon nitride thin films extracted from their FT-IR spectra as a function of $R_{N2/SiH4}$. 61
Table 10: Overview on the deposition experiments for determining the influence of CCP plasma on ICP-CVD a-SiN_x:H thin film properties. 63
Table 11: Comparison of Type I and Type II ICP-CVD silicon nitride thin films. 76
Table 12: Effect of elevated substrate temperature during RF magnetron sputter deposition ($P_{plasmaRF}$ =600 W, p_{back} = 5 µbar) on the resulting properties of SiN_x thin films. 86
Table 13: Etch rates of DC magnetron sputter deposited SiN_x thin films in HF wet etch (isotropic) and in CF_4:O_2 RIE dry etching as a function of the deposition parameters $P_{plasmaDC}$ and $p_{back.}$ 98
Table 14: Parameter sets for the synthesis of ICP-CVD silicon nitride thin films used in the leakage current and dielectric breakdown measurements. 101
Table 15: Conduction mechanisms in insulators according to [152]. The symbols used in the expressions above are: A** = the effective Richardson constant, Φ_B = barrier height, ε_i = permittivity of the insulator, E_i = electric field in the insulator, m* = effective mass, d = thickness of the insulator, ΔE_{ac} = electron activation energy, ΔE_{ai} = ion activation energy, while a, b, c, and d' are constants... 106
Table 16: Electrical parameters of RF magnetron sputter deposited SiN_x thin films. Φ_B is averaged over $P_{plasmaRF}$, and n_0 is averaged over both $P_{plasmaRF}$ and d values. 135
Table 17: Leakage current parameters for ohmic conduction and Poole-Frenkel emission in 100 nm thin RF magnetron sputter deposited silicon nitride films in dependence of the deposition parameters. 141
Table 18: Biaxial stress of RF magnetron sputter deposited SiN_x thin films over the course of 72 hours. 175

List of Symbols and Abbreviations

List of Symbols

Symbol	Unit	Description
A	$cm^{-2}\cdot s^{-1}$	arrival rate
A_f	-	anisotropy factor
A_r	cm^2	area
A^{**}	$A\cdot m^{-2}\cdot K^{-2}$	effective Richardson constant
B	T	magnetic field
c	$m\cdot s^{-1}$	speed of light
d	m	thickness/distance
E	$MV\cdot cm^{-1}$	electric field
E_A	eV	effective activation energy
$E_{A,PF}$	eV	Poole-Frenkel activation energy
$E_{A,\Omega}$	eV	Ohmic activation energy
E_i	$MV\cdot cm^{-1}$	electric field in the insulator
E_s	GPa	Young's Modulus of the substrate
E_f	GPa	Young's modulus of the film
ΔE_{ac}	eV	electron activation energy
ΔE_{ai}	eV	ion activation energy
F	$cm^{-2}\cdot s^{-1}$	molecular flux
f	Hz	frequency
h	eV·s	Planck constant
H	GPa	hardness
I	A	current
I_{limit}	A	current compliance limit
J	$A\cdot cm^{-2}$	current density
J_{PF}	$A\cdot cm^{-2}$	Poole-Frenkel leakage current density
J_Ω	$A\cdot cm^{-2}$	Ohmic leakage current density
k_B	$eV\cdot K^{-1}$	Boltzmann constant
m^*	kg	effective mass
m_0	kg	rest mass
n	-	refractive index
N	cm^{-3}	spatial density of molecules
N_0	$cm^{-2}\cdot s^{-1}$	material evaporation constant
n_0	cm^{-3}	volumetric defect density
n_{Si}	-	refractive index of silicon
n_{Si3N4}	-	refractive index of silicon nitride
p	Pa, bar, Torr	pressure
p_m	$kg\cdot m\cdot s^{-1}$	momentum
P	N	load
p_{back}	µbar	sputtering back pressure
p_{dep}	mTorr	deposition pressure
P_{ICP}	W	inductively coupled plasma power

$P_{plasmaDC}$	W	DC sputter power
$P_{PlasmaRF}$	W	RF sputter power
P_{RF}	W	capacitively coupled plasma power
q	C	elementary charge
R_{dep}	$nm \cdot min^{-1}$	deposition rate
r_{HF}	$nm \cdot min^{-1}$	hydrofluoric acid etch rate
r_{L}	$nm \cdot min^{-1}$	lateral etch rate
r_{N2}	sccm	flow rate of nitrogen
$R_{N2/SiH4}$	-	precursor gas ratio
r_{RIE}	$nm \cdot min^{-1}$	RIE etch rate
r_{SiH4}	sccm	flow rate of silane
r_{V}	$nm \cdot min^{-1}$	vertical etch rate
S	$N \cdot m^{-1}$	stiffness
T	K	absolute temperature
t	s	time
T_{anneal}	°C	annealing temperature
T_{m}	°C	melting point
T_{max}	°C	maximum temperature
T_{s}	°C	substrate temperature
T_{set}	°C	set temperature
U_{s}	eV	surface binding energy
V	V	voltage
v	$m \cdot s^{-1}$	velocity
V_{max}	V	maximum voltage
V_{t}	V	minimal ignition voltage
WER	$nm \cdot min^{-1}$	wet etch rate
x	-	N/Si atomic concentration ratio
Y	-	sputter yield
Z	-	atomic number
α_{1}	-	primary ionization coefficient
α	cm^{3}	polarizability
β	rad	angle of substrate normal to radial vector
γ	-	2nd Townsend coefficient
γ_{i}	-	secondary amplification
ε_{i}	-	permittivity of insulator
θ	rad	angle of source normal and radial vector
λ	nm	mean free path
λ_{B}	nm	de-Broglie wavelength
μ	$m^{2} \cdot V^{-1} \cdot s^{-1}$	electron mobility
ν_{s}	-	Poisson-ratio of the substrate
ρ	$\Omega \cdot cm$	electrical resistivity
ρ_{m}	$g \cdot cm^{-3}$	weight density
σ	MPa	biaxial Stress
σ_{Ω}	S	ohmic conductivity
Φ_{B}	eV	barrier height
Φ_{E}	eV	activation energy
ω_{CE}	Hz	cyclotron angular frequency

List of Abbreviations

Abbreviation	Description
AC	Alternating Current
AFM	Atomic Force Microscopy
amu	Atomic Mass Unit
ANOVA	Analysis of Variance
APC	Automated Pressure Control
APCVD	Atmospheric Pressure Chemical Vapour Deposition
ARDE	Aspect Ratio Dependent Etching
BD	Dielectric Breakdown
BNC	Bayonet Neill-Concelman
Cat-CVD	Catalytic Chemical Vapour Deposition
CCD	Charge Coupled Device
CCP	Capacitively Coupled Plasma
CVD	Chemical Vapour Deposition
DC	Direct Current
DIR	Diffractive Infrared
DoE	Design of Experiments
DRIE	Deep Reactive Ion Etching
ECR-CVD	Electron Cyclotron Resonance Chemical Vapour Deposition
EDP	Ethylenediamine Pyrocatechol
EDX	Energy Dispersive X-ray Spectroscopy
EEDF	Electron Energy Distribution Function
EELS	Electron Energy Loss Spectroscopy
FT-IR	Fourier-Transform Infrared Spectroscopy
FWHM	Full Width at Half Maximum
GPIB	General Purpose Interface Bus
HM-TEM	High-magnification Transmission Electron Microscopy
ICP-CVD	Inductively Coupled Plasma Chemical Vapour Deposition
IEDF	Ion Energy Distribution Function
IEEE	Institute of Electrical and Electronics Engineers
IR	Infrared
ISE	Inverted Plasma Etcher
LC	Leakage Current
LM-TEM	Low-magnification Transmission Electron Microscopy
LPCVD	Low Pressure Chemical Vapour Deposition
MANOVA	Multivariate Analysis of Variance
MBE	Molecular Beam Epitaxy
MEMS	Microelectromechanical System
MIS	Metal - Insulator - Semiconductor
PBS	Phosphate Buffered Saline
PCB	Printed Circuit Board
PCI	Peripheral Component Interconnect
PECVD	Plasma Enhanced Chemical Vapour Deposition
PVD	Physical Vapour Deposition
RBS	Rutherford Backscatter Spectrometry
RF	Radio Frequency

RIE	Reactive Ion Etching
SAD	Selected Area Diffraction
SEM	Scanning Electron Microscopy
SNR	Signal-to-Noise Ratio
SR	Spectral Reflectometry
STEM	Scanning Transmission Electron Microscopy
TCE	Temperature Coefficient of Expansion
TEM	Transmission Electron Microscopy
TMAH	Tetramethyl Ammonium Hydroxide
TTV	Total Thickness Variation
UV	Ultraviolet
VUV	Vacuum Ultraviolet
XPS	X-Ray Photoelectron Spectroscopy
XRD	X-Ray Diffraction

About the Author

Dávid Dergez

Address:	Nádasdi u. 13 9400 Sopron, Hungary
E-Mail:	david.dergez@zkw-elektronik.at
Date of birth:	20/11/1986
Place of birth:	Sopron
Nationality:	Hungary

Education

since Nov. 2011	PhD programme in Engineering Science Electrical Engineering Technische Universität Wien, Austria
Feb. 2009 – Okt. 2011	MSc Electrical Engineering Microelectronics Technische Universität Wien, Austria
Sept. 2005 – Jan. 2009	BSc Electrical Engineering Budapest University of Technology and Economics, Hungary
Jun. 2005	‘Matura’ – higher education entrance qualification, Széchenyi István Gimnázium, Hungary

List of Publications

D. Dergez, J. Schalko. A. Bittner, U. Schmid, *Fundamental properties of a-SiN$_x$:H thin films deposited by ICP-PECVD for MEMS applications*, Applied Surface Science 284 (2013), 348-353

D. Dergez, A. Bittner, J. Schalko, U. Schmid, *Low-stress and long-term stable a-SiN$_x$:H films deposited by ICP-PECVD*, Procedia Engineering 87 (2014), 100-103

D. Dergez, J. Schalko, S. Löffler, A. Bittner, U. Schmid*, Impact of auxiliary capacitively coupled plasma on the properties of ICP-CVD deposited a-SiN$_x$:H thin films*, Sensors and Actuators A: Physical 224 (2015), 156-162

D. Dergez, M. Schneider, A. Bittner, U. Schmid, *Mechanical and electrical properties of DC magnetron sputter deposited amorphous silicon nitride thin films*, Thin Solid Films 589 (2015), 227-232

D. Dergez, M. Schneider, A. Bittner, N. Pawlak, U. Schmid, *Mechanical and electrical properties of RF magnetron sputter deposited amorphous silicon-rich silicon nitride thin films*, Thin Solid Films 606 (2016), 7-12

Appendix

A: Biaxial stress stability of sputter deposited SiN_x thin films

Sample #	σ [GPa] after 24h	σ [GPa] after 48h	σ [GPa] after 72h
MOS22_01	-1.497	-1.496	-1.498
MOS22_02	-1.495	-1.495	-1.498
MOS22_03	-1.523	-1.524	-1.524
MOS22_04	-1.270	-1.268	-1.256
MOS22_05	-1.172	-1.184	-1.189
MOS22_06	-1.310	-1.318	-1.306
MOS22_07	-1.596	-1.596	-1.596
MOS22_08	-1.622	-1.619	-1.618
MOS22_09	-1.539	-1.539	-1.537
MOS22_10	-1.628	-1.622	-1.618
MOS22_11	-1.475	-1.476	-1.473
MOS22_12	-1.555	-1.555	-1.547
MOS22_13	-1.529	-1.530	-1.529
MOS22_14	-1.611	-1.610	-1.610
MOS22_15	-1.383	-1.402	-1.388
MOS22_16	-1.495	-1.498	-1.497

Table 18: Biaxial stress of RF magnetron sputter deposited SiN_x thin films over the course of 72 hours.

B: Parameter-dependence of bias voltage for DC magnetron sputtering of SiN_x

60 sccm Ar

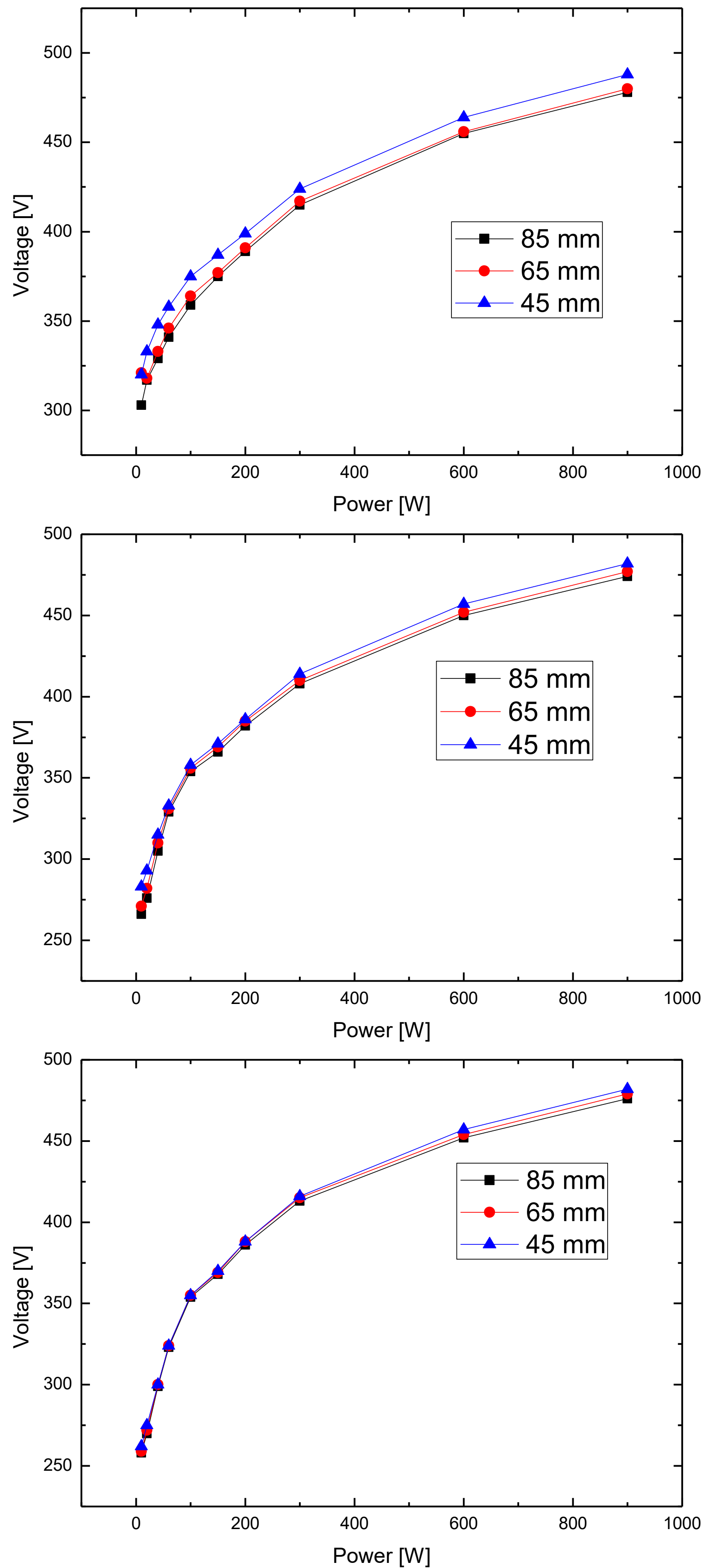

Figure 111: Bias voltage during DC magnetron sputtering from a poly-Si target, as a function of the inter-electrode distance and DC power, with a gas flow of 60 sccm Ar, with back pressures of 10, 6, and 2 µbar from top to bottom.

40 sccm Ar, 20 sccm N_2

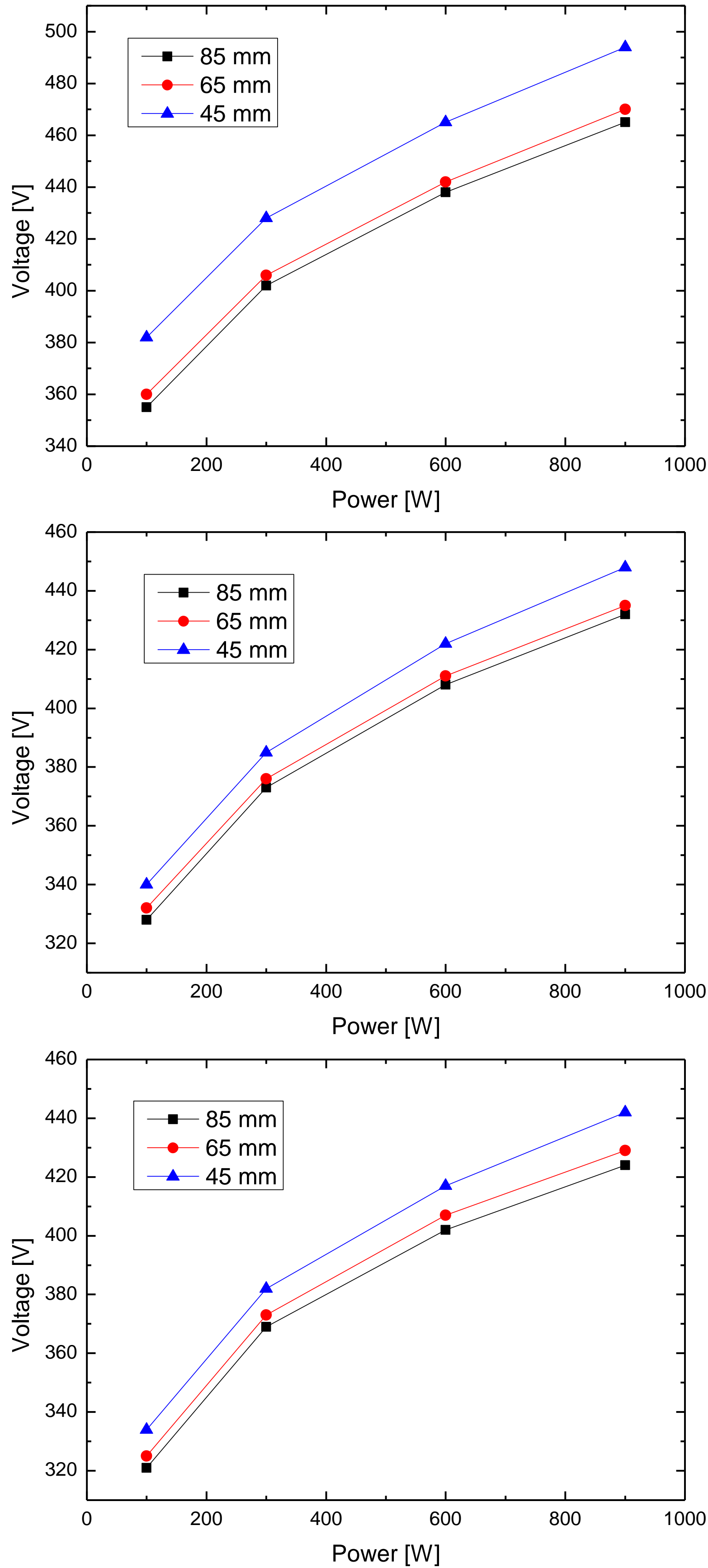

Figure 112: Bias voltage during DC magnetron sputtering from a poly-Si target, as a function of the inter-electrode distance and DC power, with a gas flow of 40 sccm Ar, 20 sccm N_2, with back pressures of 10, 6, and 2 µbar from top to bottom.

20 sccm Ar, 40 sccm N_2

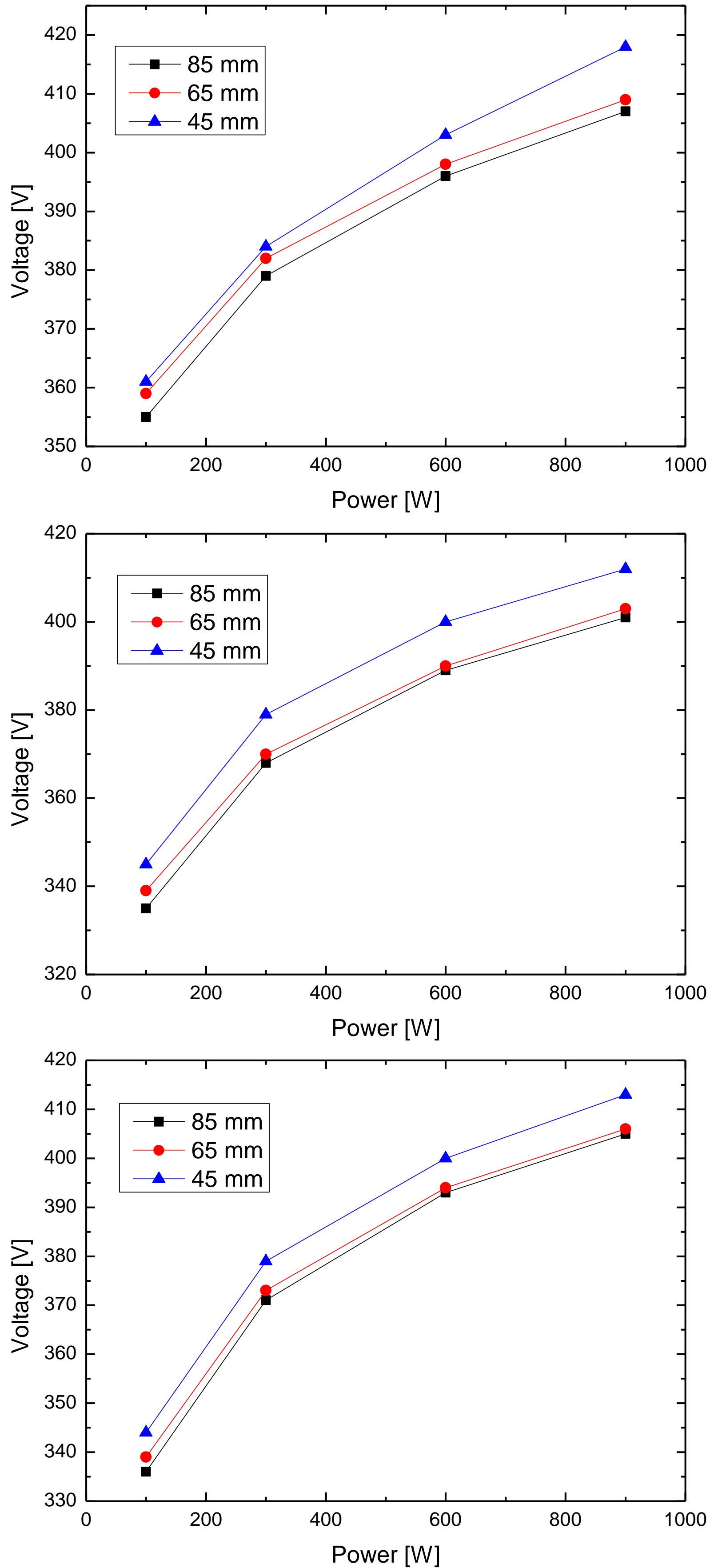

Figure 113: Bias voltage during DC magnetron sputtering from a poly-Si target, as a function of the inter-electrode distance and DC power, with a gas flow of 620 sccm Ar, 40 sccm N_2, with back pressures of 10, 6, and 2 µbar from top to bottom.

60 sccm N_2

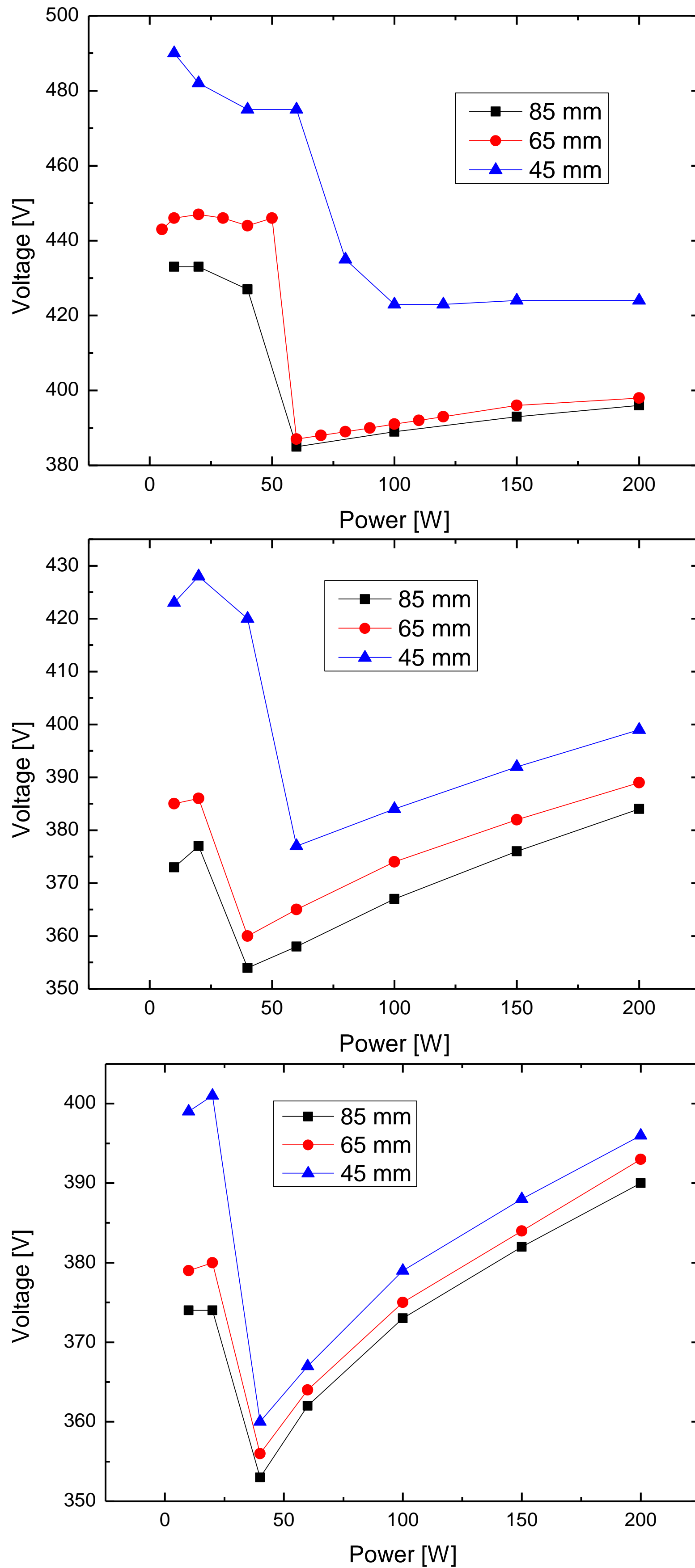

Figure 114: Bias voltage during DC magnetron sputtering from a poly-Si target, as a function of the inter-electrode distance and DC power, with a gas flow of 60 sccm N_2, with back pressures of 10, 6, and 2 µbar from top to bottom.

C: Temperature correction curve for the wafer probe station

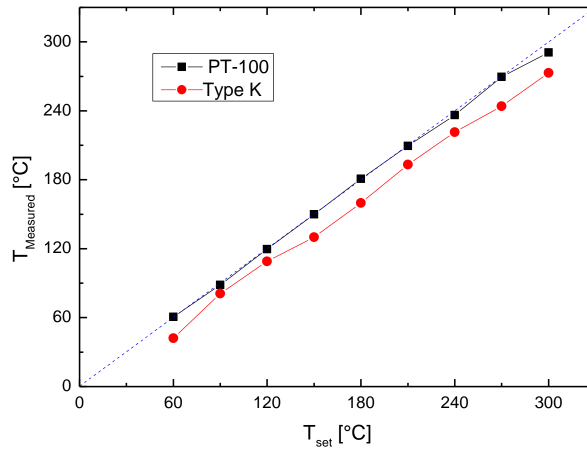

Figure 115: Measurements on the sample surface using a PT-100 resistance thermometer and a Type K thermocouple for the determination of the temperature correction curve for the wafer probe station.

D: Supplementary leakage current measurements of *Type I* a-SiN_x:H films

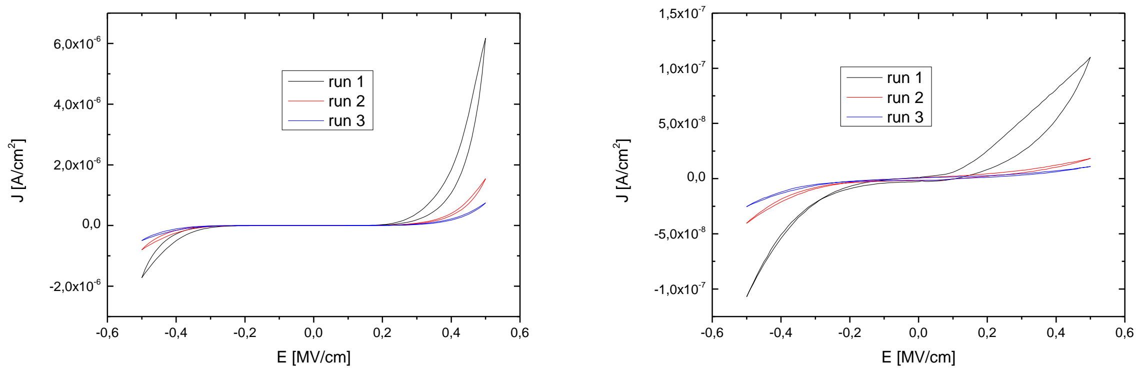

Figure 116: Evolution of the leakage current of 100 nm thin Type I ICP-CVD deposited a-SiN_x:H samples. The measurements have been cyclically repeated 3 times at T = 180°C (left side) and T = 300°C (right side).

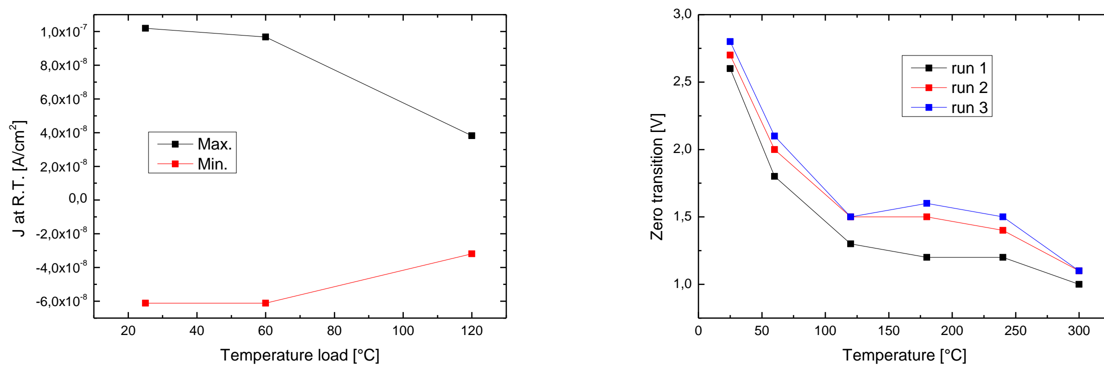

Figure 117: Evolution of the leakage current at the maximum load of ±0.5 MV/cm (on the left) and the zero-transition point of the leakage current characteristics (on the right) of Type I ICP-CVD deposited a-SiN_x:H samples. The measurements have been repeated 3 times.

E: Breakdown characteristics of 50/300m thick *Type I* a-SiN_x:H films

BD statistics

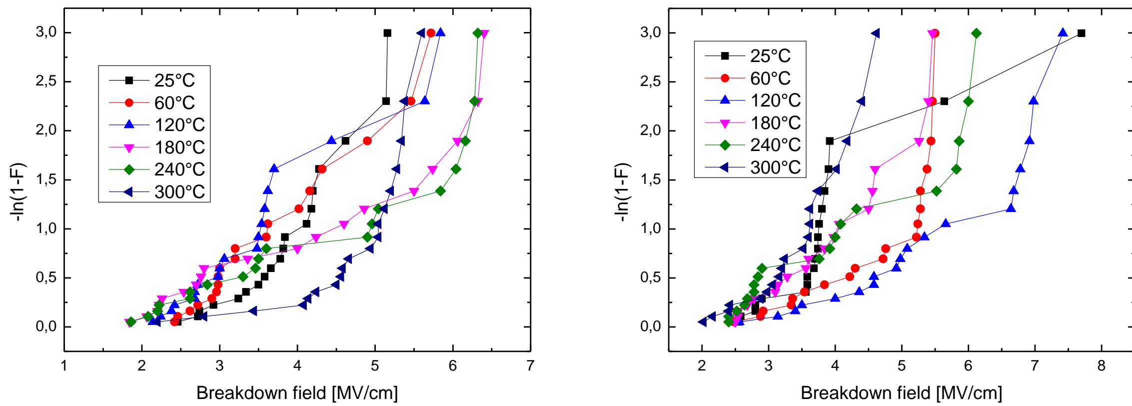

Figure 118: Weibull plot showcasing the breakdown strength of "as deposited" (on the left) and "annealed" (on the right) 50 nm thin Type I ICP-CVD a-SiN_x:H samples, with F being the cumulative distribution function.

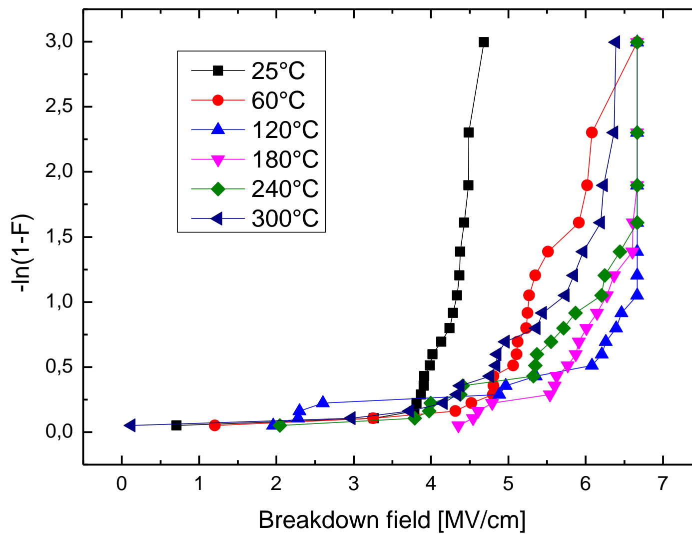

Figure 119: Weibull plot showcasing the breakdown strength of "as deposited" 300 nm thin Type I ICP-CVD a-SiN_x:H samples, with F being the cumulative distribution function.

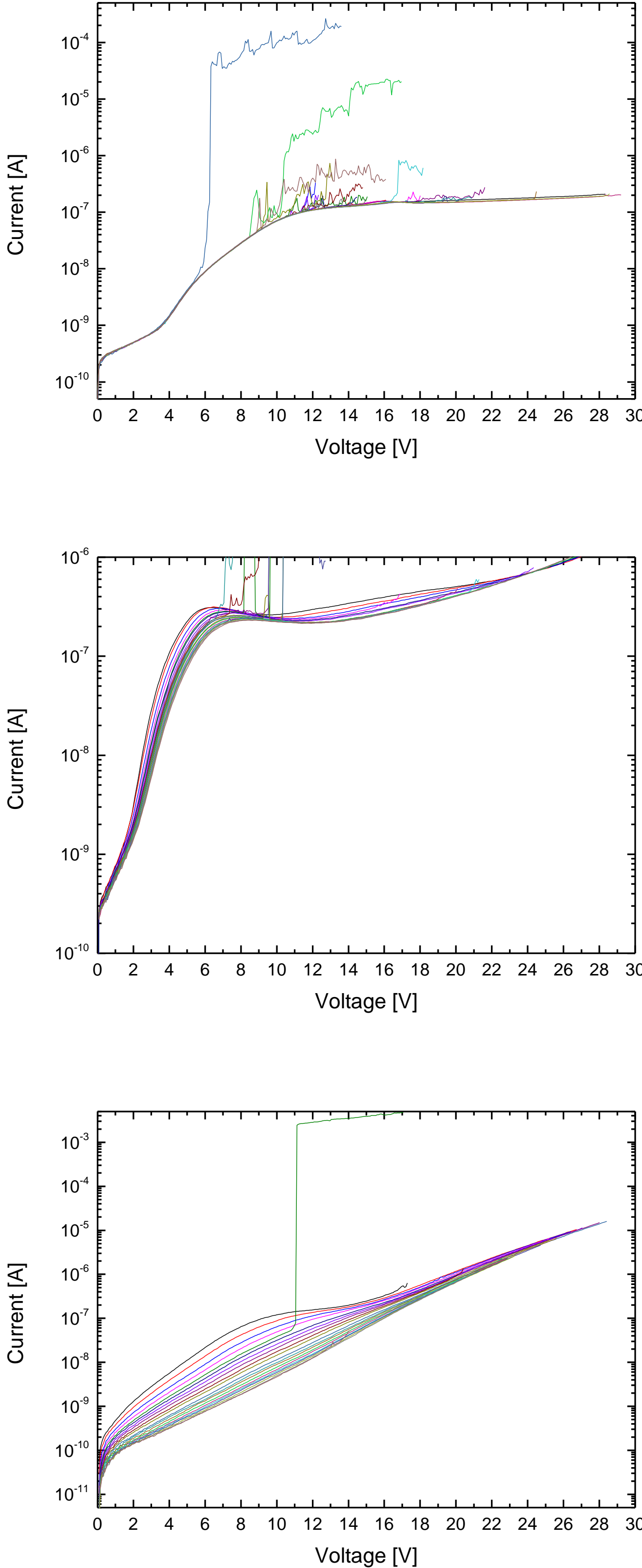

Figure 120: Breakdown characteristics of 50 nm thin "as deposited" Type I ICP-CVD a-SiN$_x$:H samples measured at temperatures of 60°C, 180°C and 300°C (top to bottom) using 500 µm diameter pads. The curves in each group have been recorded in immediate succession after each other.

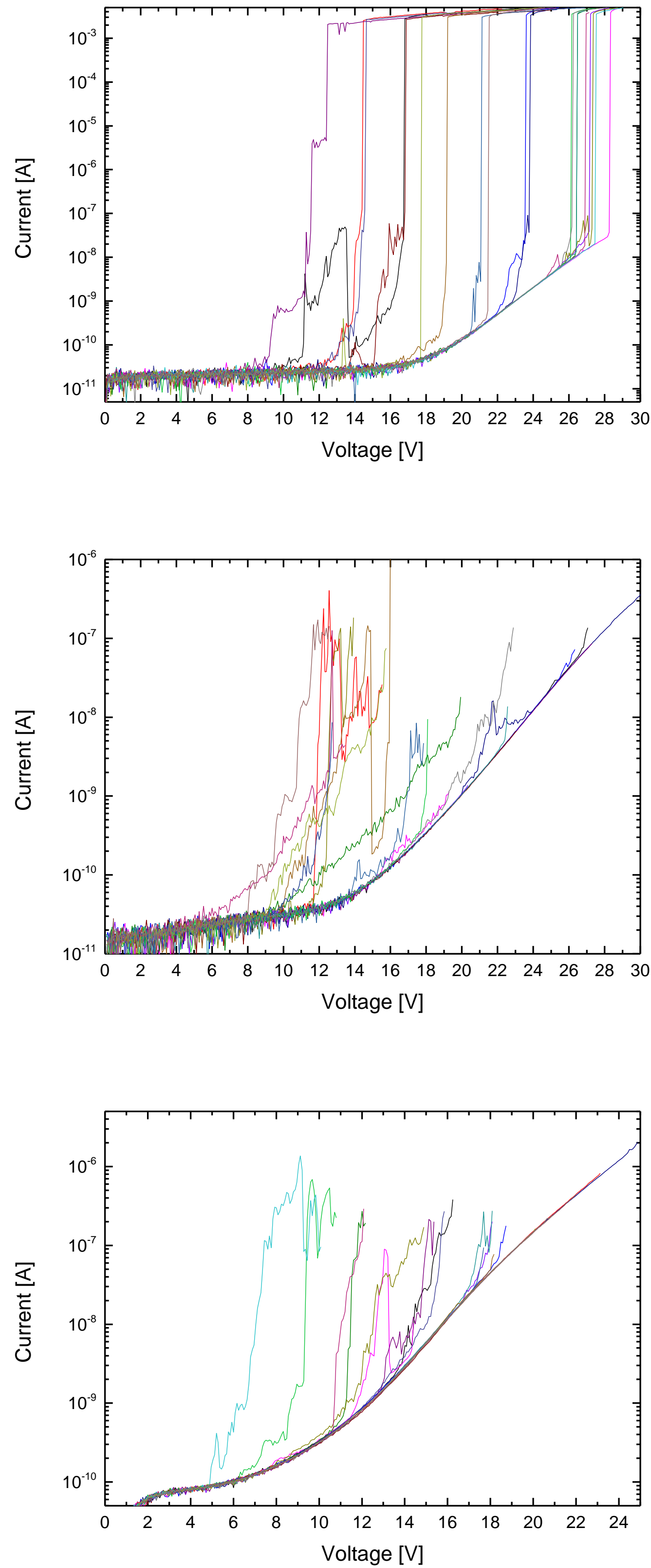

Figure 121: Breakdown characteristics of 50 nm thin annealed Type I ICP-CVD a-SiN$_x$:H samples measured at temperatures of 60°C, 180°C and 300°C (top to bottom) using 500 µm diameter pads. The curves in each group have been recorded in immediate succession after each other.

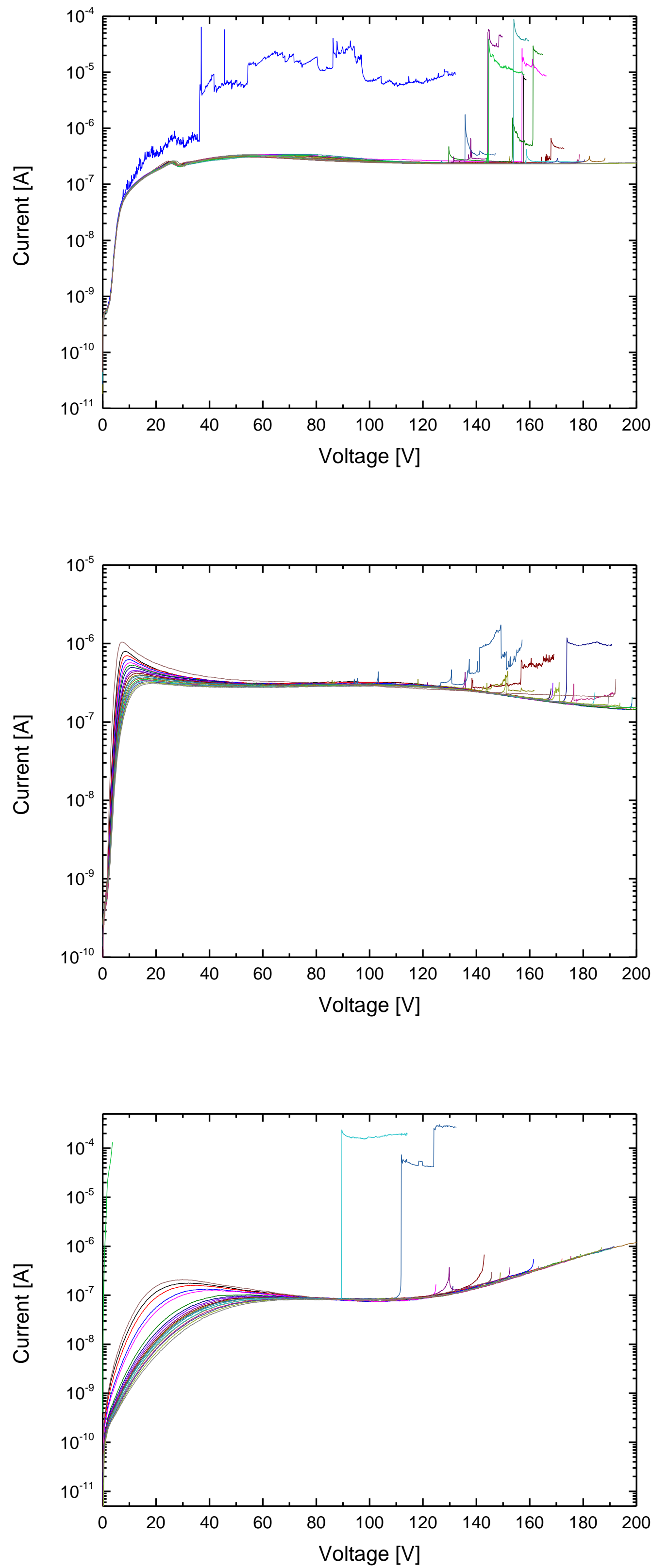

Figure 122: Breakdown characteristics of 300 nm thin "as deposited" Type I ICP-CVD a-SiN$_x$:H samples measured at temperatures of 60°C, 180°C and 300°C (top to bottom) using 500 µm diameter pads. The curves in each group have been recorded in immediate succession after each other.

F: Additional leakage current characteristics of sputter deposited SiN_x thin films

RF sputtered SiN_x

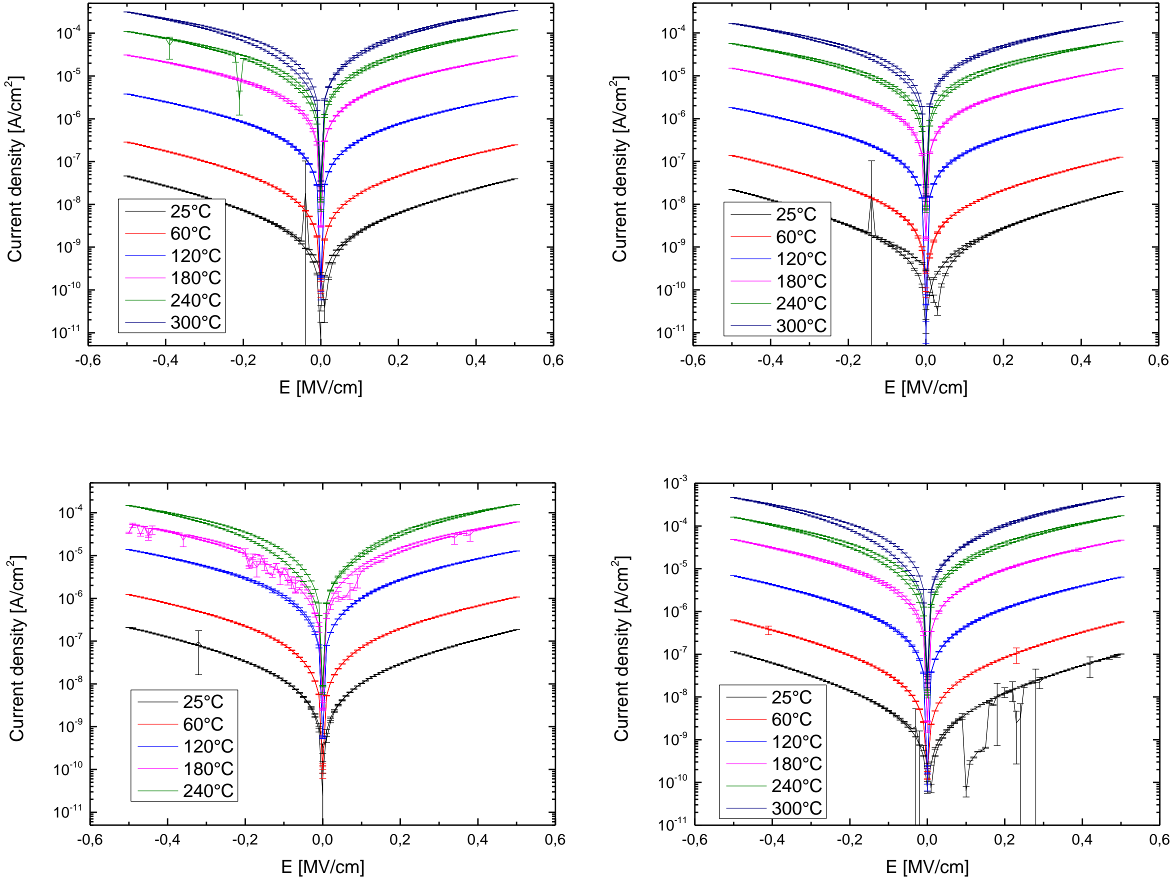

Figure 123: Leakage current characteristics of 40 nm thin RF sputtered SiN_x samples between T =25°C and 300°C. Deposition parameter sets from top left to bottom right: 450 W / 3µbar; 450 W / 9 µbar; 900 W / 3 µbar; 900 W / 9 µbar.

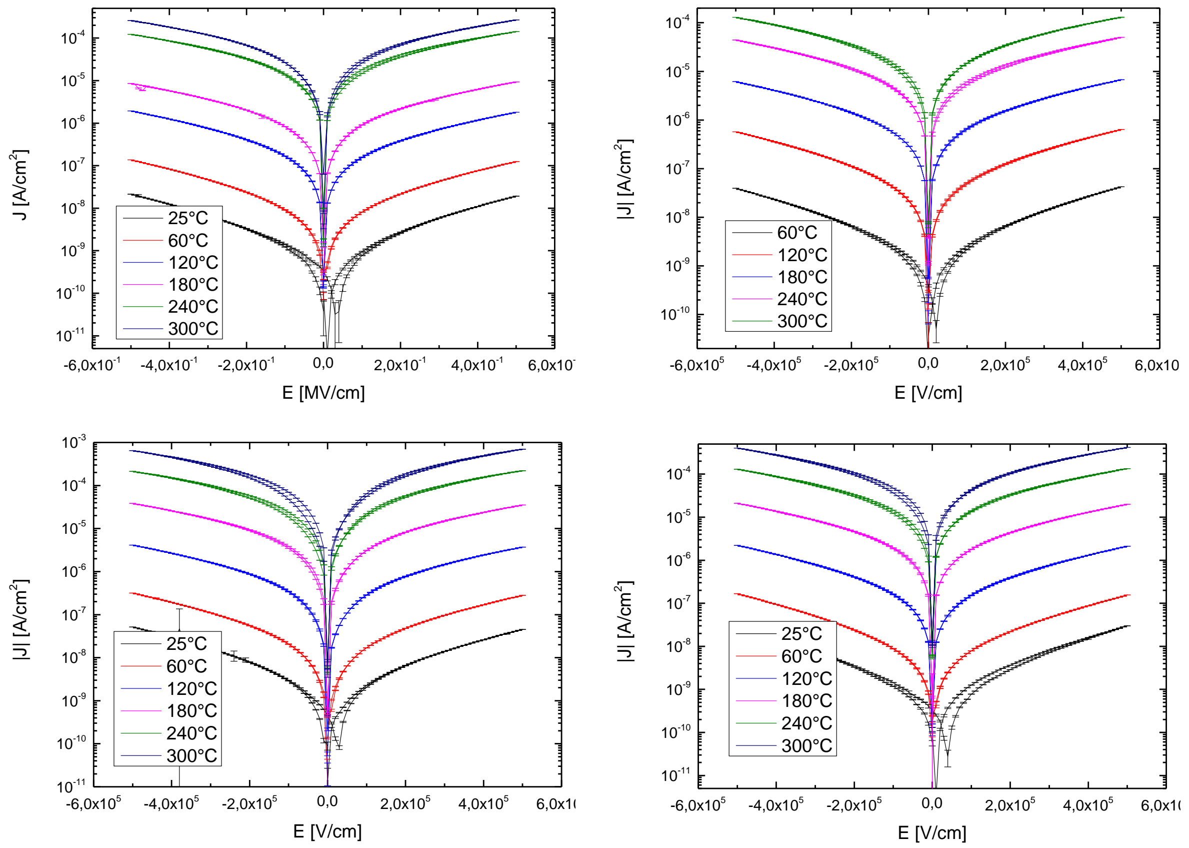

Figure 124: Leakage current characteristics of 100 nm thin RF sputtered SiN_x samples between T =25°C and 300°C. Deposition parameter sets from top left to bottom right: 450 W / 3µbar; 450 W / 9 µbar; 900 W / 3 µbar; 900 W / 9 µbar.

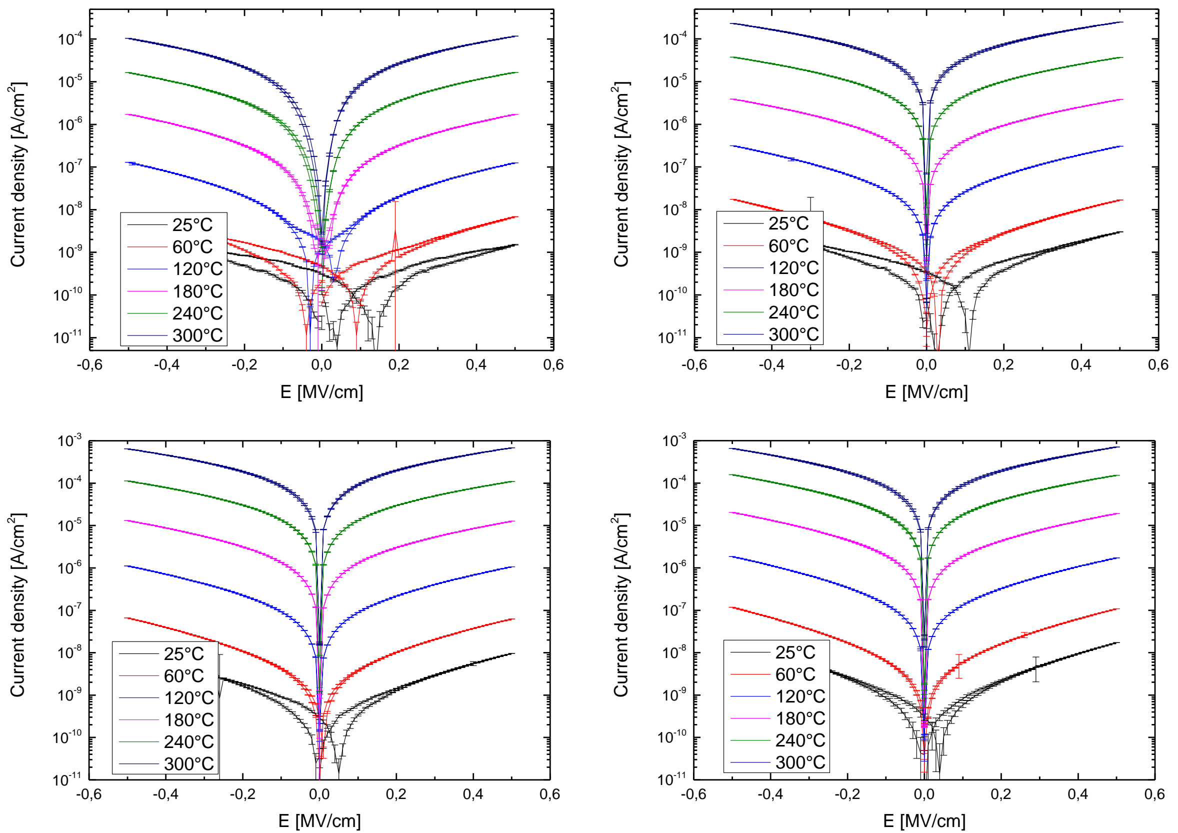

Figure 125: Leakage current characteristics of 300 nm thin RF sputtered SiN_x samples between T =25°C and 300°C. Deposition parameter sets from top left to bottom right: 450 W / 3µbar; 450 W / 9 µbar; 900 W / 3 µbar; 900 W / 9 µbar.

DC sputtered SiN_x

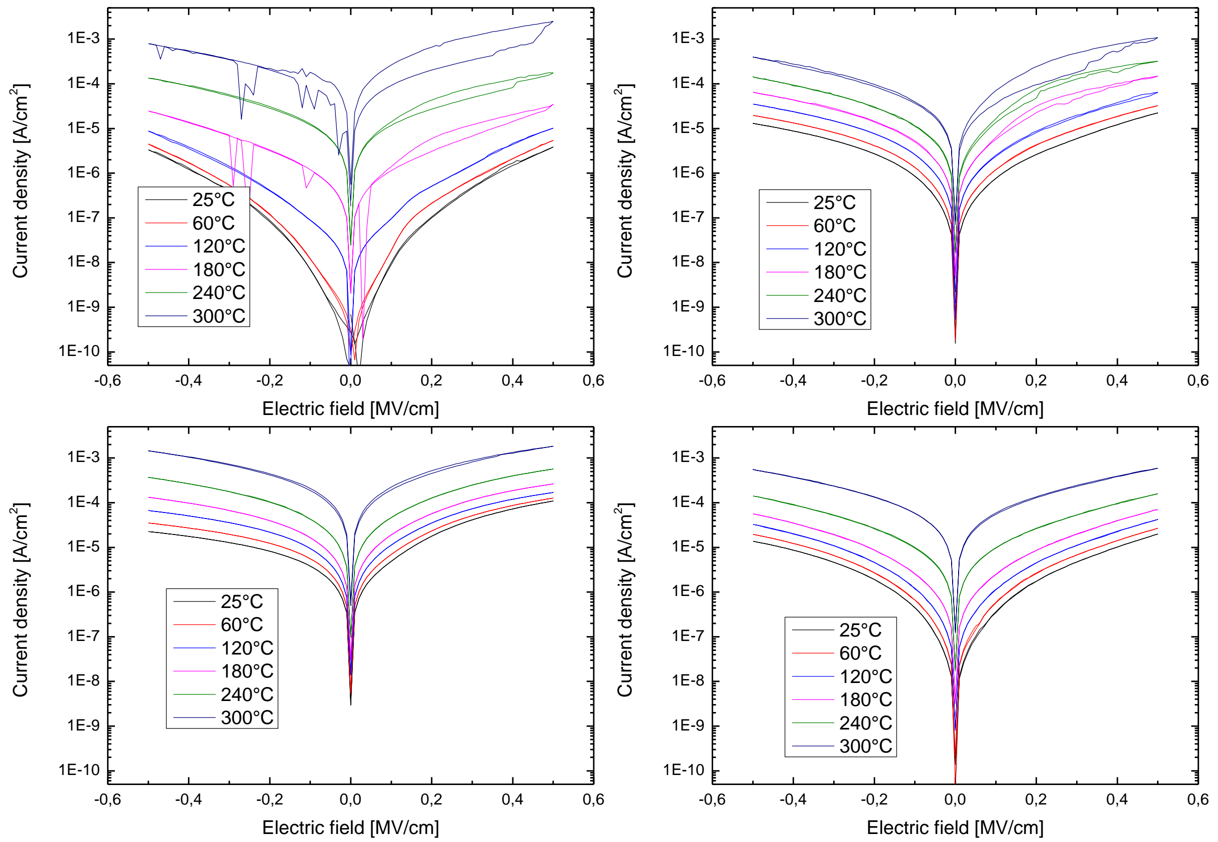

Figure 126: Leakage current characteristics of 40 nm thin DC sputtered SiN_x samples between T =25°C and 300°C. Deposition parameter sets from top left to bottom right: 450 W / 3µbar; 450 W / 9 µbar; 900 W / 3 µbar; 900 W / 9 µbar.

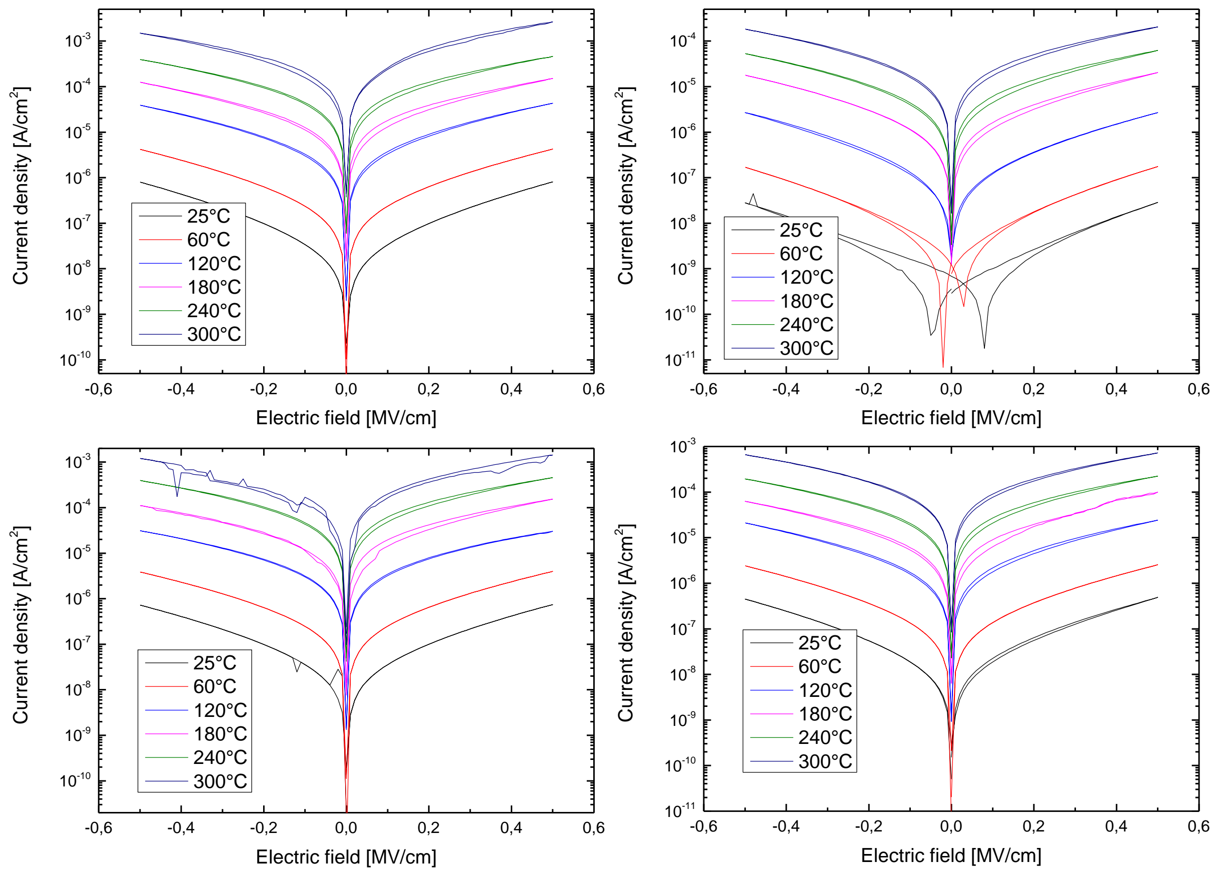

Figure 127: Leakage current characteristics of 100 nm thin DC sputtered SiN_x samples between T =25°C and 300°C. Deposition parameter sets from top left to bottom right: 450 W / 3µbar; 450 W / 9 µbar; 900 W / 3 µbar; 900 W / 9 µbar.

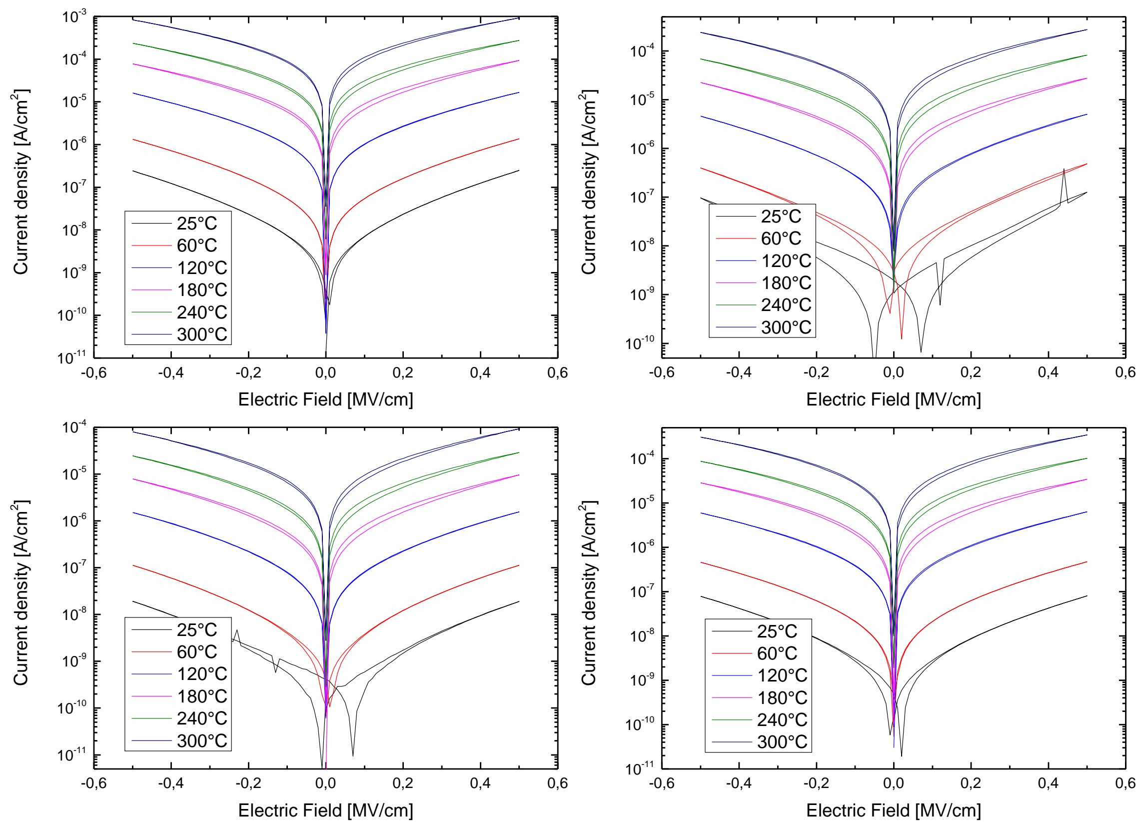

Figure 128: Leakage current characteristics of 300 nm thin DC sputtered SiN_x samples between T =25°C and 300°C. Deposition parameter sets from top left to bottom right: 450 W / 3µbar; 450 W / 9 µbar; 900 W / 3 µbar; 900 W / 9 µbar.

G: Additional breakdown measurements of RF sputtered SiN_x thin films

100 nm thin RF sputtered films

For the curves with the parameter set of $P_{plasmaRF}$ = 450W and p_{back} = 3 µbar, see Chapter 6.3.

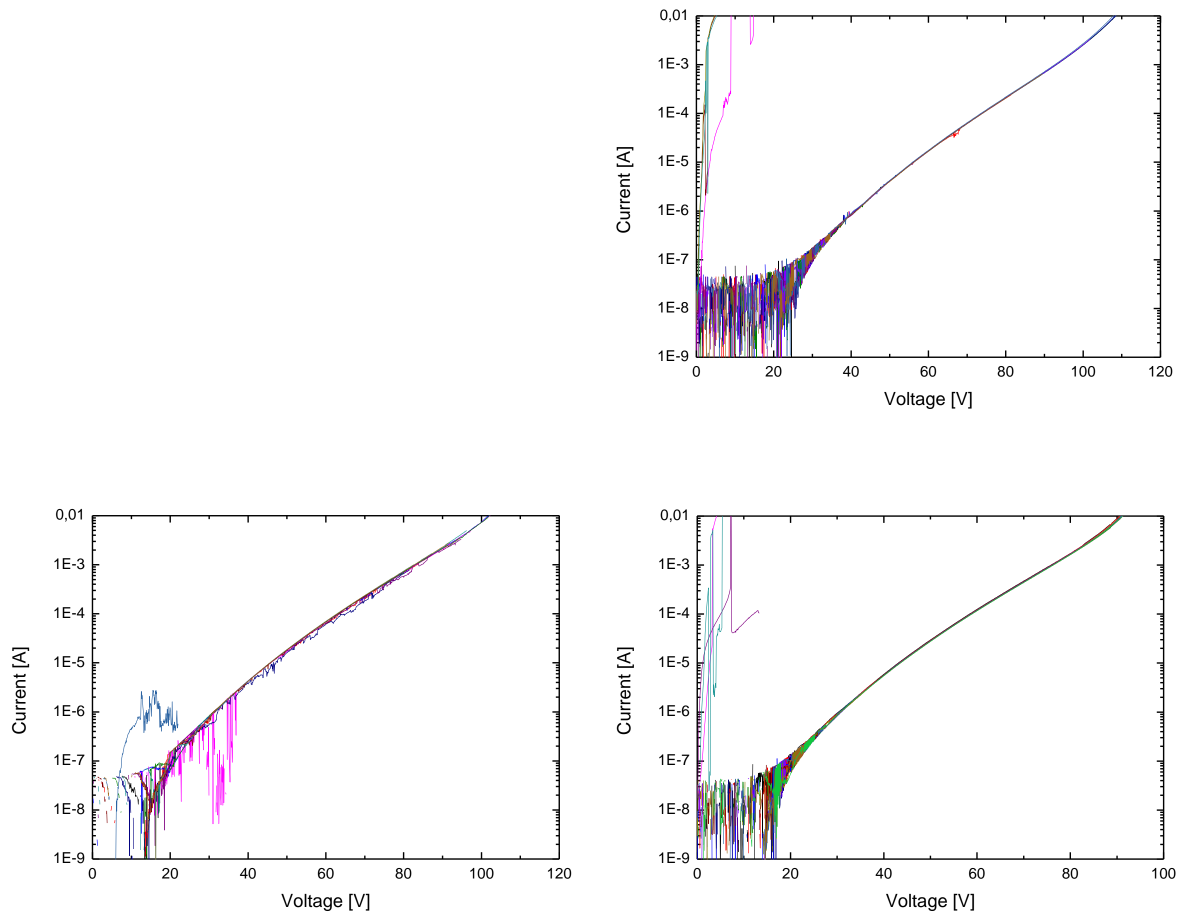

Figure 129: Current-voltage characteristics of 100 nm thin RF magnetron sputter deposited SiN_x thin film samples during a time-zero dielectric breakdown measurement performed at T = 120°C using 500 µm diameter pads. The deposition parameters were: 450 W/ 9 µbar (top right), 900 W/ 3 µbar (bottom left), and 900 W/ 9 µbar (bottom right), respectively.

40 nm thin RF sputtered films

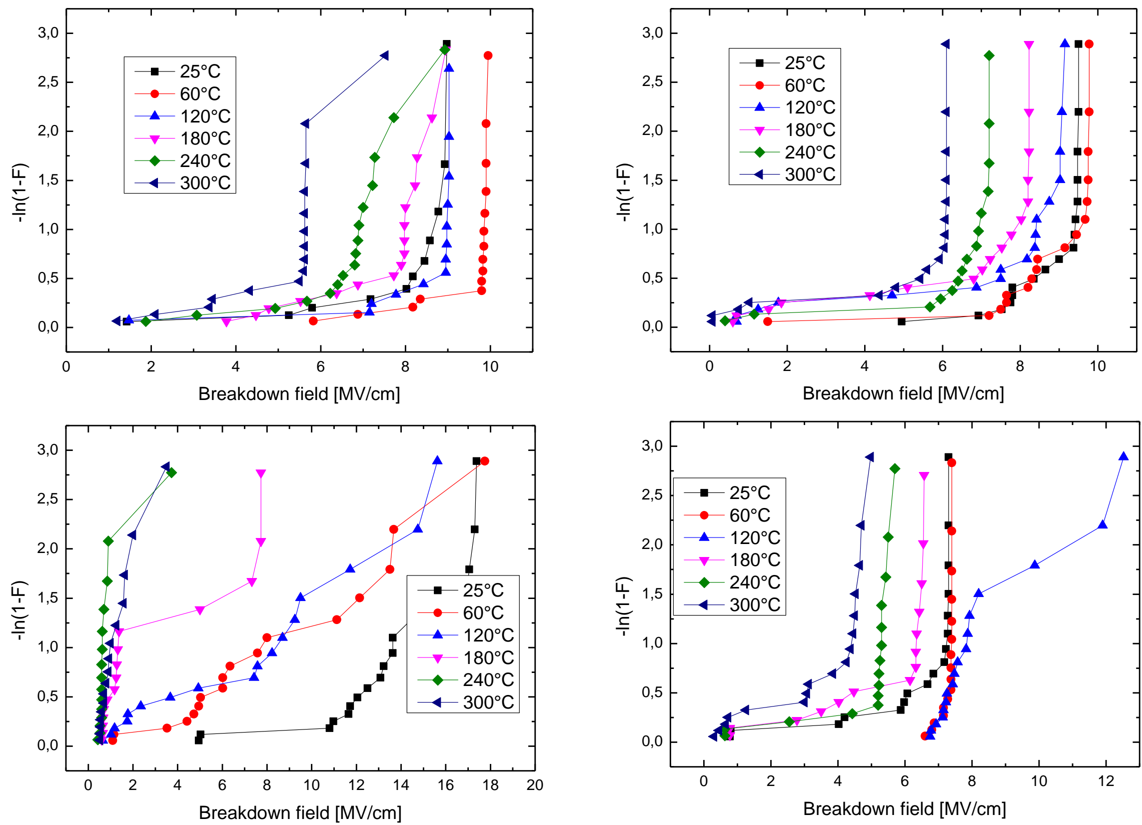

Figure 130: Weibull-plots of the dielectric breakdown strengths of 40nm thin DC magnetron sputter deposited SiN_x samples. Deposition parameters were (from top left to bottom right): 450 W/ 3µbar; 450 W/ 9 µbar; 900 W/ 3 µbar; 900 W/ 9 µbar.

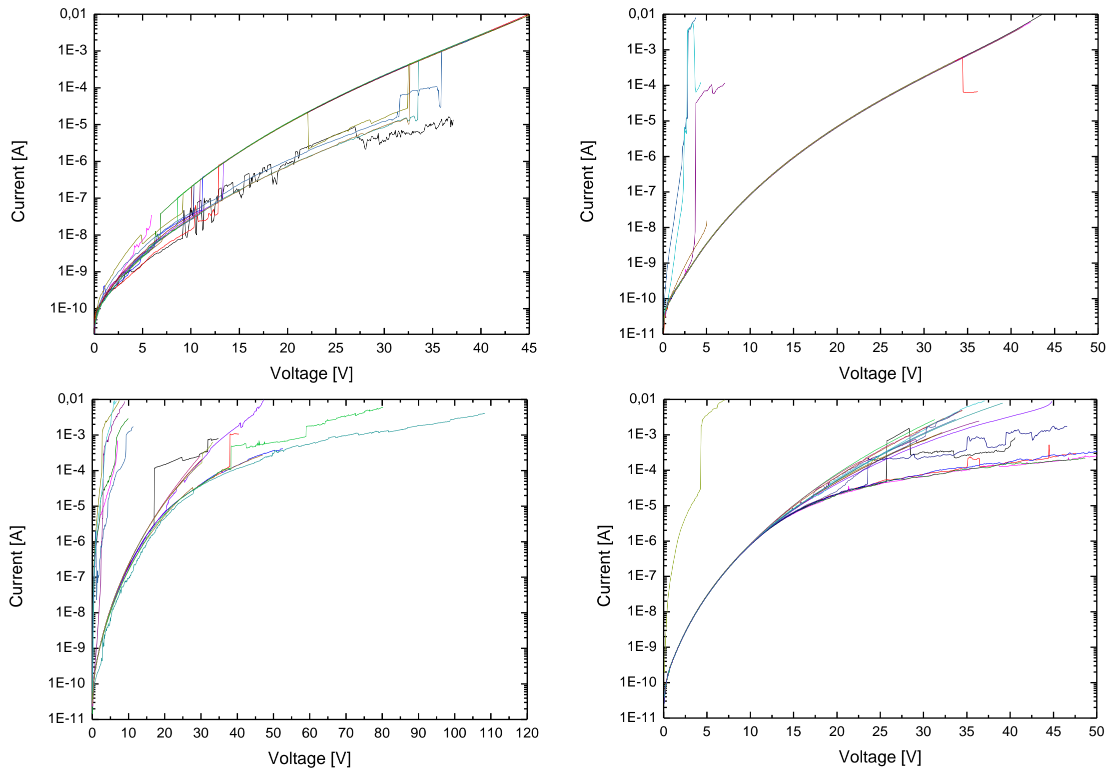

Figure 131: Current-voltage characteristics of 40 nm thin RF magnetron sputter deposited SiN_x samples during a time-zero dielectric breakdown measurement performed at T = 120°C using 500 µm diameter pads. Deposition parameter sets were (from top left to bottom right):450 W and 3µbar; 450 W and 9 µbar; 900 W and 3 µbar; 900 W and 9 µbar.

300 nm thin RF sputtered films

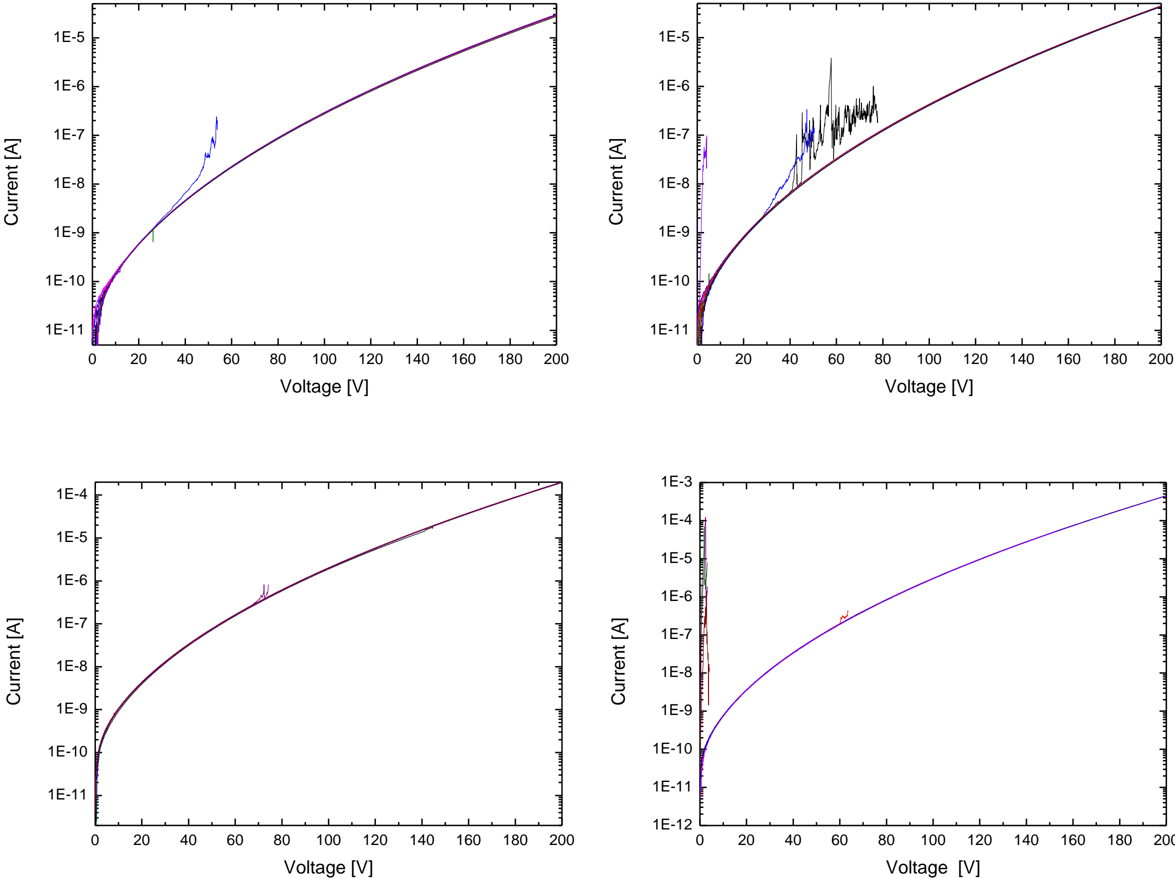

Figure 132: Current-voltage characteristics of 300 nm thin RF magnetron sputter deposited (450 W and 3 µbar) SiN_x samples during a time-zero dielectric breakdown measurement performed at T = 120°C using 500 µm diameter pads. Deposition parameter sets were (from top left to bottom right): 450 W and 3µbar; 450 W and 9 µbar; 900 W and 3 µbar; 900 W and 9 µbar.

H: Additional breakdown measurements of DC sputtered SiN_x thin films

100 nm thin DC sputtered films

For the curves with the parameter set of $P_{plasmaDC}$ = 450W and p_{back} = 9 µbar, see Chapter 6.4.

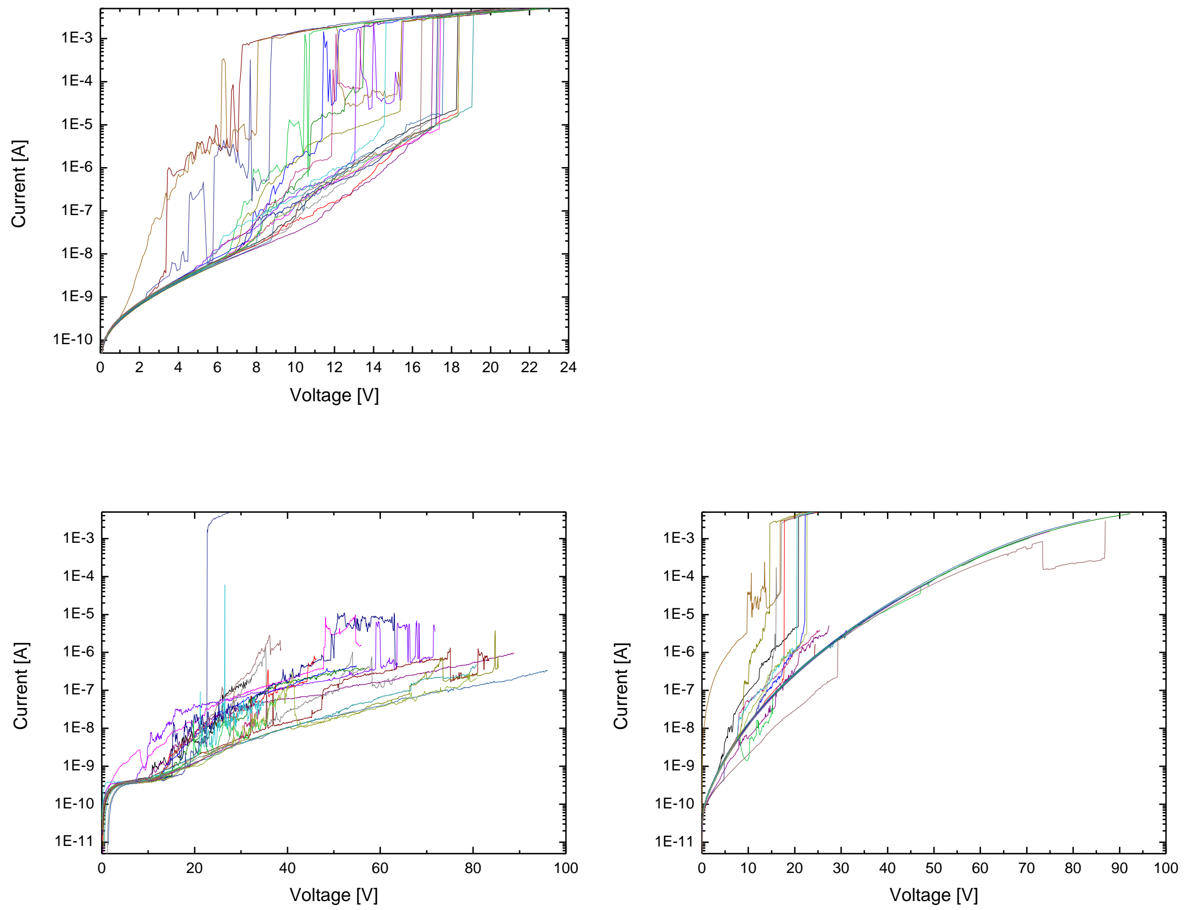

Figure 133: Current-voltage characteristics of 100 nm thin DC magnetron sputter deposited SiN_x samples during a time-zero dielectric breakdown measurement performed at T = 120°C using 500 µm diameter pads. The deposition parameters were: 450 W and 3 µbar (top left), 900 W and 3 µbar (bottom left), and 900 W and 9 µbar (bottom right), respectively.

40 nm thin DC sputtered films

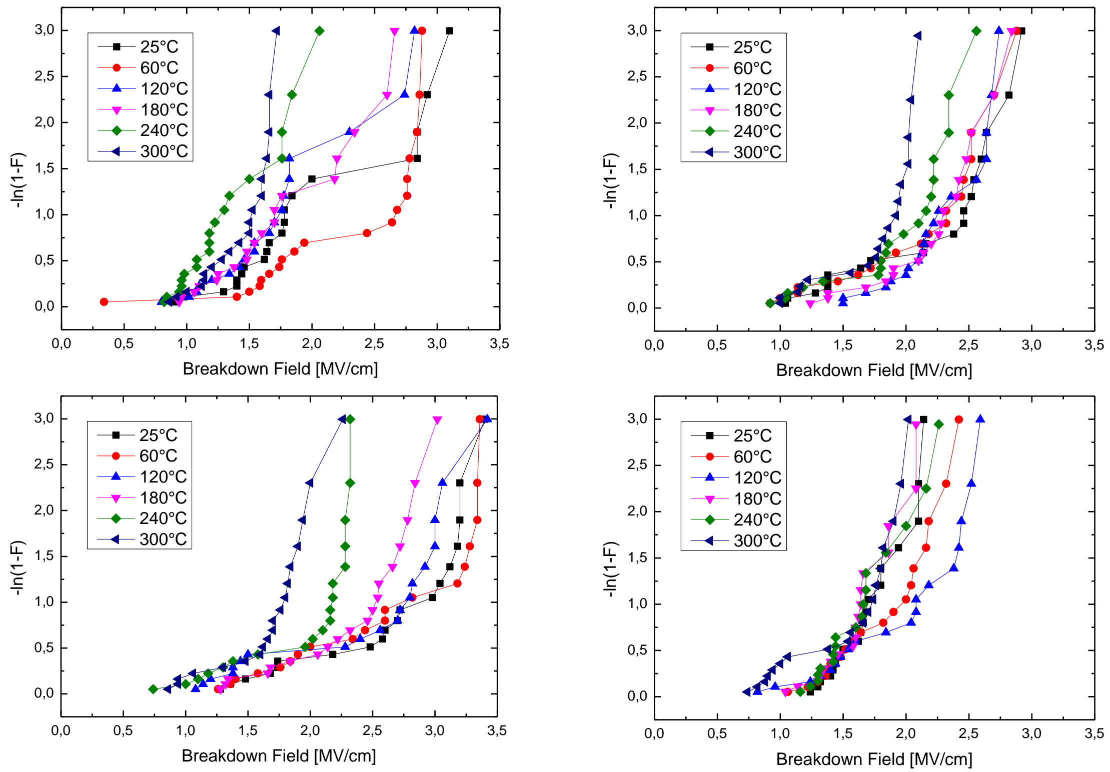

Figure 134: Weibull-plots of the dielectric breakdown strengths of 40 nm thin DC magnetron sputter deposited SiN_x samples. Deposition parameters were (from top left to bottom right): 450 W/ 3µbar; 450 W/ 9 µbar; 900 W/ 3 µbar; 900 W/ 9 µbar.

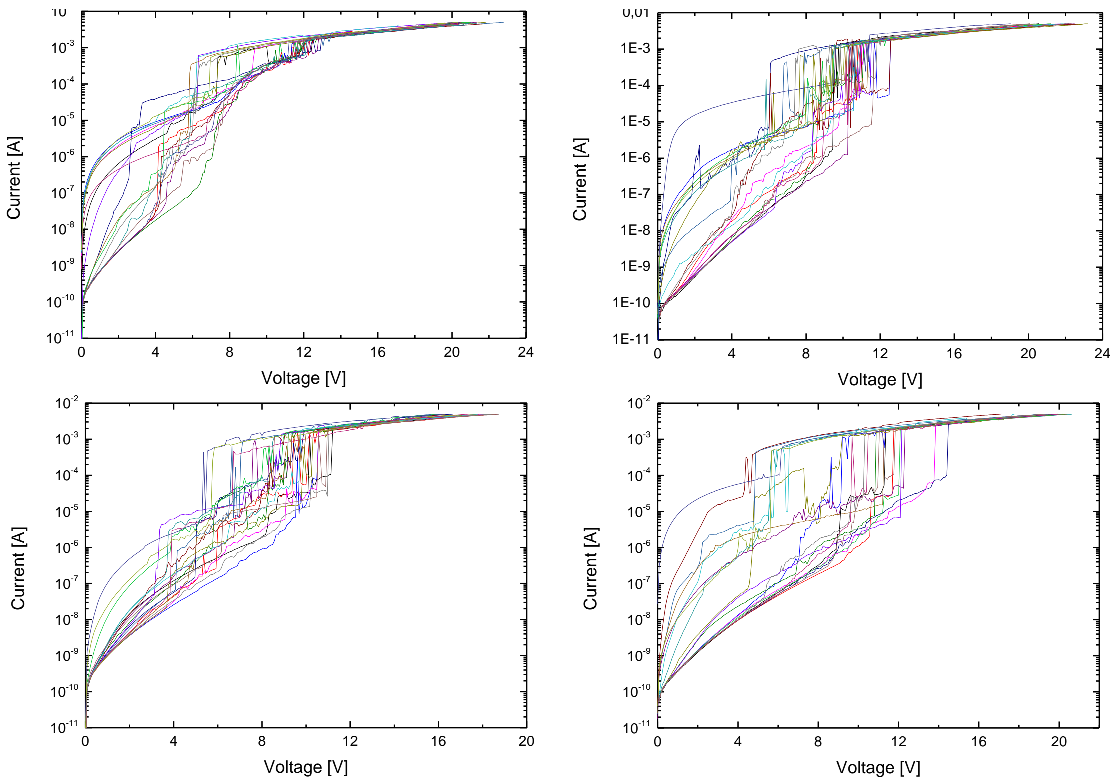

Figure 135: Current-voltage characteristics of 40 nm thin DC magnetron sputter deposited SiN_x samples during a time-zero dielectric breakdown measurement performed at T = 120°C using 500 µm diameter pads. Deposition parameter sets were (from top left to bottom right): 450 W/ 3 µbar; 450 W/ 9 µbar; 900 W/ 3 µbar; 900 W/ 9 µbar.

300 nm thin DC sputtered Films

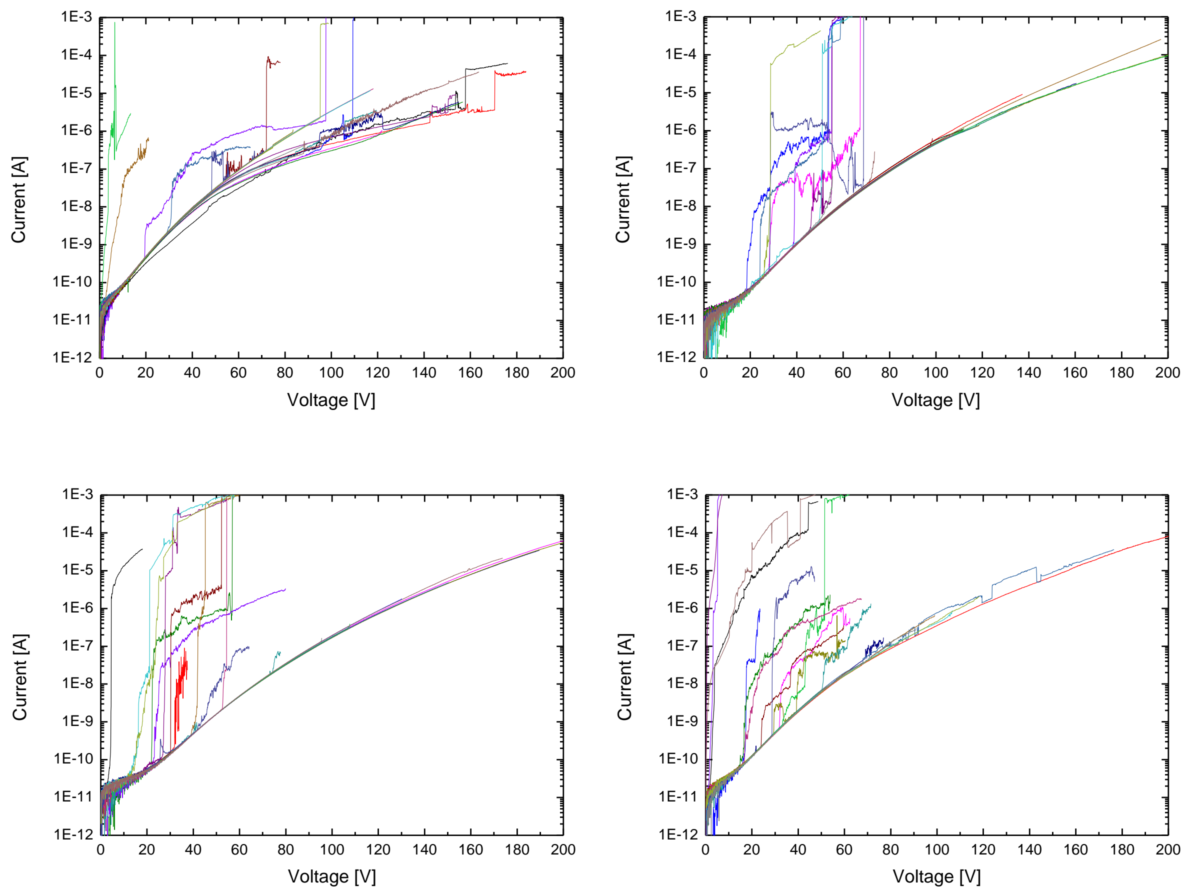

Figure 136: Current-voltage characteristics of 300 nm thin DC magnetron sputter deposited SiN_x samples during a time-zero dielectric breakdown measurement performed at T = 60°C using 500 µm diameter pads. Deposition parameter sets were (from top left to bottom right): 450 W and 3µbar; 450 W and 9 µbar; 900 W and 3 µbar; 900 W and 9 µbar.